



**HAL**  
open science

# Hydrogéologie des milieux volcaniques insulaires: apports d'une étude intégrée aux îles Galapagos

Alexandre Pryet

► **To cite this version:**

Alexandre Pryet. Hydrogéologie des milieux volcaniques insulaires: apports d'une étude intégrée aux îles Galapagos. Hydrologie. Université Pierre et Marie Curie - Paris VI, 2011. Français. NNT : . tel-00747313

**HAL Id: tel-00747313**

**<https://theses.hal.science/tel-00747313>**

Submitted on 31 Oct 2012

**HAL** is a multi-disciplinary open access archive for the deposit and dissemination of scientific research documents, whether they are published or not. The documents may come from teaching and research institutions in France or abroad, or from public or private research centers.

L'archive ouverte pluridisciplinaire **HAL**, est destinée au dépôt et à la diffusion de documents scientifiques de niveau recherche, publiés ou non, émanant des établissements d'enseignement et de recherche français ou étrangers, des laboratoires publics ou privés.

THÈSE DE DOCTORAT  
DE L'UNIVERSITÉ PIERRE ET MARIE CURIE

Spécialité: Sciences de la Terre, Hydrogéologie  
École doctorale Géosciences et Ressources Naturelles

présentée par

Alexandre PRYET

pour obtenir le grade de:

Docteur de l'Université Pierre et Marie Curie

---

**Hydrogeology of volcanic islands: a case-study  
in the Galapagos Archipelago (Ecuador)**

---

Soutenue le 28 Novembre 2012 devant le jury composé de:

M.	Ghislain de MARSILY	Président du Jury
M.	Philippe DAVY	Examinateur
M.	Bertrand AUNAY	Examinateur
M.	Jean-Paul LHOMME	Rapporteur
M.	Philippe RENARD	Rapporteur
M <sup>lle</sup>	Sophie VIOLETTE	Directeur de thèse
M.	Benoit DEFFONTAINES	Co-encadrant
M <sup>lle</sup>	Noémi D'OZOUVILLE	Invité



## Abstract

With a growing population and limited freshwater resources, the hydrogeology of the Galapagos Islands remains to a great extent unknown. Rainfall is relatively weak and unevenly distributed in space and time. The economical center of the archipelago, Santa Cruz Island, has only small intermittent streams, while several permanent streams are present on San Cristóbal Island. In the frame of this study, an interdisciplinary approach is used to characterize the hydrogeology of the archipelago.

A new method has been developed to enhance the interpretation of airborne electromagnetics surveys. With geostatistical interpolation techniques, this method allows the construction of a 3D grid of resistivity. SkyTEM surveys completed in Galapagos were processed with this technique, and confronted to surface analysis with remote sensing and field work. The first hydrogeological conceptual model is proposed for San Cristóbal Island.

Climatic conditions have been investigated with the installation of a monitoring network along the windward side of Santa Cruz Island. The occurrence of fog during six months of the year presents an additional input in the water budget and increases groundwater recharge. This input has been quantified with a physically based canopy interception model.

The basal aquifer of Santa Cruz Island has been investigated from the analysis of tidal signal propagation, hydraulic tests, as well as fault and fracture mapping. Results show that young basalts, densely fractured by cooling joints, are highly permeable. Because they are poorly connected, faults have a limited impact over regional groundwater flow.

Contrasting hydrogeological configurations in the Galapagos Islands are explained by an evolution pattern. In relatively young islands, such as Santa Cruz, basalts are fractured and permeable. Seawater intrusion is strong and freshwater rapidly flows to the ocean. On the opposite, conditions are more favorable for groundwater storage in older volcanic islands, where the regional permeability is smaller and valley incision leads to the existence of springs.

**Keywords:** Galapagos ; Groundwater ; Kriging ; Airborne electromagnetics ; Cloud water interception ; Tidal signal propagation.



## Résumé

Avec une population croissante et des ressources en eau de surface limitées, l'hydrogéologie des îles Galápagos reste pour une grande part inconnue. Les précipitations sont relativement faibles et inégalement réparties dans le temps et l'espace. Le centre économique de l'archipel, l'île de Santa Cruz, ne dispose que de quelques cours d'eau intermittents tandis que l'île de San Cristóbal présente plusieurs rivières pérennes. Dans le cadre de ce travail, une approche pluridisciplinaire est utilisée afin de caractériser l'hydrogéologie de l'Archipel.

Une nouvelle technique d'interprétation des sondages électromagnétiques hélicoptérés a été développée. Grâce à des méthodes géostatistiques, elle permet la construction d'une grille 3D de la résistivité électrique. Les données issues de la mission SkyTEM réalisée sur les îles de Santa Cruz et San Cristóbal en 2006 sont mises en perspectives. Confrontée aux observations de surface collectées par télédétection et sur le terrain, la géophysique permet de proposer un modèle conceptuel pour l'île de San Cristóbal.

Les conditions climatiques ont été suivies avec la mise en place de stations météorologiques le long du versant au vent de l'île de Santa Cruz. La présence de brouillard pendant 6 mois de l'année représente un apport supplémentaire pour la recharge des aquifères. Cet apport a été quantifié avec une méthode basée sur un modèle d'interception à base physique.

L'aquifère de base de l'île de Santa Cruz a été étudié avec la propagation du signal de marée, des essais de pompage, et la cartographie de la fracturation. Ces travaux montrent que les basaltes "jeunes" fracturés ont une forte perméabilité. En revanche, les failles n'ont qu'un effet limité sur l'hydrogéologie régionale, car elles sont peu connectées.

Les configurations hydrologiques contrastées au sein de l'archipel sont expliquées par un schéma d'évolution. Dans les îles relativement jeunes, telles que Santa Cruz, les basaltes fracturés sont perméables. Ils offrent peu de résistance à l'intrusion saline et l'eau douce est rapidement drainée jusqu'à la mer. Les conditions sont plus favorables dans les îles plus âgées. Les perméabilités plus faibles et l'incision des vallées permettent l'émergence de sources.

**Mots-clés :** Galapagos ; Hydrogéologie ; Krigeage ; Electromagnétique aéroporté ; Précipitations occultes ; Propagation du signal de marée.



## Resumen

A pesar de la falta de agua dulce, la población de las islas Galápagos sigue creciendo. Las precipitaciones son escasas y mal distribuidas en el tiempo y el espacio. El centro económico del Archipiélago, la Isla Santa Cruz, ni siquiera tiene un río permanente mientras que San Cristóbal, situada a 70 km al este, tiene numerosos. Este estudio se basa en un enfoque multidisciplinario para caracterizar la hidrogeología del Archipiélago y interpretar estos contrastes.

Una nueva técnica ha sido desarrollada para visualizar los modelos geofísicos de sondeos electromagnéticos aerotransportados en 3D. Los datos recogidos en las islas San Cristóbal y Santa Cruz fueron visualizados y analizados con datos geomorfológicos. Un primer modelo conceptual hidrogeológico ha sido propuesto para la isla San Cristóbal.

Una red de monitoreo hidroclimático fue instalado en el lado barlovento de la Isla Santa Cruz para caracterizar el gradiente climático. La presencia de neblina durante la temporada de garúa agrega un aporte adicional en el balance hídrico de la parte alta de la isla. Este aporte ha sido cuantificado a partir de un modelo de intercepción con bases físicas.

El acuífero basal ha sido caracterizado a partir de un estudio de la propagación de la onda de marea, pruebas de bombeo y un mapeo de la fracturación de las rocas basálticas. Estos estudios muestran que los basaltos jóvenes, altamente fracturadas, tienen una alta permeabilidad. Sin embargo, las fallas tienen un efecto limitado sobre la hidrogeología regional, debido a que no están conectadas.

Las configuraciones hidrogeológicas contrastadas en las Islas Galápagos pueden ser interpretadas con un modelo de evolución. En las islas relativamente jóvenes como Santa Cruz, las rocas basálticas permeables ofrecen poca resistencia a la intrusión salina y el agua dulce rápidamente llega al mar. Las condiciones son más favorables en las islas con mayor edad geológico. Las permeabilidades más bajas pueden retener el agua dulce y la presencia de encañadas profundas permite la aparición de fuentes.

**Palabra clave :** Galápagos ; Hidrogeología ; Geoestadístico ; Geofísica aerotransportada ; Intercepción de la neblina.



## Avant Propos

Cette thèse a été réalisée d’octobre 2008 à octobre 2011 au sein de l’UMR Sisyphe de l’Université Pierre et Marie Curie à Paris, sous la direction de Sophie Violette. Elle s’inscrit dans le projet “Galapagos Islands Integrated Water Studies” (GIIWS), initié par Noémi d’Ozouville et Sophie Violette en 2002.

Ces recherches ont été effectuées en collaboration avec de nombreux partenaires en France comme à l’international, dont Benoit Deffontaines (*UPE, Laboratoire GTMC, Marne-La-Vallée*), Jean-Paul Chilès (*MINES ParisTech, Centre de Géoscience, Fontainebleau*), James Ramm et Esben Auken (*Hydrogeophysic Group, Université de Aarhus, Danemark*), Marcos Villacís, Christian Dominguez, et Andrés González (*Université Polytechnique de Quito, Equateur*), Pilar Fuente Tomai (*Ecole de Génie Forestier, Université Polytechnique de Madrid, Espagne*), Jérôme Fortin (*Laboratoire de Géologie, ENS, Paris*), Pierre Adler et Tan Minh Vu (*Sisyphe, UPMC, Paris*).

Pour faciliter la diffusion des résultats, cette thèse est rédigée en anglais. Chaque chapitre suit la structure d’une communication scientifique standard. Un article a été accepté, un autre soumis, et deux supplémentaires le seront prochainement. Certaines informations peuvent ainsi paraître redondantes, mais elles autorisent la lecture indépendante de chacun des chapitres.



## Remerciements

C'est avec un peu d'appréhension que j'aborde la partie de ma thèse qui sera probablement la plus lue. Mais je le fais de bon coeur car ce travail a bénéficié de la participation de très nombreuses personnes, que je tiens à remercier ici.

Noémi d'Ozouville a eu l'audace de commencer ce projet, ce sans quoi je n'aurais pu le continuer. Je la remercie aussi pour ses commentaires et corrections sur mes travaux. Merci à Sophie Violette de m'avoir accordé une grande confiance tout au long de ce projet et de m'avoir donné tous les moyens pour conduire ces recherches, je lui en suis très reconnaissant.

Benoit Deffontaines m'a accompagné des premiers aux derniers jours de cette thèse. Ses encouragements, sa motivation et son imagination "sans faille" ne l'ont pas empêché d'en faire la cartographie à Puerto Ayora.

Merci à tous ceux qui m'ont apporté leur expertise au long de cette thèse. Un grand merci à Jean-Paul Chilès pour sa disponibilité, ses connaissances en géostatistiques ont apporté beaucoup à cette étude. Merci à Jérôme Fortin pour ses nombreux conseils et corrections. Les nombreuses astuces et la participation de Cédric Chaumont ont été d'une grande aide pour l'installation des stations météo.

Mon entrevue avec Jacques Bertrand, organisée par Ghislain de Marsily m'a fait comprendre beaucoup sur le rôle d'un chercheur aux Galapagos, je tiens à les remercier tous deux. Merci à Marcos Villacís, qui m'a apporté un point de vue original sur ce travail.

Tout au long de cette thèse, j'ai reçu le soutien de nombreux étudiants français, équatoriens, et espagnol : Christian Dominguez, Pilar Fuente Tomai, Andrés Gonzales, Justine Lichter, Wafa Ramdani, David Fauchet. Non seulement ils ont apporté beaucoup, que ce soit sur le terrain ou à Paris, mais ce fut un grand plaisir de travailler avec eux.

Des recherches aux Galapagos, cela ne se réussit pas sans le soutien logistique de Sisyphe. Dans le carcan des lourdeurs administratives, rares sont les gestionnaires sympathiques qui comprennent ce qu'est la réalité de terrain. Valérie Girard fait partie de ceux là, je tiens à la remercier.

Même si j'étais souvent en vadrouille, j'ai passé de très bons moments à Sisyphe. Un grand merci à Jacques Thibiéroz, "le" géologue de Sisyphe qui m'a fait découvrir la géologie des Cévennes et les joies du pastis saucisson devant le lac de Villefort.

Les relations du labo, c'est avant tout au bureau. J'ai souvent décliné les proposition de thé de Paul. Son breuvage dilué dans de l'eau bouillie et rebouillie

puis dégusté dans une tasse crasseuse m'a rarement tenté. Claire, dommage que tu sois arrivée si tard, même si tu nous as fait peur avec ta coqueluche. Wilfried a participé à la décoration du bureau avec les post-it (et les pages de codes "Stics"). Depuis les Galapagos, un grand merci à ces co-bureaux qui imprimeront ma thèse, ce n'est pas un détail.

J'ai eu la chance de garder de bonnes relations avec mes "ex" : Vincent et Guillaume. Je ne ferai pas l'inventaire des "craquages", mais le lancé d'une poule pleine de vieux café au travers du bureau reste inoubliable [*Vilain*, 2010].

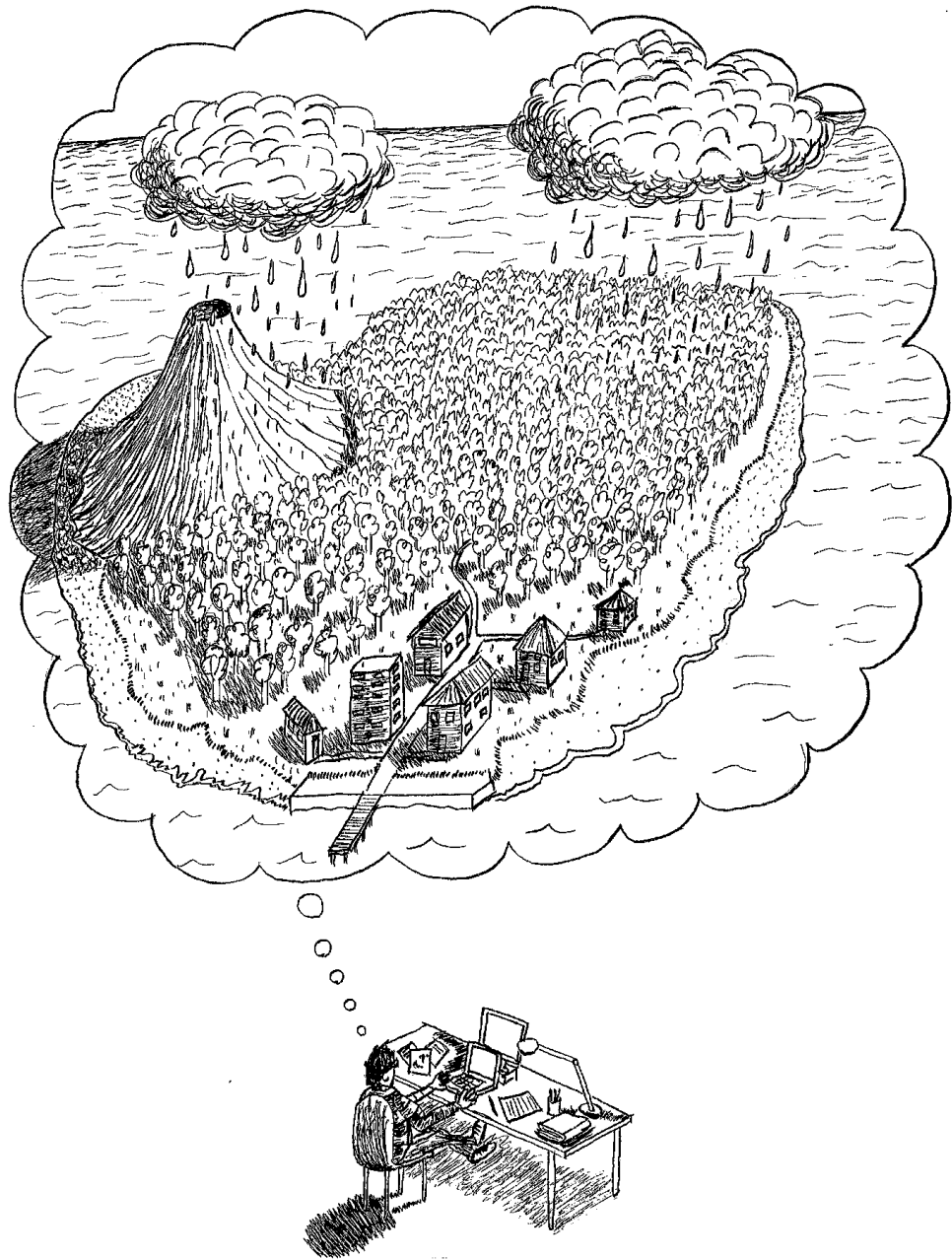
Heureusement, les relations du labo ne s'arrêtent pas au bureau. L'inévitable café du matin était pris avec François, qui par ailleurs ne manquait pas non plus la bière du soir. Agnès étais aussi au rendez des Cigognes, un bar mythique qui sans surprise mais avec grand regret a fait faillite.

We spent hours with James in the Galapagos fog trying to acquire magnetic decay, whose results were not even worth presenting in this thesis. Nevertheless, working with him was fun and even profitable as we finally managed to visualize the SkyTEM results in 3D. I'm very grateful to Esben Auken for his subliminal but brilliant interventions and continuous backing.

A mis buenos compañeros de Galápagos, fue un gran placer trabajar y disfrutar de la vida con ustedes. Gracias a todos, no solo aprendí el Español, pero pasé momentos geniales, bailando, poco borracho en El Bongo o todavía peor, más tarde a la Panga. Todd, Carlos, Ángela, Maria-Fernanda, Josselin, Andrea, Jessie, . . . casi todos se fueron de Galápagos, pero hemos pasado buenos momentos. Mucha consideración a Christian, con el hicimos todo desde nada. Pilar, nuestra especialista de la selva, lo siento por el estrés de la EGU pero eres una chica genial, muchas gracias por tu participación. Andrés, fue un gran placer trabajar con tigo, suerte para tu tesis.

Merci à mes parents et amis, désolé d'avoir été lointain pendant ces trois ans. Merci à Marie-Madeleine, d'avoir toléré mes absences prolongées lors des missions, et sans rancune, de m'avoir aidé pour le choix des couleurs dans les figures. Sans toi, j'aurais peut-être écrit un chapitre de plus. Mais avec toi, j'ai pu garder une vie suffisamment équilibrée pour envisager l'avenir, ce qui est l'essentiel.

*Puerto Ayora, Galapagos le 10 octobre 2011*



*Writing a thesis on the Galapagos Islands. Artist view by David, hydrogeologist and excellent friend.*



*Caminante no hay camino, se hace camino al andar.*<sup>1</sup>

Antonio Machado

*The power of accurate observation is commonly called cynicism by those who  
have not got it*

George Bernard Shaw

---

<sup>1</sup>“wanderer, there is no road, the road is made by walking”.



# Contents

List of Figures	xix
List of Tables	xxiii
<b>I General Introduction</b>	<b>1</b>
<b>1 Context</b>	<b>5</b>
1.1 Geographical context . . . . .	6
1.2 Geological context . . . . .	7
1.3 Climatic conditions . . . . .	10
1.4 Ecological singularity . . . . .	13
1.5 Historical background . . . . .	16
1.6 The water issue in the Galapagos Islands . . . . .	19
<b>2 Methodology</b>	<b>25</b>
2.1 The approach . . . . .	26
2.2 Timeline . . . . .	27
2.3 Structure of this dissertation . . . . .	28
<b>II Internal structure</b>	<b>33</b>
<b>3 Hydrogeology of basaltic islands</b>	<b>37</b>
3.1 Introduction . . . . .	39
3.2 Volcanic rocks and edifices . . . . .	42
3.3 Hydraulic properties of volcanic formations . . . . .	49
3.4 Recharge processes . . . . .	53
3.5 Groundwater occurrence . . . . .	55
3.6 Discussion . . . . .	62
3.7 Conclusions . . . . .	68

<b>4</b>	<b>3D resistivity gridding of AEM surveys</b>	<b>71</b>
4.1	Introduction . . . . .	73
4.2	Methodology . . . . .	74
4.3	Uncertainties and validation . . . . .	77
4.4	Case study: Galapagos Islands, Ecuador . . . . .	80
4.5	Conclusion . . . . .	88
4.6	Acknowledgements . . . . .	88
<b>5</b>	<b>Hydrogeological framework of San Cristóbal</b>	<b>91</b>
5.1	Introduction . . . . .	93
5.2	Geographical settings . . . . .	94
5.3	Structural and hydrological analysis . . . . .	96
5.4	Airborne electromagnetics SkyTEM survey . . . . .	102
5.5	Discussion . . . . .	107
5.6	Conclusions . . . . .	115
5.7	Acknowledgments . . . . .	115
<b>III</b>	<b>Recharge processes</b>	<b>117</b>
<b>6</b>	<b>Quantification of cloud water interception</b>	<b>121</b>
6.1	Introduction . . . . .	123
6.2	Study Area . . . . .	124
6.3	Materials and methods . . . . .	130
6.4	Results . . . . .	138
6.5	Discussion . . . . .	146
6.6	Summary and conclusions . . . . .	150
6.7	Acknowledgments . . . . .	152
<b>IV</b>	<b>Groundwater flow</b>	<b>153</b>
<b>7</b>	<b>Modeling basal aquifers</b>	<b>157</b>
7.1	Introduction . . . . .	159
7.2	Analytical solutions . . . . .	162
7.3	Numerical modeling . . . . .	170
7.4	Discussion . . . . .	176
7.5	Conclusion . . . . .	183
<b>8</b>	<b>The basal aquifer of Santa Cruz Island</b>	<b>185</b>
8.1	Introduction . . . . .	187
8.2	Geographical settings . . . . .	187

8.3	Structural analysis and fracture mapping . . . . .	194
8.4	Hydraulic properties . . . . .	200
8.5	Discussion . . . . .	216
8.6	Conclusions . . . . .	217
8.7	Acknowledgments . . . . .	218
<b>9</b>	<b>High-level groundwater in Santa Cruz Island</b>	<b>219</b>
9.1	Introduction . . . . .	221
9.2	Climatic conditions . . . . .	223
9.3	Re-processing of geophysical data . . . . .	230
9.4	Discussion . . . . .	241
9.5	Conclusion . . . . .	244
	Appendix . . . . .	245
<b>V</b>	<b>Conclusions</b>	<b>247</b>
<b>10</b>	<b>Hydrogeology of basaltic volcanic islands in perspectives</b>	<b>249</b>
10.1	AEM surveys in volcanic contexts . . . . .	250
10.2	Fog interception . . . . .	251
10.3	Evolution of basaltic islands . . . . .	251
<b>11</b>	<b>Solutions for Galapagos</b>	<b>255</b>
11.1	Conceptual models for Santa Cruz and San Cristóbal Islands . . .	256
11.2	Solving the Galapagos “water issue” . . . . .	257
<b>12</b>	<b>Perspectives</b>	<b>259</b>
	<b>References</b>	<b>261</b>
<b>VI</b>	<b>Appendices</b>	<b>285</b>
<b>A</b>	<b>Carbon footprint of this thesis</b>	<b>287</b>



# List of Figures

1.1	Map of the Galapagos Islands . . . . .	6
1.2	3D view of the Galapagos Archipelago . . . . .	7
1.3	Ages of the main inhabited islands of the Galapagos Archipelago . . . . .	8
1.4	The Central Pacific Dry Zone, by <i>Colinvaux</i> [1972] . . . . .	11
1.5	Climatic patterns at Puerto Ayora . . . . .	11
1.6	Vegetation staging along the windward slope of Santa Cruz Island . . . . .	12
1.7	Photograph from Puerto Ayora, Santa Cruz . . . . .	13
1.8	Engraving: “Catching Turtle.” In “Cruise of the Essex” . . . . .	14
1.9	Blue footed boobies are very good parents. . . . .	15
1.10	Sea lions resting on a beach . . . . .	15
1.11	Statistics on touristic admissions in the Galapagos Archipelago . . . . .	18
2.1	Objectives of the thesis and structure of this document . . . . .	27
3.1	Worldwide system of hot-spots . . . . .	39
3.2	A hot-spot based schematic model for the evolution of a <i>Mercedes-type</i> rift zone . . . . .	43
3.3	Structure of a lava flow sequence . . . . .	45
3.4	Review of hydraulic conductivities reported in basaltic contexts . . . . .	52
3.5	Distribution of mean annual rainfall over La Réunion Island . . . . .	54
3.6	Review of conceptual models proposed for basaltic volcanic islands . . . . .	56
3.7	Hydrogeological conceptual model developed for low-lying basal aquifer of the Hawaiian Islands . . . . .	57
3.8	Conceptual model proposed by <i>Join et al.</i> [2005] for La Fournaise volcano (La Réunion Island) . . . . .	57
3.9	Groundwater flow pattern proposed by <i>Violette et al.</i> [1997] for La Fournaise volcano (Réunion Island) . . . . .	60
3.10	Simplified sketch of a freshwater basal aquifer . . . . .	62
3.11	Freshwater aquifer water table height for varying $\chi$ and $\xi$ values . . . . .	64
3.12	Shape of the water table height $h'$ for various values of $\chi$ . . . . .	64

3.13	Geological age of principal basaltic oceanic islands and conceptual models proposed for the basal aquifer . . . . .	66
4.1	3D gridding of resistivity . . . . .	75
4.2	Validation of the prediction method using data split into two subsets	79
4.3	Location of SkyTEM survey . . . . .	81
4.4	Sample variograms and models used for the interpolation of the first geophysical layer . . . . .	83
4.5	Analysis of misfit between original models and interpolated from S1 subset over S2 area . . . . .	84
4.6	Uncertainty on log-transformed resistivity of the first layer . . . .	85
4.7	3D view of SkyTEM survey on Santa Cruz Island reveals the geometry of a large low-resistivity formation . . . . .	86
4.8	3D view of total uncertainty on resistivity, integrating error from both inversion and interpolation processes . . . . .	87
5.1	Geographical context of San Cristóbal Island . . . . .	95
5.2	Surface morphology of the southwestern shield of San Cristóbal island . . . . .	97
5.3	Photographs of San Cristóbal island . . . . .	99
5.4	Mapping of streams on San Cristóbal . . . . .	101
5.5	Typology of springs . . . . .	102
5.6	Geophysical results of San Cristóbal . . . . .	104
5.7	Depth to the <i>Salt Water Interface</i> (SWI) . . . . .	105
5.8	3D view of the SkyTEM 4-layer resistivity model . . . . .	108
5.9	Hydrogeological conceptual model for San Cristóbal Island . . . .	109
5.10	Comparison of the southern watersheds of San Cristóbal and Santa Cruz . . . . .	111
5.11	Distribution of elevations along the windward watersheds of San Cristóbal and Santa Cruz . . . . .	112
5.12	Evolution pattern of basaltic shields from observations in Santa Cruz and San Cristóbal Islands . . . . .	114
6.1	Santa Cruz Island, at the center of Galapagos Archipelago (Ecuador)	125
6.2	Vegetation zonation along the windward slope of Santa Cruz island	126
6.3	The two instrumented study plots . . . . .	129
6.4	Schematic summary of the modified Rutter interception model . .	133
6.5	2010 context compared to 1985-2010 records . . . . .	139
6.6	Weekly rainfall records for CDF2, MESF and HEES stations . . .	139
6.7	Estimation of canopy characteristics $p$ and $S$ with the within-event analysis . . . . .	142

6.8	Climatic variables and modeled canopy water storage . . . . .	144
6.9	Statistics of cloud water interception rates classified for four wind speed intervals at the HEES plot . . . . .	145
6.10	Canopy water budget at the MESF plot and the HEES plot . . . . .	149
7.1	Two configurations reported for the basal aquifer . . . . .	159
7.2	Symmetry of volcanic islands edifices . . . . .	160
7.3	Description of the first model, a freshwater aquifer with a constant head at the coast . . . . .	162
7.4	Description of the second model: seawater intrusion is modeled with the Ghyben-Herzberg assumptions. . . . .	163
7.5	Description of <i>Verruijt</i> [1968] model . . . . .	166
7.6	Water table and SWI estimated from the analytical solutions for two different configuration . . . . .	168
7.7	Geometry of the numerical model . . . . .	170
7.8	Result of the coupled simulation for case 1 . . . . .	176
7.9	Water table heights and SWI from the numerical model compared to the analytical solutions, case 1 . . . . .	177
7.10	Fields of equivalent freshwater head and relative salt concentration, case 1 . . . . .	178
7.11	Water table heights and SWI from the numerical model compared to the analytical solutions, case 2 . . . . .	179
7.12	Relative error $\epsilon'$ on water table estimates with respect to the numerical model estimate . . . . .	180
7.13	Freshwater aquifer water table height at a mid-distance from the coast for varying $\chi$ and $\xi$ values . . . . .	181
7.14	Shape of the water table height for various values of $\chi$ . . . . .	182
8.1	The coastal apron in the vicinity of Puerto Ayora . . . . .	188
8.2	Fault scarps on the southern apron of Santa Cruz Island . . . . .	190
8.3	Hydrogeological diagram of the basal aquifer of Santa Cruz Island . . . . .	191
8.4	Fractures mapped with Google Earth® . . . . .	195
8.5	Block diagram and Google-Earth images displaying the termination of a fault with a ramp and ramified tension joints . . . . .	196
8.6	Structural diagram of Puerto Ayora grabben . . . . .	197
8.7	Fracture mapping at <i>Grieta Finch</i> . . . . .	199
8.8	Statistics on fracture network from mapping along fault scarps <i>Finch</i> . . . . .	200
8.9	Filtering of water level records . . . . .	203
8.10	Data processing of water level records . . . . .	203
8.11	Tidal signal at <i>Grieta FCD</i> . . . . .	204

8.12	Cross-correlation diagram between the high-frequency components of sea level and groundwater level . . . . .	205
8.13	Linear regression of the amplitude ratio $\ln(\alpha)$ and phase shift $\Delta t$ .	206
8.14	Linear regression of the amplitude ratio $\ln(\alpha)$ and phase shift $\Delta t$ (subset) . . . . .	207
8.15	Characteristic curve of the pumping well from multiple step well test. . . . .	209
8.16	Pumping test under the influence of tidal fluctuations . . . . .	212
8.17	Idealized network of hexagonal columnar vertical cooling joints . .	213
9.1	Geophysical cross-sections from [ <i>d'Ozouville et al.</i> , 2008a] . . . . .	221
9.2	The three simplified hydrogeological conceptual models that could be <i>a priori</i> proposed for Santa Cruz Island. . . . .	222
9.3	Eco-climatic staging of the windward slope of Santa Cruz Island .	224
9.4	Hydrological conceptual model of the very humid zone . . . . .	225
9.5	Rainfall records at the four weather stations for 2010/2011 . . . . .	226
9.6	Seasonal distribution of rainfall and orographic gradient . . . . .	227
9.7	Surface resistivity of the 19 layers resistivity model. . . . .	230
9.8	3D View of the 50-200 ohm.m resistivity threshold . . . . .	231
9.9	3D View of the 30-70 ohm.m resistivity threshold, draped by the DEM from <i>d'Ozouville et al.</i> [2008b]. . . . .	232
9.10	Cross sections in the 3D resistivity grid . . . . .	233
9.11	Depth from ground surface (threshold 50-200 ohm.m) . . . . .	235
9.12	Depth from ground surface (threshold 30-70 ohm.m) . . . . .	235
9.13	Thickness (threshold 50-200 ohm.m) . . . . .	236
9.14	Thickness (threshold 30-70 ohm.m) . . . . .	236
9.15	Slope (threshold 50-200 ohm.m) . . . . .	237
9.16	Slope (threshold 30-70 ohm.m) . . . . .	237
9.17	Depth to the Salt Water Interface (SWI) . . . . .	238
9.18	Small portion of a perched aquifer over an impervious layer, with recharge flux $\phi$ restricted to the left boundary . . . . .	241
9.19	Idealized model of a perched aquifer. . . . .	245
10.1	Simplified evolution sketch of the hydrogeological settings of basaltic islands . . . . .	251
11.1	Simplified hydrogeological conceptual models proposed for Santa Cruz and San Cristóbal islands . . . . .	256
A.1	Carbon emissions (CO <sub>2</sub> /year) . . . . .	288

# List of Tables

3.1	Statistics on basaltic volcanic islands: population, rainfall, and age.	40
3.2	Characteristics of hydrogeological numerical models implemented for volcanic islands basal aquifers . . . . .	51
4.1	Variogram model parameters of the log-transformed resistivity . .	82
5.1	Springs identified by <i>Adelinet</i> [2005] and further field studies . . .	100
6.1	Physical conditions and characteristics of the vegetation at the two study plots . . . . .	128
6.2	Canopy characteristics as used in the modified <i>Rutter</i> model . . .	141
7.1	Parameter values chosen for the two simulations. . . . .	174
7.2	Values and descriptions of parameters kept constant for the simulations. . . . .	174
8.1	Location of monitoring points in the basal aquifer . . . . .	192
8.2	Characteristics of the two wells (loc. 7, Fig. 8.1) . . . . .	193
8.3	Results of the multiple step pumping test on the <i>pozo testigo</i> pumping well [ <i>Dixon Hydrogeology Limited</i> , 1996] . . . . .	209
8.4	Results of fracture mapping at the outcrop scale . . . . .	215
9.1	Statistics on rainfall heights measured at stations CDF1 and CDF2	227
9.2	Statistics on the geometry of 50-200 and 30-70 ohm.m thresholds .	239
A.1	Carbon emissions per flights (roundtrip from Paris) . . . . .	287



**Part I**  
**General Introduction**



This dissertation deals with the hydrogeology of basaltic islands, with a focus on the Galapagos Archipelago. At the exception of one island, this world famous archipelago is nearly devoid of freshwater. Hydrogeological settings are poorly known, basic climatic data are missing and there are few drill holes. A multidisciplinary approach was implemented to answer following questions: *Where is fresh groundwater ? What are recharge processes ? What are the factors explaining the contrasting configurations from one island to the other?*

This first part, **General Introduction** presents the context and methodology of this thesis.

Chapter *Context* presents the geological, climatic and ecological singularities of the Galapagos Islands. A brief historical summary is proposed, followed by a description of the “water issue” in the Galapagos Islands.

Chapter *Methodology*, presents the interdisciplinary problematic of this thesis and details the different phases of its development.



# Chapter 1

## Context

## 1. CONTEXT

---

### 1.1 Geographical context

The Galapagos Archipelago straddles the Equator, 90° west of *Greenwich*. It is located in the Pacific Ocean, 1000 km west of the South-American continent. There are 15 main islands, 3 smaller islands, and 107 rocks and islets (Fig. 1.1). Isabela is the largest and biggest island of the archipelago, culminating on Isabela Island at Volcan Wolf, 1707 m a.s.l.

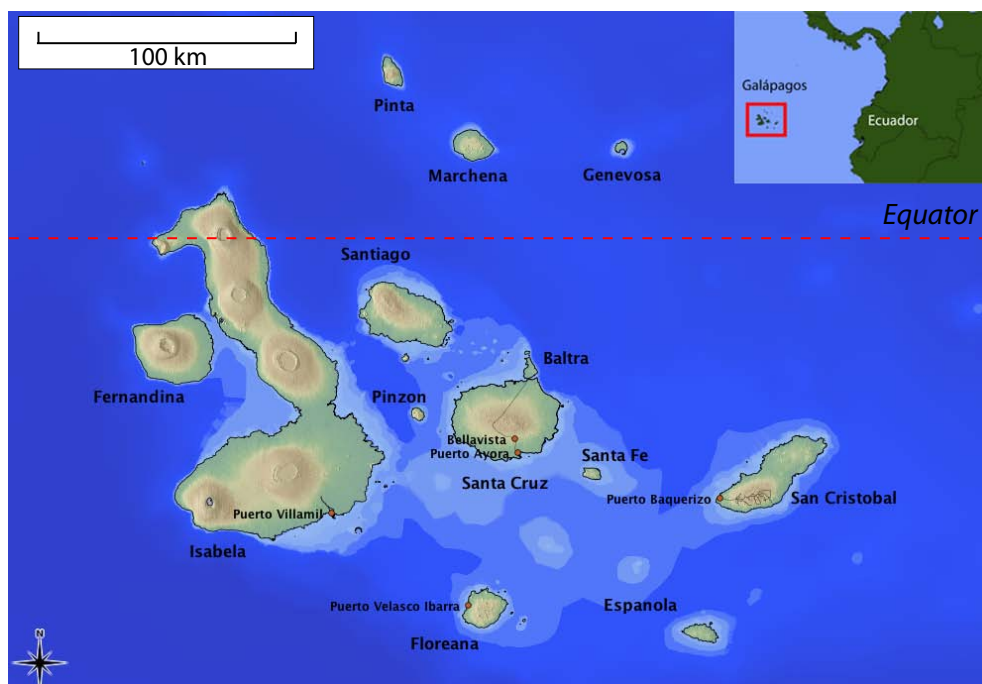


**Figure 1.1:** The Galapagos Islands. Populated centers are indicated with red dots. Topography and bathymetry from SRTM-PLUS.

Only four of the islands are inhabited (Fig. 1.1): Santa Cruz the economical capital (ca. 13 000 inhabitants), San Cristóbal the political capital (ca. 6500 inhabitants), Isabela (ca. 2000 inhabitants) and Floreana (ca. 400 inhabitants). [INEC-CGG, 2010]. The total permanent population is about 22 000, but around 160 000 tourist visit Galapagos every year [PNG, 2010]. Assuming the average duration of stay to be 5 days, it adds ca. 2200 inhabitants (+10% of the total population). Furthermore, illegal migrants are not counted in the statistics and actual population may be bigger.

Most of the cultivable lands are dedicated to agriculture, but a large proportion of the emerged surfaces of the archipelago (97%) is not colonized and belongs to the Galapagos National Park.

## 1.2 Geological context

The Galapagos Archipelago owes its existence in the ocean due to the activity of a hot-spot. Similarly to Iceland and Azores Archipelago, the structure and organization of the islands are affected by the presence of a segmented neighboring mid-ocean ridge, the *Galapagos Spreading Center* (GSC), a hundred km north (Fig. 1.2).

The oceanic crust on which the islands are built was formed by the GSC and belongs to the Nazca plate. It can be no older than 10 Ma [Simkin, 1984]. The spreading half rate of the *East Pacific Rise* (EPR), 1000 km west of the archipelago, is higher ( $> 70$  mm/year) than that the GSC (21 to 36 mm/y), which confers the Nazca plate a speed of 71 mm/y in the direction N102°, toward the Peru-Chile subduction trench [Hey *et al.*, 1977].

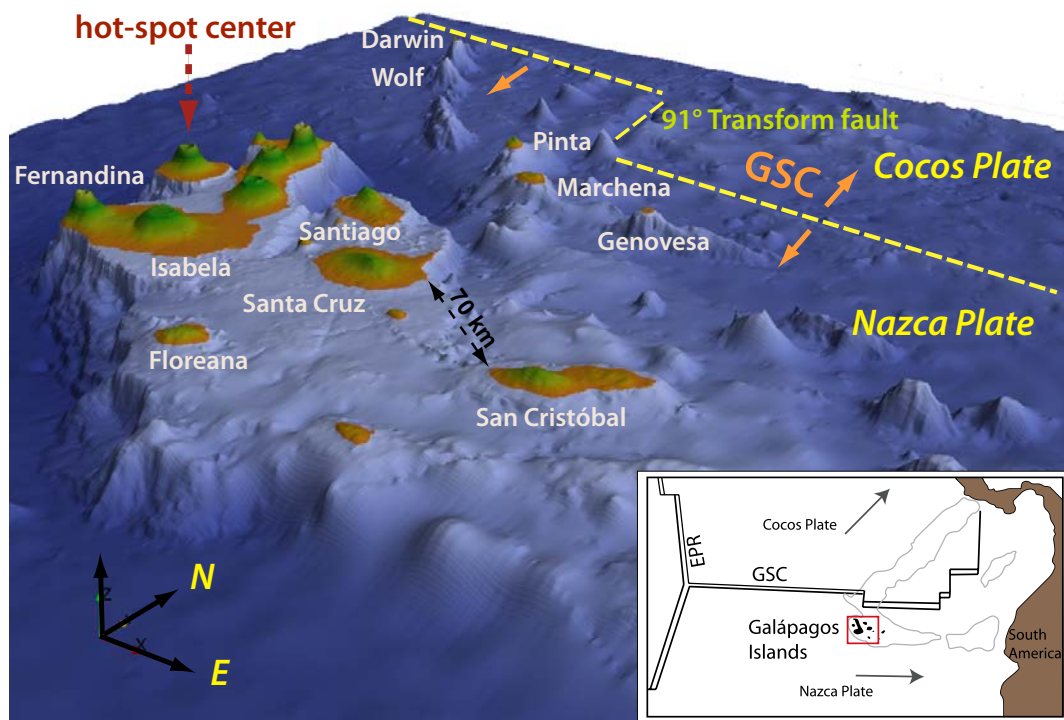


**Figure 1.2:** The Galapagos Archipelago lies over a large platform, a hundred km south of a mid-oceanic ridge, the *Galapagos spreading center*. Inset from Geist *et al.* [2008], topography and bathymetry from SRTM-PLUS

At the exception of Darwin and Wolf islands, at the northern edge of the archipelago, the Galapagos Islands do not lie directly on the sea floor (ca. 3000 m below sea level), but over a relatively shallow platform some 250 m below sea

## 1. CONTEXT

---

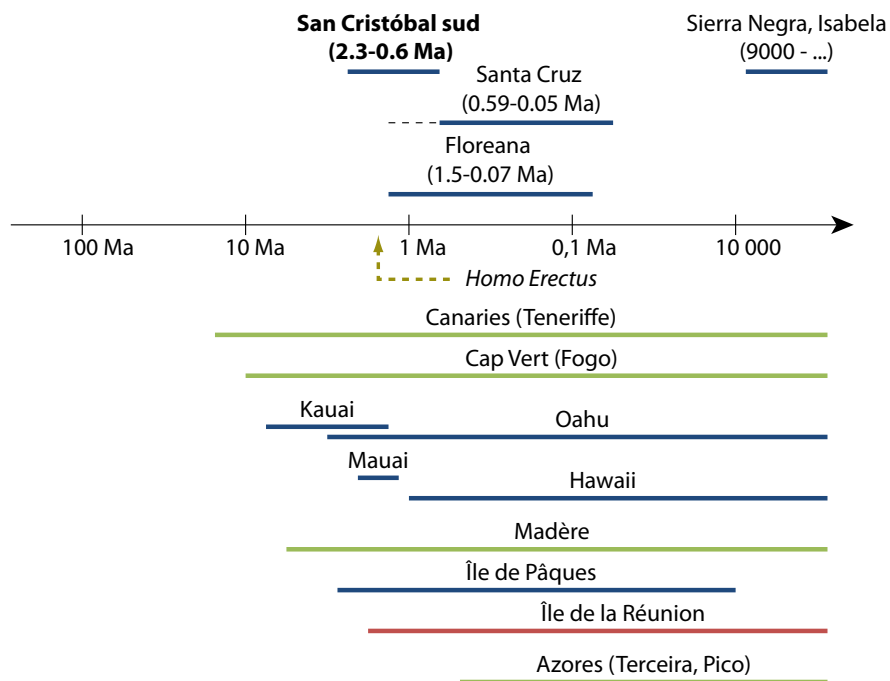


**Figure 1.3:** Ages of the main inhabited islands of the Galapagos Archipelago, compared to similar volcanic islands. The log time scale is logarithmic. For the Galapagos Islands, ages from *Geist and Reynolds* [1998]. For others, see Chap. 3

level (Fig. 1.2). The existence of this platform, built by numerous thick lava flows is explained by high volume and continuous eruptions, which is probably related to the interaction between the hot-spot and the mid-ocean ridge [*Geist et al.*, 2008; *Mittelstaedt and Ito*, 2005; *Wilson and Hey*, 1995]. Though the platform continues in the direction of the continental mainland, there is no geological evidence that the Galapagos Archipelago has ever been connected, even by a range of islands with the mainland, 1000 km east [*Simkin*, 1984].

*McBirney and Williams* [1969] divided the archipelago into four geological subprovinces:

- The *old subprovince* comprises Española, Santa Fe, Seymour and Baltra Islands. These islands are the strongly faulted remnants of ancient subaerial volcanoes that were active from about 3 to 1 Ma ago. These islands are aligned along a N30° W direction, i.e. parallel to the regional alignment of the younger western Galapagos.
- The *central subprovince* is made up by San Cristóbal, Santa Cruz, and Santiago Islands. The volcanoes have relatively gentle slopes, lack a caldera and each has aligned systems of satellite vents. Lavas of Floreana do not actually fit this subdivision. This island has a long-lived history, with eruptions from late parasitic cones.
- The *western subprovince* is made up by the historically active volcanoes of Isabela and Fernandina islands. These shields have roughly symmetric forms, steep slopes, and enormous calderas.
- The *northern subprovince* is composed by isolated, small islands exceedingly diverse petrologically: Wolf, Darwin, Genovesa, Marchena and Pinta.

While the large western volcanoes are built of tholeiitic basalt, those of the central part of the archipelago are mainly of alkaline parentage. The 91° fracture zone crosses the Galapagos platform (Fig. 1.2) and creates an estimated 5 Ma age discontinuity in the lithosphere [*Feighner and Richards*, 1994]. This probably explains that volcanoes of the western sub-province have distinct morphology [*Chadwick and Dietrich*, 1995; *Nordlie*, 1973].

At the beginning of eruptions, high gas content (mainly H<sub>2</sub>O and CO<sub>2</sub>) induce explosive events and the deposit of finely comminuted pyroclastic material, from lapilli to hash. Pyroclastic cones are present in Isabela [*Reynolds et al.*, 1995], Floreana, and Santa Cruz [*Bow*, 1979] islands. Thick tephra deposit cover Fernandina volcano [*Simkin*, 1984]. Yet, explosive events were relatively scarce, and pyroclastic formations constitute only a small portion of the total volume of the islands. The volcanism of Galapagos is relatively similar to Hawaiian, Azores, Canary and Réunion islands. Eruptions were to a great extent of effusive type.

Fluid *pahoehoe*, and clinker scoriaceous *aa'* lava flows are both reported and form a large portion of the edifices. Continuous eruptions with large volumes of lava lead to the formation of long and thick flows, which formed subdued profiles with gently sloping coastal apron as in Santa Cruz [*Bow*, 1979], and Isabela Islands [*Reynolds et al.*, 1995]. The eruption of fluid *pahoehoe* flows were accompanied by the formation of lava tunnels. They are numerous on Isabela

## 1. CONTEXT

---

[*Reynolds et al.*, 1995] and Santa Cruz Island [*Bow*, 1979]. These natural caves may have an importance in hydrogeology, forming semi-continuous conduits for groundwater.

Due to uplift, subsidence, and sea level change, islands coastlines and the proportion of emerged surfaces varied with ages. Numerous evidences of regional and local uplift up to a few meters in magnitude are reported on Santa Cruz [*Bow*, 1979], Isabela [*Amelung et al.*, 2000; *Reynolds et al.*, 1995] and Fernandina islands [*Simkin*, 1984]. Sea level changed significantly during the construction phase of current emerged islands (ca. 1.5 Ma to present). It stayed generally below current level, oscillating between -20 to -70 m [*Miller et al.*, 2005].

Fumarolic activity is relatively scarce on the Archipelago, sulphuric degassing are reported in Isabela [*Reynolds et al.*, 1995] and Fernandina Islands [*Simkin*, 1984] but Santa Cruz, Floreana, and San Cristóbal are apparently devoid of such phenomenon.

In contrast to other still-active oceanic archipelagos likes the Azores, Canary and Samoa Islands, the Galapagos islands are relatively young [*Simkin*, 1984] (Fig. 1.3). Most of the Galapagos volcanoes are now extinct and historically active centers are located on Isabela and Fernandina Islands, below the current location of the hot-spot.

### 1.3 Climatic conditions

*This is a summary on the climate of Galapagos. Other information are available in Chap. 6.*

Climatic conditions in the Galapagos Islands are controlled by winds and sea currents, with seasonal and inter-annual alternates. South-eastern trade winds induce marked contrasts between windward and leeward slopes of the main islands. The archipelago is located at the edge of the Central Pacific dry zone (Fig. 1.4), which confers anomalously arid conditions with respect to the equatorial location [*Colinvaux*, 1972]. Median annual rainfall in Puerto Ayora (Santa Cruz, + 4 m a.s.l.) is 277 mm [*Trueman and d'Ozouville*, 2010].

Due to the north-south migration of the *Inter-Tropical Convergence Zone* (ITCZ), seasons alternate between the warm *invierno* and the cool *garúa* seasons (Fig. 1.5) [*Trueman and d'Ozouville*, 2010]:

- During the hot *invierno* season (January to May): the ITCZ migrates southward in the direction of the archipelago. The influence of trade winds slackens, sea and air temperature rise. Evaporation rates are higher and rainfall convective.

### 1.3 Climatic conditions

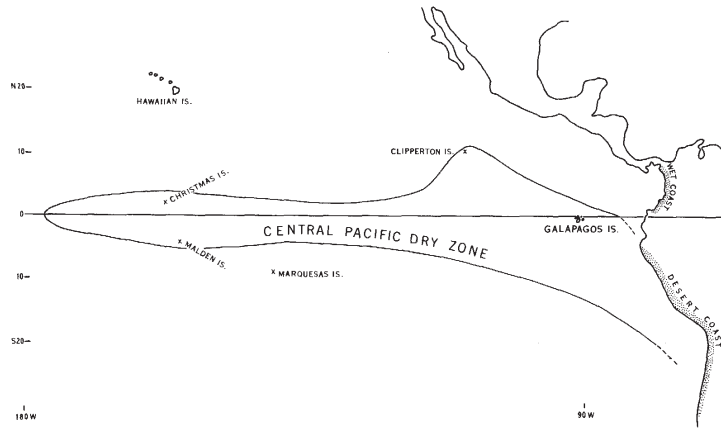


**Figure 1.4:** The Central Pacific Dry Zone during the months of the northern hemisphere summer [Colinvaux, 1972].)

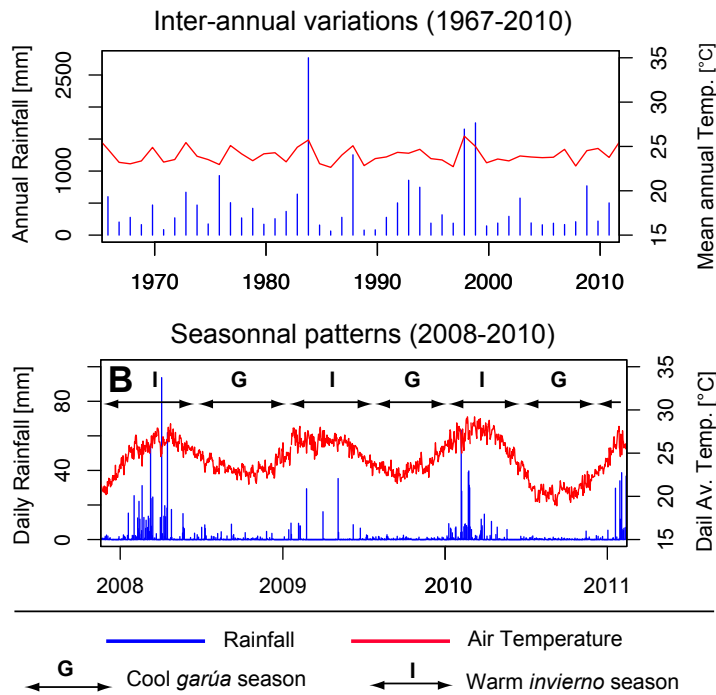


**Figure 1.5:** (A) Inter-annual total precipitations and average temperature. (B) 2008-2010 daily records. Data collected by the Charles Darwin Foundation at Puerto Ayora (+ 4 m a.s.l.), Santa Cruz Island.

## 1. CONTEXT

- During the cool *garúa* season (June to December), a semi-permanent fog covers the wind-ward sides of the main islands from ca. 400 m a.s.l. up to the temperature inversion layer (ca. 750-... m a.s.l.). Precipitations are continuous and of weak intensity.

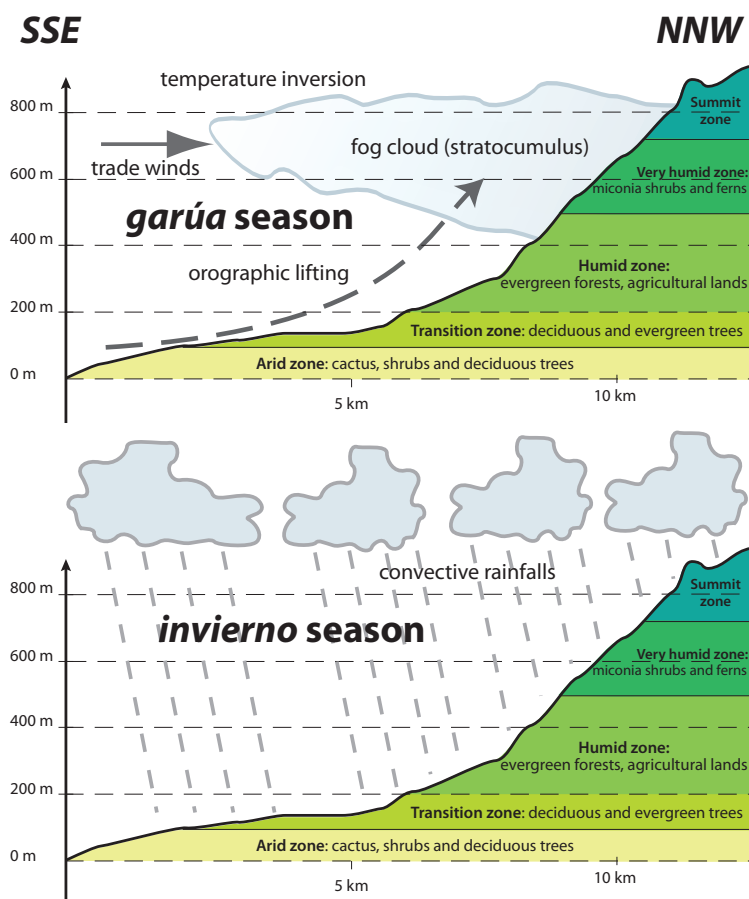


**Figure 1.6:** Vegetation staging along the windward slope of Santa Cruz island after *Hamann* [1979]. (A) Configuration during the cool *garúa* season with the occurrence orographic rainfall and fog. (B) Configuration during the hot *invierno* season, when rainfall are convective and evenly distributed.

Hot season rainfall is strongly correlated with sea surface temperature, whereas cool season rainfall is consistent from year to year, and not so closely correlated with sea surface temperature [*Trueman and d'Ozouville*, 2010]. During the cool season, spatial contrasts are strong. While high elevation areas stay in a permanent fog, coastal areas may be totally deprived of precipitations (Fig. 1.6). Precipitations are more evenly distributed in the space during the hot season.

Extreme inter-annual variations are attributed to the *El Niño* Southern Oscillation (ENSO) with a warm phase, *El Niño* and a cool counterpart *La Niña*. During El Niño events, sea surface temperature warms as south-eastern trade winds slacken, upwelling weakens, rainfall are convective and intense [Cane, 2005; Conroy et al., 2008; Snell and Rea, 1999]. Since 1880, ENSO events have occurred roughly every 2-7 years, with no clear periodicity [Cane, 2005]. A combination including high sea-surface temperatures and weak winds promotes tremendous evaporation of water into the atmosphere, leading to abnormally strong convective storms and great rainfall (Fig. 1.5).

Potential consequences of global warming in Galapagos are difficult to predict, but may include a sea level rise, a modification of the frequency of occurrence of El Niño/ La Niña alternates, and the rise of the cloud base during the cool garúa season [Sachs and Ladd, 2010].



**Figure 1.7:** The windward side of Santa Cruz Island, photograph from Puerto Ayora in March 2011.

## 1.4 Ecological singularity

Geological evidences of a recent ( $< 1$  Ma) landbridge is absent [Simkin, 1984], and the current distance to the continent is 900 km. Galapagos endemic species are said to originate from America, the Caribbean, Asia and Australasia [Grehan, 2001]. A popular belief states that current species are the descendant of brave survivors, who crossed the ocean (probably unintentionally), over small drafts detached from river banks or seashore at the occasion of flooding or storms. This is partly true, but the history of the Galapagos biota may be much older. Biogeographical evidences over the past dozen million years account for continental

## 1. CONTEXT

---

drift and show that the Galapagos biota may have developed from a whole series of ancestral Galapagos islands, allowing land colonization [Grehan, 2001].

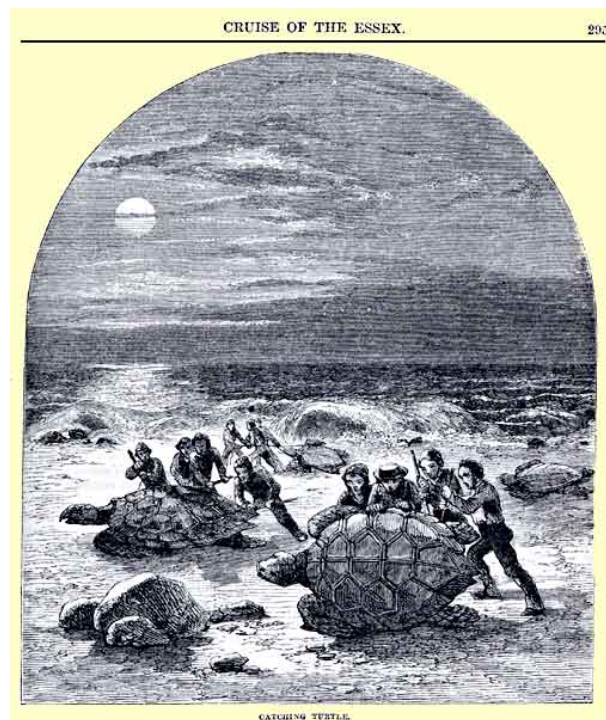


**Figure 1.8:** Engraving: “Catching Turtle.” In “Cruise of the Essex” in Harper’s New Monthly Magazine, Vol. XIX, August, 1859, pp.289-310. New York: Harper Brothers from [www.galapagos.to/ephemera/index.htm](http://www.galapagos.to/ephemera/index.htm).

Contrary to some misconceptions, biodiversity is extremely poor on the Galapagos Islands. Plants and animals species which survived in the harsh conditions are in a limited number. But most of *native* Galapagos species are to be found nowhere else: there is a high rate of *endemism*. Environmental conditions are not identical in each island, and the distances between each islands within the archipelago are relatively big (50-100 km). Though they had common ancestors, Galapagos species on each island remained isolated and evolved differently. These observations were first made by Darwin on terrestrial tortoises and finches, which constituted an argument for his revolutionary theory on the evolution of species [Darwin, 1859].

Though biodiversity is weak, plants and animals in the Galapagos are to be seen nowhere else, which makes the place attractive. The Galapagos marine iguana is the only species able to graze seaweeds and desalinate seawater. Sea lions, tortoises, iguanas and birds are tame so that amateur photographers can



**Figure 1.9:** Blue footed boobies are very good parents.



**Figure 1.10:** Sea lions rest hours lying on the beach. They are tame and love playing with tourists.

## 1. CONTEXT

---

come close to these fascinating animals. This, together with fantastic landscapes, from paradisaical to lunar, probably explain current attractiveness of Galapagos, more than the endemism of species itself.

Long term isolation made insular biota singular, but as well particularly vulnerable to the introduction of foreign species. Similarly to many other islands (e.g. Easter and Réunion Islands), Galapagos territories are deeply affected by the invasion of introduced plants and animals, either intentionally or not. For example, introduced animals (mainly goats) devastated the highlands and deprived endemic tortoises of food, blackberry proliferated in San Cristóbal and quinine tree covered the highlands of Santa Cruz.

### 1.5 Historical background

*This is a short introduction to the History of Galapagos. The reader may refer to d'Ozouville [2007a] and a very well documented website [www.geo.cornell.edu/geology/GalapagosWWW/GalapagosHistory.html](http://www.geo.cornell.edu/geology/GalapagosWWW/GalapagosHistory.html)*

On his journey from Panama to Peru in 1535, the ship of the Archbishop Tomás de Berlanga became becalmed and was carried west by currents. Short of water, they reached totally accidentally the Galapagos Archipelago. When they landed, the ship's crew was more frightened than amazed by the mysterious creatures they saw: marine iguanas and gigantic tortoises. The soil was bare and covered by spiny brushes and cactuses. The archbishop's crew wandered on the islands in sake for freshwater, several men and horses died before they found the precious liquid. Unfortunate discoverer of Galapagos, Tomás de Berlanga left such a terrifying description of the Archipelago that during more than a century, no one was tempted by a comeback. But by the seventieth century, the British crown was eager to limit the prosperous development of the South-American Spanish Empire and gave its blessing to pirates and buccaneers. They settled their base in Galapagos, evidences of their stay were found in Floreana and Santiago Islands. Giant tortoises were particularly appreciated by mariners because they could survive in the ship's hold for months without food or water. But more tasty and useful animals were introduced in the islands: goats, pigs, and donkeys. These species proliferated in the island better than any expectations, and actually invaded the archipelago. By the eighteenth century, pirates gave place to whalers and seal hunters. In less than two centuries, they decimated tortoise and whale populations.

In 1830, the city of Quito gained independence, after the battle of Pichincha lead by Antonio José de Sucre. By 1832 an Ecuadorian governor was installed in

## 1.5 Historical background

---

Galapagos. Followed different attempts of colonisation by utopian communities, cultivators, or convicts. A famous penal colony was setted on the island of Isabela. Ruins of a huge wall, *El Muro de las Lagrimas* (literally the “wall of tears”) is still visible today. It was elevated by convicts from large blocks of basalts.

In 1835, the British naturalist, Charles Darwin visited the island aboard the *HMS Beagle*. His investigations in Galapagos do not represent a fundamental argument in the construction of the revolutionary theory of evolution, published twenty years later, but Darwin became the most famous visitor of Galapagos and participated to its renown.

By 1869, Manuel Cobos developed successfully plantations of coffee and sugar in San Cristóbal, the only island with perennial streams. By means of a network of small channels, water was diverted from the rivers to the plantations and the village of *El Progreso*. The workers in Cobo’s farm were almost slaves and the tyrant was eventually assassinated by one of his employees. Yet, San Cristóbal became at that time the most prosperous colony and was declared capital of the archipelago.

Lured by paradisaical descriptions by adventurer’s novels or in sake for a simpler life, European settlers arrived in the twenties from Norway, Germany, and Belgium to settle in Santa Cruz and Floreana islands. A few months after the attack of Pearl Harbour in 1942, the US asked permission to install a military base on one of the smallest and most inhospitable island of the archipelago: Baltra, north of Santa Cruz. The Ecuadorian government accepted, which lead to an unprecedented development of the archipelago. More than 3000 soldiers and workers populated Baltra. Freshwater, which was totally absent on Baltra was imported from San Cristóbal by a barge. Vegetables, fruits and meat were bought to farmers in Santa Cruz and San Cristóbal. The American left the island in 1946, leaving a large airport, the first of the archipelago.

With limited, but growing colonization, invasive plants and animals, the need for conservation was recognized in 1959. The Galapagos National Park and the Darwin Research Station were funded and installed permanent offices in Santa Cruz. Though freshwater was scarce on this island, it was close to Baltra airport and already colonised.

The boundary of the Galapagos National Park were designated in 1974, and comprises about 97% of the islands surface. Touristic visiting sites were defined, and access to the rest of the territory strictly prohibited. The Galapagos National Park was integrated to the UNESCO World Heritage list in 1978.

Conservation is the main activity of the National Park Services and the Darwin research stations. Several projects were implemented, such as the *Project Isabela* (1997-2006), which consisted in eradicating populations of about 100 000 goats on the islands of Isabela and Santiago. As well, a vast eradication program was implemented for the quinine tree (*Cinchona pubescens*) which invaded the

## 1. CONTEXT

---

highlands of Santa Cruz. But some species such as blackberry, which invaded San Cristóbal remain out of control and expand their territory to Santa Cruz and Isabela.

By 2010, 160 000 tourists visit Galapagos every year. This is small compared to touristic activity in Canary Archipelago, which receives 8 million tourists per year [ISTAC-IET, 2010]. But the number of visitors was multiplied by a factor of 10 in about 20 years. This drove a rapid economical growth, and standard of living increased. This attracted numerous migrants from all Ecuador in the eighties. Today, the permanent population is bigger than 21 000 and only half of the population was born in the archipelago [INEC-CGG, 2010]

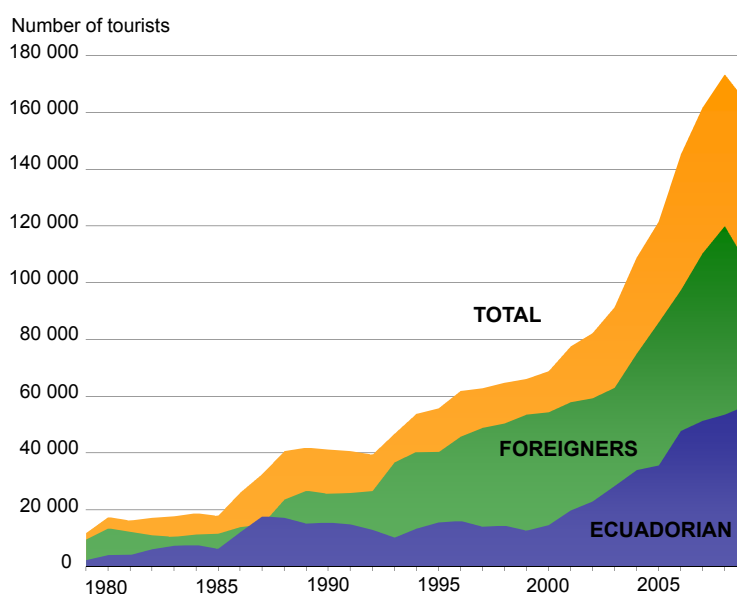


**Figure 1.11:** Statistics on touristic admissions in the Galapagos Archipelago [PNG, 2010].

In 1998, a special law was announced to limit immigration and tourism. It became theoretically difficult for Ecuadorian to migrate to Galapagos. To limit the entries and fund conservation projects, a \$100 fee was required to any tourist entering the archipelago. Despite this legislation, the situation remained critical. In 2007, the UNESCO mission reported “growing encroachment of invasive species, increasing human immigration, uncontrolled development of tourism, and the failure of various institutions and agencies to deal with these threats”. The archipelago joined the list of World Heritage in Danger. The government of Ecuador acknowledged that the Galapagos Archipelago was at risk and declared its conservation and environmental management as a national priority. In 2010,

---

## 1.6 The water issue in the Galapagos Islands

Galapagos was removed from the list of World Heritage in Danger. Political efforts are real, but law enforcement is difficult. Despite the success of several conservation projects, invasive species are still present and expand. In fact, little changed since 2007.

Cultivable lands of the archipelago are located along the humid windward slopes of the volcanoes. A vast majority of them were appropriated by national and foreign migrants before the boundaries of the park were delimited. Farms are relatively big and dedicated to livestock farming, milk production, and coffee plantations. Local production of market products (fruits and vegetables) is small. Today, it is much more profitable to invest in tourism than agriculture. Rates of pay of workers are higher in Galapagos than on the continental mainland. Importing food, even by plane, is cheaper than growing it in Galapagos. Inhabited islands and particularly Santa Cruz are totally dependent on food importation. This present a threat, the importation of food has been proven to be at the origin of the introduction of several invasive species (plants and insects).

## 1.6 The water issue in the Galapagos Islands

### 1.6.1 The situation

There is a serious “water issue” in the Galapagos Islands. Though iguanas and tortoises evolved to cope with arid conditions, human beings did not. Populations of pirates and whalers identified small springs in the highlands. First settlers had no alternative but drinking brackish water withdrawn from fault scarps, the *grietas*, and harvested rainwater.

At the exception of San Cristóbal (ca. 6500 inhabitants) where freshwater is abundant, other inhabited islands suffer from acute freshwater scarcity: Santa Cruz (ca. 13 000 inhabitants), Isabela (ca. 2000 inhabitants) and Floreana (160 inhabitants) [INEC-CGG, 2010].

San Cristóbal has numerous perennial springs and streams and water resource meets the needs [d’Ozouville, 2007a]. Yet, water shortages are reported in the main city, Puerto Baquerizo. The only issue there is the poorly maintained 15 km long tubing, with numerous leaks.

Only one little freshwater spring was identified on Floreana, but the precious liquid is evenly distributed to the 160 inhabitants with a network of small tubing in perfect state. Water is rationed but of good quality, this is a great example of efficient community management.

The situation is critical in Isabela and Santa Cruz: the unique perennial resource identified is the brackish and contaminated water of the basal aquifer. Little data is available on Isabela Island, what is reported below originates from

## 1. CONTEXT

---

studies conducted on Santa Cruz Island. The situation is probably similar, but less critical on Isabela, which is less populated.

There is no proper sewage system in Puerto Ayora the main city of Santa Cruz and wastewater is sent to private septic tanks [Guyot-Tephany, 2010]. The numerous cracks allow rapid drainage to the underground, numerous households drive their wastewater directly to the aquifer.

High contamination levels are reported in the basal aquifer of Santa Cruz [Liu, 2011]. Contaminated brackish water is distributed by the Municipality without any form of treatment. Part of the groundwater production sites are still located in populated areas.

Surveys show that the population is aware of the issue. A large majority of the inhabitants consider that tap water is of bad quality and never drinks it [Guyot-Tephany, 2010; INEC-CGG, 2010; Liu, 2011]. Drinking water originates from various small desalination plants and rainwater harvesting (4% of the population, particularly in the highlands [INEC-CGG, 2010]). Drinking water is sold by small private companies around 0.13\$/L that is 133\$/m<sup>3</sup> [Guyot-Tephany, 2010], which is extremely expensive.

Though tap water is restricted to domestic use, skin and intestinal diseases are frequent [Liu, 2011]. From a survey conducted in 2010 in Santa Cruz, Guyot-Tephany [2010] reports that in each household, at least one member of the family had been affected by a disease related to water in the last six months. 40% of the admission at the hospital of Santa Cruz are related to water diseases (skin, intestine).

From recent studies of Liu [2011] and Guyot-Tephany [2010], following observations emerge for Santa Cruz:

- Tap water is so contaminated that it is not even appropriate for domestic use. Having a wash may expose to skin diseases. Cleaning vegetables or dishes induce a risk of contamination.
- The quality of purified water used for drinking purposes is variable, and storage conditions in households are inappropriate.

To summarize, freshwater resources are scarce and unevenly distributed in the Galapagos Archipelago. On the main island, Santa Cruz, distributed water is brackish and contaminated. It is not suitable for drinking purposes and not even for domestic use. Bacterial contamination, rather than the presence of salt, is responsible of the numerous diseases.

### 1.6.2 Previous studies on the hydrology of Galapagos

First hydrogeologists were pirates, whalers and settlers in desperate search for fresh-water. Following the traces of tortoises and birds [d'Ozouville, 2007a], they identified all the currently known springs on Floreana, Santiago, Santa Cruz and Isabela Islands. On San Cristóbal numerous springs and streams allowed the development of a relatively prosperous agriculture by the time of Manuel Cobos, and provided water to the American military base of Baltra by World War II.

Though scientific publications are abundant on Galapagos botany and geology, very few publications deal with the water resources of the Galapagos Islands. Calls for groundwater investigations were made by *McBirney and Williams* [1969] and *Simkin* [1984]. Given the critical situations of Santa Cruz, Isabela, and Floreana islands [d'Ozouville, 2007b, 2008], the lack of groundwater investigations is relatively striking.

By the eighties, an extensive mapping project was conducted in collaboration with the French development agency (ORSTOM, now IRD) and local authorities [Ingala et al., 1989]. Springs and streams were mapped from field work and aerial photography.

Very few drill holes were executed in Galapagos. Some dispersed attempts were made in the highlands of Floreana and Santa Cruz at imprecise locations. Only one drill hole is used for groundwater abstraction on Santa Cruz [Dixon Hydrogeology Limited, 1996]. In similar islands such as Canary and Hawaiian Archipelagos, hundreds of drill holes and horizontal galleries have been executed since centuries. It remains striking that drill holes are so scarce in Galapagos, and this situation does not facilitate the understanding of local hydrogeology.

At the instigation of Noémi d'Ozouville and Sophie Violette in 2003, the very first academic investigations in hydrogeology were launched by the University Pierre et Marie Curie (UPMC, Paris) in collaborations with local partners, namely the Charles Darwin Foundation, the Galapagos National Park, and the Municipality of Puerto Ayora. The project, entitled *Galapagos Islands Integrated Water Studies* (GIIWS), started with a PhD thesis in 2002 [d'Ozouville, 2007a]. A radar-grammetric DEM was built for Santa Cruz Island [d'Ozouville et al., 2008b] and an extensive air-borne electromagnetics survey was conducted over San Cristóbal and Santa Cruz islands [Auken et al., 2009; d'Ozouville et al., 2008a], revealing interesting features. These studies were accompanied by first socio-economic descriptions of the "water issue" on Santa Cruz island [d'Ozouville, 2007b, 2008].

As a conclusion, hydrogeological investigations started recently in Galapagos and very few drill holes were executed. Climatic conditions are poorly known, the conditions of groundwater occurrence are subjected to many uncertainties.

### 1.6.3 Why should a French research institution investigate the hydrogeology of Galapagos ?

Hydrogeological settings of the Galapagos Islands are poorly known and there are two serious issues regarding water resources: the lack of freshwater, and the contamination of the resource by inappropriate sewage system.

Galapagos is a province of Ecuador, one may wonder why should a French institution do research there and attempt to solve these scientific and development issues. The GIIWS project is not a substitute to national universities and consulting firms, but aims to provide a neutral scientific expertise to stakeholders. To this effect, we collaborate with the National Polytechnic School of Quito and local authorities: the Galapagos National Park, the Galapagos provincial government and the Municipality of Santa Cruz.

The Galapagos Archipelago has been recognized a World Heritage by the UNESCO. It attracted scientists over the world, and should deserve world care. The objective of the GIIWS project is to conduct scientific research that may help addressing conservation challenges regarding water resources and promote sustainable development.

As well, it is beneficial for French researchers to collaborate with international partners in foreign territories. Galapagos is a world famous Archipelago and an attractive area for Ecuadorian and international scientists. Conducting research overseas allows the confrontation with international colleagues. The scientific objective of the GIIWS project are not restricted to Galapagos issues, but aim to improve global knowledge on volcanic insular contexts, which are found worldwide, including in France (La Réunion Island).

The discovery of hidden freshwater resources may have practical consideration in Galapagos. Our investigations raises the concern of some observers, particularly our colleagues dealing with conservation of ecosystems. They know that unreasonable human development threatens the Galapagos pristine ecosystems, and are concerned by the development of investigations that may attract more migrants and tourists, and finally increase the human impact over the environment.

These concerns to see a scientific program in water sciences fostering development in Galapagos can be balanced by following considerations:

- The lack of freshwater has never been a limiting factor to modern human development in Galapagos. As a simple evidence, Santa Cruz, the island the most deprived of freshwater resources is the most developed. Most of the tourist ignore the water issue in Galapagos, and the situation probably does not limit touristic attractiveness of the archipelago.
- Although they live in a national park, inhabitants of Galapagos deserve

## 1.6 The water issue in the Galapagos Islands

---

freshwater quality. Numerous skin and intestine diseases caused by the poor quality of water are not acceptable. To the author's opinion, it is not ethically valid to control human development with unsanitary conditions.

- A better knowledge of the hydrogeological configuration could promote sustainable management of resources, and potentially avoid expensive desalination techniques, which require the importation of fuel and the disposal of brines.

As a consequence, we consider that doing research in water sciences could improve the living conditions of local inhabitants and limit their impact over the environment. It participates to the improvement of the understanding of groundwater occurrence in volcanic insular contexts, with world-wide applications.



# Chapter 2

## Methodology

## 2. METHODOLOGY

---

### 2.1 The approach

This PhD thesis is part of the *Galapagos Islands Integrated Water Studies* (GI-IWS). Investigations were oriented in function of the (un-)availability of data and funding. Instead of focusing on a specific field of research, we focused on a place and a problematic: characterizing groundwater occurrence in Galapagos. Investigations conducted in the frame of this thesis were various and interdisciplinary.

We concentrated our efforts in the accessible, inhabited islands (Santa Cruz, San Cristóbal, Isabela, and Floreana islands) where the needs are the most conspicuous and access to the field is eased (though not necessarily easy).

At the start of this thesis, it was identified that:

- The large airborne electromagnetics SkyTEM dataset collected by *d'Ozouville* [2007a] was difficult to visualize and could reveal further insights.
- The lack of climatic records in the highlands was a serious issue for groundwater studies. In particular, the input from cloud water interception was totally unknown.
- Very contrasting hydrogeological configurations are reported for Santa Cruz and San Cristóbal islands, though they share very similar climatic and geological patterns.
- Hydrogeological investigations regarding the basal aquifer of Santa Cruz Island deserved to be extended. In particular, the importance of normal faults on groundwater flow was poorly understood.

After such observations, it was decided to conduct investigations in following three thematics directly related to groundwater occurrence (Fig. 2.1):

- **Internal structure.** By means of geophysics, geomorphology, and remote sensing, the internal structure of volcanic edifices is investigated. The description of the geometry and properties of volcanic formations is crucial for hydrogeological investigations.
- **Recharge processes.** By means of climatic monitoring, vegetation and soil instrumentation, spatial and temporal distribution of precipitations were characterized. The description of groundwater recharge processes provides important insights on the hydrogeological potential and allows the estimate of the renewable freshwater resource.
- **Groundwater flow.** By means of analytical modeling, analysis of tidal signal propagation, aquifer tests, and fracture mapping at several scales,

groundwater dynamics was investigated. This provides insights in the understanding of hydrogeology of volcanic islands, with practical implications for the Galapagos Archipelago.

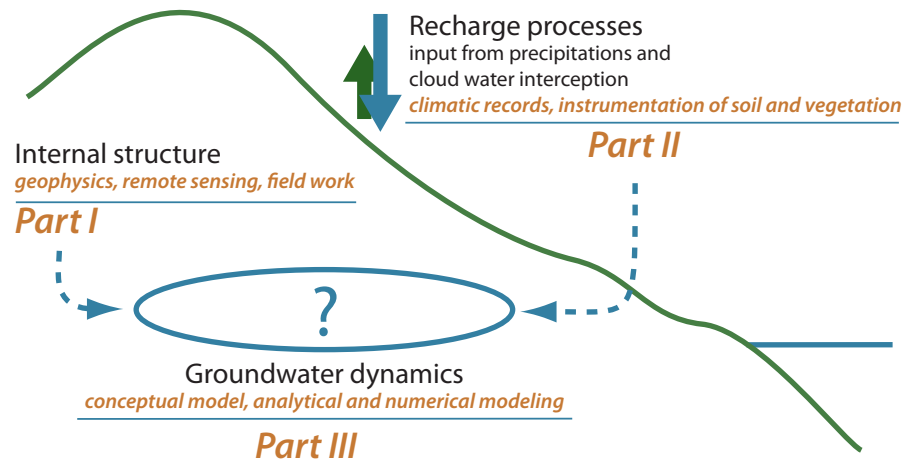


**Figure 2.1:** Objectives of the thesis and structure of this document. Investigations conducted in the frame of thesis were various and interdisciplinary, but directly related to groundwater occurrence in volcanic insular context.

Whether it was worth, justified, and relevant to launch simultaneous investigations in such diverse fields is a question under debate. Whatever the answer is, this interdisciplinary approach provided the candidate a broad scientific overview on several thematic directly related to water sciences, which may appear as a valuable experience to start a career in this domain. If the answer is no, at least it provided the PhD candidate an excellent lesson: better to focus efforts on a specific topic.

## 2.2 Timeline

This thesis was conducted from October 2008 to October 2011 and included more than 8 months of field work in Galapagos. Investigations were conducted in three phases:

- Investigations started in 2008 with a literature review on the hydrogeology of volcanic islands. Exploratory field work was conducted in the islands of Santa Cruz, San Cristóbal, and Isabela.

## 2. METHODOLOGY

---

- In 2009, a new visualization technique for airborne electromagnetics surveys was developed. It was then used for the interpretation of the SkyTEM dataset collected by my predecessor in Santa Cruz and San Cristóbal.
- By mid-2010, the GIIWS project took a determining turn, as it received funding from the French *Agence Nationale de la Recherche* (ANR). A network of weather stations was installed in collaboration with Ecuadorian students of the Polytechnic School of Quito (EPN).
- Climatic and hydrogeological data processing. Writing of the dissertation.

### 2.3 Structure of this dissertation

As the reader probably realized, this dissertation was not written in French as it is the tradition in this university, but in English. This language was chosen in order to make this study accessible to any person interested by the topic, and first of all, to allow the diffusion of the results to our Ecuadorian colleagues and partners. They did contribute to this work and may be interested by the results.

Results of this PhD thesis have, or will be submitted for publication in peer-reviewed international journals. One chapter constituting this document has already been published, another is under review, and two others will be submitted shortly. To this effect, the structure of each chapter follows the classical structure of scientific communications and intend to be self-standing. Though it was limited to the minimum, some information may therefore appear redundant from one chapter to the other.

As presented by Fig. 2.1 this dissertation is divided into three main parts: **Internal Structure**, **Recharge processes**, and **Groundwater dynamics**. This structure gives a consistence to the document, but boundaries between respective parts are relatively permeable, and chapters are inter-dependent.

Part II, **Internal Structure** aims to describe the interior of basaltic islands, with a focus on groundwater occurrence.

Chapter 3, *Hydrogeology of basaltic islands: geological age as a determining factor* is a literature review regarding groundwater occurrence in basaltic islands. In Chapter 4, *3D resistivity gridding of AEM surveys*, a new technique allowing enhanced interpretation of airborne electromagnetics is presented. Based on this visualization method, Chapter 5, *Hydrogeological framework of San Cristóbal island* proposes the first hydrogeological conceptual model of San Cristóbal island. Results are compared with the hydrogeological settings of Santa Cruz islands, which shares common geological and climatic patterns but is devoid of freshwater resources.

## 2.3 Structure of this dissertation

---

Part III, **Recharge processes**, aims to describe the processes contributing to groundwater recharge in insular contexts. Results are based on climatic data collected by weather stations installed in the frame of this thesis.

In Chapter 6, *Quantification of cloud water interception*, we propose the first estimation of cloud water interception in the Galapagos Islands.

Part IV, **Groundwater dynamics** is dedicated to groundwater dynamics and estimates of hydraulic properties.

Chapter 7, *Analytical and numerical modeling of basal aquifers* proposes a review of analytical solutions modeling seawater intrusion in coastal aquifers, with special reference to volcanic islands basal aquifers. Chapter 8, *The basal aquifer of Santa Cruz Island* is a multi-scale approach aiming to characterize hydraulic properties of Santa Cruz Island. Chapter 9, *High-level groundwater in Santa Cruz Island* is a discussion on conditions of groundwater occurrence in Santa Cruz island, based on geophysical results, climatic data, and hydrogeological evidences gathered in the frame of this thesis.

The conclusions of this study are presented in Part V. They are divided into general results (Chapter 10), and solutions specific to the Galapagos Islands (Chapter 11).





*Man wondering whether it is good to know a little bit about everything, or everything about a little thing: an allegory of multidisciplinary research?*



# Part II

## Internal structure



This part, **Internal Structure**, deals with the interior of basaltic volcanic islands with a focus on groundwater occurrence.

The first chapter, *Hydrogeology of basaltic islands: geological age as a determining factor*, is a literature review. This study reveals that the geological age of volcanic islands conditions their hydrogeological settings. This review served as the basis for exploratory studies in Galapagos and allowed analogies with other well studied islands.

Following chapter *3D resistivity gridding of AEM surveys* details a methodology developed in the frame of this thesis, which aims to enhance visualization and interpretation of airborne electromagnetics surveys. This method is applicable to any geological contexts, and allowed unprecedented imaging of volcanoes interior.

An application of the 3D visualization technique is illustrated on subsequent chapter, *Hydrogeological framework of San Cristóbal Island after SkyTEM survey: insights in the morphological evolution of basaltic shields*. The first hydrogeological conceptual model is proposed for this unique island of the Galapagos Islands, characterised by numerous springs and streams. In a comparative approach with Santa Cruz Island, apparently devoid of water resources, the two islands are shown to share common geological and climatic patterns but differ by their “stages” of hydrogeological evolution.



## Chapter 3

# Hydrogeology of basaltic islands: geological age, a determining factor

## Hydrogeology of basaltic islands: geological age, a determining factor

---

### Abstract

Basaltic islands owe their existence to intra-plate volcanism, they are scattered over the world oceans and host ca. 6 million inhabitants. Freshwater shortages are common and populations are expected to grow. Volcanic formations are complex and heterogeneous, their hydraulic properties are highly variable. Due to chemical and mechanical effects, permeability decreases with time and depth. Climatic conditions are very contrasted between the humid windward side where water may be abundant and an arid leeward side, devoid of water resources. Groundwater is found in (1) a *basal aquifer* subjected to seawater intrusion, (2) high-elevation *perched* and (3) *dike-impounded* aquifers. The basal aquifer remains at low elevation in young islands, where regional hydraulic conductivity is high ( $K \approx 1 \times 10^{-3}$  m/s) and hydraulic gradient low. In contrast, the basal aquifer is identified at much higher elevation in older islands, and forms a *thick freshwater lens* feeding springs and streams. This latter configuration is related to lower regional hydraulic conductivity ( $K \approx 1 \times 10^{-6}$  m/s), rather than enhanced recharge rates. Though effects of ageing are modulated by climatic conditions, there is a clear relationship between the age of the island and its hydrogeological potential.

---

### 3.1 Introduction

Under favorable climatic and geological conditions, groundwater resources of volcanic islands may be substantial [Whittier *et al.*, 2010], but volcanic islands often have poor perennial stream network and freshwater resources may be limited to a thin freshwater lens [Falkland, 1999]. Freshwater shortages are acute in several islands, e.g. the Galapagos and Canary islands [Custodio, 2004; d'Ozouville, 2007b]). The total population living on basaltic islands is estimated to 6 millions (Table 3.1). On some of the islands, population is growing and challenges regarding freshwater supply arise (e.g. Réunion Island (INSEE, 2010) and the Galapagos Archipelago (INEC, 2006)). In many islands, groundwater abstraction rates appear to exceed recharge (e.g. Canary Islands [Custodio *et al.*, 1988]). This explains why, though the sparsity of volcanic islands, their groundwater resources deserve greater effort of investigation (e.g. [Cruz and Silva, 2001]). Desalination of sea- or brackish-water turns to be the last resort and has been implemented in some of the islands (e.g. Canary Islands [Veza, 2001], and Galapagos [d'Ozouville, 2007b]). With rising energy costs and large-scale development, energy consumption and brine disposal may turn to be serious issues. Yet, it may be mitigated with the improvement of desalination technologies [Veza, 2001], or the use of sustainable energies [García-Rodríguez, 2002].

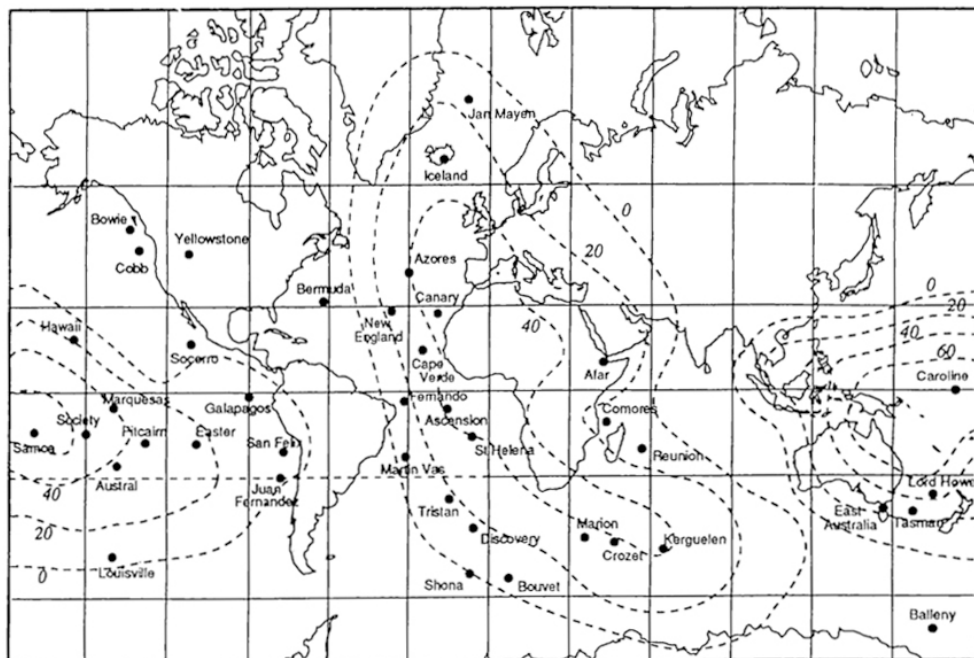


Figure 3.1: Worldwide system of hot-spots [Duncan and Richards, 1991]

### 3. HYDROGEOLOGY OF BASALTIC ISLANDS

---

	Name	Pop. ( $10^6$ )	Rf. [mm]	Age ( $10^6$ years)
1	Azores Arch.	0.24	2000	1-4 (SM)
2	Canary Arch.	2.1	1000	1.0-20
3	Cape Verde Arch.	0.505	500	?
4	Comoros Arch.	0.8	?	?
5	Easter Isl.	0.0037	1100	0.36
6	Galapagos Arch.	0.02	1200	0.5 (SZ), 0.65 (SC)
7	Hawaii Arch.	1.2	4800	1.3(Ma), 3 (Oa), 5.1 (Ka)
8	Jeju Isl.	0.53	2000	0.7-1.2
9	Madeira Isl.	0.25	3000	0.007
10	Mauritius Isl.	1.27	2.0	3
11	Réunion Isl.	0.78	4200	1.0 (PdN), 0.2 (F)

**Table 3.1:** Population, rainfall and age of the main basaltic volcanic islands. Pop. stands for population, Rf. stands for median rainfall at mid slope along windward sides, Age, for the mean geological age of the most representative massif. 1. Pop. INE Lisbon (2009), Rf: *Cruz* [2003], Age: *Cruz* [2003]; *Cruz and Silva* [2001], SM (São Miguel). 2. Pop. INE Madrid, (2009), Rf. *Cabrera and Custodio* [2004] ; Age: *Custodio et al.* [1988]; *Ecker* [1976]. 3. Pop. World Bank (2009), Rf. *Carreira et al.* [2010]; *Heilweil et al.* [2009], Age: ; *Carreira et al.* [2010]; *Heilweil et al.* [2009]. 4. Pop. World Bank (2009). 5. Pop. SUBDERE, Santiago (2002), Rf. *Herrera and Custodio* [2008], Age *Herrera and Custodio* [2008]. 6. Pop. INEC, Quito (2006), Rf. *Trueman and d'Ozouville* [2010], Age *Bow* [1979]; *Geist et al.* [1986], SZ (Santa Cruz), SC (San Cristóbal). 7. Pop. US Census Bureau (2009), Rf. *Giambelluca et al.* [1986], Age *Peterson and Morre* [1987], Ma (Maui), Oa (Oahu), Ka (Kauai). 8. Pop. Jeju Spec. Gov. website (visited 2011), Rf. *Won et al.* [2006], Age *Hahn et al.* [1997]; *Won et al.* [2005]. 9. Pop. INE Lisbon (2009), Rf: *Prada et al.* [2005]. 10. Pop. World Bank (2009), Rf. *Dhurmea et al.* [2010], Age *Jawaheer and Proag* [1988]. 11. Pop. INSEE Paris, 2006, Rf. *Soler et al.* [1997], Age *Upton and Wadsworth* [1966], PdN (Piton des Neiges), F (La Fournaise).

This study focuses on the hydrogeology of volcanic islands with basaltic petrology and sub-tropical or sub-equatorial climate. Cold climatic conditions, particularly the presence of glacier in Iceland has a significant impact over the geomorphology and will not be specifically addressed in this study. The case of arc-islands (e.g. Caribbean, Aeolian islands) will not be considered either, as they are characterized by andesitic explosive volcanism and hydrogeological settings differ (see e.g. *Charlier et al.* [2011]). Even though they may have basaltic past [*Vacher and Quinn*, 1997], the hydrogeology of carbonate islands (e.g. French Polynesia) is different to that of basaltic islands and will not be addressed in this study (see e.g. *Mark R. Underwood* [1992]; *Pouchan et al.* [1988]).

Basaltic islands are found in all the oceans (Fig. 3.1), they are located on oceanic plates, along the trail of *hot-spots* (e.g. Hawaiian Archipelago, Réunion Island) or straddling a mid-ocean ridge (e.g. Iceland, Azores), or both. These islands are composed by one or several coalescing *shield volcanoes*, built by series of lava flows alternating with pyroclastics units. Climatic conditions between the tropics are warm and often humid, which facilitates rock weathering and soil development.

In spite of common processes at the origin of their existences, each basaltic island has its own geological history and climatic singularity, both having a strong influence on the hydrogeological settings. This comparative study aims to identify common hydrogeological features and explain contrasts between the islands. While most of the investigations have been concentrated in populated islands of developed countries (e.g. Hawaii, Canary Islands), this study may benefit to islands where hydrogeological investigations are in a limited number.

Essential notions of physical volcanology are first presented so as to describe the nature, structure, and geometry of volcanic rocks and formations. From a review of the literature, we investigate the hydraulic properties of volcanic rocks. After a short description of peculiar aspects regarding groundwater recharge in insular oceanic environments, the different modes of groundwater occurrence are reviewed. Various schematic conceptual models are synthesized. Related methods of groundwater development are described as well as water quality issues encountered in volcanic contexts. By means of a simple analytical solution, we discuss possible explanations to interpret the contrasted hydrogeological situations of basaltic islands.

### 3.2 Volcanic rocks and edifices

#### 3.2.1 Origins and evolution of a volcanic island

##### 3.2.1.1 Initial stages of a volcanic island

Although most Earth volcanism is associated with subduction zones at plate boundaries, many islands are basaltic and emerge as the consequence of mid- or intra-plate volcanism [Fowler, 2005]. When islands form a chain with ages increasing in one direction, they were built as the lithospheric plate moved over what is commonly called a *hotspot* (e.g. Hawaiian Archipelago in the Pacific Ocean, La Réunion Island in the Indian Ocean). Basaltic volcanic islands may also be organized along a mid-oceanic ridge, where pressure fall induce massive partial melting (e.g. Azores Archipelago, Iceland).

Basalt is a family of lavas relatively mafic (rich in magnesium and iron) and basic (poor in silica). They are divided according to their normative mineral content into alkali-olivine basalts (relatively more alkaline, i.e. rich in  $K_2O$  and  $Na_2O$ ) and tholeiitic basalts. The former are more likely to originate from *hotspot* contexts where partial melting is weaker, while tholeiitic basalts generally originate from oceanic ridges, where partial melting is higher, forming less depleted lavas (richer in Mg, Fe) [Bardintzeff and McBirney, 2006]. Basaltic lavas flows at a temperature of ca. 1200 °C and are relatively fluid, which allows continuous degassing and effusive eruptions. Yet, beginning of effusive eruptive events are characterized by high gas content and may be accompanied by short explosive period accompanied by ash deposit.

Extruded from one or several shield volcano(s), basaltic volcanic islands are the visible part of larger edifices lying on the sea-floor several kilometer deep under sea level. Lava flows originate from vents and fissures, possibly aligned along a rift zone intruded by numerous feeding dikes [Thouret, 1999]. The organization of rift zones is controlled by tectonic settings, than can be modified by local stresses such as gravitational sliding [Acocella and Neri, 2009; Carracedo et al., 2009].

##### 3.2.1.2 Erosion and subsidence

Both of constructive (eruptions) and destructive (erosion) processes are effective simultaneously during the active life of the volcano, after which destructive agents alone control the morphological evolution.

Volcanic formations are easily erodible and steep slopes around eruption areas are prone to fast destruction by gravity and running water, as well as by sea abrasion in coastal areas. Slope instability leads to large-scale slumping and landslides. They may be at the origin of modifications of surface and groundwater

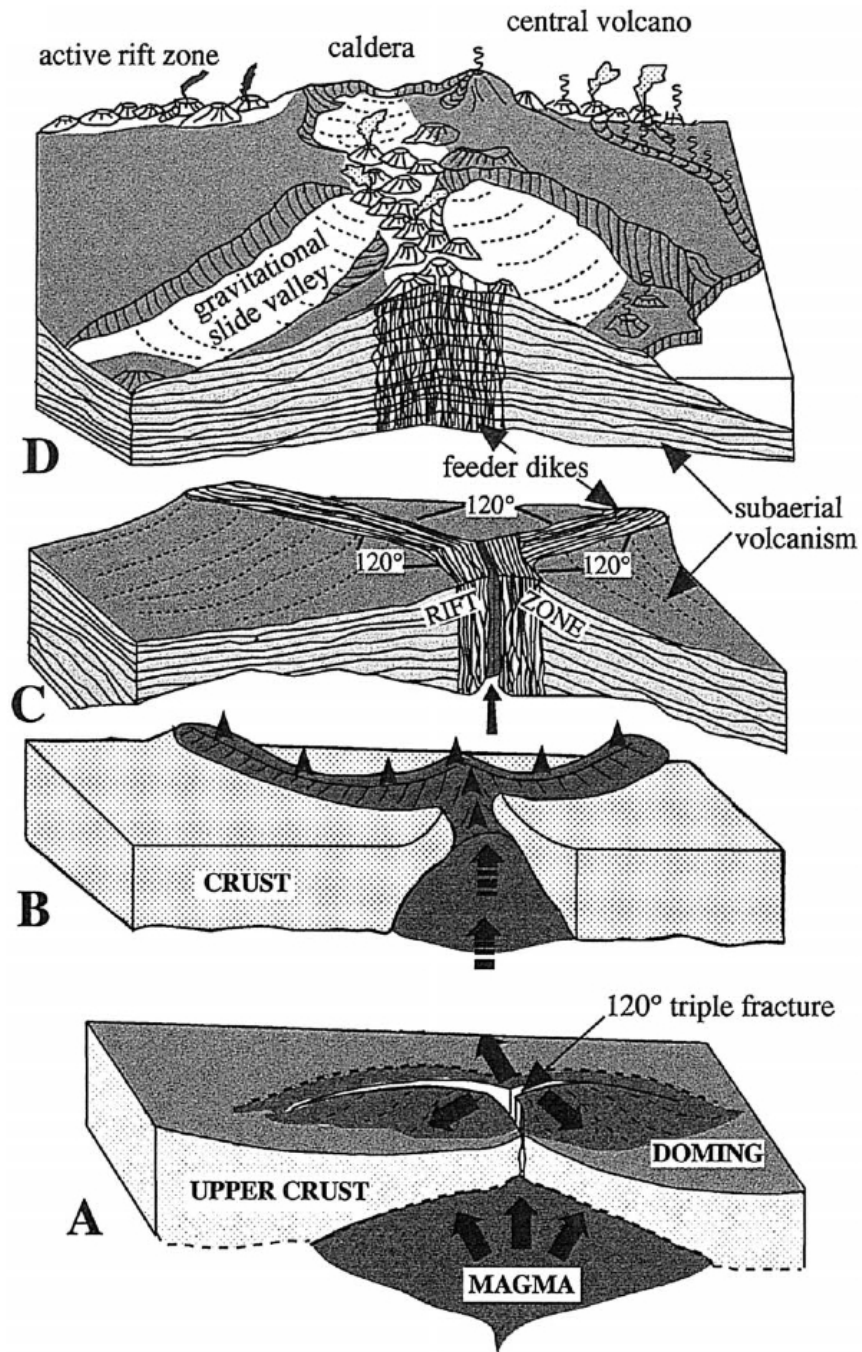


**Figure 3.2:** A hot-spot based schematic model for the evolution of a *Mercedes-type* rift zone. From *Thouret* [1999].

### 3. HYDROGEOLOGY OF BASALTIC ISLANDS

---

flow systems [Custodio, 2004; Join *et al.*, 2005]. In the Galapagos Islands, springs originate from the dismantlement of pyroclastic cones (*author's observation*).

Streams dissect volcanic material and transport it downstream, eventually redepositing it in valleys in the coastal areas, or possibly on the submarine flanks on the volcanoes [Peterson and Morre, 1987].

The thin oceanic lithosphere sags downward because of the weight of the edifice [Thouret, 1999] so that subaerial extruded lavas are brought down under sea level [Peterson and Morre, 1987]. Meanwhile, uplift may be responsible of submarine volcanic rock outcropping (e.g. Isabela Island, Galapagos *Amehung et al.* [2000]).

#### 3.2.1.3 Final stages of a volcanic island

With decreasing volcanic activity, increasing subsidence and erosion, island altitude progressively reaches sea level and disappears. In tropical and equatorial contexts, calcareous sediments are produced by marine organisms and may form a ridge around the island, a reef barrier [Vacher and Quinn, 1997]. This may lead to the formation of an *atoll* [Vacher and Quinn, 1997].

## 3.2.2 Volcanic formations

### 3.2.2.1 Lavas: *pahoehoe* and *aa'*

When it reaches the surface, more or less degassed magma forms lavas, which spread away from vents and fissures. They are classified depending on their viscosity and emplacement conditions into two types, *pahoehoe* and *aa'*, borrowed from the Hawaiian native language.

*Pahoehoe* (ropy type) lavas are fluid and tend to spread out rapidly, forming thin lava flows on sloping ground, or large lava fields in flat areas. They have smoothly undulating surface, they are generally thin, and contain cracks and voids of various sizes, which are collapsed in places. However, ponding of *pahoehoe* lava in depressions or on gentle slopes can result in thick accumulations of massive *pahoehoe* [Peterson and Morre, 1987].

Eruptions of *pahoehoe* lavas are usually accompanied by the formation of lava tubes or tunnels. They form when a solidified crust develop at the top of the flow, while lava keeps flowing beneath [Valerio *et al.*, 2008]. When the lava flux ceases, the tunnel may be emptied, leaving tunnels from 1 m to 20 m in diameter and several kilometer long (Valerio *et al.* [2008] and references herein).

Depending on their viscosity, cooling speed and gas content, *pahoehoe* lavas commonly grade into *aa'* (clinkery type) lavas with increasing distance from the eruptive vent. *Aa'* lava flows are typified by a central core of massive rock about

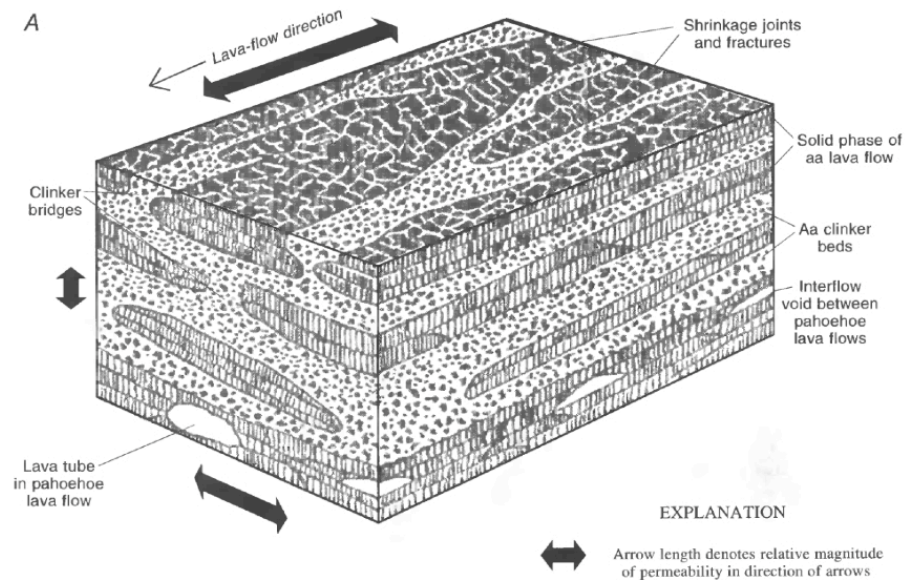


**Figure 3.3:** Structure of a lava flow sequence, composed by piles of *pahoehoe* and *aa'* flows with clinker beds. From *Hunt* [1996].

a meter to several meters thick, with a surface layer of coarse, fragmental rubble known as *aa'* clinker, or flow-top breccias [Fowler, 2005]. Beneath the clinker, the core of viscous, incandescent lava continues to spread, carrying along the clinker [Peterson and Morre, 1987]. As the flow moves forward, clinker and blocks around the massive core cascade down the front of the flow and are overridden by it. Subsequent cooling and volumetric contraction of the core result in well-developed joints. Vertical joints are most conspicuous, although lateral and oblique joints resulting from shear stresses within the flowing core are also common [Fowler, 2005]. As for *pahoehoe*, emplacement of *aa'* on gentler slopes results in thicker, more massive lava flows.

Viscous lavas originate from more acidic magmas, that may originate from a basaltic magmatic source after a long differentiation process in a magmatic chamber. This kind of lavas tends to pile up around the outflow pit. In some cases only a plug of semi-solid hot rock has extruded, possibly accompanied by sudden outburst of ash flows [Custodio, 2004].

Submarine volcanic deposits include the *pillow* lavas common at mid-oceanic ridges, formed at depth with high hydrostatic pressure. Shallower submarine lava extrusion turns to be explosive and form finely comminuted glassy ash (hyaloclastite) and breccias, possibly with bioclastic material [Hunt, 1996]. These formations may outcrop after uplift but are relatively scarce in the sub-aerial part

### 3. HYDROGEOLOGY OF BASALTIC ISLANDS

---

of the islands.

The bulk of a basaltic island is thus composed of dike-free effusive basaltic rocks formed by subaerial undifferentiated *aa'* and *pahoehoe* 1-10 m thick, that make up a gently dipping stratified fabric extending from land surface to considerable depth [Gingerich and Voss, 2005] (Fig. 3.3).

#### 3.2.2.2 Pyroclasts

Gases may exsolve more or less violently in the form of bursts, in which part or much of the magma is fragmented and thrown into the air, forming pyroclasts (tephra) varying in size from coarse blocks to fine dust (ashes). Pyroclasts may be deposited as cooled fragments which remain loose, or as hot fragments which may be welded to some extent [Fowler, 2005]. The block, gravel and sand size pyroclasts (lapilli) pile up around the outflow area, forming a cone, which is symmetrical or deformed, depending on wind strength- and land slope.

Near the volcano, the ratio of lavas to pyroclasts is highly variable. It can be high in some basaltic shield volcanoes such as in Hawaii, but very low in explosive eruptions of acidic type, or when the rising magma meets groundwater (phreatomagmatism) [Clarke *et al.*, 2009]. This contact between intruding magma and groundwater may lead to violent explosions, that leave a peculiar hole on the surface, called *maar* which may later form a lake since weathering rapidly produces a clayey impermeable layer [Bardintzeff and McBirney, 2006].

#### 3.2.2.3 Dikes

Dikes are thin, sub-vertical massive sheets of intrusive rock [Fowler, 2005]. They have a high importance in hydrogeology and often form groundwater barriers [Custodio, 2004]. For this reason, dike physical properties and spatial distribution deserve to be detailed.

The density of dikes is higher close to a magmatic chamber, rift zones, and calderas, where magmatic activity is concentrated. From observations in Iceland, Gudmundsson [2002] distinguished inclined thin dike-sheets forming dense swarms, and regional sub-vertical dikes 4-6 m thick and several kilometers long. In both situations, Gudmundsson [2002] state that dike density decreases with altitude in the lava pile.

Stress regimes in volcanic contexts are the result of tectonic, magmatic, and gravitational stresses. Dikes develop perpendicularly to the local least compressive stress. They may align along a main simple rift zone, or a «Mercedes»-type stellate complex [Thouret, 1999] (Fig. 3.2). But the presence of a volcanic edifice and flank instability complicates the simple dependence on the regional tectonic setting, introducing significant deviations from expected dike patterns [Acocella

and Neri, 2009]. Dikes at many volcanic edifices show characteristic radial and/or circumferential patterns, suggesting control by a local stress field imposed by a pressurized magma reservoir and/or the load of the edifice [Acocella and Neri, 2009; Chadwick and Howard, 1991]. Flank collapses induce a perturbation of the stress regime and lead to horseshoe-shaped rift zones such as in Canary Islands [Carracedo et al., 2009; Walter et al., 2005].

Dikes are not necessarily straight and continuous, but may re-use previous fracture paths, form *en echelon* segments, be deviated or interrupted by changes in the lithology [Acocella and Neri, 2009; Clemente et al., 2007; Gudmundsson, 2002]. Horizontal dikes are called *sill*, they form when magma intrudes weaker sub-horizontal interflows.

Dikes are affected by cooling joints perpendicular to the cooling surface, and fracture can be later formed by brittle deformation at the occasion of an active tectonic period or subsequent dike intrusion.

Volcanic formations originate from rift zones or eruptive centers that are characterized by the concentration of intrusive formations, sub-vertical dikes through which basalts were extruded at the surface [Peterson and Morre, 1987]. These eruptive zones form the topographic crests of the volcanoes and their submarine extensions. Within each rift zone, a dike complex zone and a marginal dike zone can be delineated (Fig. 3.2). Dikes are most heavily concentrated in the dike complexes [Carracedo et al., 2009], where they commonly constitute more than 10% or more of the total rock. Most of the dikes dip steeply and are arranged in a sub-parallel pattern roughly aligned parallel to the trends of the major rift zones. Away from the rift zones, on the flanks of the volcanoes, dikes are sparse or absent, they account for less than 5% of the total rock [Hunt, 1996].

### 3.2.2.4 Paleo-soils, lahar

Chemical weathering and particularly hydrolysis of basaltic rocks result in the formation of erodible soils and thick zones of clay-rich saprolite where textural features of the parent rock are retained [Hunt, 1996]. Subsequent lava flows may spread over such formations. The heat “bakes” the underlying material, which acquires a reddish color (rubefaction). The extension of this red layer depends of the initial extension of the soil and the extension of the overlying lava flow. Due to its contrasting color, this horizon may be easily mapped kilometer long along scarps where it crops out [Custodio, 2004].

Volcanoes commonly have steep slopes close to the geotechnical equilibrium. Erosion, earthquakes and uplifting due to deep magma emplacement may trigger large landslides that deeply affect volcanic formations and leave deep scars in landscapes [Carracedo et al., 2009]. Along the sliding surface, pressure and friction may form a layer of finely crushed material, sometimes rich in bentonite

### 3. HYDROGEOLOGY OF BASALTIC ISLANDS

---

[*Custodio*, 2004]. Landslides may be accompanied by mudflows (lahar), which form clay-rich impervious units between lava flows.

Subsequent lava flows, colluvial, or alluvial material may cover landslide scars and fault scarps, which complicates the identification of initial features [*Custodio*, 2004; *Thouret*, 1999].

#### 3.2.3 Evolution of volcanic rocks

##### 3.2.3.1 Fractures and faults

Massive basalts are commonly dissected by a dense network of cooling joints, possibly forming characteristic columnar units [*Khaleel*, 1989]. Joints develop perpendicular to the cooling surface, i.e. sub-vertically in lava flows, and sub-horizontally in sub-vertical dikes.

At the regional scale, oceanic islands are often dissected by major (mostly normal) faults related to regional extensional tectonic regime or flank collapse such as in the Canary, Hawaii, and Galapagos archipelagos [*Martel and Langley*, 2006; *Parfitt and Peacock*, 2001; *Podolsky and Roberts*, 2008; *Walter et al.*, 2005].

##### 3.2.3.2 Hydrothermalism

Over a long time (up to several million years) the slow cooling of magma chambers, is accompanied by the release of large quantities of hot gases, mostly CO<sub>2</sub> and water vapor. They have important impact on groundwater chemistry and modify rock properties by secondary mineralization and thermal metamorphism [*Cruz*, 2003; *Custodio*, 2004; *Keller et al.*, 1979]. Hydrothermalism extends outward with progressively decreasing intensity. Fissures tend to be progressively filled with new minerals and impart a very low permeability to the surrounding of the volcanic center. The formation of zeolite, a secondary mineral in pores of lavas in La Réunion dramatically reduces rock porosity [*Join*, 1991].

##### 3.2.3.3 Weathering

Due to their glassy nature and great specific surface, chemical alteration of ashes, breccias and scorias is enhanced and lead to the formation of clayey minerals. Massive lavas and dense ignimbrites are much more resistant to chemical alteration, conserving some of their primary and secondary properties for a much longer time, up to tens of millions of years [*Hunt*, 1996]. The effects of alteration are dependent of the availability of water, so that formations of the windward sides are more altered.

---

### 3.3 Hydraulic properties of volcanic formations

---

Fluxes of colloids, leaching, and hydrothermal mineralization induce clogging of fractures and pores. Minerals from overlying material are redeposited at greater depths in the saprolite to form clay-rich zones, sand sheets and concretions of iron oxides. These deposits reduce permeability.

## 3.3 Hydraulic properties of volcanic formations

### 3.3.1 Estimating hydraulic properties

Various techniques are employed to estimate hydraulic properties, each of them providing a value for an equivalent porous medium at a given scale. Permeability measurements are shown to be particularly scale-dependent in volcanic contexts [*Ingebritsen and Scholl, 1993*].

Estimates can be performed at the laboratory on core samples (scale of 1-10 cm). At the scale of the outcrop (1-10 m), portable air permeameter may be used to estimate the permeability of porous media *Folio* [2001]. Fractured media can be characterized from fracture network mapping [*Folio, 2001; Khaleel, 1989*]. The equivalent horizontal and vertical hydraulic conductivities of composite media can be estimated from the arithmetic and harmonic means respectively (e.g. *Folio* [2001]).

Pumping tests allow a direct measurement of equivalent transmissivity and storage coefficient of an area surrounding the well (10-1000 m). They are generally interpreted in the same way as the tests carried out in granular material (Jacob, Theis, and Hantush methods) [*Custodio, 2004; Gingerich, 1999; Rotzoll et al., 2007*], which were developed for isotropic and homogeneous media. These estimates, and particularly storage coefficient estimate, may be irrelevant in heterogeneous formations [*Meier et al., 1998*].

In coastal areas, aquifer diffusivity can be estimated from phase shift and attenuation of the tidal signal [*Cruz, 2003; Ferris, 1952; Rotzoll et al., 2007*]. This method provides an estimate representative of a larger area (1-5 km) than pumping tests, but is particularly sensitive to the coastal boundary conditions [*Slooten et al., 2010*].

At the regional scale (1-10 km), equivalent hydraulic properties may be estimated by means of numerical models calibrated to observed groundwater levels (e.g. [*Custodio et al., 1988; Gingerich and Voss, 2005; Violette et al., 1997*]).

### 3.3.2 Lava flows and pyroclastic deposits

Although most rocks in basaltic formations have similar chemical compositions, the diversity of their mode of emplacement causes a large variety of physical

### 3. HYDROGEOLOGY OF BASALTIC ISLANDS

---

properties. The voids that constitute porosity in volcanic rocks may be classified into four categories (after *Hunt* [1996]):

1. Vesicular voids originate from gas bubbles exsolved from lavas during eruptions. They are sensitive to weathering and are poorly connected, they contribute little to effective porosity.
2. Fracture voids are constituted by cooling joints, cracks and interflow separations.
3. Intergranular voids are found in fragmental tephra, including cinders, rubble, and clinkers that are analogous to clean, coarse gravel.
4. Conduit voids are large openings such as lava tubes and interflow voids that take forms similar to karstic conduits in limestones, but they may be filled, and collapse at depth.

The mixture of voids and fractures imparts initial high porosity and permeability to young *pahoehoe* flows. But where *pahoehoe* flows are massive or weathered, effective porosity and permeability are comparatively low. The intergranular porosity of *aa'* clinker (at top and bottom of the lava flow) is analogous to the intergranular porosity of coarse, well sorted gravel. Matrix porosity and permeability of central massive cores of *aa'* flows is negligible.

The bulk porosity of basalt flow ranges between 0.8 and 20%, and 0.1 to 8% for the effective porosity, depending on the texture of the lava [*Custodio*, 2004]. Averaged over several sequences, drainable porosity of dike-free lava flows ranges between 2% and 8%. Values for compressive matrix storage applicable to layered basalt are based on a compressibility range given for jointed rocks, ranging from  $10 \times 10^{-8}$  to  $10 \times 10^{-10}$  Pa<sup>-1</sup> (Freeze and Cherry, 1979 in: *Souza and Voss* [1987]). This range includes significantly greater matrix compressibility than the compressibility of water. Specific-yield coefficients obtained from the calibration of numerical models range between 0.05 and 0.01.

Hydraulic properties of layered lava flow sequences are controlled by the nature of the alternating layers. Widespread beds of weakly weathered clinker contribute to increase horizontal permeability while the occurrence of unconformities such as impervious cooked-soils, weakly fractured massive lava flows, lahar or welded tuff present a barrier to the vertical permeability. This imparts a relative high anisotropy ratio to this volcanic formation, with the largest permeability in the longitudinal direction of the lava flow, and the smallest permeability normal to bedding.

Hydraulic conductivity of individual flow units ranges between  $10 \times 10^{-10}$  to  $10 \times 10^{-4}$  m/s, also depending on the texture of the lava (dense, unfractured to young, highly brecciated,...) [*Custodio*, 2004] (Fig. 3.4). Horizontal permeability

### 3.3 Hydraulic properties of volcanic formations

---

is often higher (up to two orders of magnitude) than vertical permeability [*Custodio*, 2004; *Hunt*, 1996; *Oki*, 1997]. Lateral hydraulic conductivity of lava flow sequences ranges between  $10 \times 10^{-7}$  and  $10 \times 10^{-4}$  m/s, with horizontal to vertical ratios between 3:1 and 200:1 [*Custodio*, 2004].

Island	Canary (Teneriffe)	Hawaii (Kauai)	Hawaii (Maui)	Hawaii (Oahu)	Réunion (Fournaise)	Réunion (Fournaise)
Reference	(1)	(2)	(3)	(4)	(5)	(6)
Code/mesh	2D vert, hz.	SUTRA 2D vert.	SHARP 2D vert.	SUTRA 3D	MODCOU 2D	FEMWATER 3D
Interface with sea	not simu- lated	diffuse interface	sharp inter- face	diffuse interface	not simu- lated	not simu- lated
Conceptual model	high elev.	high elev.	high elev.	low elev.	low. elev.	high elev.
Recharge [m/y]	10?	0.76	3	2	2.4	4.9
$K_h$ [m/s]	$2 \times 10^{-7}$	$5 \times 10^{-6}$	$1 \times 10^{-6}$	$5 \times 10^{-3}$	$1 \times 10^{-3}$	$1 \times 10^{-2}$ to $1 \times 10^{-6}$
$K_v : K_h$	50:1	10:1	1:1	200:1	-	1:1

**Table 3.2:** Characteristics of hydrogeological numerical models implemented for volcanic islands basal aquifers. References: (1) *Custodio et al.* [1988] (2) *Izuka and Gingerich* [2003] (3) *Gingerich* [1998] (4) *Gingerich and Voss* [2005] (5) *Violette et al.* [1997] (6) *Join et al.* [2005].

Pyroclastic deposits include ash, cinder, spatter, clinker, lapilli and larger blocks. The porosity and permeability of such deposits are essentially from granular type. Young coarse pyroclastic deposits are often loose and very permeable, while ashes have a relative good bulk porosity, but being very fined-grained the permeability is weaker. *Custodio* [2004] reports effective porosity values between 5-10% for loose pyroclasts and 1-5% for fresh ash falls. Permeability ranges between  $10 \times 10^{-6}$  to  $10 \times 10^{-4}$  m/s for loose pyroclasts and  $10 \times 10^{-7}$  to  $10 \times 10^{-6}$  m/s for ash falls.

Estimates of hydraulic conductivity obtained from numerical model calibration at the regional scale may differ from local estimates from pumping tests. Regional estimates integrate heterogeneities such as conductive faults or impervious barriers. Median model values range between  $1 \times 10^{-7}$  and  $5 \times 10^{-2}$  m/s (Table 3.2). Comparisons between islands become difficult when hydraulic properties are not homogeneous in the model (e.g. the layered permeability model of *Join et al.* [2005]).

### 3. HYDROGEOLOGY OF BASALTIC ISLANDS

---

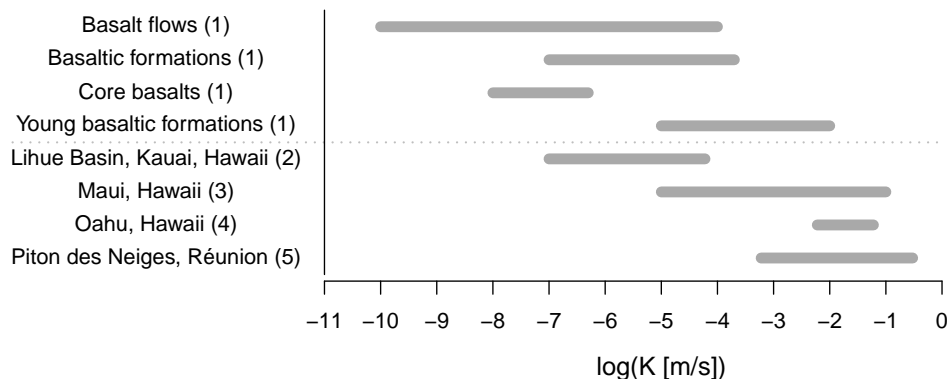


**Figure 3.4:** Review of hydraulic conductivities reported in basaltic contexts. (1) from the review in undifferentiated basaltic contexts by *Custodio* [2004], others are examples from pumping tests performed in insular volcanic contexts: (2) *Gingerich* [1999], (3) *Rotzoll et al.* [2007], (4) *Hunt* [1996], (5) *Join* [1991].

#### 3.3.3 Paleo-soils and lahar

Similarly to ash deposits, paleo soils and lahar are often impermeable units that confine aquifer or sustain perched saturated horizon in the unsaturated zone [*Hunt*, 1996]. Lahars (mudflows) have permeabilities ranging between  $1 \times 10^{-4}$  and  $1 \times 10^{-7}$  m/s [*Custodio*, 2004]. To the author's knowledge, permeability estimates of paleo-soils are not available in the literature, but they are probably similar to that of mudflows.

#### 3.3.4 Intrusive formations

Dikes and sills, with their fine grained texture generally behave as hard-rock with solely fracture porosity and permeability [*Hunt*, 1996]. Cooling joints and fractures from magmatic and tectonic origins improve dike permeability. Last-generation dikes are expected to be the most impervious, since their are unlikely to be affected by tectonic fracturing.

Dikes are often considered as impervious barriers. Meyer and Souza (1995) (in: *Oki* [1997]), suggest that the hydraulic conductivity of a dike complex ranges from about  $3 \times 10^{-7}$  to  $3 \times 10^{-8}$  m/s. The permeability of the dike itself ranges between  $3 \times 10^{-8}$  m/s and  $3 \times 10^{-11}$  m/s. Nevertheless, studies performed in volcanic (but not insular) contexts show that dikes may be more conductive than the host rock [*Singhal and Gupta*, 2010]. The equivalent, regional hydraulic conductivity of a

rift zone decreases as the number of dike intrusion increases. Where dikes strike in a preferential direction, the permeability is expected to be anisotropic with the greater value striking parallel to the dikes [Oki, 1997].

### 3.3.5 Evolution of permeability with depth and age: basement, and core of the island

Hydrothermalism (c.f. section 3.2.3.2) and weathering (c.f. section 3.2.3.3) both induce a reduction of porosity and permeability with time and depth.

Due to the effects of alteration, initially permeable formations may evolve to a low permeability mass in only a hundred thousand to a few million years [Cruz, 2003; Hunt, 1996; Oki, 1997]. Undifferentiated volcanic massifs of several million years old are generally impervious and generally behave as aquitards if not as aquicludes [Hunt, 1996]. From gas-permeameter permeability surveys on scoriaceous layers in La Fournaise massif (Réunion, France), Folio [2001] showed that despite significant heterogeneities at the scale of the formation, deeper and older formations had weaker permeability. Comparing the results of pumping tests performed in 65 different wells, Cruz [2003] found that transmissivity was weaker in older formations.

With increasing depth and lithostatic pressure, a non negligible fraction of fractures and voids may be closed [Gingerich, 1998; Ougier-Simonin et al., 2011]. The reduction of permeability can be modeled with an exponential law, stating that permeability is divided by a factor of 100 every 400-1700 m, depending of geological contexts [Ougier-Simonin et al., 2011; Saar and Manga, 2004]. The reduction of permeability with depth is more acute in the presence of a geological discontinuity, such as impervious older volcanics. This is the case in La Fournaise (Réunion Island) [Rançon et al., 1989]. Hydrothermalized, densely dike-intruded formations form an impervious core below eruptive centers [Hunt, 1996; Keller et al., 1979].

At the scale of the edifice, poorly permeable formations form a *substratum*, which may rise at high elevations below the eruptive center.

## 3.4 Recharge processes

Surrounded by the ocean, under the influence of tradewinds and relative high temperature, tropical and equatorial islands have some peculiar climatic characteristics. Rainfall is variable in time because of local and regional seasonal patterns. Under the influence of persistent trade-winds, spatial distribution of rainfall is controlled by the *orographic* and *shadow* effects. As a consequence,

### 3. HYDROGEOLOGY OF BASALTIC ISLANDS

---

the distribution of precipitations is affected by great discrepancies between a wet windward side and a dryer leeward side. Mean annual precipitation varies between 250 to more than 11000 mm in Hawaii [Giambelluca *et al.*, 1986], and from 1000 to 12000 mm on La Réunion Island [Soler *et al.*, 1997].

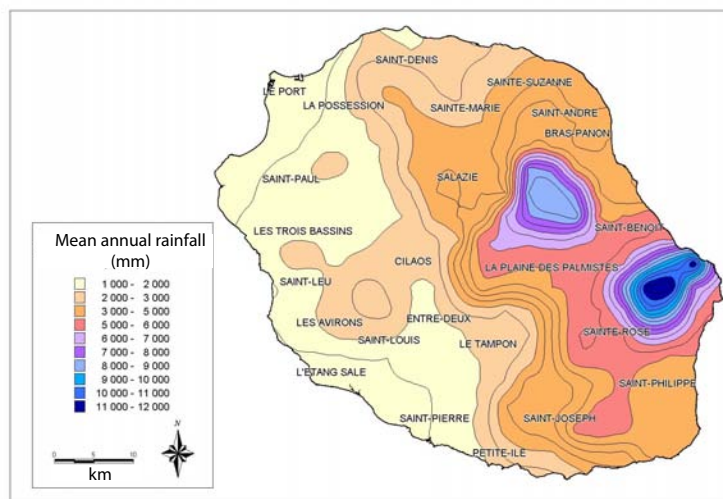


**Figure 3.5:** Distribution of mean annual rainfall over La Réunion Island [Soler *et al.*, 1997].

The occurrence of fog, likely to increase effective precipitation height, is reported in many oceanic islands such as in Hawaii (US) [Brauman *et al.*, 2010; Giambelluca *et al.*, 2011; Takahashi *et al.*, 2011], La Réunion Island (France) [Gabriel and Jauze, 2008], Madeira Island (Portugal) [Prada *et al.*, 2009], Canary Islands (Spain) [García-Santos and Bruijnzeel, 2011], and Galapagos Islands [Pryet *et al.*, 2012].

The amount of groundwater recharge is the volume of rainfall, fog drip and irrigation water that is not lost to runoff or evapotranspiration or stored in the soil [Gingerich and Oki, 2000]. Using the water budget approach, Izuka *et al.* [2010] computed recharge for a large dataset in Hawaii and developed a simple relation between precipitation and recharge, valid for annual precipitations ranging between 880 and 8900 mm. According to their results, groundwater recharge corresponds to 0 up to 64% of incident precipitation.

Soil water tends to move vertically downwards towards the water table but the actual detailed movement is probably through the layers and blocks and not through the fissures, except when recharge is intense, after heavy rains [Custodio, 2004]. Hydraulic properties and thickness of soils control the partition between infiltration, runoff and losses by evapotranspiration. In average, recharge values

range typically between 10 to 50% of incident precipitations on a regional scale [Gingerich and Oki, 2000].

## 3.5 Groundwater occurrence

### 3.5.1 Basal aquifer

#### 3.5.1.1 Two contrasting conceptual models

A *basal aquifer* is reported in each volcanic island, it is defined as the groundwater mass lying under a “main water table below which all the permeable rocks are saturated” [Meinzer, 1930]. In reference to its peculiar relationship with the ocean, the basal aquifer is also defined as the *freshwater lens*, buoying over seawater [Gingerich and Oki, 2000]. Most often, the water table remains at low elevation in coastal areas, but two contrasting configurations are reported inland.

In a first model, the *low-elevation basal aquifer* (Fig. 3.6(A), 3.7, and 3.9), the slope of the water table remains low inland, reaching a few tens of meters above sea level to its highest level. This model was formerly called the *Hawaiian model*, but is not applicable to all the archipelago. In this configuration, the existence of springs at higher elevation is interpreted by the existence of *perched* or *dike-impounded* aquifers (Fig. 3.6, A and 3.7, and 3.9). Current examples of *low-elevation basal aquifer* include the islands of Oahu and Hawaii (US) [Gingerich and Voss, 2005], Cabo Verde Islands [Heilweil et al., 2009], Piton de la Fournaise [Violette et al., 1997], and Santa Cruz Island (Galapagos) [d’Ozouville, 2007a].

In the second model, the *high-elevation basal aquifer*, alternatively called *Canary Islands model* (Fig. 3.6(C,D), and 3.8), the water table elevation is reported to increase markedly toward the center of the island (hydraulic gradient greater than 0.01 and sometimes exceeding 0.1) and the water table reaches several hundreds of meters above sea level [Custodio, 2004]. *High-elevation basal aquifers* have been identified in Tenerife Island (Canary Archipelago, Spain) [Custodio et al., 1988], Kauai Island (Hawaii, USA) [Izuka and Gingerich, 2003].

Reasons invoked for the occurrence of high-level basal aquifer are generally a sensible loss of permeability concomitant with a sufficient recharge rate. Dikes were initially invoked to explain the occurrence of high level groundwater in the Southern Liuhe Basin (Kauai, Hawaii, US), but later hydrogeological investigations showed that dike-free lava flows had a sufficiently small permeability to sustain this groundwater mass [Gingerich, 1998; Izuka and Gingerich, 2003].

The difference between models C and D (Fig. 3.6) is sometimes disregarded. In model C, a high-elevation freshwater lens develops in poorly conductive, *dike-free* formations. In model D, the continuation of the basal aquifer inland is im-

### 3. HYDROGEOLOGY OF BASALTIC ISLANDS

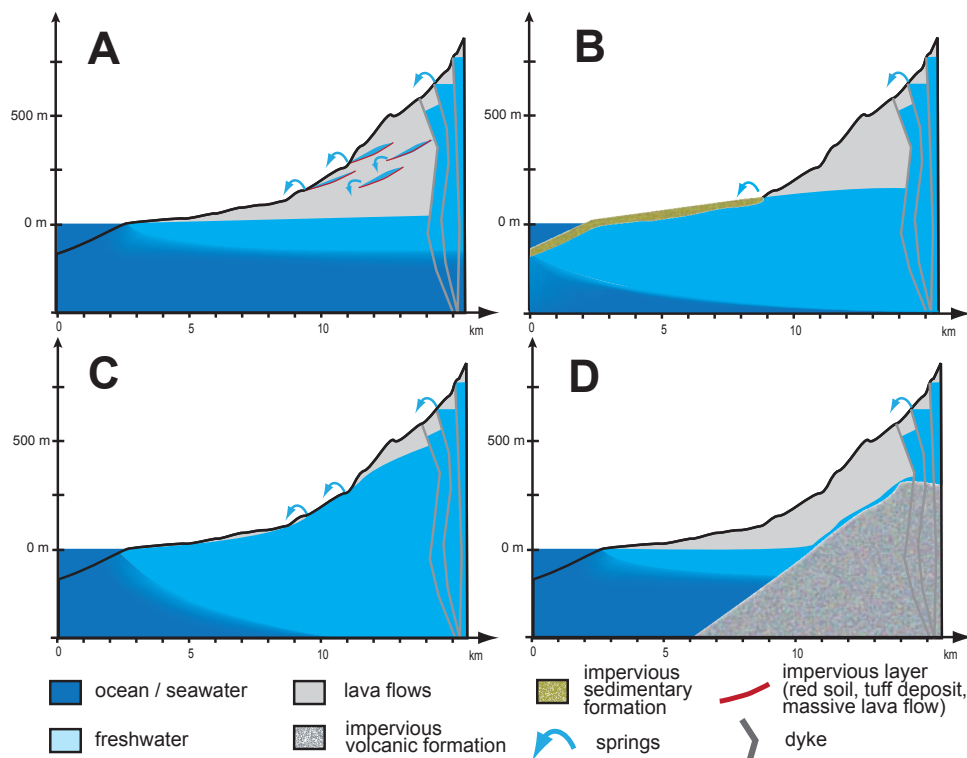


**Figure 3.6:** Review of conceptual models proposed for basaltic volcanic islands. (A) low-lying basal aquifer, dike-impounded, and perched aquifers. (B) basal aquifer covered by an impervious coastal sedimentary caprock. (C) high level basal aquifer (thick freshwater lens) and dike-impounded aquifers. (D) low-lying basal aquifer and *skin-flow* over impervious (saturated) hydrothermalized *core* formations. Coordinates are indicative and do not refer to a specific location. Vertical exaggeration ca. 10x

### 3.5 Groundwater occurrence

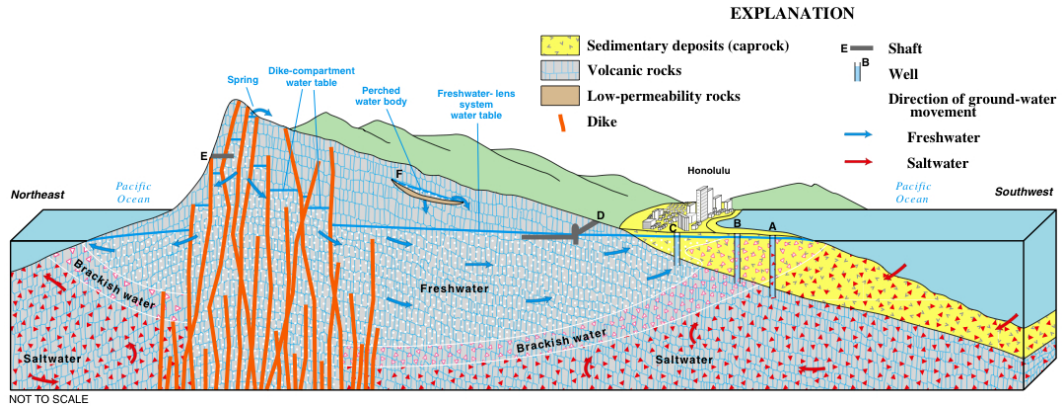


**Figure 3.7:** Hydrogeological conceptual model developed for low-lying basal aquifer of the Hawaiian Islands [Gingerich and Oki, 2000]. A basal aquifer subjected to seawater intrusion gives place to dike impounded groundwater bodies inland. Recharge may transit via perched aquifer bodies (F). Groundwater is abstracted from vertical bore wells (C), horizontal shafts close to sea level (D) or higher through dikes (E)

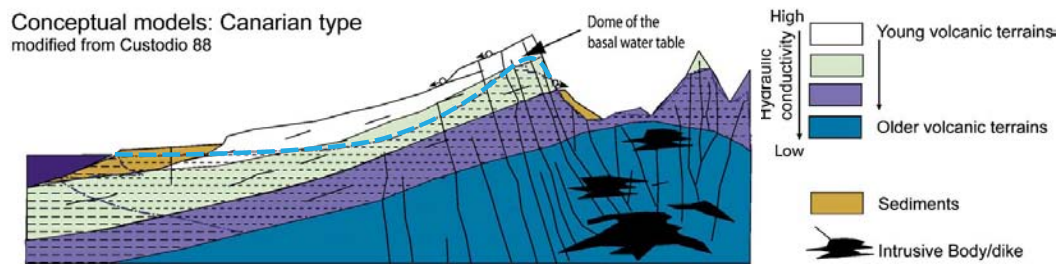


**Figure 3.8:** Conceptual model with a layered distribution of permeability and a thick basal aquifer reaching high elevation, proposed by Join *et al.* [2005] for La Fournaise volcano (Réunion Island).

### 3. HYDROGEOLOGY OF BASALTIC ISLANDS

---

peded by the presence of an impervious (saturated) core, formed by hydrothermalized dike-impounded old volcanics. The aquifer is thinner but may reach high elevation. A *skin flow* is maintained in conductive formations overlying the impervious core. Such a model is discussed for Easter island by *Herrera and Custodio* [2008]. The model proposed by *Join et al.* [2005] (Fig. 3.8) is close to model D, but instead of an abrupt contrast between two formations, he considers a layered permeability distribution with decreasing permeabilities at depth.

Recharge and discharge conditions of the basal aquifer depend on the geometry of the aquifer (Fig. 3.6). The recharge of *low-elevation basal aquifers* is generally restricted to marine outlets in coastal areas. In this configuration, subaerial discharge via perched, dike-impounded aquifers, and streams is very limited. *Low-elevation basal aquifers* have similar recharge conditions, but discharge conditions are contrasting: discharge occurs mainly subaerially from highland springs (feeding streams) rather than directly to the ocean [*Izuka and Gingerich*, 2003].

#### 3.5.1.2 Monitoring and modeling seawater intrusion

The freshwater/seawater interface is generally inferred from the water table elevation with the Ghyben-Herzberg (G-H) equation [*Bear*, 1999]. Salt and freshwater are supposed immiscible, the Dupuit assumption of horizontal flow is assumed, and seawater is supposed to be static.

The reality is closer to a diffuse interface with vertical gradients and slowly flowing saltwater. Groundwater flow tends to follow preferential paths such as little-altered brecciated zones and open joints [*Custodio*, 2004]. This type of flow has great consequences on the dispersive properties of the volcanic medium. Series of small sharp salinity changes are observed in open boreholes [*Gingerich and Voss*, 2005], they are due to heterogeneities in the aquifer fabric, associated with more or less conductive sections in the lava flow stack. This, in addition with tidal effects and recharge fluctuations, induces hydrodynamic dispersion and forms a transition zone of mixed water between the freshwater and the underlying saltwater that can reach several hundreds of meters thick [*Gingerich and Voss*, 2005; *Hunt*, 1996].

Several studies developed numerical models to investigate seawater intrusion. Some of them with the assumption of a sharp interface [*Gingerich*, 1998; *Oki*, 1998], others with a diffuse interface [*Gingerich and Voss*, 2005; *Izuka and Gingerich*, 1998a; *Souza and Voss*, 1987]. Compared to the numerical models, the G-H solution may provide uncertain estimates of the 50% mixing line between salt- and freshwater. For instance, the G-H estimate for Oahu aquifer (Hawaii, USA) oscillated between 10% and 50% mixing line during the last 100 years [*Gingerich and Voss*, 2005]. The misfit may be higher in other situations [*Izuka and*

*Gingerich*, 1998b]. Comparisons of the G-H depth indicate discrepancies of up to 100 m in some wells [*Rotzoll et al.*, 2010]

Due to the existence of vertical head gradients and water mixing in bore wells, measuring and to a greater extent, monitoring the thickness of the freshwater lens is not trivial [*Izuka and Gingerich*, 1998a; *Rotzoll*, 2010; *Rotzoll et al.*, 2010]. During drilling, a reliable estimate can be obtained from the salinity profile. After drilling, aquifer segments should ideally be isolated with packers.

### 3.5.2 High level aquifers

#### 3.5.2.1 Dike impounded groundwater

Steeply dipping volcanic dikes may impound freshwater to great heights, in compartments of permeable lavas, that may be detected with high elevation spring outflow [*Custodio*, 2004; *Hunt*, 1996; *Pouchan et al.*, 1988]. This type of aquifer mainly occurs in rift zones, but elevation of the groundwater table is reported in other areas, and is interpreted as the effect of dikes perpendicular to slope. At depth, the connection of dike-impounded aquifers to the basal aquifer is possibly affected by the very low permeability of this environment, so that the G-H relation may not be valid [*Hunt*, 1996].

#### 3.5.2.2 Perched aquifers

A saturated, perched horizon is formed where vertical percolation flux exceeds the capacity of the geologic medium to transmit fluid in unsaturated state [*Wu et al.*, 1999], and is often associated with an abrupt change in lithology or structure [*Hinds et al.*, 1999]. A contrast in lithology may form an impervious substratum for a perched, saturated horizon where groundwater may be stored and flow sub-horizontally within relatively permeable unit.

In volcanic islands, the unsaturated zone above the basal water table may be very thick (several hundreds of meters) and can include discrete layers of weak permeability such as cooked paleo-soils, landslide sliding surface, sills, tuff deposits, or massive lava flows [*Hunt*, 1996]. Perched saturated zones are not rare along the windward sides of the islands. Seepage areas and springs testify the presence of these aquifers. Yet, the outflow is generally only a fraction of recharge [*Custodio*, 2004]. The rest returns to the basal aquifer after a second transit through the underlying unsaturated zone. Perched aquifers may remain buried in young islands, whereas conditions are more favorable to outcropping in evolved islands, with deeply incised valleys and flank collapses.

Perched water occurs in far less volume than basal or dike-impounded water and it responds more readily to extremes in climate such as droughts and episodic

### 3. HYDROGEOLOGY OF BASALTIC ISLANDS

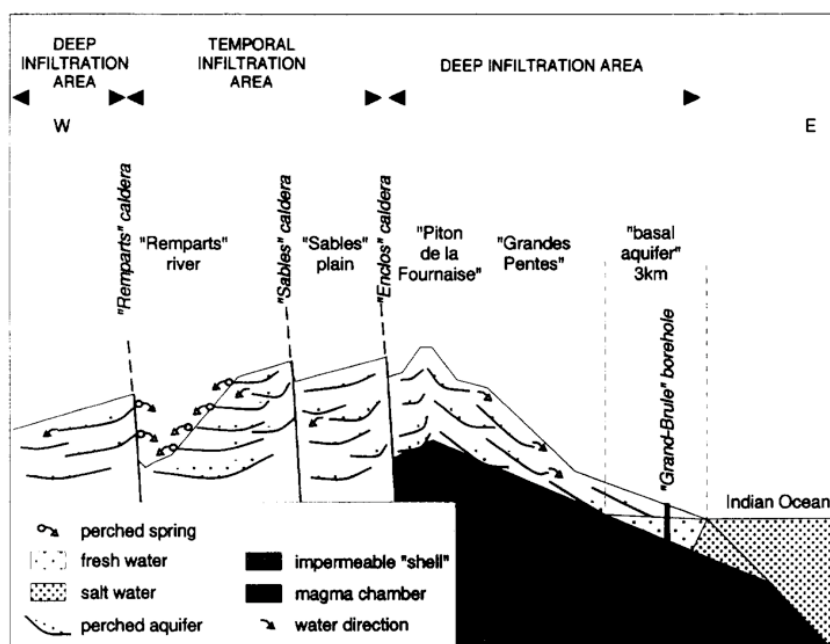


**Figure 3.9:** Groundwater flow pattern proposed by *Violette et al.* [1997]. The occurrence of high-level groundwater is interpreted by the existence of series of perched aquifer.

recharge events [Hunt, 1996] but may be of higher quality (low salt content, reduced risk of contaminations) [Cruz, 2003]. Perched aquifers are reported in several islands, as in Hawaiian Islands [Hunt, 1996; Ingebritsen and Scholl, 1993] (Fig. 3.7), La Fournaise (Réunion) [Violette et al., 1997] (fig. 3.9), Pico Island [Cruz and Silva, 2001], and the Galapagos Islands [d'Ozouville, 2007a].

### 3.5.3 Groundwater development and quality issues

Groundwater constitutes a large proportion of freshwater resources in volcanic islands (e.g. in the Hawaiian Archipelago [Gingerich and Oki, 2000], Azores [Cruz, 2003], and Madeira [Prada et al., 2005]). Numerous sub-horizontal shafts have been drilled in Hawaiian and Canary Islands [Custodio et al., 1983; Gingerich and Oki, 2000].

Bore wells are commonly executed with pneumatic down-the-hole hammer rigs, but face peculiar problems in unconsolidated sections and lava tunnels [Custodio, 2004]. Groundwater is abstracted from horizontal wells and galleries (Fig. 3.7).

Horizontal galleries allow gravity driven groundwater collection. When seawater intrusion is acute, pumping bore wells provide brackish water and drawdown induces a rise of the freshwater/saltwater interface. As an alternative, water may be skimmed at the aquifer surface from sub-horizontal shafts.

Withdrawals for irrigation purpose are proven to be unsustainable in Canary Islands [Custodio et al., 1988]. In Hawaii, the thinning of the freshwater lens is interpreted by a reduction of recharge (rainfall and irrigation return-flow) combined with rising withdrawals [Gingerich and Voss, 2005; Izuka, 2006; Rotzoll et al., 2010].

Islands, particularly when they are small, are highly vulnerable to sea water intrusion (e.g. Cruz and Silva [2001]; Falkland [1999]). If recharge rates are low and permeability is high, freshwater easily discharges to the ocean and the freshwater lens is thin. Groundwater abstraction, a fall of recharge rates caused by land use or climate change are prone to alter the hydrodynamic equilibrium between sea and freshwater and have an impact over sea water intrusion (e.g. Oki et al. [1998]).

Other water-quality issues are not addressed in this study, they are not specific to volcanic insular contexts or to other geological contexts, agriculture, industrial activities, and the lack of sewage systems are responsible of a marked degradation of groundwater quality in volcanic islands [Custodio et al., 1983; d'Ozouville, 2007b]. In the coastal area of Santa Cruz island, the basal aquifer is shallow and unconfined. Due to defective sewage system, wastewater reaches the water table after a short transit through the numerous cooling joints.

## 3.6 Discussion

Common hydrogeological features have been identified in basaltic volcanic islands: a basal aquifer in connection with the ocean, perched, and dike-impounded aquifers. Yet, two contrasting hydrogeological conceptual models emerge: a low elevation basal aquifer with weak hydraulic gradient, or the development of a thick freshwater lens with a water table reaching high elevations. Parameters which may explain such a contrast are numerous: the geology (hydraulic properties), climatic conditions (recharge rates), and morphology of the island. Using a schematic model of a symmetric *strip* island (Fig. 3.10), we investigated the respective influence of these controlling parameters on the geometry of an idealized freshwater coastal aquifer. This model serves further discussion on conceptual models.

### 3.6.1 Analytical modeling of the basal aquifer

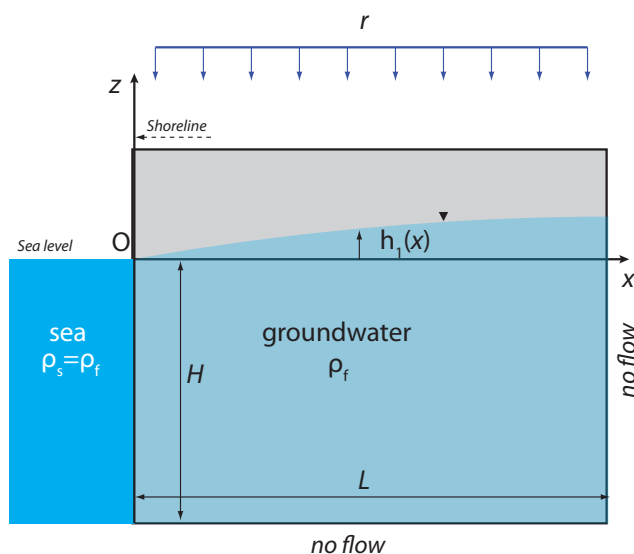


**Figure 3.10:** Simplified sketch of a freshwater basal aquifer. A constant head is imposed at sea level, recharge is homogeneous from the top boundary. Right and bottom boundaries are impermeable.

We consider the simplified sketch of a coastal aquifer, infinite and uniform in the  $y$  horizontal direction with a vertical beach. A groundwater divide is present at a distance  $L$  from the coast, with homogeneous density:

- steady state,
- fluid of constant density,
- isotropic, homogeneous permeability.
- Dupuit hypothesis (horizontal flow),
- vertical beach at  $x = 0$ .

The diffusivity equation [*de Marsily*, 1986] can be written as follow in the 2D space  $(O, x, z)$ :

$$\frac{\partial}{\partial x} \left[ \int_{-H}^{h(x)} K dz \frac{\partial h}{\partial x} \right] = -r \quad (3.1)$$

where  $h(x)$  [m] is the hydraulic head,  $K$  [m/s] the hydraulic conductivity,  $H$  [m] the thickness of the aquifer below sea level,  $L$  is the half-width of the island,  $r$  [m/s] the recharge rate at the upper boundary. Given the boundary conditions  $h(0) = 0$  and  $-K \cdot \frac{\partial h}{\partial x}(L) \cdot (h(x) + H) = 0$ , Eq. 3.1 can be integrated into:

$$h(x) = -H + \sqrt{-\frac{r}{K} \cdot x^2 + 2\frac{rL}{K} \cdot x + H^2} \quad (3.2)$$

defined for  $x \in [0; L]$ . Following dimensionless parameters can be defined:

$$h' = \frac{h}{L} ; x' = \frac{x}{H} ; \chi = \frac{r}{K} ; \xi = \frac{L}{H} \quad (3.3)$$

where  $x'$  is the dimensionless spatial coordinate,  $h'$  the dimensionless water table height,  $\xi$  the aspect ratio, and  $\chi$  the recharge parameter. Eq. 3.2 can be translated to a dimensionless form, defined for  $x' \in [0; \xi]$  :

$$h'(x') = -1 + \sqrt{-\chi x'^2 + 2\chi x' + 1} \quad (3.4)$$

Assumptions made to obtain such a simple relation are relatively crude and deserves to be discussed.

Due to seawater intrusion, fluid density is not constant. It can be shown that when the freshwater lens is thin, the intrusion of denser seawater (+2.5%) induces a rise of the water table. With rising water table, seawater intrusion becomes restricted to a small edge and induces a negligible rise of the water table. As detailed further in this work (Chapter 7),  $h'$  (Eq. 3.4) provides a reasonable estimate of the basal aquifer water table for a broad range of  $\chi$  and  $\xi$ . Nevertheless,  $h'$  is under-estimated when seawater intrusion is strong (low water table, low values of *chi*).

### 3. HYDROGEOLOGY OF BASALTIC ISLANDS

---

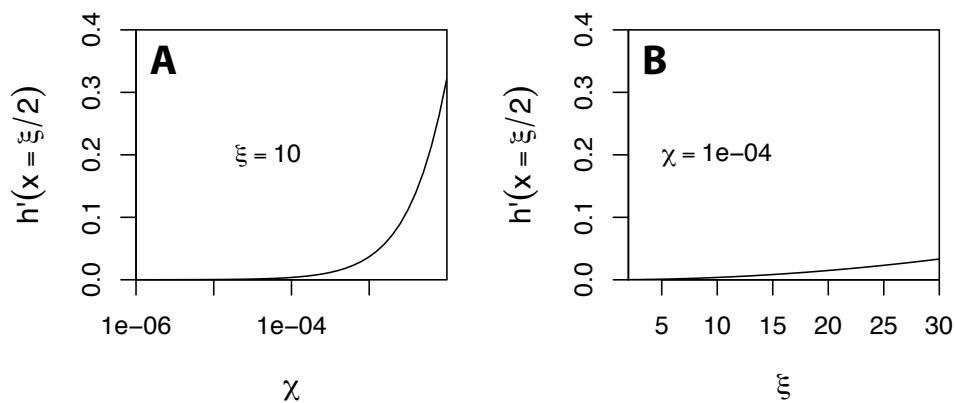


**Figure 3.11:** Freshwater aquifer water table height  $h'$  at a mid-distance from the coast ( $x' = \xi/2$ ) for varying  $\chi$  (A) and  $\xi$  values (B). Given the shortest range of variation of  $\xi$ , effect of changes in  $\chi$  are higher.

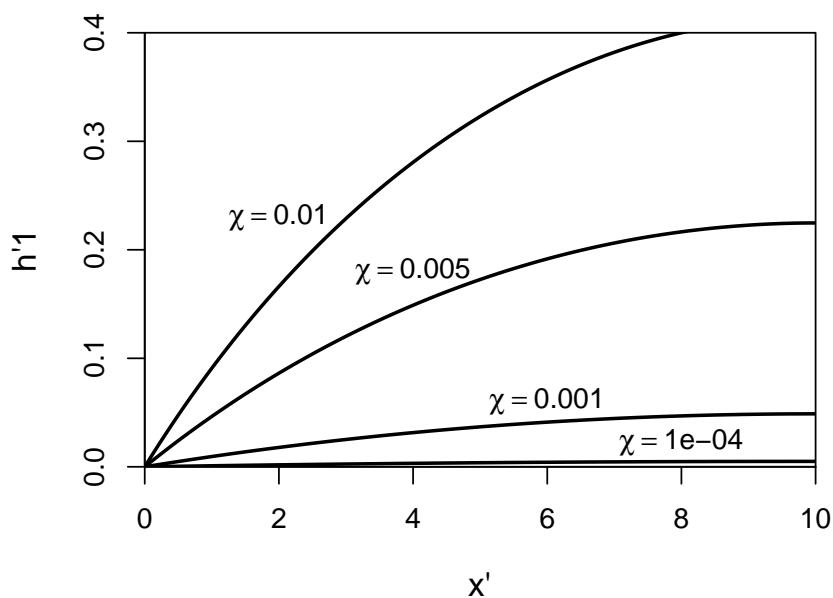


**Figure 3.12:** Shape of the water table height  $h'$  for various values of  $\chi$ .

Volcanic formations are heterogeneous and permeability is not expected to be homogeneous. The effects of heterogeneities may be significant, but are site-specific and difficult to handle in a comparative study. The value considered in this study is the regional permeability. If the groundwater conceptual model is well-defined, this value can be obtained with a numerical model properly calibrated on observed groundwater levels.

It should further be noted that discharge to springs and streams were disregarded in this study. This causes  $h'$  to be overestimated when the water table is high (close to the ground surface), for high values of  $\chi$ . Again, it is challenging to handle such processes that are site-specific, particularly dependent of the topography, incision by valley, or possible flank collapse.

As a consequence, values of  $h'$  may provide erroneous values if compared to local measurements at specific locations. Yet, Eq. 3.4 provide a reasonable estimate for a large range of contexts, and allows a comparative study.

Common values of controlling parameters accept following ranges:  $1 \times 10^{-8}$  -  $1 \times 10^{-7}$  m/s for recharge (ca. 0.3-3 m/y), hydraulic conductivity between  $1 \times 10^{-6}$  -  $1 \times 10^{-2}$  m/s. The corresponding range of  $\chi$  is  $1 \times 10^{-6}$  -  $1 \times 10^{-1}$ . The semi-length of the island range between 3 and 30 km. As permeability decreases with depth, groundwater flow is expected to become negligible at a depth varying between ca. 400 m and 1200 m. This value was fixed to 1000 m. The corresponding range of  $\xi$  is 3-30.

Given these range of variation, the water table height at mid-slope ( $x' = \xi/2$ ) is compared for various values of  $\chi$  and  $\xi$  respectively (Fig. 3.11). It highlights the great sensitivity of the water table height  $h'$  to  $\chi$  for higher values of this parameter. In contrast, parameter  $\xi$  appears to have little effect for a median value of  $\chi$ .

Parameter  $\chi$  owes its large variation range to variations of the hydraulic conductivity  $K$ , this parameter is identified as the major controlling factor likely to explain the difference of basal aquifer thickness observed from one island to another.

### 3.6.2 The age of the island, a determining factor?

The presence of “skin flow” over a deep impervious substratum is virtually expected on any island, whatever its age (Fig. 3.6, D). On the opposite, the occurrence of a “thick lens of fresh groundwater” [Izuka and Gingerich, 2003], with outlets at high-elevation (Fig. 3.6, C) is restricted to older islands (Fig. 3.13): Kauai [Izuka and Gingerich, 2003], Maui [Gingerich, 1998], and Tenerife [Custodio *et al.*, 1988].

The analytical model (Eq. 3.4) showed that changes in permeability can

### 3. HYDROGEOLOGY OF BASALTIC ISLANDS

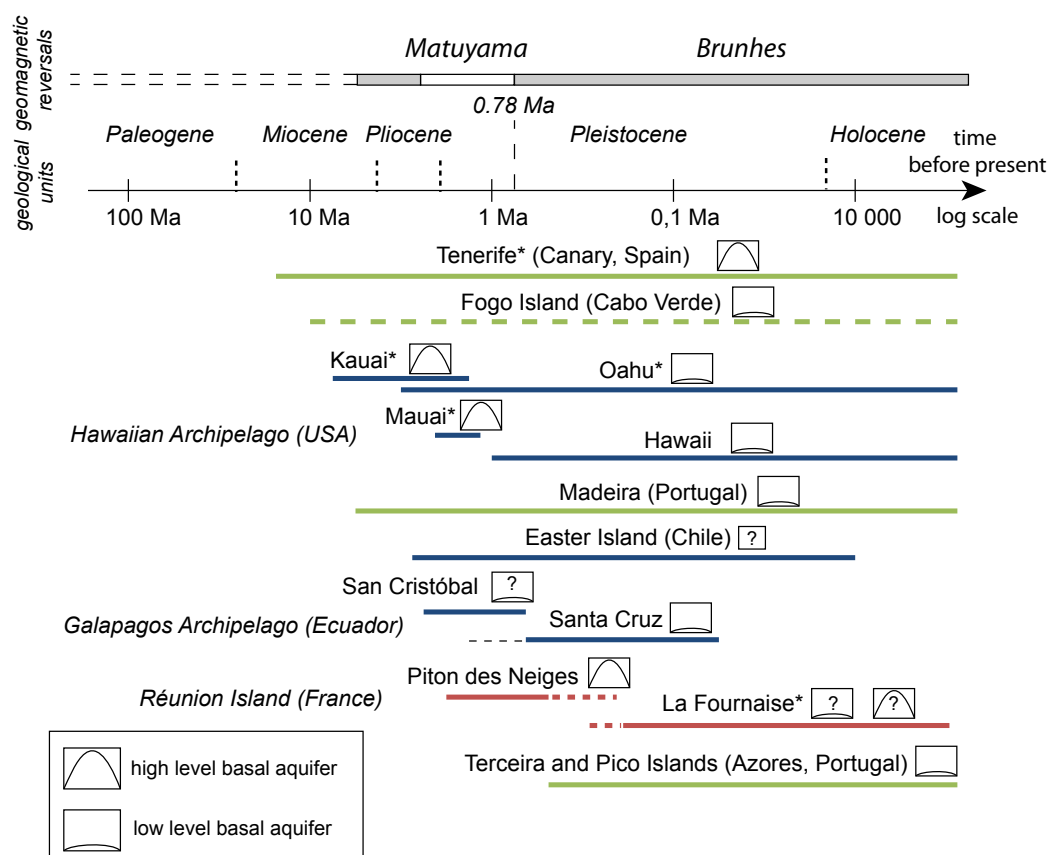


**Figure 3.13:** Geological age of principal basaltic oceanic islands and conceptual models proposed for the basal aquifer. For references, see Table 3.1. A star at the end of the island name indicates that a numerical model is available.

best explain the marked variations in basal aquifer geometries (Fig. 3.11). This assertion is confirmed with calibrated permeability values from numerical models (Table 3.2): younger islands with a thick freshwater lens are attributed regional permeabilities ranging around  $2 \times 10^{-7}$  -  $5 \times 10^{-6}$ , while younger islands with a low-lying basal aquifer have regional permeabilities 3 orders of magnitudes higher.

Processes that can explain a reduction of permeability with the age of the formation are related to rock weathering and hydrothermalism (alteration of primary minerals, secondary mineralization, pore and fracture filling) [Cruz, 2003; Hunt, 1996; Oki, 1997]. At depth, compaction and fracture closure amplify the loss of conductivity. Larger volcanic edifices have greater likelihood to present lower hydraulic conductivity and a higher parameter  $\chi$ , which may allow the existence of a high elevation basal aquifer.

Actually, several processes appear to increase the hydrogeological potential with the evolution of the island:

- Young basaltic formations are permeable ( $K \approx 1 \times 10^{-3}$  m/s), while old lava flows are generally poorly conductive ( $K \approx 1 \times 10^{-6}$  m/s). Old islands are thus more favorable to groundwater storage, while infiltrated waters may rapidly reach the ocean in younger islands.
- Runoff results in the incision of valleys, and formerly hidden groundwater bodies can be revealed [Jefferson *et al.*, 2010]
- Eroded materials are transported downstream and eventually forms an impervious sedimentary unit, the cap-rock, which may confine the basal aquifer (Fig. 3.6), impedes freshwater discharge, and protects from seawater intrusion (Fig. 3.6 B, Izuka and Gingerich [2003]).

It should be noted that leeward arid slopes appear younger than humid windward slopes, though they have much chance to have the same geological age. This highlights that effects of ageing are modulated by climatic conditions.

### 3.6.3 Defining an island conceptual model

Defining the hydrogeological conceptual model is critical for groundwater management purpose. It provides valuable information on the resilience or vulnerability of the system to droughts, over-pumping, and seawater intrusion.

We showed that recharge parameter  $\chi = r/K$  plays a determining role in the existence of a thick freshwater lens. This parameter is difficult to obtain: recharge ( $r$ ) and particularly hydraulic conductivity ( $K$ ) are both difficult to estimate. While Eq. 3.4 provides a simple expression to investigate the main controlling factors, it appears challenging to define an island conceptual from this

### 3. HYDROGEOLOGY OF BASALTIC ISLANDS

---

expression. As well, more complex numerical models suffer from uncertainties on input parameters.

When they are available and sufficiently deep, drill holes and galleries provide a much more reliable information. To confirm the existence of a thick freshwater lens (and not to mistake for a perched aquifer), a drill hole must be executed through the aquifer down to sea level, depth below which the occurrence of unsaturated horizon is impossible. If water level falls significantly after the perforation of a relatively impervious layer, the intercepted groundwater body is a perched aquifer.

Defining whether the occurrence of a high-level groundwater body is due to dike-impounding, or to a reduction of the medium permeability is a delicate question. While the existence of dikes in eruptive zones of the islands central areas is indisputable, the apparent absence of eruptive cones and fissures does not necessarily implies that the underground is dike free. If they are available, horizontal galleries can provide valuable information. If not, hydraulic pumping tests may be performed to define whether the hydraulic conductivity is sufficiently low to sustain a thick freshwater lens.

#### 3.7 Conclusions

Volcanic formations are heterogeneous and form complex structures. Extensive lava flows interlayered by pyroclastics and colluvial units form the bulk of the island. At the center of the island, eruptive zones underline the presence of dyke swarms and dense hydrothermalized impervious formations. Due to chemical and mechanical effects, permeability and porosity tend to decrease with age and depth of the formation, but effects of ageing are modulated by climatic conditions.

A basal aquifer in connection with the ocean is reported in every island. It is subjected to seawater intrusion at various extents, depending on the equilibrium between groundwater recharge and discharge. This basal aquifer remains at low elevation if regional permeability is high ( $K \approx 1 \times 10^{-3}$  m/s), which is the case in younger islands ( $< 1$  Ma). Skin-flow over an impervious substratum or core formation is virtually expected on any island. But the existence of a thick freshwater lens, where the basal aquifer feeds springs and streams in the highlands is restricted to poorly permeable regional permeability ( $K \approx 1 \times 10^{-6}$  m/s) of older volcanic islands ( $> 1$  Ma).

Other occurrences of high-level groundwater is attributed to *perched aquifers* over poorly permeable interbeddings (ash deposits and paleo-soils), and *dike-impounded* aquifers. These groundwater bodies have more chances to outcrop in older volcanic edifices, which are dissected by valleys and affected by flank collapse.

### 3.7 Conclusions

---

Climatic contrasts between the windward humid and the leeward arid slopes induce different grades of rock alteration, uneven recharge potentials, and contrasting hydrogeological configurations. Leeward sides appear younger than their windward counterparts.



## Chapter 4

# 3D resistivity gridding of AEM surveys: a step toward enhanced geological interpretation

# 3D resistivity gridding of large AEM datasets: A step toward enhanced geological interpretation\*

---

## Abstract

We develop a technique allowing 3D gridding of large sets of 1D resistivity models obtained after inversion of extensive airborne EM surveys. The method is based on the assumption of a layered-earth model. 2D kriging is used for interpolation of geophysical model parameters and their corresponding uncertainties. The 3D grid is created from the interpolated data, its structure accurately follows the geophysical model, providing a lightweight file for a good rendering. Propagation of errors is tracked through the quantification of uncertainties from both inversion and interpolation procedures. The 3D grid is exported to a portable standard, which allows flexible visualization and volumetric computations, and improves interpretation. The method is validated and illustrated by a case-study on Santa Cruz Island, in the Galapagos Archipelago.

---

\* In collaboration with James Ramm<sup>1</sup>, Jean-Paul Chilès<sup>2</sup>, Esben Auken<sup>1</sup>, Benoit Deffontaines<sup>3</sup>, and Sophie Violette<sup>4</sup>. Published in *Journal of applied geophysics*, Volume 75, Issue 2, October 2011, Pages 277-283, <http://dx.doi.org/10.1016/j.jappgeo.2011.07.006>.

<sup>1</sup>University of Aarhus, HydroGeophysics Group, Department of Earth Sciences, Høgh-Gulbergs Gade 2, 8000 Århus C, Denmark.

<sup>2</sup>MINES ParisTech, Center of Geosciences and Geoengineering, Fontainebleau, France

<sup>3</sup>UPE, GTMC Laboratory, Marne-La-Vallée, France

<sup>4</sup>UPMC Univ. Paris 6 & CNRS, UMR Sisyphe, 4 place Jussieu, 75252 Paris cedex 05, France

## 4.1 Introduction

Airborne Electromagnetic (AEM) surveying can cover extensive areas in a short space of time, collecting thousands of soundings along hundreds of kilometers of flight lines. Numerous field surveys, based on frequency (FEM) and time-domain (TEM) electromagnetics have been successfully conducted in various complex environments and reported in literature [Bosch *et al.*, 2009; Mogi *et al.*, 2009; Steuer *et al.*, 2009; Supper *et al.*, 2009].

Recent advances to provide 3D imaging of the subsurface [Cox *et al.*, 2010] are not widespread and may not significantly improve the quality of resistivity mapping [Viezzoli *et al.*, 2010]. As a consequence, most AEM datasets are inverted with a 1D model and are typically viewed as cross sections or 2D interpolated maps (e.g. d'Ozouville *et al.* [2008a]; Mullen and Kellett [2007]; Viezzoli *et al.* [2008]). Some attempts are made to visualize the results in 3D [Bosch *et al.*, 2009; Palamara *et al.*, 2010], but without quantification of related uncertainties.

There is a need for an efficient and reliable methodology to visualize in 3D the structures identified by AEM surveys. To this end, it is important to understand under which assumptions, a 1D model description can reasonably resolve 2D and 3D structures.

An early paper on the subject [Newman *et al.*, 1986] calculate the TEM response caused by 3D electromagnetic scattering and shows that the thickness of conductive overburdens and the depth to sedimentary layers beneath volcanic structures can be successfully resolved with 1D inversion. However, 3D conductors are often replaced by a conducting layer at similar depth and 1D inversion of 3D structures invariably results in non-unique models. Auken *et al.* [2008] studied the problem by calculating the EM forward response over theoretical 2D/3D buried valley structures and inverted with a 1D laterally constrained least-squares inversion code Auken and Christiansen [2004]. It is found that resistivities are well resolved when the slope of the dipping structures is below 30% and that resistivity contrasts are not much higher than 1:10. Advances in inversion techniques improve images of the subsurface and also offer, crucially, estimates of the model fit and resolution of model parameters. Spatially constrained inversion [Viezzoli *et al.*, 2008], implements spatial constraints between models allowing the user to bias the outcome of the inversion to reflect the geological variability of the area. The effect of the constraints is that the model description is 3D with local 1D inversion kernels. It is clear that while 1D inversion does not produce flawless reconstructions of the subsurface, results over 3D structures are acceptable when the structures are much larger than the footprint of the geophysical system (see Reid *et al.* [2006]).

The problem addressed in this paper is not the 3D visualization of the inversion results, but of accurately representing a scattered dataset of 1D models as

## 4. 3D RESISTIVITY GRIDDING OF AEM SURVEYS

---

a 3D grid. In turn, a 3D grid allows volumetric computations and is convenient to use for 3D visualization. In order to produce worthwhile and accurate images, two requirements shall be addressed by the gridding method:

1. At each 1D model location, the 3D grid should honor the model – i.e. resistivity and layer interfaces shall be preserved.
2. Away from the 1D models (between flight lines) the 3D grid of resistivity should be reliable enough to allow interpretation – i.e., uncertainties have to be quantified and should remain below some quality threshold.

After a presentation of the methodology to translate datasets of 1D models into a 3D grid of resistivity, we describe how to quantify the propagation of uncertainty from both the inversion and interpolation procedures. The method is validated on a case study in volcanic settings, the Galapagos Islands.

### 4.2 Methodology

The most straightforward technique to represent the resistivity in 3D from a collection of 1D vertical inversion models is to use 3D interpolation. Currently known 3D interpolation algorithms require discrete data in all directions, discarding the layered approach used in the inversion, and leading to a smoothing effect between previously defined layer boundaries. The other alternative, presented in this paper, is to interpolate the geophysical model parameters of the 1D models (layers resistivities and e.g. layer thicknesses) in the 2D horizontal space.

We start from the model vector  $\mathbf{m} = (\mathbf{m}_1, \dots, \mathbf{m}_N)^T$ , a set of  $N$  vertical resistivity models obtained after the inversion of  $N$  soundings over the region of interest. Each vertical inversion model  $\mathbf{m}_i = (p_{i,1}, \dots, p_{i,2L})^T$  is described by a vector of  $2L$  scalars  $p_{i,k}$  describing the resistivity and geometry (thickness, or depth, or elevation) of the  $L$  layers. Inversion models have the same number of layers throughout the study area. In some cases, the initial distribution of the geometry parameters is sufficiently close to normal so that transformation is not necessary before interpolation. Transformation of variables (e.g. by the logarithmic function) may be required before interpolation of some parameters, in particular resistivities. Note  $\mathbf{m}'_i = (p'_{i,1}, \dots, p'_{i,2L})^T$ , the vector of transformed parameters of inversion model  $i$  and  $\mathbf{m}' = (\mathbf{m}'_1, \dots, \mathbf{m}'_N)^T$  the whole set of transformed inversion models.

Layer thicknesses are not required in the case of “smooth” inversions with numerous layers whose thicknesses are fixed. To obtain a finite thickness of the 3D model, the thickness of the last layer (usually assumed to be infinite) is arbitrarily fixed to two or three times the thickness of the overlying layer.

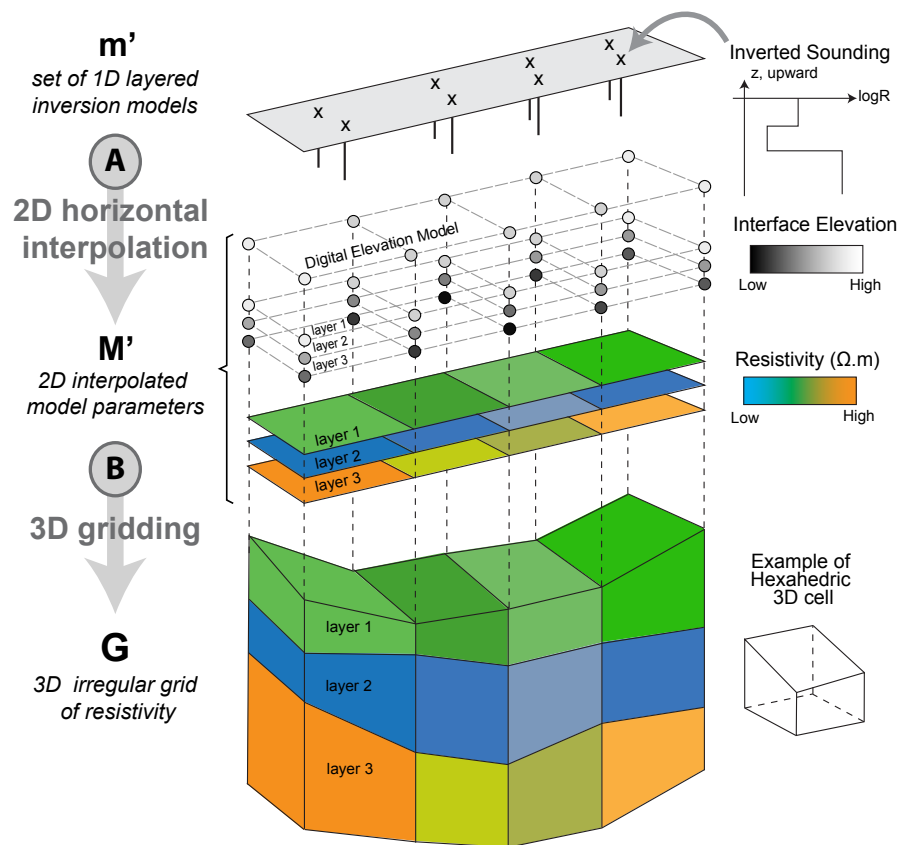


**Figure 4.1:** 3D gridding of resistivity (top to bottom). (A) From the set of 1D vertical inversion models, geophysical model parameters are interpolated in the 2D horizontal space. (B) The 3D grid is constructed from 3D vertex positions and filled with resistivity values from corresponding resistivity maps.

## 4. 3D RESISTIVITY GRIDDING OF AEM SURVEYS

---

The construction of the 3D grid of resistivity can be described by the succession of two operations.

First (Fig. 4.1, A), the  $2L$  transformed model parameters  $p'_1, \dots, p'_{2L}$  in  $\mathbf{m}'$  are interpolated in the 2D horizontal space to matrices  $\hat{\mathbf{P}}'_1, \dots, \hat{\mathbf{P}}'_{2L}$ , whose size is equal to the number of cells discretizing the 2D domain. To obtain coherent 3D grids, the discretization must be the same for all parameters. These matrices are gathered into the  $2L$ -vector  $\hat{\mathbf{M}}' = \hat{\mathbf{P}}'_1, \dots, \hat{\mathbf{P}}'_{2L}$  containing all interpolated parameters (resistivity and geometry) of the layered resistivity model over the study area.

In a second phase (Fig. 4.1, B), the 3D log-resistivity field  $\hat{\mathbf{G}}'$  is deduced from  $\hat{\mathbf{M}}'$ . It is represented by a 3D grid composed by hexahedral cells. The horizontal resolution of the grid is identical to the resolution of the 2D matrices. Vertically, there is one cell per geophysical layer so that the resolution of the grid follows the resolution of the resistivity model in that direction. The vertical coordinates,  $z$ , of the cell vertices are deduced from the digital elevation model (DEM) and the interpolated geometry parameter.

When dealing with 1D models where layer thicknesses vary, the choice of the geometry parameter to be interpolated (layer thickness, depth or elevation) has to be made with care. If the geometry of the geological formation is expected to follow the topography, layer thickness or interface depth is preferred, while interpolation of interface elevation should be chosen in other cases [*Chilès and Delfiner, 2011*].

The model parameters are interpolated by kriging. Among linear predictors, kriging is optimal in the sense that it minimizes the variance of the prediction error. Moreover, it provides a “prediction” or “kriging” variance  $\sigma_{KRI}^2$  which quantifies the magnitude of the interpolation error. Kriging assumes that the spatial covariance or variogram of the parameters are known. An experimental variogram has to be computed for each parameter and variogram models have to be fitted.

Kriging requires no special assumption relative to the distribution of the studied parameter. Nevertheless, when the spatial distribution of the parameter is Gaussian, kriging provides the best linear unbiased estimator. Therefore it is recommended to apply kriging to variables whose histogram is not too far from a normal distribution [*Chilès and Delfiner, 2011*]. Resistivity often has a lognormal distribution and is therefore transformed into its logarithm. In contrast, the parameter describing the geometry is often not too far from normality.

Interpolation is performed by kriging with the *Gstat* package [*Pebesma and Wesseling, 1998*]. The search radius shall be chosen to be larger than the spacing between flight lines in order to obtain a continuous 3D model. However, extending it to an unreasonable distance would slow the kriging algorithm with-

out significant improvement. The resolution of the 2D grids must be adjusted depending on the variability of model parameters, the expected precision, and the acceptable computation time. Values of resistivity are predicted as “block” values, which allows the prediction of averaged values in the cell [Pebesma, 2001]. Since the 3D cells of the grid are defined by their vertices, the parameters of the 3D grid (layer thickness, depth, or elevation) are also interpolated at cell vertices.

## 4.3 Uncertainties and validation

### 4.3.1 Management of uncertainties

Two sources of error affect the quality of the 3D grid of resistivity: the uncertainty on model parameters estimated by geophysical inversion, and the uncertainty due to the interpolation.

The inversion uncertainty, if provided by the inversion code, can be incorporated into the grid together with resistivity. Geophysical inversion based on a least-squares criterion provides an estimation of the uncertainty on estimated parameters from the linearized approximation to the covariance of the estimation error [Auken and Christiansen, 2004]. The magnitude of the inversion uncertainty on  $p_{i,k}$  the  $k$ -th model parameter at inversion model  $i$  is quantified by the standard deviations  $\sigma_{INV|i,k}$ . The 1D model at sounding  $i$  is extended to  $\mathbf{m}_i = (p_{i,1}, \dots, p_{i,2L}, \sigma_{INV|i,1}, \dots, \sigma_{INV|i,2L})^T$ . The inversion uncertainty can be due to poor signal quality during the sounding procedure or a lack of compatibility between the proposed geophysical model and the measured data during the inversion procedure [Auken and Christiansen, 2004]. In spatially constrained inversion, an additional source of uncertainty may occur when a sounding is closely surrounded by others, with significant contrast in the signal. These sources of uncertainty are often likely to be spatially correlated and as a consequence, the standard deviations should be propagated by interpolation. Similarly to the inversion model parameters  $p_k$ , the inversion standard deviations  $\sigma_{INV|k}$  can be interpolated by kriging, leading to matrices  $\hat{\mathbf{S}}_{INV|1}, \dots, \hat{\mathbf{S}}_{INV|2L}$  in the 2D horizontal space.

The magnitude of the uncertainty due to the interpolation of model parameters  $p_k$  is characterized by the kriging standard deviations matrices  $\hat{\mathbf{S}}_{KRI|1}, \dots, \hat{\mathbf{S}}_{KRI|2L}$ . These 2L matrices are obtained as by-products of the kriging of the parameters  $p_k$ . As explained previously, the inversion variance  $\sigma_{INV|k}^2(x, y)$  depends on the quality of the soundings and the success of the inversion, while the kriging variance  $\sigma_{KRI|k}^2(x, y)$  depends on the spatial variability of the parameter and the distance to data points. As a result, the two variances are considered as independent and can be summed to form the total uncertainty variance on model parameter  $p_k$ ,

## 4. 3D RESISTIVITY GRIDDING OF AEM SURVEYS

---

defined as  $\hat{\sigma}_{TOT,k}^2(x, y) = \hat{\sigma}_{INV,k}^2(x, y) + \hat{\sigma}_{KRI,k}^2(x, y)$ . If uncertainties from inversion are handled, the vector of 2D matrices of interpolated model parameters are therefore extended to  $\widehat{\mathbf{M}} = \widehat{\mathbf{P}}_1, \dots, \widehat{\mathbf{P}}_{2L}, \dots, \widehat{\mathbf{S}}_1, \dots, \widehat{\mathbf{S}}_{2L}$  with total standard deviation matrices defined by Eq. 4.1. This leads to the construction of a 3D grid containing not only resistivity values but also related uncertainty.

$$\widehat{\mathbf{S}}'_{TOT,k} = \sqrt{\widehat{\mathbf{S}}'^2_{INV,k} + \widehat{\mathbf{S}}'^2_{KRI,k}} \quad (4.1)$$

To facilitate interpretation, log-transformed parameters such as resistivities are back-transformed by exponentiation (in the Gaussian case, they are therefore median estimators). The related uncertainties are expressed by the Standard Deviation Factors (STDF) obtained by exponentiation of the log-resistivity total standard deviations. For parameter  $p_k$  at location  $(x, y)$  of the discretized 2D space, the standard deviation factor is obtained from Eq. 4.2:

$$STDF_k(x, y) = \exp(\sigma_{TOT|k}(x, y)) \quad (4.2)$$

Under the assumption that the error on log-resistivity is Gaussian and independent of the kriged estimate, the  $(1 - \alpha)$  confidence interval can be inferred with Eq. 4.3, where  $\hat{p}_k(x, y) = \exp(\hat{p}'_k(x, y))$  is the back-transformed estimate  $\hat{p}'_k(x, y)$  and  $z_\beta$  is the normalized Gaussian value corresponding to the cumulative probability  $(1 - \alpha/2)$ . With  $z_\beta = 1$ , we obtain the 68% confidence interval.

$$\frac{\hat{p}_k(x, y)}{STDF_k(x, y)^{z_\beta}} \leq p_k(x, y) \leq \hat{p}_k(x, y) \cdot STDF_k(x, y)^{z_\beta} \quad (4.3)$$

The confidence intervals of parameters that have not been transformed (e.g. layer thicknesses) can be derived directly from the total variances. These confidence intervals are however approximations because thicknesses are not exactly Gaussian.

### 4.3.2 Validation of the 3D grid

Two aspects deserve to be addressed in order to validate the 3D resistivity grid. Before kriging, the applicability of the interpolation method to the given data set must be investigated. After kriging, the consistence of the interpolated parameters and inversion models should be estimated.

In order to validate the prediction method, the collection of 1D models is split into two subsets S1 and S2 similar to the white and black squares of a chessboard (Fig. 4.2). Parameters of inversion models falling within the “black” squares (within S2) are predicted from values falling within the “white” squares (within S1). For the method to be relevant, artificial gaps of data have to be at least

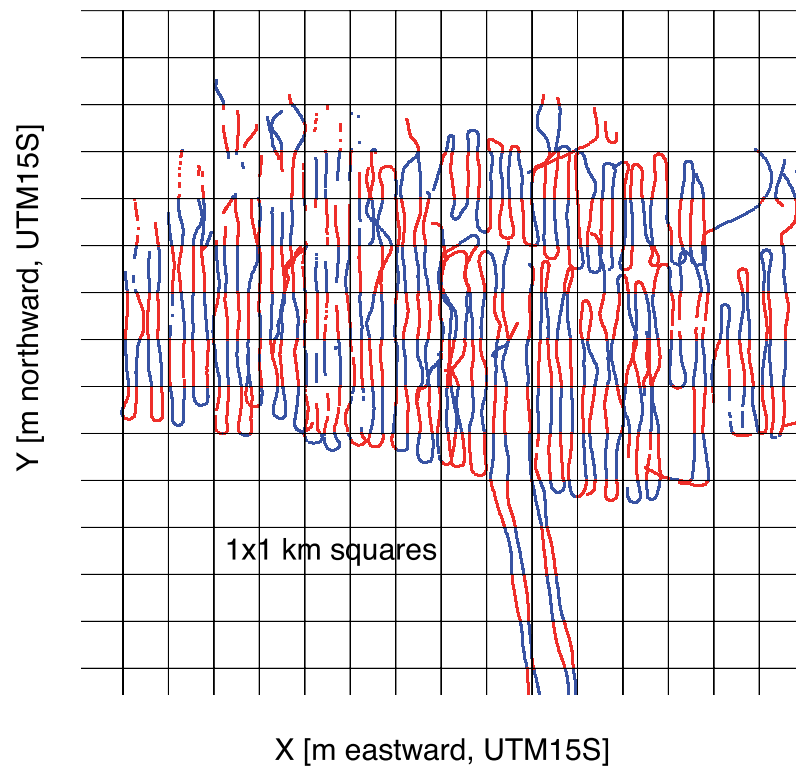


**Figure 4.2:** Validation of the prediction method using data split into two subsets S1 (blue) and S2 (red). Values at locations of S2 are predicted from S1. Example from SkyTEM data set collected by *d'Ozouville et al.* [2008a].

## 4. 3D RESISTIVITY GRIDDING OF AEM SURVEYS

---

as big as natural gaps, determined by spacing between flight lines. At inversion model  $i$  in S2, the misfit between estimated values and original model parameters, the prediction error  $e(i)$ , is obtained from Eq. 4.4.

$$e(i) = \hat{p}'_k(x_i, y_i) - p'_k(i) \quad (4.4)$$

where  $p'_k(i)$  is the  $k$ -th parameter of the  $i$ -th inversion model, and  $\hat{p}'_k(i)$  the estimate at model location  $(x_i, y_i)$ . If the statistical model is compatible with the dataset and the variogram model fits the experimental model, errors calculated on S2 should have a zero mean and for variance the kriging variance  $\hat{\sigma}_{KRI}^2$  [Chilès and Delfiner, 2011]. Moreover, interpolated model parameters values should be found at 68% probability within the interval  $\pm\sigma_{KRI}$  from the estimates. As an additional precaution, it is recommended to repeat the operation switching S1 and S2. Under those conditions, kriging is considered applicable to the dataset, and predicted values  $\hat{p}'_k(i)$  will be provided with the confidence interval  $\pm\sigma_{KRI}(x_i, y_i)$  at 68%. After kriging with all data (S1 and S2), the fit between interpolated parameters and the inversion models should finally be estimated. If the validation step was successful and the horizontal resolution of the grid sufficiently fine, the fit between 2D matrix of interpolated parameter  $p_k$  and original 1D models is expected to be good. It can be assessed with the root mean square error (RMSE) expressed in Eq. 4.5 where  $p_k(i)$  stands for the value of parameter  $k$  at the  $i$ -th 1D inversion model and the estimate of parameter  $p_k$  at location  $(x_i, y_i)$  of the 2D discretized horizontal space, the closest to the  $i$ -th 1D inversion model.

$$RMSE(p_k) = \sqrt{\frac{1}{N} \sum_{i=1}^N (\hat{p}_k(x_i, y_i) - p_k(i))^2} \quad (4.5)$$

### 4.4 Case study: Galapagos Islands, Ecuador

#### 4.4.1 Presentation of the survey

In the frame of the project Galapagos Islands Integrated Water Studies (GIWS) a large variety of investigations are under progress on the main inhabited island of Galapagos Archipelago, Santa Cruz. This basaltic island, whose last significant shield-building phase has been dated to approx. 500 000 y.b.p [Bow, 1979] is arid with the exception of the highlands. Rapid population growth rates have promoted the use of expensive desalination techniques while the lack of a sewage system leads to high contamination levels in the basal aquifer. There is an obvious need for a better understanding of hydrogeological processes on the island. To this end, an extensive SkyTEM survey has been conducted on the southern windward

#### 4.4 Case study: Galapagos Islands, Ecuador

side of Santa Cruz (Fig. 4.3). Thousands of soundings have been collected along the 500 km of flight lines. Due to the nature of airborne surveys, the distribution of soundings is inhomogeneous, with a high density of soundings along flight lines (one sounding every 10 meters), and gaps of data in between (usually 250 meters wide). Results revealed interesting buried low-resistivity bodies in Santa Cruz, presented by *d'Ozouville et al.* [2008a] and *Auken et al.* [2009].

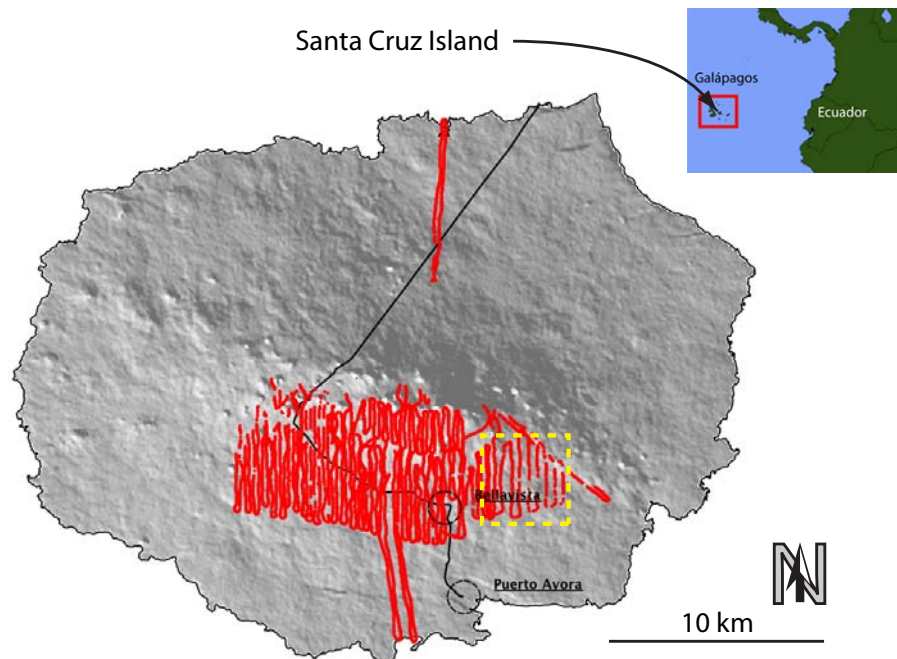


**Figure 4.3:** Location of SkyTEM survey: Santa Cruz Island, Galapagos Archipelago. Red dots show the flight lines, yellow box shows the data extent in Fig. 4.6

The soundings have been newly processed and inverted using the Spatially Constrained Inversion scheme (SCI) [*Viezzoli et al.*, 2008] to a 19 layer “smooth” resistivity model, where the layer thicknesses are distributed logarithmically from the surface down to 250 m below topography. While the use of a spatially constrained inversion scheme is not compulsory, it provides more consistent sets of neighboring models, and leads to the construction of more coherent 3D grids of resistivity.

For each layer, experimental variograms are computed for the log-transformed resistivity and the standard deviation from inversion. Fig. 4.4 presents the two variograms used for the first layer. The parameters of the variogram models for all the 19 layers are gathered in Table 4.1. The variograms of log-transformed

#### 4. 3D RESISTIVITY GRIDDING OF AEM SURVEYS

---

Layer	Variogram model of $\log(R)$			Variogram model of $\sigma_{INV}$		
	Bessel model			Exponential model		
	$C_N$	$a$ [m]	$C_F$	$C_N$	$a$ [m]	$C_F$
1	0	92.6	3.28E-01	3.05E-04	7.3	4.15E-03
2	0	87.8	2.81E-01	5.26E-04	6.9	3.40E-03
3	0	87.3	2.42E-01	5.10E-04	6.6	3.46E-03
4	0	106.6	2.64E-01	2.50E-04	6.7	2.85E-03
5	0	107.6	2.82E-01	2.91E-04	6.8	2.77E-03
6	0	105.0	2.92E-01	2.56E-04	6.9	2.77E-03
7	0	131.5	3.60E-01	2.86E-06	6.8	2.11E-03
8	0	172.9	5.61E-01	2.45E-05	6.9	2.08E-03
9	0	164.5	5.38E-01	3.79E-05	6.9	2.06E-03
10	0	163.5	5.10E-01	3.58E-05	6.8	2.02E-03
11	0	159.1	5.00E-01	2.59E-05	6.8	2.01E-03
12	0	152.5	4.91E-01	0.00E+00	7.1	1.56E-03
13	0	127.5	4.15E-01	0.00E+00	7.1	1.55E-03
14	0	114.3	3.85E-01	0.00E+00	7.5	1.09E-03
15	0	100.4	4.09E-01	0.00E+00	7.5	1.07E-03
16	0	94.1	5.57E-01	9.11E-06	7.6	1.06E-03
17	0	97.5	7.51E-01	3.16E-05	9.7	2.92E-04
18	0	80.0	8.85E-01	3.34E-05	10.0	2.89E-04
19	0	68.8	1.36E+00	4.67E-05	10.9	2.84E-04

**Table 4.1:** Variogram model parameters of the log-transformed resistivity ( $R$ , [ohm.m]) fitted to 1st order K-Bessel model, and  $\sigma_{INV}$  fitted to exponential model for the 19 layers of the Santa Cruz SkyTEM dataset.  $C_N$  is the nugget,  $a$  the scale parameter, and  $C_F$  the variance of the continuous component.

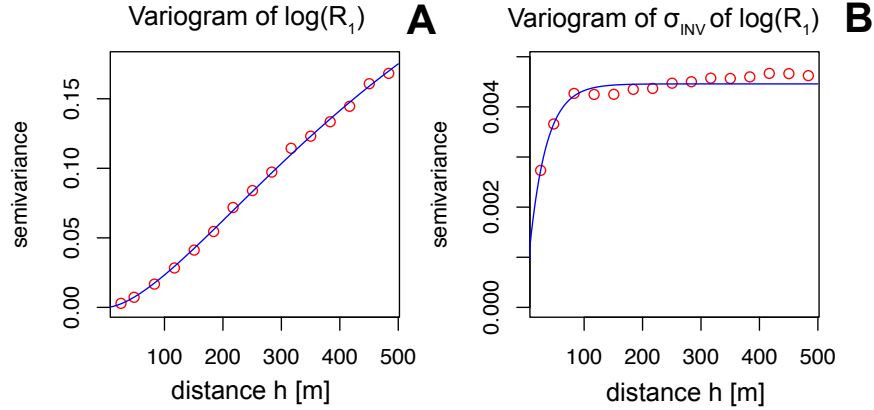


**Figure 4.4:** Sample variograms (red dots) and models (blue lines) used for the interpolation of the first layer. (A) For the log-transformed resistivity  $\log(R)$ , a first order Matérn or K-Bessel model ( $\nu = 1$ ,  $a=92$  m,  $C_F = 0.33$ ,  $C_N = 0$ ) fits well to the data. (B) For the standard deviation from inversion  $\sigma_{INV}$ , an exponential model is more appropriate ( $a = 7.28$  m,  $C_F = 4.15 \times 10^{-3}$ ,  $C_N = 3.05 \times 10^{-4}$ ).

resistivity fit well to isotropic Matérn models (also known as K-Bessel models) with shape parameter  $\nu = 1$  [Chilès and Delfiner, 2011; Pebesma and Wesseling, 1998]. The variogram model reads  $\gamma(h) = C_N + C_F \left(1 - \frac{h}{a} K_1\left(\frac{h}{a}\right)\right)$  where  $C_N$  is the nugget effect,  $K_1$  is the modified Bessel function of the second kind of order  $\nu = 1$ ,  $a$  and  $C_F$  are the model parameters, and  $h$  is the distance. The variograms of standard deviation from inversion  $\sigma_{INV}$  fits better to the isotropic exponential model defined by [Pebesma and Wesseling, 1998]. As presented in Table 4.1, the variograms of log-transformed resistivity, do not present a nugget effect ( $C_N = 0$ ), and the sill ( $C_F$  in this case) increases for deeper layers. This is interpreted as the consequence of the sharp resistivity contrasts induce by sea water intrusion. The variograms of standard deviation from inversion  $\sigma_{INV}$  present a nugget effect, which represent the random component of inversion error. For deeper layers, a rise of the scale parameter  $a$  is observed, while  $C_F$  and  $C_N$  decrease. This corresponds to a smaller sill and a larger range and reflects that for deeper layers,  $\sigma_{INV}$  is less variable and more spatially correlated.

#### 4.4.2 Validation of the method

Before interpolation of parameters and construction of the 3D model, the applicability of the prediction method was investigated for the Santa Cruz survey. As

## 4. 3D RESISTIVITY GRIDDING OF AEM SURVEYS

described in section 4.3.2, the data set was split into two halves, S1 and S2, with a 1 km-resolution regular grid (Fig. 4.2). Parameter values at locations of S2 were predicted from the parameter values in the subset S1.

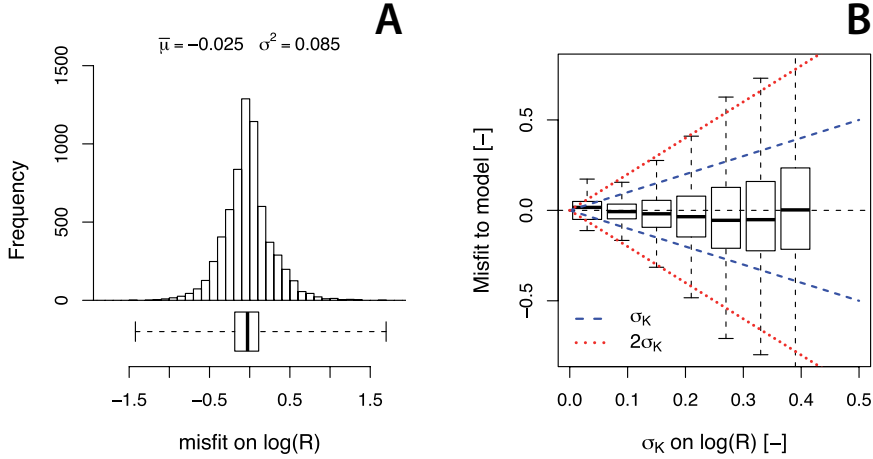


**Figure 4.5:** Analysis of misfit between original models and interpolated from S1 subset over S2 area using resistivity of the 1st layer as an example. (A) Misfit has a mean close to zero and standard deviation close to the average value of  $\sigma_K$ . (B) Misfits increase with distance to inversion models and remains within about  $\pm\sigma_K$  at 68%.

As depicted in Fig. 4.5 (A), the misfit of predicted values of resistivities in S2 have a mean close to zero and a variance of  $\sigma^2 = 0.08$ , which is close to the average prediction variances on this parameter  $\sigma_{KRI}^2 = 0.1$ . In Fig. 4.5 (B), the misfit logically increases with kriging variances (i.e., with distance to data points in S1), but remains within the  $\pm\sigma_{KRI}$  confidence interval at 68%. This means not only that prediction is relatively accurate, but as well that the estimation of uncertainty provided by kriging is reliable on this dataset. The behavior is similar for all other parameters of this model without marked differences. Yet, prediction performs better for layers where the distribution of resistivity is closer to log-normal. Finally, we tested that inverting the two subsets S1 and S2 had no significant effect on the preceding conclusions. As a consequence, the interpolation method can be considered as applicable on this dataset. After kriging of parameters with the whole dataset, the agreement between interpolated 2D matrices of model parameters and 1D inversion models is quantified. For this dataset interpolated at 30 m resolution, averaged RMSE of log-transformed resistivity is 0.06, corresponding to an error factor of 1.06 for resistivity, which is acceptable.

### 4.4.3 Management of uncertainties

Once the model is built, the analysis of uncertainties away from data (i.e. between flight-lines) is made possible from the prediction of standard deviation  $\sigma_{KRI}$ , available at each cell of the 2D matrices (Fig. 4.6, A). As expected, the kriging standard deviation increases with the distance to flight lines. It is shown that in this context, values of log-transformed resistivity, interpolated between the 250 m-spaced flight lines, have a kriging standard deviation of about 0.1. When combining interpolation uncertainty with inversion uncertainty (Fig. 4.6, B), the uncertainty increases but remains within an acceptable range, with a total standard deviation of about 0.2 (STDF=1.2).

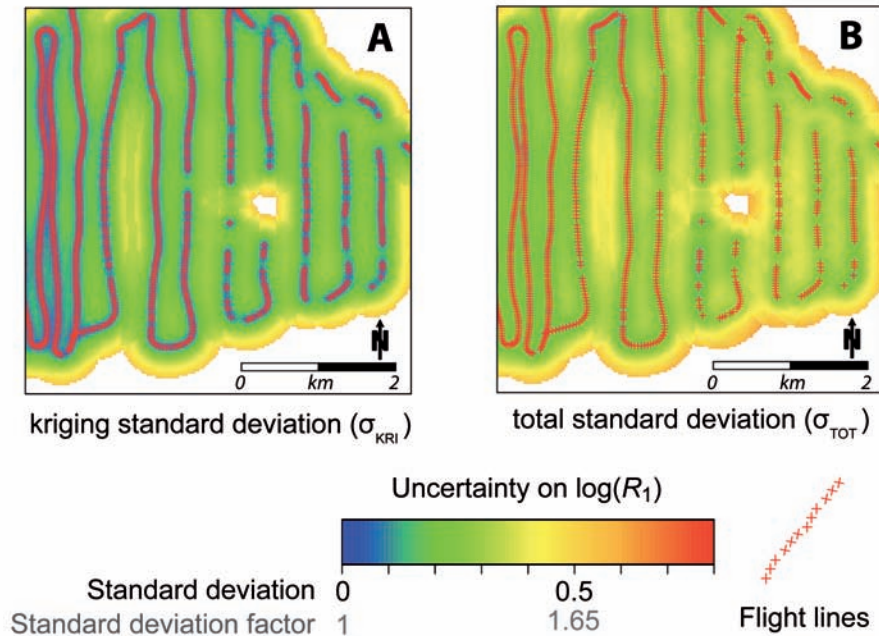


**Figure 4.6:** Uncertainty on log-transformed resistivity of the first layer. The area corresponds to the yellow perimeter outlined on Fig. 4.3. Left (A): kriging standard deviation  $\sigma_{KRI}$  increases away from flight lines (red crosses). Right (B): the total standard deviation  $\sigma_{TOT}$  combines uncertainties from inversion and kriging.

These results were presented for the 1st layer of the geophysical model. Conclusions remain roughly the same for other layers, at the exception of deeper layers where an increase of kriging standard deviation is observed. This loss of accuracy is due to sharp resistivity contrasts for these layers, which is a consequence of sea water intrusion. Yet, larger misfit on resistivity is restricted to a

## 4. 3D RESISTIVITY GRIDDING OF AEM SURVEYS

---

fringe located at the end of the area of detection of sea water intrusion.

### 4.4.4 3D Visualization

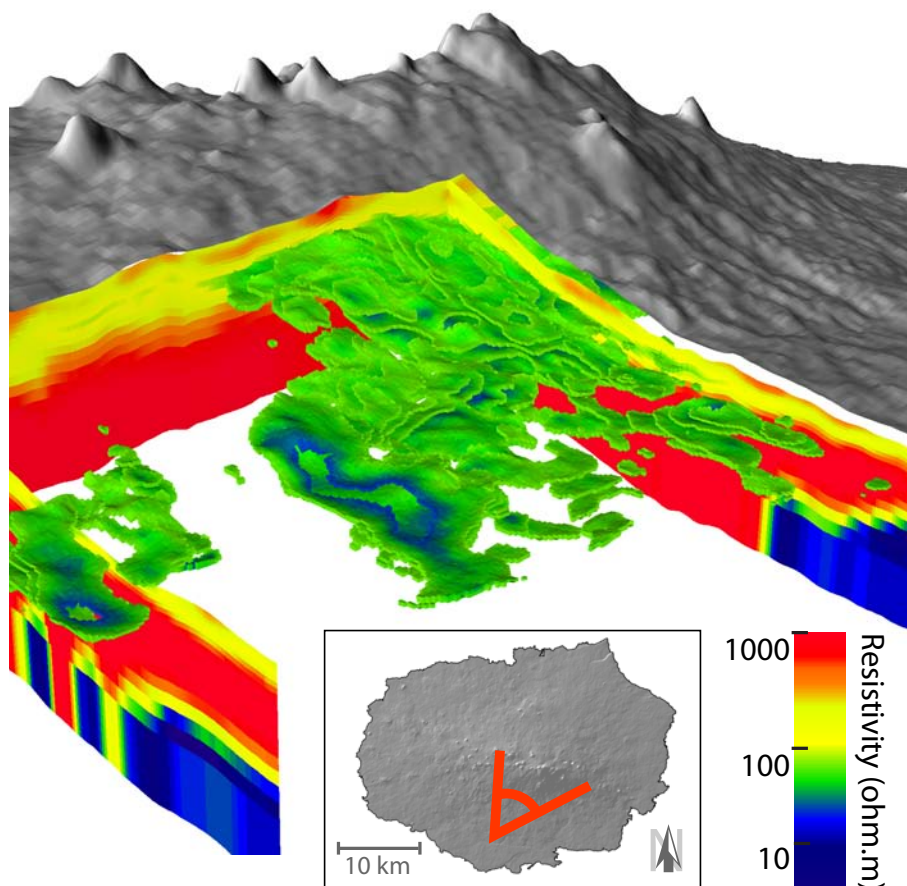


**Figure 4.7:** 3D view of SkyTEM survey on Santa Cruz Island reveals the geometry of a large  $6 \text{ km}^3$  low-resistivity formation, extracted with a 30-70 ohm.m threshold on resistivity values and draped by a high resolution DEM [d'Ozouville *et al.*, 2008b]. The red line on inset shows the location and orientation of the virtual camera.

The 3D grid is exported into binary VTK file format, which allows a flexible visualization in VTK-compatible software such as Paraview <sup>®</sup>R ([www.paraview.org](http://www.paraview.org)). The VTK file containing all geometry and data (resistivity, uncertainties on resistivity and thickness) is easily loadable on a standard machine (tested on

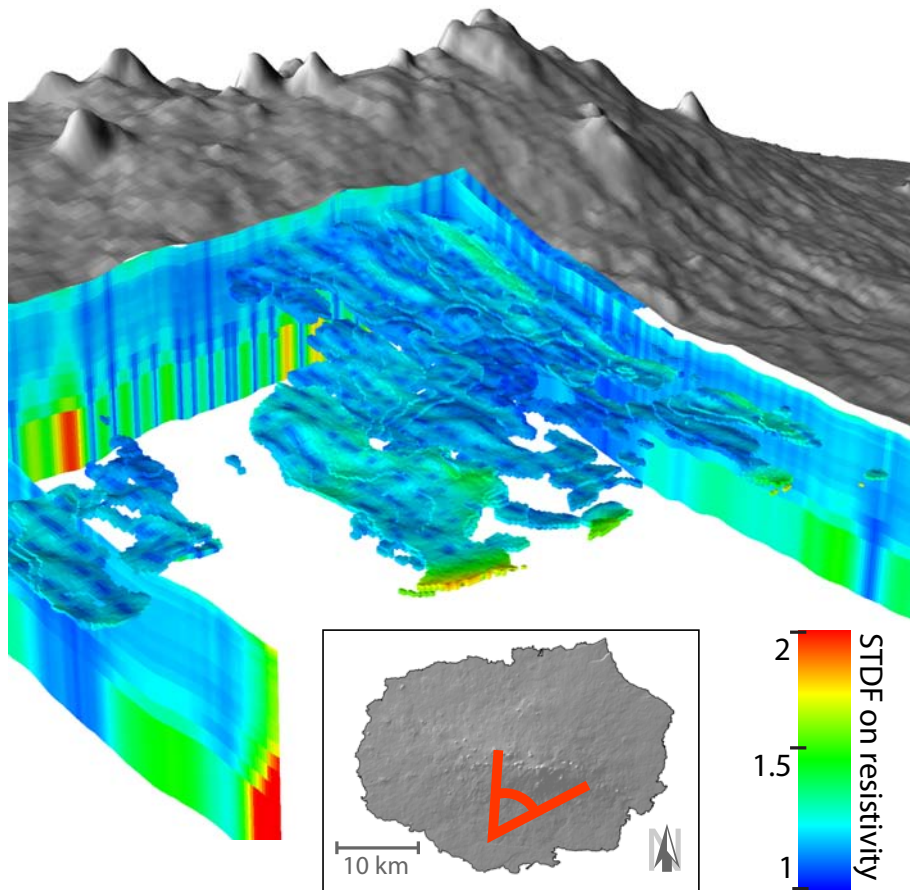


**Figure 4.8:** 3D view of total uncertainty on resistivity, integrating error from both inversion and interpolation processes, and expressed as standard deviation factor (STDF). In the background low uncertainty traces (dark-blue) are the imprints of flight lines. The low resistivity formation extracted from resistivity threshold is well resolved. The red line on inset shows the location and orientation of the virtual camera.

## 4. 3D RESISTIVITY GRIDDING OF AEM SURVEYS

---

2.4GHz Intel Core 2 Duo ®, with 4GB RAM). Fig. 4.7 shows the combined 3D view of “classic” cross-sections, together with a subset of cells extracted by a threshold on resistivity between 30 and 70 ohm.m, and covered by the shaded relief map of a high-resolution DEM [d’Ozouville *et al.*, 2008b]. This image highlights the 3D geometry of a large low-resistivity body, first identified by [d’Ozouville *et al.*, 2008a]. This feature covers about 50 km<sup>2</sup> and appears to be relatively continuous, with a total volume of 6 km<sup>3</sup> and a mean thickness of about a 30 m. The 3D map of total uncertainty on resistivity (Fig. 4.8), expressed as standard deviation factor, illustrates that this feature is well-resolved, with a mean STDF of 1.2. Although the execution of exploration drill holes is still missing to validate this hypothesis, available climatic and geological data can be compatible with the existence of a water saturated and potentially clayey formation, which could fit in the resistivity range of this feature.

### 4.5 Conclusion

To date, most airborne AEM datasets are inverted with a 1D model description and most of them are visualized as 2D interpolated maps. Numerous extensive AEM datasets have been collected in various 3D geological contexts. They have proven to perform successfully as long as 3D heterogeneities in the subsurface are bigger than the footprint of the soundings. The methodology presented in this paper allows 3D visualization of inversion models and volumetric computations. The 2D interpolation by kriging of the model parameters is based on the “layered-earth approach”. It insures a good coherence with 1D models and conserves the vertical resolution of the inversion, while providing fast grid generation and lightweight files. The quantification of errors combines uncertainties from interpolation and inversion. Using a volcanic case-study, we showed that for a flight line spacing of 250 m, the total uncertainty remains within an acceptable range. However, the uncertainty may increase with larger line spacing and sharp contrasts in resistivity. Because the method is fast and simple, a 3D grid of resistivity can be easily built from extensive surveys covering large scale 3D geological structures. Visualization options include thresholding of resistivity and uncertainty, allowing the user to extract different 3D geological bodies based on resistivity ranges and conceal the data with high uncertainty. This is a step toward enhanced interpretation of AEM datasets.

### 4.6 Acknowledgements

This work has been funded by the French Agence Nationale de la Recherche

## 4.6 Acknowledgements

---

(ANR-blanc 2010 GIIWS *n*° 601-01). The Charles Darwin Research Station and the Galapagos National Park collaborated to the 2006 SkyTEM survey in Galápagos, which was funded by Foundation de France, Foundation Véolia Environnement, Fondation Schlumberger-SEED, Chancellerie des Universités de Paris, UGAFIP-BID and Municipality of Santa Cruz.



## Chapter 5

# Hydrogeological framework of San Cristóbal Island after SkyTEM survey: insights in the morphological evolution of basaltic shields

# Hydrogeological framework of San Cristóbal Island after SkyTEM survey: insights in the morphological evolution of basaltic shields\*

---

## Abstract

San Cristóbal is the only island of the Galapagos Archipelago with freshwater springs and a network of permanent streams. Through a joint use of airborne electromagnetics (SkyTEM), remote sensing and fieldwork, we propose a first hydrogeological conceptual model for this island. This model comprises: (1) a low-elevation basal aquifer subjected to seawater intrusion, (2) high-level, probably perched groundwater bodies feeding springs and streams, and (3) a probable dike-impounded aquifer in the summit area. This configuration, developed for San Cristóbal Island, could be similar to that of Santa Cruz Island which shares similar geological and climatic contexts with San Cristóbal. But configurations are contrasting: Santa Cruz is totally devoid of surface freshwater. We propose an evolution pattern for the evolution of basaltic shields accounting for these contrasts. Younger volcanic shields (e.g. Santa Cruz) present monotonous morphology and regional permeability is high. Due to the effects of weathering, the permeability of volcanic formations decreases with time. Older islands, such as San Cristóbal, are more favorable to groundwater storage. Surface runoff induces the incision of valleys and therefore the existence of springs. The hydrogeological settings of volcanic shields are shown to depend not only of the geological context, but as well of the effects of ageing, which are modulated by climatic conditions.

---

\* In collaboration with Noémi d'Ozouville<sup>1</sup>, Benoit Deffontaines<sup>2</sup>, Sophie Violette<sup>1</sup>. With the participation of David Fauchet, Wafa Ramdani, and Fabian Lindner. This chapter formed a basis for an article submitted to *Hydrology and Earth System Sciences*. The reader may refer to the online version, [www.hydrol-earth-syst-sci-discuss.net/papers\\_in\\_open\\_discussion.html](http://www.hydrol-earth-syst-sci-discuss.net/papers_in_open_discussion.html).

<sup>1</sup>UPMC Univ. Paris 6 & CNRS, UMR Sisyphe, 4 place Jussieu, 75252 Paris cedex 05, France

<sup>2</sup>GTMC Laboratory, UPE, Marne-La-Vallée, France

## 5.1 Introduction

San Cristóbal Island is located at the easternmost of the Galapagos Archipelago, about 1000 km west of the South-American continent. The windward slopes are covered by a network of permanent streams fed by numerous springs. Surface water is abundant, deep ravines incise the volcanic rocks. This configuration contrasts with other islands of the archipelago, and particularly Santa Cruz Island, ca. 70 km west, where freshwater is totally absent or restricted to small intermittent springs.

The availability of freshwater shaped the history of San Cristóbal, which was the first successful longterm settlement in the Galapagos Archipelago. By 1869, Manuel Cobos, a despotic land owner, diverted streams to irrigate sugar and coffee plantations [d'Ozouville, 2007a]. Though he was eventually killed by one of his worker, Cobos left a flourishing domain. Puerto Baquerizo, the main city of San Cristóbal became the capital of the Galapagos province, part of the Republic of Ecuador. About seventy years later, during World War II, San Cristóbal gained a strategic importance as the US Army occupied Baltra, a small and dry islet 100 km west of the island. The Americans installed water catchments on San Cristóbal and transported freshwater with barges to Baltra [d'Ozouville, 2007a]. Today, San Cristóbal is the second populated island of the archipelago, with 6500 inhabitants [INEC-CGG, 2010].

The hydrogeological settings of San Cristóbal are virtually unknown, but may share similar configurations with other, well-studied basaltic islands such as the Hawaiian or Canary islands. In coastal areas, all volcanic islands have a rather shallow *basal aquifer* in connection with the ocean. This aquifer is subjected to seawater intrusion at different extents, depending on the equilibrium between groundwater recharge and discharge. The occurrence of springs at higher elevation, as observed on San Cristóbal, can be explained either by the rise of the basal aquifer water table, or by the existence of *perched* and/or *dike-impounded* aquifers. The first configuration, with a thick basal aquifer is rather found in "old" volcanic islands (e.g. Tenerife (Canary) and Kauai (Hawaii) islands [Custodio et al., 1988; Izuka and Gingerich, 2003]. Low-lying basal aquifers, together with perched and dike-impounded aquifers, are reported in e.g. Hawaii, Azores, Réunion and Cape Verde Islands [Cruz and Silva, 2001; Heilweil et al., 2009; Oki, 1998; Violette et al., 1997].

To investigate the internal structure of San Cristóbal Island, an extensive airborne electromagnetics *SkyTEM* survey was conducted over the southern, windward part of the island [d'Ozouville, 2007a]. It was combined with field-based investigations and remote sensing. After a presentation of the geographical settings, we describe the surface structure of the island. The results of the geophysical survey are then presented and serve as a base for the definition of the

## 5. HYDROGEOLOGICAL FRAMEWORK OF SAN CRISTÓBAL

---

hydrogeological conceptual model. From these results, we propose a morphological evolution pattern for basaltic shields, which accounts for the contrasting configuration of Santa Cruz and San Cristóbal.

### 5.2 Geographical settings

#### 5.2.1 Geology

San Cristóbal lies on the Nazca plate, at the eastern end of the Galapagos Archipelago. It has an elongated shape, 50 km long in the south-east direction and 14 km orthogonally, for a total surface of 56 km<sup>2</sup>. It is the most remote island from the position of the hot-spot, currently located below Fernandina Island ca. 200 km west [Geist and Reynolds, 1998]. Contrary to the Hawaiian islands, there is no simple relationship between the age of the edifices and the distance to the hot-spot. Volcanism in the archipelago was affected by the presence of the *Galapagos Spreading Center*, a faulted mid-ocean ridge a few hundreds km north [Mittelstaedt and Ito, 2005]. Volcanoes of the Archipelago align along north-northwest and east-northeast directions commonly called the *Darwinian trends* [Chadwick and Howard, 1991].

Together with Santa Cruz and Santiago islands, San Cristóbal belongs to the central geological sub-province [McBirney and Williams, 1969]. These volcanoes lie on the *Galapagos Platform*, have relatively gentle slopes and lack a caldera. San Cristóbal can be divided into two sub-regions: an older southwestern sub-region where volcanic activity coalesced to form a major shield culminating at 710 m a.s.l, and a younger flat sub-region to the northeast, characterized by recent fissured-fed eruptions [Geist et al., 1986]. This study will focus on the older inhabited southwestern part, where springs and streams are present, while the northeastern part is arid and belongs to the Galapagos National Park.

The oldest lavas of San Cristóbal have been dated to 2.3 Ma. They outcrop at the south-western edge of the island close to Puerto Baquerizo and are locally present at the north-east [Geist et al., 1986] (Fig. 5.1). Reversely polarized flows of the Matuyama epoch ( $> 0.78$  Ma) outcrop at the base of the southwestern shield, but most of the volcano is covered by younger lava flows of the *Bruhnes* epoch. Eruptions were relatively continuous up to 0.66 Ma, and characterized by moderately thick (1 to 3 m) *pahoehoe* and *aa'* flows [Geist et al., 1986]. They are locally interbedded by red, “baked” soils [d’Ozouville, 2007a]. Pyroclastic material forms an exceedingly small part of the volume of the volcano, restricted to eruptive cones [Geist et al., 1986]. Nevertheless, at least 10 m of tephra were deposited over the entire summit during the culminating eruptions [Geist et al., 1986]. With the humid conditions prevailing in the highlands, it was rapidly

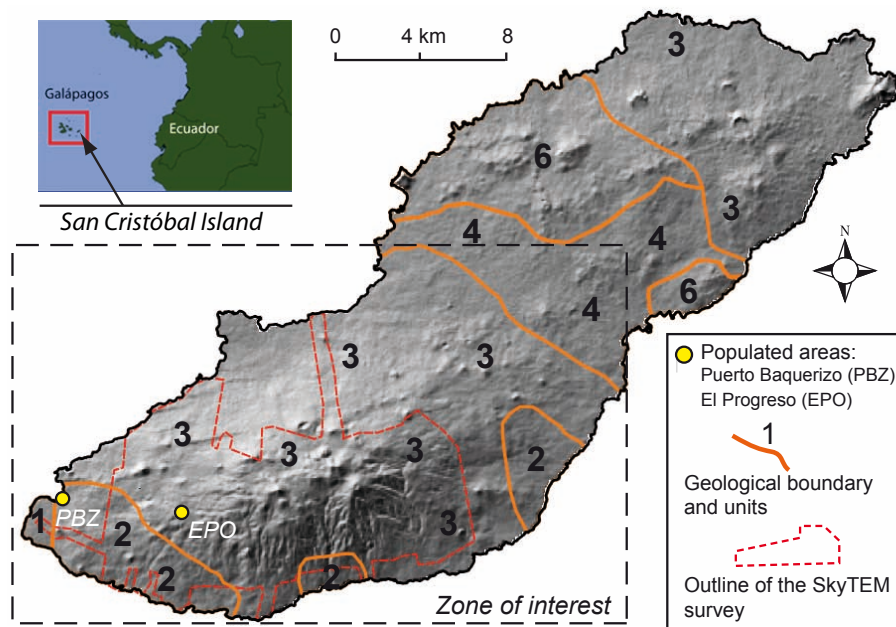


**Figure 5.1:** Geographical context of San Cristóbal Island. Shaded relief map from the SRTM digital elevation model. Geological boundaries from *Geist et al.* [1986], with ages from the older (**1**, 2.3 Ma) to younger (**6**, historical) formations. Dashed red outline corresponds to the boundary of the domain surveyed with SkyTEM.

## 5. HYDROGEOLOGICAL FRAMEWORK OF SAN CRISTÓBAL

---

weathered to form a thick poorly permeable soil cover [Adelinet *et al.*, 2008].

### 5.2.2 Climate

Climate of the Galapagos Islands is relatively dry with respect to its equatorial location [Colinvaux, 1972]. Rainfall at low elevation are particularly weak, with a median of 368 mm (1977-1983, INHAMI) at Puerto Baquerizo (+6 m a.s.l.). Precipitations over the Galapagos islands are highly variable in time and space. Season alternates between a hot season (Jan. to May), and a cool season (June to December) [Trueman and d'Ozouville, 2010]. The hot season is dry, but accompanied by convective rainfall, particularly intense during *El Niño* events. During the cool season, the presence of an atmospheric temperature inversion layer impedes further rise of moist air evaporated from the ocean, and leads to the existence of a semi-permanent fog layer from ca. 400 m a.s.l. to the summit [d'Ozouville, 2007a; Trueman and d'Ozouville, 2010]. During the cool season, precipitations are orographic and increase with altitude until mid-elevation along the southeastern windward slopes. Only short-term climatic records are available at San Cristóbal. Climatic processes on this island will be considered to be similar to Santa Cruz island, where rainfall orographic gradient was estimated to ca. 415 mm/year from the coast up to the elevation of 440 m a.s.l ([d'Ozouville, 2007a] and Chap. 9). Under these assumptions, the annual mean precipitation over San Cristóbal is 1580 mm (see section 5.5.2.2).

## 5.3 Structural and hydrological analysis

### 5.3.1 Cones and dike swarms

Dike swarms are of particular importance in the hydrogeology of volcanic islands. They are often impermeable and form groundwater divides at the center of rift zones [Custodio, 2004]. Few dikes naturally outcrop on San Cristóbal, but can be identified in the center of a mine exploiting a big pyroclastic cone in the vicinity of Puerto Baquerizo. The position of dikes may be inferred from their superficial expressions: eruptive fissures and cones. When cones are elongated or aligned, they are likely to be the superficial expression of major dyke swarms [Acocella and Neri, 2009; Chadwick and Howard, 1991].

From the maps provided by Ingala *et al.* [1989], Google Earth ® images and the NASA Shuttle Radar Topography Mission digital elevation model (SRTM DEM), a comprehensive mapping of volcanic cones was completed on San Cristóbal island (Fig. 5.2). Antithetic normal faults intruded by dykes can be identified on the shaded relief map at the northern slope of the southwestern shield of San

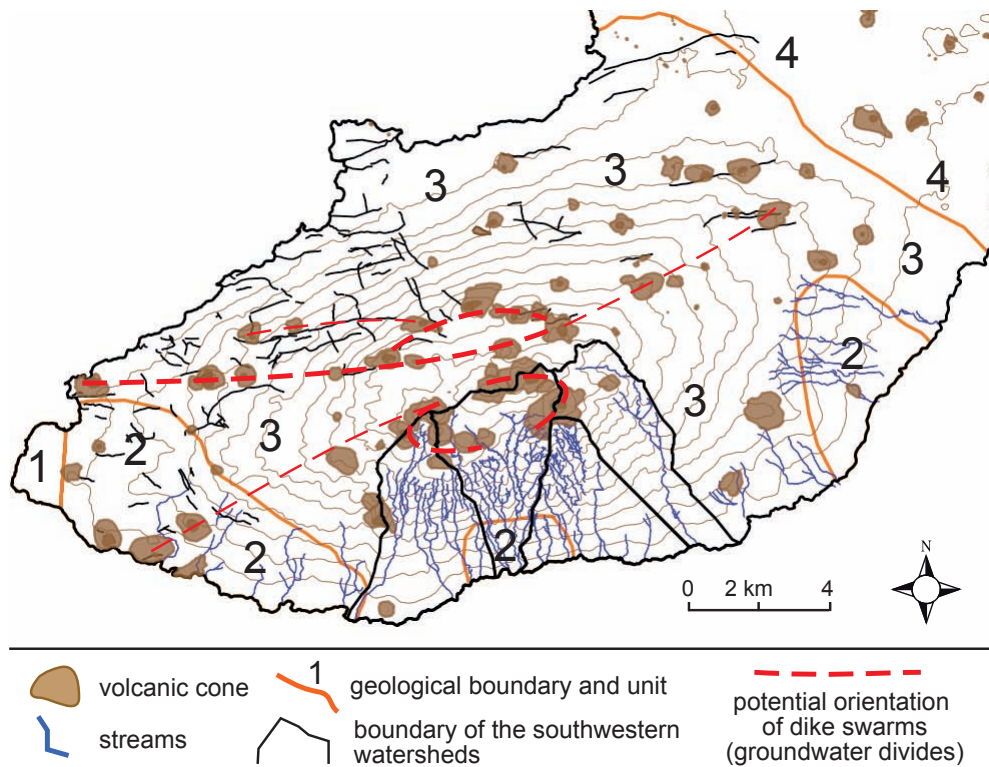


**Figure 5.2:** Surface morphology of the southwestern shield of San Cristóbal island. Geological boundaries from *Geist et al.* [1986]. Drainage network and volcanic cones were mapped from the Google Earth ® SPOT imagery and SRTM DEM.

## 5. HYDROGEOLOGICAL FRAMEWORK OF SAN CRISTÓBAL

---

Cristóbal (Fig. 5.1). They are the evidences of a N-S extensive tectonic context, which allowed the co-evolution of faults and controlled the position of the eruptive zones. Cones do not follow a single alignment as it is the case in other islands of the Archipelago, such as Santa Cruz. Nevertheless, they are organized along several E-W alignments and form an elongated ellipsoid at the summit, constituted by two semicircles (Fig. 5.2).

The structural pattern of cones (Fig. 5.2) are likely to underline dike swarms, which usually behave as groundwater barriers [Custodio, 2004].

### 5.3.2 Springs and streams

The mapping of the drainage network provided by *Ingala et al.* [1989] was improved and completed with the high resolution images available on Google Earth ®. This mapping could not be comprehensive in vegetated areas where the position of the stream was not visible. Flowing streams and springs were mapped from a field GPS campaign conducted by *Adelinet* [2005]. Air photographs allowed additional morphological analysis.

The northern leeward slopes are dry and monotonous (Fig. 5.3). Streams and ravines are numerous along the windward side and originate from the summit area (Fig. 5.3 B and C). A drainage network is visible at the southwestern and southeastern flanks, over the older reversely polarized formations of age 2 (Fig. 5.1). This highlight that the age of the formation partly controls the development of the drainage network.

Springs were mapped after several field surveys [*Adelinet*, 2005; *d'Ozouville*, 2007a] (Fig. 5.4, Table 5.1). A first family of springs (num. 6-8 and 9-12) is located at the bases of two major eruptive cones, ca. 550 m a.s.l. (Fig. 5.4), and a second family at break slope, 450 m a.s.l. (num. 1-5). Three other springs are identified at mid-slope (alt. 210 m a.s.l.). Springs num. 16-18 are found within ravines. "Villemaluca" spring (num. 17) is found at the flank of the valley, right over an interbedding of red "baked" soil.

Springs were classified following the typology defined by *Fetter* [1994] into *break slope* or *depression* springs (Table 5.1):

- depression springs are formed when the water table reaches the land surface. The change in topography creates a corresponding undulation in the water table configuration (Fig. 5.5, A).
- contact springs are located at geological interfaces, where permeable rock units overlie rocks of much lower permeability (Fig. 5.5, B).

Volcanic activity over the main shield of San Cristóbal ceased c.a. 0.66 Ma ago [*Geist et al.*, 1986] and no hydrothermal activity is reported on San Cristóbal.

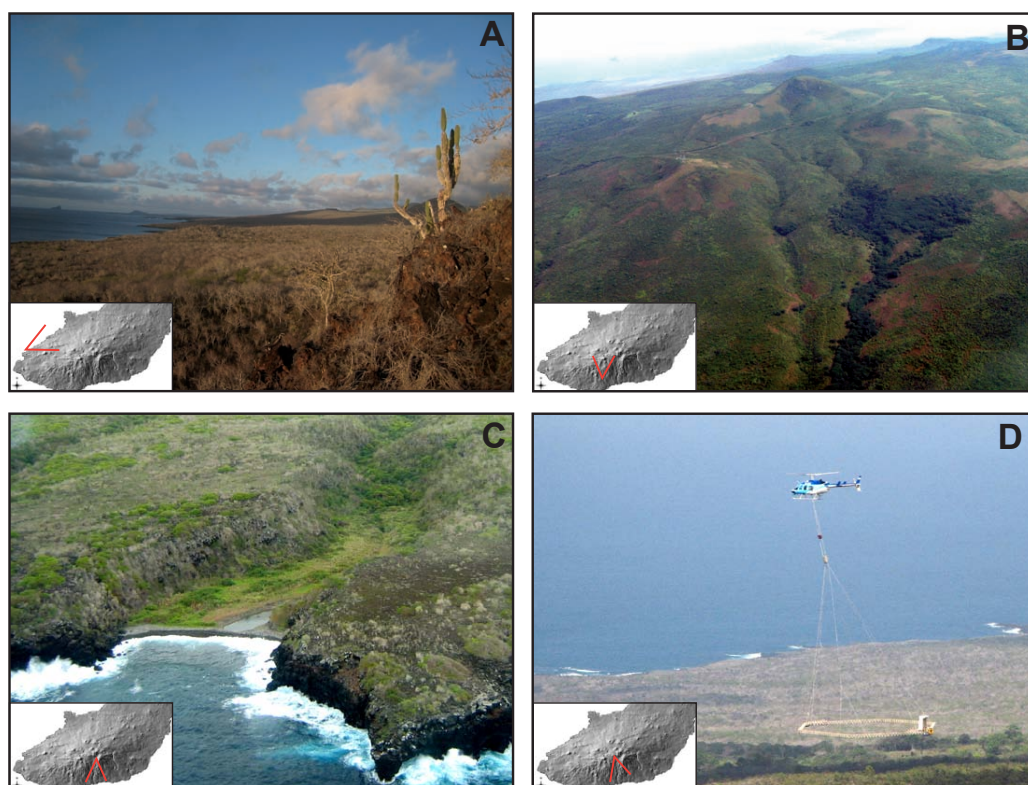


**Figure 5.3:** (A) Photographs of the dry leeward slopes. (B) Aerial photograph of El Junco lake and Cerro Santa Tomás, where streams start. (D) Aerial photograph of Cerro San Joaquín, affected by a flank collapse at the south. (D) Aerial photograph of the windward slopes incised by valleys, where streams reach the sea. Aerial photographs were taken by Noémi d'Ozouville and Mathilde Adelinet, the first by the author.

## 5. HYDROGEOLOGICAL FRAMEWORK OF SAN CRISTÓBAL

---

Num.	Name	Type	$\chi$ range ( $\mu\text{S}/\text{cm}$ )
1	Rojas	break slope	83
2	Soarez	break slope	
3	No name	break slope	
4	La Policia II	break slope	75
5	Gutierrez	break slope ?	77
6	La Toma	break slope ?	29
7	Tributario La Toma	break slope ?	31
8	El Platano	break slope ?	29
9	Ferruginous spring	break slope ?	142
10	Bajo El Junco I	break slope ?	69
11	Bajo El Junco II	break slope ?	
12	Del Bayo	break slope ?	63
13	Milton Aguas	contact spring ?	114
14	Hector Aguas	contact spring ?	94
15	Nuevas Aguas	contact spring ?	102
16	Tributario Villemaluca	contact spring ?	163
17	Villemaluca	contact spring	115
18	Las Goterras	contact spring ?	

**Table 5.1:** Springs identified by *Adelinet* [2005] and further field studies.  $\chi$  stands for electrical conductivity of water, as measured in the field.

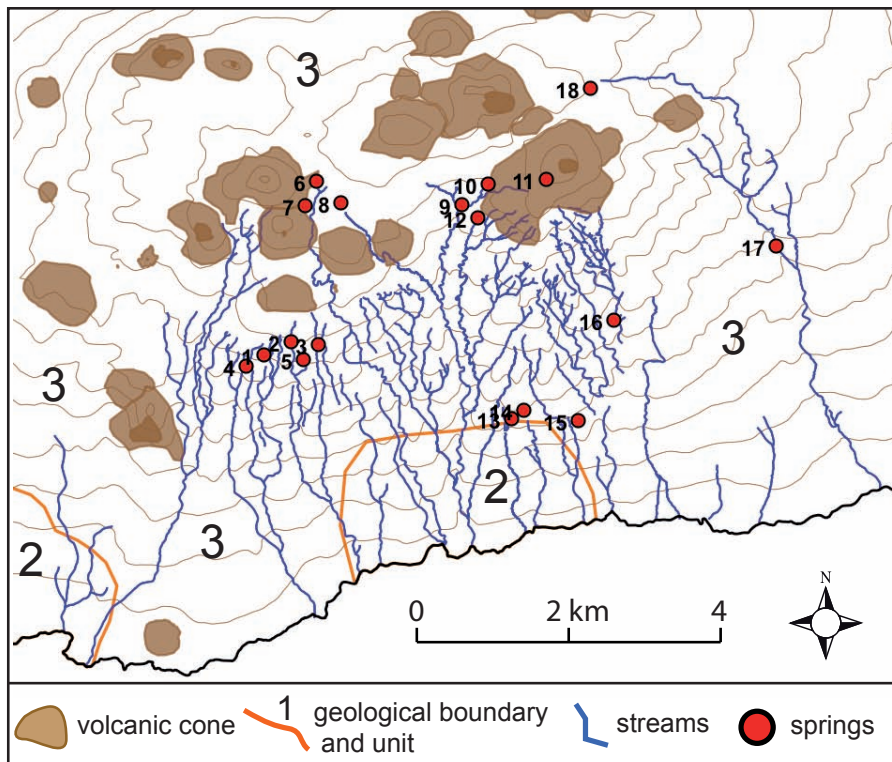


**Figure 5.4:** Mapping of streams from Google Earth® and springs from field GPS campaigns. See Table 5.1 for further information. These methods are not exhaustive, portions of streams were not visible. Due to difficulty of access, numerous springs could not be identified in the field.

## 5. HYDROGEOLOGICAL FRAMEWORK OF SAN CRISTÓBAL

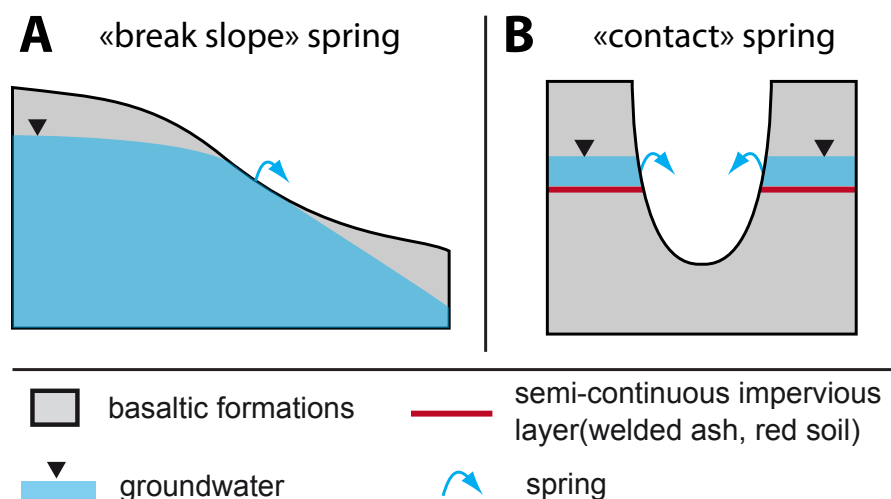


**Figure 5.5:** Two types of springs found on San Cristóbal island, typology from *Fetter* [1994]. (A) *Break slope* or *depression* springs form when an aquifer intersects surface topography. (B) As a result of erosion, boundaries between two geological units of contrasting permeability can outcrop and form springs (e.g. presence of a red “baked” soil in a valley).

Only traces of extinct fumaroles with white deposits (probably sodium sulphate) are visible on unweathered volcanic cones. Springs are poorly mineralized, with electrical conductivities ranging between 30 and 170  $\mu\text{S}/\text{cm}$  (Table 5.1) [*Adelinet*, 2005].

### 5.4 Airborne electromagnetics SkyTEM survey

#### 5.4.1 Presentation of the survey

An airborne electromagnetics SkyTEM survey was conducted over San Cristóbal Island in 2006 [*d’Ozouville*, 2007a]. About 23 000 soundings were performed along the 900 km flight lines, with one sounding each 25-50 m. Soundings were inverted to 1D vertical resistivity profiles with the spatially constrained inversion pattern (SCI) [*Viezzoli et al.*, 2008], and interpolated to a 3D grid of resistivity with the methodology proposed by [*Pryet et al.*, 2011].

In volcanic contexts, electrical resistivities are usually interpreted as follow:

- Very low resistivities ( $< 15 \text{ ohm.m}$ ) are related to weathered or hydrothermalized formations and/or formations saturated with groundwater of high

---

## 5.4 Airborne electromagnetics SkyTEM survey

---

salinity [Aizawa *et al.*, 2009; Lénat *et al.*, 2000; Muller *et al.*, 2002; Revil *et al.*, 2004].

- Intermediate resistivities (15-800 ohm.m) are interpreted as weathered or saturated formations with different grades of weathering and saturation [Descloitres *et al.*, 1997; Lénat *et al.*, 2000; Muller *et al.*, 2002]. In particular, formations between 100-250 ohm.m can be associated to freshwater saturated formations [Robineau *et al.*, 1997].
- high electrical resistivities ( $> 800$  ohm.m) are associated with unweathered dry basaltic formations Descloitres *et al.* [1997, 2000]

Above sea level, the northern leeward side of San Cristóbal is composed by resistive formations ( $> 400$  ohm.m). In contrast, the bulk of the southern windward side of San Cristóbal is composed by weakly resistive formations (50-200 ohm.m). Below sea level, a wide fringe of very conductive formations are present.

The interpretation of the SkyTEM survey is split into the three following sub-sections, where geophysical data is confronted to field observations.

### 5.4.2 The basal aquifer: imprints of salt water intrusion

The basal aquifer locally outcrops at the bottom of the Airport Mine, near Puerto Baquerizo west of the island. Groundwater electrical conductivity is high ( $\chi = 28$  mS/cm), which is the consequence of seawater intrusion.

Brackish groundwater has a very low resistivity and can easily be identified from subsurface resistivity mapping (e.g. [Auken *et al.*, 2009]). The “salt water interface” (SWI) can thus be mapped, but when the interface between sea- and freshwater is diffuse, which is often the case [Izuka and Gingerich, 1998b], the actual depth of the 50% mixing line is difficult to obtain, and requires vertical salinity profiles measured in monitor wells. Given the absence of drill holes on San Cristóbal, such data was not available. As a consequence, the SWI inferred from the SkyTEM survey provides only an indicative value.

At the exception of local artefacts, the map of the SWI computed for San Cristóbal is coherent with expectations (Fig. 5.6 and 5.7). The SWI is shallow at the dry northern and western slopes, and deeper at the southern windward side. The SWI is particularly deep below the strongly incised valley originating from the semi-circular summit cones (Fig. 5.1 and 5.7). In the rest of the surveyed area, the SWI is too deep with respect to ground level to be detected by geophysical soundings.

At the windward side of San Cristóbal, the depth to the SWI ranges between 20 and 80 m below sea level (Fig. 5.7). An estimation of the basal aquifer water table height can be inferred from the Ghyben-Herzberg formula [Bear, 1999],

## 5. HYDROGEOLOGICAL FRAMEWORK OF SAN CRISTÓBAL

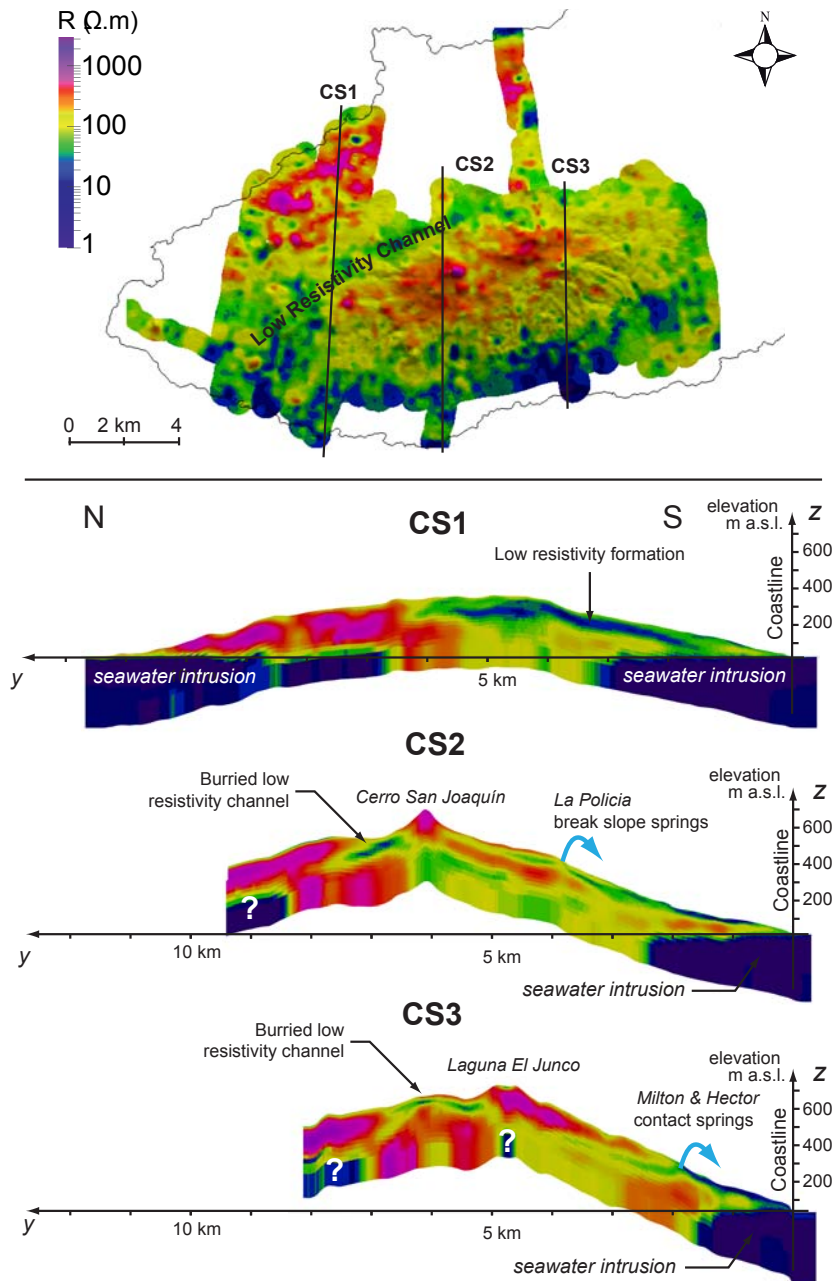


**Figure 5.6:** (A) Surface resistivity of the 19-layer SkyTEM resistivity model highlight a low-resistivity channel. (B) Cross-sections in this resistivity model show low-resistivity layers (50-200 ohm.m) intersecting the ground surface where springs were reported. As well, a low resistivity channel is present in the highlands.

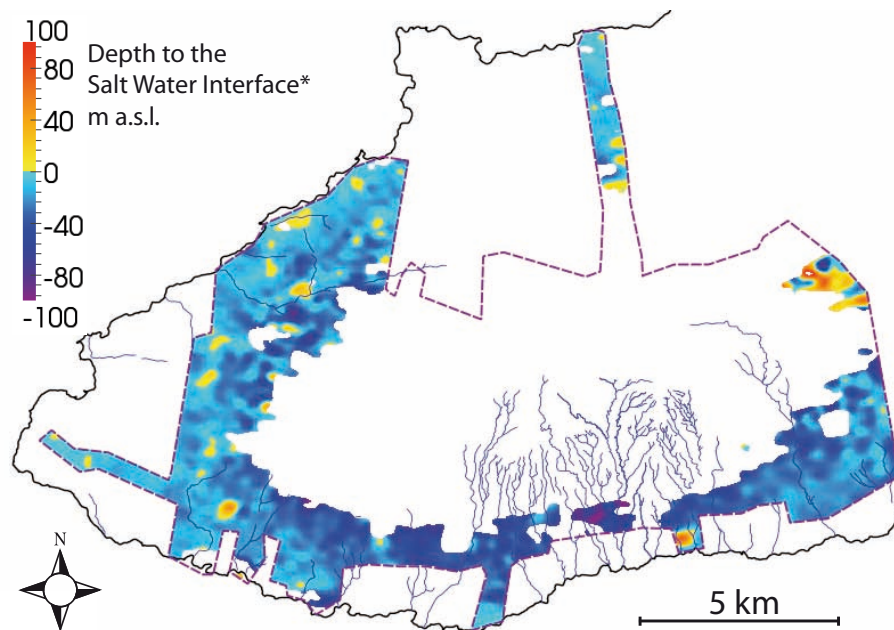


**Figure 5.7:** Depth to the *Salt Water Interface* (SWI) inferred from electrical resistivity mapping with the 4-layer model. SWI elevation is estimated from the elevation of the top of the very conductive layers ( $< 15 \text{ ohm.m}$ ). Values above sea level are artefacts and should be disregarded.

## 5. HYDROGEOLOGICAL FRAMEWORK OF SAN CRISTÓBAL

---

which assumes no-mixing between fresh- and saltwater. This yields a water table between 0.5 and 2 m above sea level. As detailed by [Izuka and Gingerich, 1998b], this method is rough, but may, in a first approach, provide an order of magnitude of the water table height.

### 5.4.3 High level groundwater

The bulk of the windward side of the island is composed by weakly resistive formations (30-200 ohm.m), which can be related to weathered volcanics, potentially water saturated.

Most springs identified at the surface are associated with low (30-100 ohm.m) subsurface resistivities (greenish colors, Fig. 5.6). Spring waters are poorly mineralized ( $\chi = 34$  to  $173 \mu\text{S}/\text{cm}$ , Table 5.1), and cannot explain alone such low resistivities found at high elevation. They are attributed to clayey minerals, associated with rock weathering.

Low resistivity units are frequently underlain by highly resistive bodies ( $> 400$  ohm.m), which are compatible with unweathered, unsaturated massive lava flows.

From these observations, combined with a literature review in this context, two hypotheses emerge for the hydrogeological settings of San Cristóbal: a thick freshwater lens, as proposed for Kauai Island (Hawaii, USA) [Izuka and Gingerich, 2003], or high level groundwater bodies such as perched aquifers or “skin” flow over impervious formations, hydrodynamically disconnected from the basal aquifer, as proposed for Hawaii Island (Hawaii, USA) [Ingebritsen and Scholl, 1993].

Two arguments can be proposed against the hypothesis of a thick freshwater lens. Some high resistivity formations are present in the windward side, below the level of springs, and have little chance to be saturated. Secondly, the water table of the basal aquifer is expected to remain at relatively low elevations (0.5 - 2 m a.s.l.) up to 1.7 km from the coast, while the first springs are identified, at 2 km from the coast, at 200 m a.s.l (CS3, Fig. 5.6). Given that dikes are not expected in this region, a “jump” of the water table from a few meters to 200 m a.s.l in 0.3 km is unlikely. In this conditions, the aquifer feeding the springs is not expected to be in hydrodynamic equilibrium with the basal aquifer.

The second alternative, with the occurrence of high-level aquifer appears more likely. Such aquifers can form over impervious units (ash deposit, “baked” soils), or over geological discontinuities, such as older impervious formations. The outcropping of “baked” soil right below Villemaluca spring (Num. 17) supports the hypothesis of perched aquifers. The relationship between springs 13-15 and the geological boundary defined by [Geist et al., 1986] (Fig. 5.4) supports the hypothesis of the geological discontinuity.

From these observations, it appears that springs of San Cristóbal are related to high-level groundwater bodies associated with weakly conductive formations or geological boundaries.

### 5.4.4 Low resistivity channel

At the center of the island, a partly buried low-resistivity channel (30-100 ohm.m) was revealed by the SkyTEM survey. Sharp resistivity contrasts are visible on the cross-sections (Fig. 5.6). They are highlighted by the high resistivity ( $> 400$  ohm.m) extraction (Fig. 5.8). Vertical edges of the high-resistivity bodies are visible, they form the lateral boundaries of the low-resistivity channel.

To some extent, the edges of the low resistivity channel correspond to the patterns of dike swarms presented on Fig. 5.2. The low resistivity channel dips westward and terminates expanding over the southwestern flank of the shield (CS1, Fig. 5.6).

The low resistivity channel is underlain by highly resistive units, probably weakly weathered massive lavas or massive caldera filling lava flows.

The presence of low resistivity formations at the center of volcanic islands is often associated with hydrothermalized formations [Aizawa *et al.*, 2009; Muller *et al.*, 2002]. Yet there is not any evidence of past, or present hydrothermal activity on San Cristóbal Island. On the windward watershed, low-resistivity formations are interpreted as water-saturated units and are associated with springs when they outcrop (Fig. 5.6). By analogy, we may associate the central, buried low-resistivity channel with a groundwater body impounded by dikes. Though no hydrogeological evidences are currently available, this hypothesis is compatible with climatic conditions and a similar configuration was reported in the Hawaiian Archipelago [Gingerich and Oki, 2000]. The particularly low resistivity area southwest of the channel may be related to enhanced weathering due to the outflow of the dike-impounded aquifer.

## 5.5 Discussion

### 5.5.1 Hydrogeological framework of San Cristóbal inferred from the SkyTEM survey

The presence of a basal aquifer was confirmed from field observations and subsurface resistivity mapping, which reveals the imprint of seawater intrusion. From available data, i.e. in the absence of drill holes, it appears that the freshwater lens is thicker at the windward side, but the water table is not expected to reach

## 5. HYDROGEOLOGICAL FRAMEWORK OF SAN CRISTÓBAL

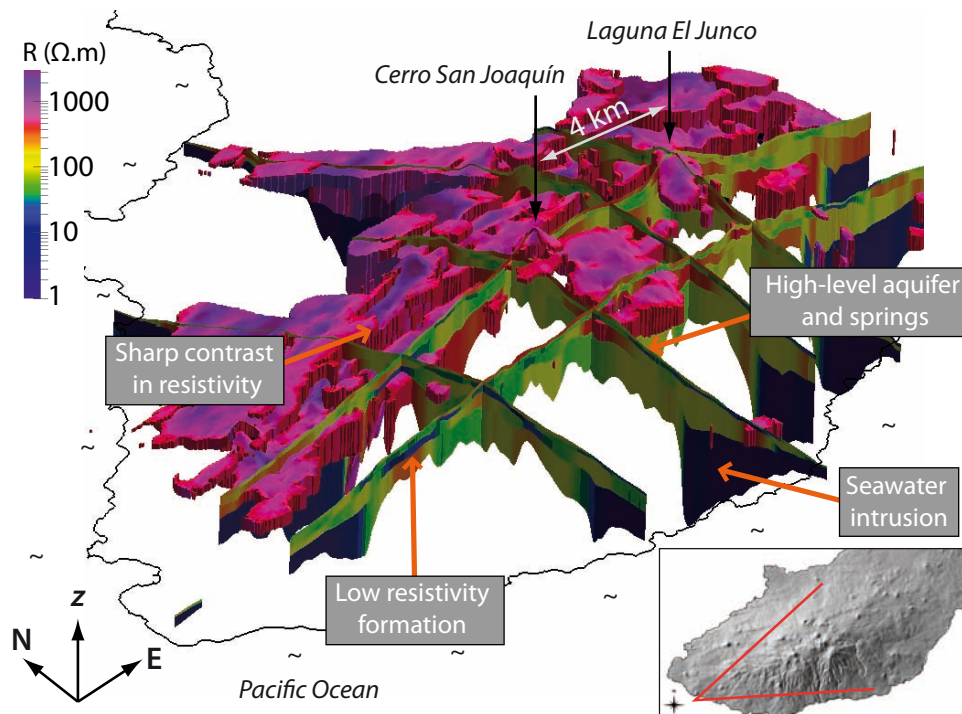


**Figure 5.8:** 3D view of the SkyTEM 4-layer resistivity model. The high resistivity extraction (threshold of resistivity  $> 400\Omega \cdot m$ ) appears dissected by scarps, with downthrows up to 100 m. These scarps form the underground lateral boundaries of the low-resistivity channel presented on Fig. 5.6.

very high elevations (ca. 0.5-2 m). The occurrence of springs at high elevation was explained by the presence of perched aquifers, over impervious formations or geological discontinuities.

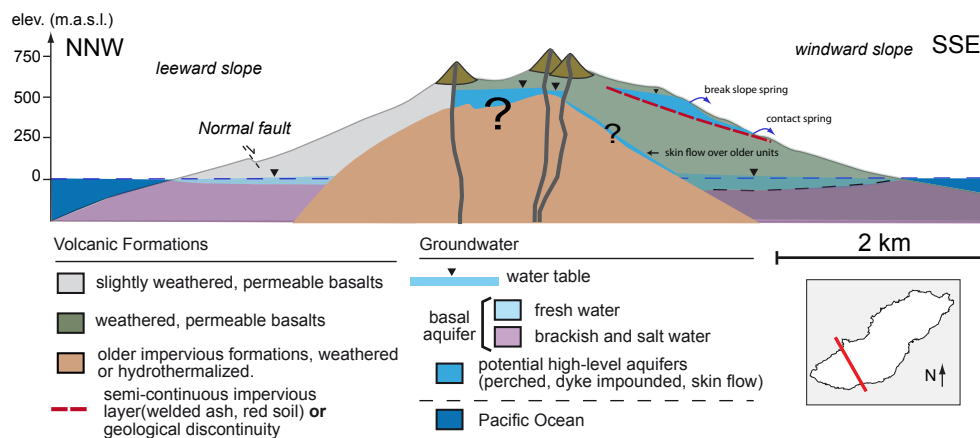


**Figure 5.9:** Hydrogeological conceptual model for San Cristóbal Island inferred from surface observations and the SkyTEM survey. Configuration is asymmetric, the basal aquifer is thin in the north, thicker in the south. Springs are fed by high-level aquifers at the south, probably perched. At the center, a dike-impounded aquifer may be at the origin of the low-resistivity channel.

These interpretations are gathered to propose a first hydrogeological conceptual model for San Cristóbal (Fig. 5.9). This model does not pretend to describe local anomalies present in complex and heterogeneous volcanic environments. Instead, it aims to describe a regional framework. It is solely based on the currently available data, that is observations made at the surface (fieldwork and remote sensing), and 3D resistivity mapping.

In eight days, the SkyTEM survey covered nearly 190 km<sup>2</sup> with 900 km of flight lines [d'Ozouville, 2007a]. It revealed unprecedented insights in the internal structure of the volcano. Nevertheless, it must be acknowledged that in the absence of drill holes in such a complex system, it is sometimes difficult to interpret the resistivity maps. There is a lack of sound geological data, which makes the *equivalence* problem (i.e. identical electrical resistivity for different formations) difficult to solve.

## 5. HYDROGEOLOGICAL FRAMEWORK OF SAN CRISTÓBAL

---

### 5.5.2 San Cristóbal vs Santa Cruz islands

#### 5.5.2.1 Contrasted configurations

San Cristóbal presents a wide network of springs and streams, contrasting with other islands in Galapagos, particularly Santa Cruz, which are devoid of surface water. Three explanations can be *a priori* proposed to explain the contrast between San Cristóbal and Santa Cruz Island:

- **A:** Due to the different morphologies of the islands, precipitations are higher in San Cristóbal.
- **B:** From the construction of the islands, geological contexts are significantly different.
- **C:** San Cristóbal, which is older, has evolved to a more favorable hydrogeological configuration.

These three hypothesis are discussed hereafter.

#### 5.5.2.2 Morphology and recharge potential

Between 1977 and 1983, that is during six “normal” years and an *El Niño* year (1983), median annual rainfall at the coast was 368 mm at Puerto Baquerizo (San Cristóbal) and 370 mm at Puerto Ayora (Santa Cruz). Longer climatic records would be required to conclude, but it appears that annual rainfall at the coast are relatively similar on the two islands.

A precipitation gradient is obvious on the two islands [d’Ozouville, 2007a]. Rainfall is higher at higher elevations, and completed by fog interception above ca. 400 m a.s.l [d’Ozouville, 2007a; Pryet et al., 2012]. The precipitation gradient was estimated to 410 mm/100 m by [d’Ozouville, 2007a] and confirmed in Chap. 9. Yet, it appears from newly available climatic data in Santa Cruz (Chap. 9), that a plateau is reached at ca. 440 m. In this conditions, the morphology of the island partly controls climatic conditions.

Santa Cruz culminates at 855 m a.s.l. and San Cristóbal at 710 m a.s.l. The profile of Santa Cruz is more subdued and presents an extensive low elevation apron (Fig. 5.10). As a consequence, the mean elevation of the southern watershed at San Cristóbal is higher (300 m a.s.l.) than that at Santa Cruz (180 m a.s.l.) (Fig. 5.11).

No precipitation records are available at high elevation on San Cristóbal, precipitations gradients will be assumed to be the same on the two islands. Under this assumption, mean rainfall is higher over the southern windward watershed

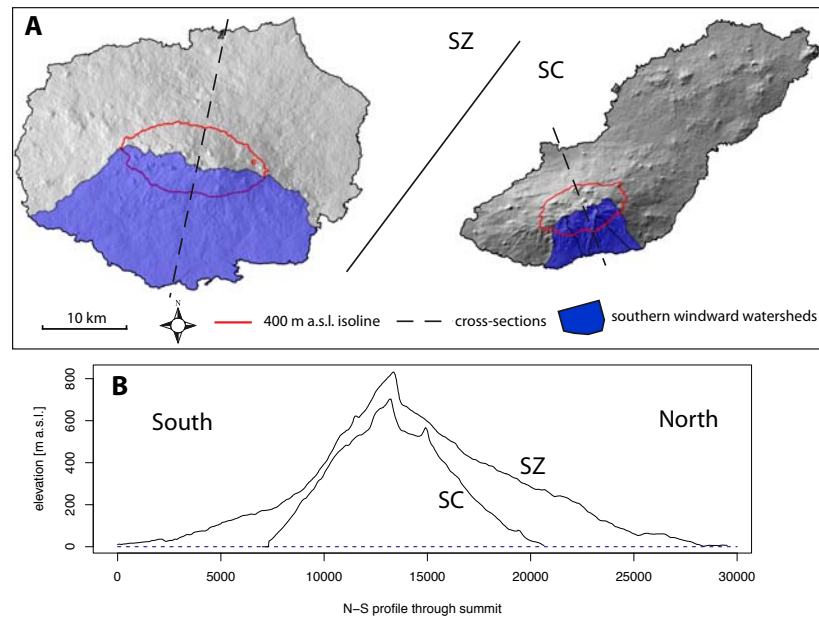


**Figure 5.10:** (A) Shaded relief maps of Santa Cruz (SZ) and San Cristóbal (SC) from radargrammetric DEM [*d’Ozouville et al.*, 2008b] and SRTM NASA DEM respectively. The mean position of the cloud bottom during the cool “fog” season is approximated with the 400 m a.s.l. iso-line (in red) [*Trueman and d’Ozouville*, 2010]. Southern watersheds were extracted with GRASS GIS (B) Compared north-south profiles from SRTM NASA DEM.

## 5. HYDROGEOLOGICAL FRAMEWORK OF SAN CRISTÓBAL

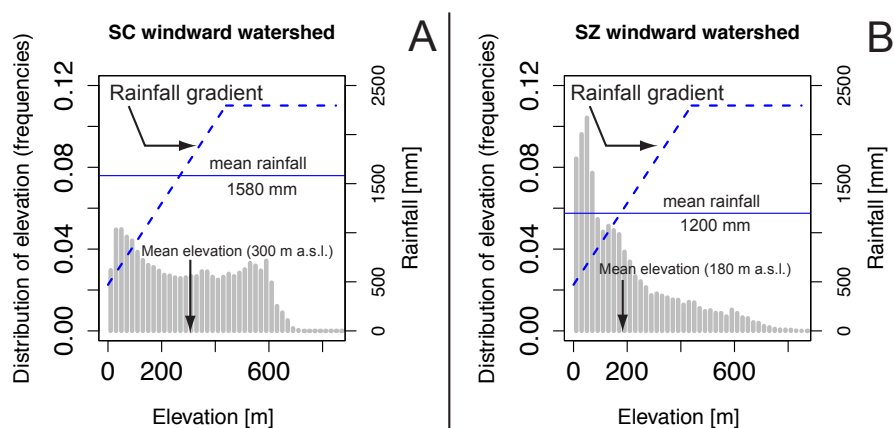


**Figure 5.11:** Distribution of elevations (NASA SRTM DEM) along the windward watersheds of (A) San Cristóbal, and (B) Santa Cruz (Fig. 5.10). Rainfall gradients from [d'Ozouville, 2007a].

of San Cristóbal (1580 mm/year) than that of Santa Cruz (1200 mm/year) (Fig. 5.10 and 5.11).

As a consequence, the southern windward watershed of San Cristóbal receives more precipitation (+30%) than Santa Cruz. Nevertheless, soils of San Cristóbal are thicker and runoff bigger [Adelinet *et al.*, 2008; d'Ozouville, 2007a], so that the portion of rainfall contributing to groundwater recharge is probably similar for the two islands. From currently available data, it appears that climatic settings cannot explain the contrasting hydrogeological configurations observed on the two islands.

### 5.5.3 Contrasting geological settings

Geological contexts of San Cristóbal and Santa Cruz are not devoid of specificities, but their volcanism is not obviously different [Bow, 1979; Geist, 1985].

A thick weathered pyroclastic blanket covers the summit area of San Cristóbal [Geist, 1985] and probably limits infiltration. This is likely to favor runoff and the development of streams. Such a pyroclastic cover is present on Santa Cruz island, but restricted to a limited extent [Bow, 1979].

Though they may have an influence, there is little likelihood that differences in chemical composition or ratios between pyroclastic and effusive materials explain alone the marked hydrogeological differences between Santa Cruz and San Cristóbal islands.

### 5.5.3.1 Geological ageing

Santa Cruz and San Cristóbal are both seated over old volcanic units [Bow, 1979; Geist, 1985], but the ages of the main shields are different.

The whole surface of Santa Cruz is normally polarized, attributed to the *Matuyamah* epoch ( $< 0.58$  Ma) [Bow, 1979]. Available datations range between  $0.59 \pm 0.27$  Ka and  $0.24 \pm 0.11$  Ka [Geist and Reynolds, 1998]

While a large surface of the southern shield San Cristóbal is normally polarized, reversely polarized lavas of the *Bruhnes* epoch ( $> 0.58$  Ma) outcrop at several places (Age 2, Fig. 5.1). Lavas of San Cristóbal were erupted without apparent hiatus between 2.3 Ma and  $0.66 \pm 0.08$  Ma [Geist, 1985].

Due to the effect of erosion, the morphology of the two islands is very contrasting. While the windward slopes of Santa Cruz are monotonous [d'Ozouville et al., 2008b], the southern flank of San Cristóbal is dissected by numerous valleys several hundreds of meter deep (Fig. 5.1). This may be explained by the effect of time.

### 5.5.4 Evolution of volcanic islands

Climatic contrasts between Santa Cruz and San Cristóbal islands are shown to be relatively small. While the chemistry and initial physical properties of erupted lavas are similar on the two islands, lavas of San Cristóbal are shown to be older.

We can propose that the very contrasting hydrogeological configurations observed between San Cristóbal and Santa Cruz islands are the result of physical evolution, controlled by rock weathering and erosion. From observations in the Galapagos islands, an hydrogeological evolution pattern can be proposed for similar environments. This could be synthesized as follow (Fig. 5.12):

- Volcanic formations are initially relatively permeable. Soils are poorly developed, runoff is limited and precipitations percolate rapidly through a thick unsaturated zone. Infiltrated water reaches the basal aquifer, and is rapidly discharged to the ocean. The freshwater lens is thin: a young volcanic island has little hydrogeological interest.
- With time, volcanic rocks are progressively weathered. Weathering of basaltic rocks induces a loss of permeability [Custodio, 2004; Hunt, 1996]. This allows the existence of perched aquifers and thickens the freshwater lens.
- Valley incision and flank collapse favor the outcropping of aquifers.

The comparison of Santa Cruz and San Cristóbal island shows that the age of the island is a determining factor. Yet, the effects of ageing are modulated by

## 5. HYDROGEOLOGICAL FRAMEWORK OF SAN CRISTÓBAL

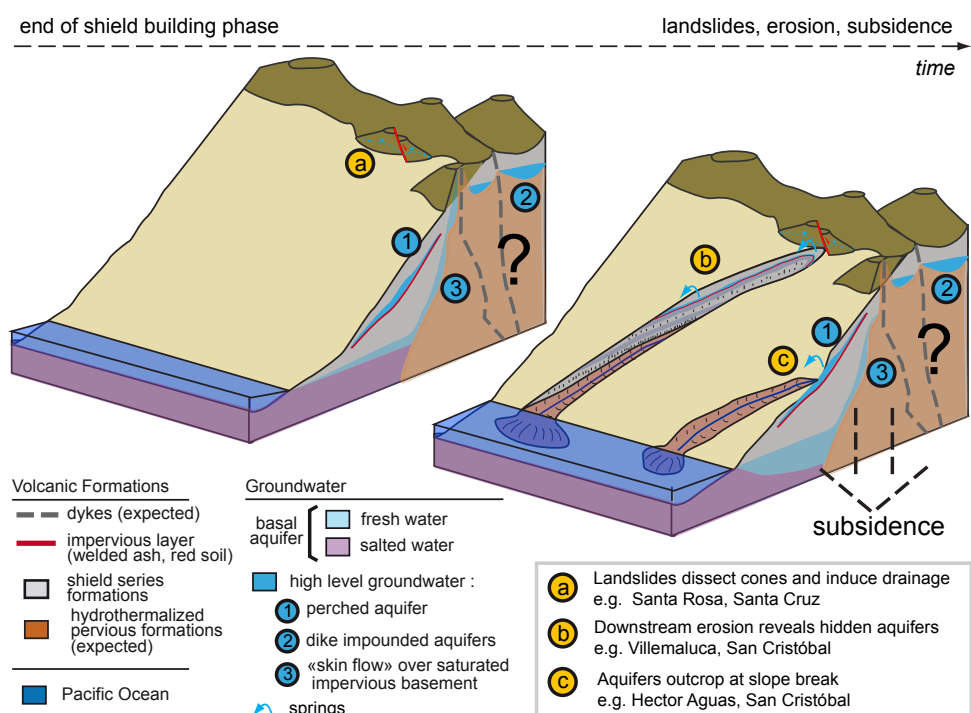


**Figure 5.12:** Evolution pattern of basaltic shields from observations in Santa Cruz and San Cristóbal Islands. At the end of the building phase, hydrogeological potential is often small. The bulk of the island is permeable and aquifer do not necessarily outcrop. With time, under favorable climatic conditions, weathering of rocks induces a loss of permeability and surface runoff incises the topography. Groundwater bodies may outcrop at slope breaks and in valleys.

the availability of water. This is conspicuous when comparing humid windward to dryer leeward sides on the two islands. Both sides have the same geological age, but present different morphological and physical properties.

## 5.6 Conclusions

This exploratory study was based on a SkyTEM airborne electromagnetics survey. A first hydrogeological conceptual model was proposed for San Cristóbal island, the only island of the Galapagos Archipelago with numerous springs and streams. From a comparative study with Santa Cruz island, which is devoid of surface water, the contrasts between the two island were explained with a physical and morphological evolution pattern. This pattern accounts for the presence of surface water on Santa Cruz, and its absence on San Cristóbal, it may as well be extended to other basaltic islands.

## 5.7 Acknowledgments

This study was performed in the frame of the project *Galapagos Islands Integrated Water Studies* (GIIWS), funded by the Agence Nationale de la Recherche (ANR-blanc 2010 GIIWS Ref. 601-01). The Charles Darwin Research Station and the Galapagos National Park collaborated to the 2006 SkyTEM survey in Galápagos, which was funded by Foundation de France, Fondation Véolia Environnement, Fondation Schlumberger-SEED, Chancellerie des Universités de Paris, UGAFIP-BID and Municipality of Santa Cruz. The authors would like to thank David Fauchet, Wafa Ramdani and Fabian Lindner for their participation for the digitalization of cones, fractures and rivers, which was performed under Qgis (<http://www.qgis.org>).



## Part III

# Recharge processes



This part, **Recharge processes** deals with a determining factor in ground-water studies, the renewal potential.

As in many islands over the world oceans, climatic conditions in Galapagos are very contrasted in space and time. The asymmetry is strong between the windward humid and the leeward dryer slopes. The presence of a fog layer brings an additional input in the water budget, that cannot be directly measured with classical rain gauges.

In the frame of this thesis, two fully-equipped weather stations were installed in the highlands of Santa Cruz, at 400 m a.s.l. and 650 m a.s.l. respectively, where climatic data were totally missing.

The chapter *Quantification of cloud water interception* provides an estimate of fog interception for the 2010 cool *garúa* season.



## Chapter 6

# Quantification of cloud water interception along the windward slope of Santa Cruz Island

# Quantification of cloud water interception along the windward slope of Santa Cruz Island\*

---

## Abstract

The Galapagos Archipelago is nearly devoid of freshwater resources, but during six months of the year, a fog layer covers the windward slopes of the main islands. In order to investigate the hydrological importance of this phenomenon, a monitoring network was set up on Santa Cruz Island, at the center of the archipelago. Meteorological parameters were monitored together with throughfall and stem-flow at two stations: a first in a secondary forest at the lowest fringe of the fog layer (400 m a.s.l.), and a second in shrub lands of the Galapagos National Park, at the center of the fog layer (650 m a.s.l.). Cloud water interception was quantified from the wet canopy water budget, based on a modified *Rutter*-type canopy interception model. This methodology allowed the estimation of fog interception for short time intervals (15 min) and exonerated from the subjective segregation into rainfall events. Fog was found to be a negligible water input at the lower site, but contributed to  $22 \pm 12\%$  of water inputs at the higher site at the center of the cloud. Wind was shown to enhance fog interception but could not explain alone the difference in fog catch between the two sites, which was attributed to higher liquid water content and more frequent fog occurrence. This study highlights that the presence of fog may induce a marked increase of net precipitation, but this effect is restricted to the summit areas blown by winds, at the center of the cloud.

---

\* In collaboration with Christian Domínguez<sup>1</sup>, Pilar Fuente Tomai<sup>2</sup>, Cédric Chaumont<sup>3</sup>, Noémi d'Ozouville<sup>4</sup>, Marcos Villacís<sup>1</sup>, Sophie Violette<sup>4</sup>. Published in *Agricultural and Forest Meteorology*, Volume 161, August 2012, Pages 94-106, <http://dx.doi.org/10.1016/j.agrformet.2012.03.018>.

<sup>1</sup>*Department of Civil and Environmental Engineering, National Polytechnic School, Quito, Ecuador*

<sup>2</sup>*Department of Silviculture and Pastures, Forest Engineering School, University Polytechnic of Madrid, Spain*

<sup>3</sup>*CEMAGREF Antony, France*

<sup>4</sup>*UPMC Univ. Paris 6 & CNRS, UMR Sisyphe, 4 place Jussieu, 75252 Paris cedex 05, France*

## 6.1 Introduction

The interception of wind-blown droplets of water by the vegetation, commonly called *cloud water interception* (*CWI*) can be a significant input to the canopy water budget. Previous studies reported fog contributions ranging between 2% and 45% of incident annual rainfall [Bruijnzeel, 2001; Bruijnzeel et al., 2011]. This phenomenon occurs during conditions of low vapor pressure deficits and weak solar radiation and is therefore associated with limited potential evapotranspiration [Bruijnzeel, 2001; Ritter et al., 2009]. Together, these processes provide optimal conditions for groundwater recharge and streamflow generation. Climate change could result in a raising of cloud base [Foster, 2001; Still et al., 1999]. Deforestation may reduce cloud occurrence, and cloud water interception by the vegetation [Brauman et al., 2010; Bruijnzeel, 2001; Lawton et al., 2001]. For regions where water resources are limited and fog occurrence is frequent, it is of the highest importance to quantify fog interception and identify its controlling processes [Bruijnzeel et al., 2011].

Air liquid water content, wind speed, and canopy structure have been identified as the main driving factors of fog interception [Bruijnzeel, 2001; Bruijnzeel et al., 2005]. *CWI* can not be measured directly, because rain gauges do not intercept horizontal wind-blown droplets of water, while artificial fog gauges do not provide a direct quantification of *CWI* by the vegetation [Holwerda et al., 2006a, 2011]. The quantification of *CWI* thus requires the measurement of throughfall and stemflow, the two components of net precipitation, along with wet canopy evaporation. The direct measurement of evaporation remains challenging even with sophisticated eddy-covariance instrumentation [Gash et al., 1999; Holwerda et al., 2012]. Recent advances have presented the wet canopy water budget as the most promising method to quantify fog interception [Bruijnzeel et al., 2011; Holwerda et al., 2006a]. This method uses the difference between measured and modelled net precipitation to quantify cloud water interception. Recent applications are numerous, most of them are based on *Gash*-type [Gash, 1979], event-based interception models (e.g. Giambelluca et al. [2011]; Holwerda et al. [2010a, b]; McJannet et al. [2007b] and Muñoz-Villers et al. [2011]), few of them used a *Rutter*-type [Rutter et al., 1972], running water budget interception model (e.g. Takahashi et al. [2011]).

The occurrence of fog is reported in many oceanic islands and has been investigated by several recent studies such as in Hawaii (US) [Brauman et al., 2010; Giambelluca et al., 2011; Takahashi et al., 2011], La Réunion Island (France) [Gabriel and Jauze, 2008], Madeira Island (Portugal) [Prada et al., 2009], and Canary Islands (Spain) [García-Santos and Bruijnzeel, 2011].

In the Galapagos Islands, a semi-permanent fog layer covers the highlands during the cool *garúa* season, from June to December [Trueman and d'Ozouville,

## 6. QUANTIFICATION OF CLOUD WATER INTERCEPTION

---

2010]. The fog has been shown to have an effect on local ecosystems [Jäger *et al.*, 2009], but its contribution to the water budget has never been investigated. As described by pioneering authors, the archipelago is nearly devoid of freshwater [Darwin, 1859; Porter, 1815]. With the rapid human population growth related to the tourism industry, there is an increasing demand for freshwater. The current situation is critical and local population relies on expensive desalination techniques [d'Ozouville, 2007a, b; INEC-CGG, 2010]. There is a need for a better understanding of the local hydrology.

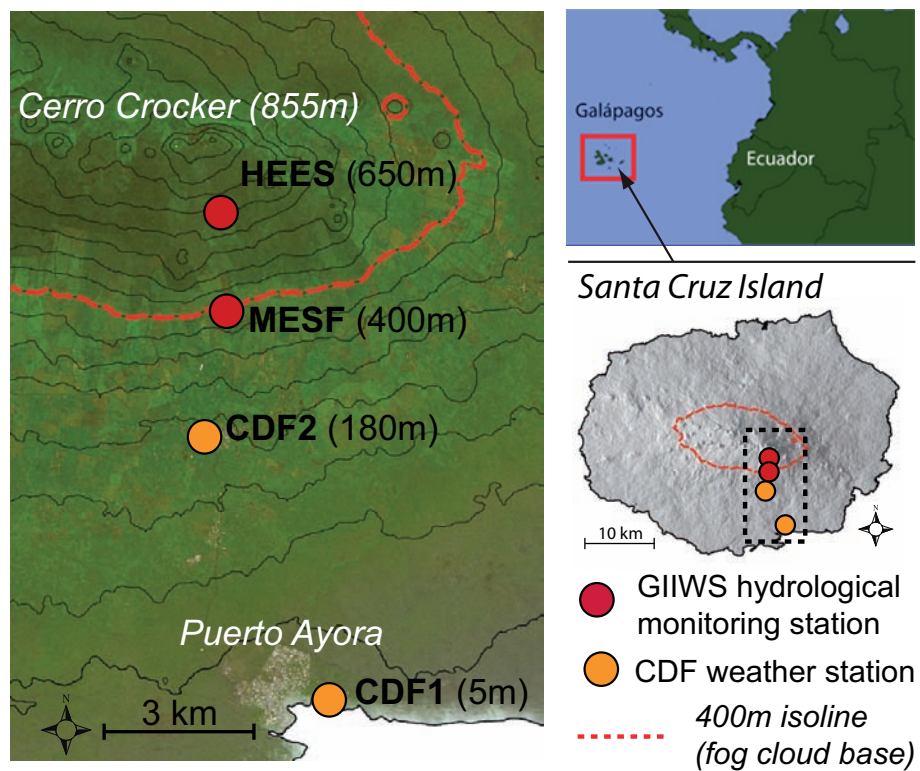
This paper presents the results of investigations performed along the windward side of Santa Cruz Island during the 2010 fog *garúa* season, and provides the first quantitative estimation of fog interception in the Galapagos Archipelago.

### 6.2 Study Area

#### 6.2.1 Regional climatic context

The Galapagos Islands lie 1000 km west of the South-American coasts in the Pacific Ocean, straddling the Equator. The climate is oceanic, with sea surface and air temperatures being anomalously low due to upwelling of the cold Equatorial and *Humboldt* ocean-currents [Eden and Timmermann, 2004]. Extreme inter-annual climatic variations observed in the islands are related to the *El Niño Southern Oscillation* (ENSO). The *El Niño* events are expressed by marked increase in precipitations while their opposite counterparts, the *La Niña* events, are characterized by a drop in precipitation and often correspond to years of drought [Snell and Rea, 1999].

Similarly to the situation in the Hawaiian Archipelago [Giambelluca and Nullet, 1991; Kolivras and Comrie, 2007; Nullet *et al.*, 1995], the orographic lifting of moist air driven by trade-winds induces clear discrepancies between the humid windward slopes subjected to orographic precipitation, and the arid leeward slopes deprived of water by the rain shadow effect. Seasons alternate between a hot *invierno* season (January to May) and a cooler *garúa* season (June to December). During the hot *invierno* season, rainfall is convective, with the amount of precipitation positively correlated with sea surface temperatures [Trueman and d'Ozouville, 2010]. During the cool *garúa* season, an inversion layer is formed, which hampers the further rise of moist air and leads to the formation of fog in the highlands. This phenomenon is observed on all the islands above ca. 400 m a.s.l. [Sachs and Ladd, 2010; Trueman and d'Ozouville, 2010]. Current meteorological patterns in the Galapagos may be affected in future by the consequences of climate change [Sachs and Ladd, 2010]. The frequency of fog occurrence could be reduced and the cloud base level raised. However, another possibility is more



## 6. QUANTIFICATION OF CLOUD WATER INTERCEPTION

frequent occurrence of the *La Niña* anomalies, which favor fog occurrence.

### 6.2.2 Climatic and vegetation zonation of Santa Cruz Island

Santa Cruz island lies at the center of the archipelago (Fig. 6.1), it is the second largest (986 km<sup>2</sup>) and the most populated island with officially 13,000 inhabitants [INEC-CGG, 2010]. It is the center of touristic activity in the archipelago, which receives a yearly flux of 173,000 tourists [PNG, 2010]. Santa Cruz is characterized by a broad low elevation coastal apron surrounding a main central shield culminating at *Cerro Crocker*, 855 m a.s.l. [d’Ozouville et al., 2008b].

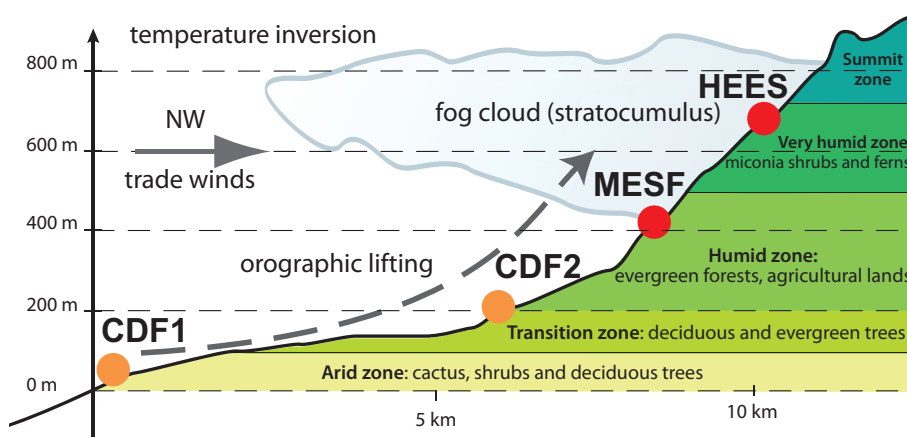


**Figure 6.2:** Vegetation zonation along the windward slope of Santa Cruz island after Hamann [1979]. The four weather stations (CDF1, CDF2, MESF, HEES) highlight the contrasting climatic conditions at the origin of the vegetation zonation.

Two long-term weather stations are operated by the *Charles Darwin Foundation* (CDF). The first (hereafter called CDF1) is located in Puerto Ayora (5 m a.s.l.) and the second (hereafter called CDF2) in Bellavista (alt. 180 m a.s.l.) (Fig. 6.1). They have been operational since 1964 and 1987, respectively. Recorded median annual rainfall totals are 277 mm and 800 mm, respectively. The coastal station (CDF1) receives the major part of annual precipitation during the convective rains of the hot *invierno* season. This is the opposite at the second station, where most of the rainfall is recorded during the cool *garúa* season [Trueman and d’Ozouville, 2010]. As described by the seasonal isohyet maps proposed by Trueman and d’Ozouville [2010], the spatial distribution of rainfall

varies with seasons. Due to the orographic effect, contrasts are more acute during the *garúa* season, when the fog layer is observed along the windward slope from 300-400 m a.s.l. up to the summit [Trueman and d'Ozouville, 2010]. The summit area occasionally remains clear of clouds, but the upper limit of the fog layer (the inversion layer) is most often above the top of the island.

These contrasting climatic and physical conditions have induced a pronounced vegetation zonation along the windward side of the island (Fig. 6.2) [Hamann, 1979]. From the coast up to 50 m a.s.l., conditions are arid, spiny shrubs and cactuses dominate. Between 50 m and 200 m a.s.l., vegetation progressively evolves to forests and soils are deeper. The humid zone extends from 200 to 450 m a.s.l. and was originally covered by the endemic *Scalesia* tree [Hamann, 1979]. With the development of agriculture, the endemic forest has been replaced by alternates between pasture and secondary forest made up mainly by introduced trees species (*Psidium guajava*, *Cedrela odorata*, *Cinchona pubescens*). The very humid zone extends above 450 m a.s.l., soils are shallower and fractured basalt outcrops. The vegetation cover is composed of ferns and the endemic *Miconia robinsoniana* shrub. The area has been invaded by the *Cinchona pubescens* introduced in the 1940s [Jäger et al., 2009], but several control programs have markedly reduced its expansion. In the summit area, shrubs become scarce, fern and sedges dominate. Territories of the *Galapagos National Park* (GNP) extend from the top of the humid agricultural zone (ca. 450 m a.s.l.) up to the summit of the island, they are devoid of any agricultural activity.

Within the area covered by fog during the *garúa* season (i.e. from ca. 400 m a.s.l. to the summit), the vegetation of Santa Cruz Island presents typical characteristics of montane cloud forests [Bruijnzeel et al., 2011; Stadtmüller, 1987], with frequent vascular epiphytes and an abundance of non-vascular epiphytes (mosses) covering branches [Hamann, 1979]. In the Galapagos Islands, fog occurs from a relatively low elevation with respect to other montane cloud forests [Scatena et al., 2010]. Given that trees and shrubs have a relatively short stature, the montane cloud forest of Santa Cruz Island area may therefore be classified as a *low-elevation elfin cloud forest* [Bruijnzeel et al., 2011; Scatena et al., 2010].

### 6.2.3 The two study plots

A first site (hereafter called MESF) was located at Mid-Elevation (400 m a.s.l.) beneath a Secondary Forest in the agricultural zone, where the dominant tree species are *Psidium guajava*, *Cestrum auriculatum*, and *Cinchona pubescens*. A second site (hereafter called HEES), was located at High-Elevation (650 m a.s.l.) beneath Endemic Shrubs (*Miconia robinsoniana*) of the very humid zone in the GNP park area (Figs. 6.1 and 6.2). At both sites, slopes are facing a south-

## 6. QUANTIFICATION OF CLOUD WATER INTERCEPTION

---

south-east direction, but the slope is steeper at the HEES site (15°) than at the MESF site (10°) (Table 6.1).

Parameter	MESF	HEES
Long/Lat	90.32° W/0.67° S	90.32° W/0.65° S
Altitude [m a.s.l.]	400	650
Slope	10°	15°
Aspect	170° E	160° E
Mean soil depth (range) [cm]	40 (8;90)	20 (5;30)
Vegetation type	Secondary forest	Evergreen shrub
Dominant tree species	<i>Psidium guajava</i>	<i>Miconia robinsoniana</i>
Mean canopy height [m]	5.45	2.8
Basal area [m <sup>2</sup> /ha]	29.8	-
Stem density [stems/ha]	3550	-
LAI	4	2.7
Canopy gap fraction	19%	26%

**Table 6.1:** Physical conditions and characteristics of the vegetation at the two study plots. LAI and gap fractions were computed with the methodology described by *Macfarlane et al.* [2007].

Throughfall and stemflow measurements were performed within 6x6 m plots beneath vegetation canopy, while other meteorological instruments were installed in open areas in the vicinity. The interception of fog and wind-blown rain is known to be enhanced at the windward edges of vegetation patches [*Bruijnzeel et al.*, 2006; *Weathers et al.*, 1995]. The location of each plot was chosen for measurements within the plots to be representative of the corresponding vegetation zones. The secondary forests of the agricultural zone occur in relatively large patches on gently sloping terrain, so that only a very limited portion of these forests is directly exposed to winds. The MESF plot was therefore located at



**Figure 6.3:** The two instrumented study plots: secondary forest at the MESF plot (top) and the endemic *Miconia robinsoniana* shrubs at the HEES plot (bottom). Throughfall troughs drain into automatic tipping bucket gauges. Manually read throughfall and stemflow collectors were present at both plots but are only visible at the MESF plot (top panel, red and white arrows, respectively)

## 6. QUANTIFICATION OF CLOUD WATER INTERCEPTION

---

the center of a relatively large (ca. 16 ha) forested patch, 40 m from a neighboring pasture. In contrast, the *Miconia* shrubs of the very humid zone grow on steeper slopes and form small patches varying in height. As a large proportion of the shrubs have a side exposed to winds, the HEES plot was located beneath a *Miconia* shrub with its southern edge exposed to winds.

Canopy coverage was characterized from photographs taken vertically [Dunkerley, 2010]. A sufficient number of pictures were taken so as to cover fully the canopy overlying the study plots. These images were processed and converted into binary mode. The gap fraction of the canopy was estimated from the proportion of black pixels [Llorens and Gallart, 2000; Macfarlane et al., 2007]. The leaf area index (LAI) was obtained from the methodology described by Macfarlane et al. [2007]. For the albedo of the MESF plot, the value estimated by Giambelluca et al. [1999] for a secondary forest in northern Thailand was used (0.13). For the HEES plot, a value of 0.10 was assumed, as measured by Holwerda [2005] for a 2 m tall evergreen elfin cloud forest in Puerto Rico.

### 6.3 Materials and methods

#### 6.3.1 Climate

Weather stations were placed in clearings close to the study plots (less than 100 m), but sufficiently distant to avoid perturbations. Measurements in open areas included rainfall, air temperature and relative humidity, wind speed and solar radiation. These variables were assumed to be representative of the conditions at the top of the canopy and were used for the estimation of potential evaporation (see Section 6.3.3 for details).

At the MESF plot, meteorological instruments were placed in a pasture adjacent to the forest, where the height of the grass varied between 0.4 m and 1 m. Solar radiation, relative humidity and temperature were measured at ca. 2 m above the ground, respectively, with a Kipp&Zonen SPLite silicone pyranometer and a Campbell CS215 T&RH sensor. Wind speed and direction were monitored with a Young WindSentry Kit composed of a cup anemometer and a vane positioned at 3.4 m above the ground. These instruments were connected to a Campbell CR1000 datalogger. At the HEES plot a HOBO Micro-Station was installed in a cleared area covered by short ferns, with the temperature probe at 2 m, the solar radiation sensor and the wind speed and direction sensors at 3 m.

At both plots, precipitation was measured with Campbell ARG100 tipping bucket rain gauges, placed at 1 m above the vegetation. Following the methodology described by Calder and Kidd [1978], precipitation data were corrected for losses during bucket rotation using dynamic calibration at the laboratory. The

relatively low wind speeds and the aerodynamic profile of the ARG100 rain gauge did not justify a correction for wind losses [Frumau *et al.*, 2011]. The two plots were located in sloping terrain with dominant winds trending perpendicular to the slope, the correction coefficient proposed by Sharon [1980] was applied following the procedure detailed by Ritter *et al.* [2008].

To compare the intensity of fog interception at the two sites, two identical cylindrical fog gauges (height 40 cm, 12 cm in diameter) made of a fine plastic mesh (1 mm) were placed at ca. 2 m above the ground in the clearings. Intercepted water was collected with a funnel at the base of the cylinder and diverted to a plastic container.

### 6.3.2 Throughfall and stemflow

Due to the existence of dripping points and shaded drier areas, the spatial variability of throughfall is usually high. To limit sampling error, an appropriate sampling scheme must be implemented [Staelens *et al.*, 2006; Zimmermann *et al.*, 2010]. Throughfall was measured using two sampling designs [Domínguez González, 2011]: (1) a continuous record from a set of troughs draining into a tipping bucket gauge, and (2) manually read small collectors [Holwerda *et al.*, 2006b; Ziegler *et al.*, 2009].

The troughs were made of 3m long PVC pipes of diameter 15 cm cut in half. To facilitate drainage, they were inclined at an angle greater than  $15^\circ$  from the horizontal. A set of 4 troughs were installed at the MESF plot (collection area of  $1.8 \text{ m}^2$ ), while only 3 troughs could be fitted underneath the shrubs of the HEES plot (collection area of  $1.3 \text{ m}^2$ ) (Fig. 6.3). Collected water was directed to a modified ARG100  $10 \text{ cm}^3$  tipping bucket rain gauge. This instrumentation was calibrated in the field at a static rate with the following procedure. The troughs were initially wetted to avoid water storage. A precise amount of water was then dispersed over the troughs at a constant rate, and bucket tips were recorded until complete drainage. Water was poured at a rate of ca.  $1 \text{ mm h}^{-1}$ , which is close to the observed median rainfall rate, and sufficiently small to neglect losses from bucket rotation. For both plots, the amount of water measured by the tipping bucket was ca. 10% smaller than the amount added. These losses were attributed to evaporation and splash from the tipping bucket, and could also be the consequence of a slight deviation of the tipping-bucket leveling. This correction factor derived from static field-calibration was applied to all throughfall data measured by the troughs. A correction derived from dynamic calibration of the ARG100 tipping bucket in the laboratory was applied, but given the weak intensity of throughfall during the period of investigation, this correction had only a negligible effect.

## 6. QUANTIFICATION OF CLOUD WATER INTERCEPTION

---

Water collected by the troughs was directed to a single automatic gauge, so that sampling error could not be inferred from these measurements. To this effect, small collectors were built from funnels 25 cm in diameter placed over 5-L containers. 33 collectors (total area of 1.6 m<sup>2</sup>) were distributed randomly at the MESF plot while only 13 collectors (total area of 0.6 m<sup>2</sup>) could be installed at the HEES plot [Domínguez González, 2011]. The arrangement of these collectors remained fixed during the period of interest, measurements were performed manually, as far as possible after each precipitation events. Yet, difficulties of access to the field limited the number of readings.

Assuming throughfall spatial distribution to be random, relative sampling error expressed as percentage of the mean reads (e.g. *Holwerda et al.* [2006b]; *Kimmins* [1973]; *Thimonier* [1998]):

$$r_{se} = \frac{t_{\alpha, N-1} CV}{\sqrt{N}} \quad (6.1)$$

where  $t_{\alpha, N-1}$  is the Student's t-value at the  $\alpha$  level,  $N$  the number of collectors, and  $CV$  the coefficient of variation. Though throughfall collectors had different shapes (linear for troughs, and circular for small manual collectors), sampling total areas were similar for both collection methods, and sampling errors of trough measurements were inferred from  $r_{se}$  for the manual gauges. This is expected to overestimate trough sampling error since trough sampling area were somewhat larger than total collector area.

Stemflow was measured on each tree trunk within the MESF and HEES plots (26 and 12 trees, respectively). The stems were first cleaned of epiphytes and mosses in the area where the collecting spiral was to be installed. Stemflow collection was performed following a methodology similar to *Crockford and Richardson* [2000] and *McJannet et al.* [2007b]. At 0.5-1.0 m above the ground, a split plastic hose (internal diameter 15 mm) was attached with staples to the stem following a spiral and then sealed with silicone. Containers of 2 L capacity were used to collect the water, and were emptied after weighing using a portable electronic scale each two-three days. All the 26 tree trunks of the MESF plot, and all the 12 shrub stems of the HEES plot were instrumented. Although a few trees extended outside of the surface of the plot, this was most probably compensated by other trees with crowns overlapping the plot. Stemflow was converted to equivalent depth of water by dividing the total volume of water by the surface of the plot.

### 6.3.3 Interception model

Canopy evaporation and drainage were estimated with a modified *Rutter* model for interception losses [*Rutter et al.*, 1972, 1975; *Valente et al.*, 1997]. Contrary

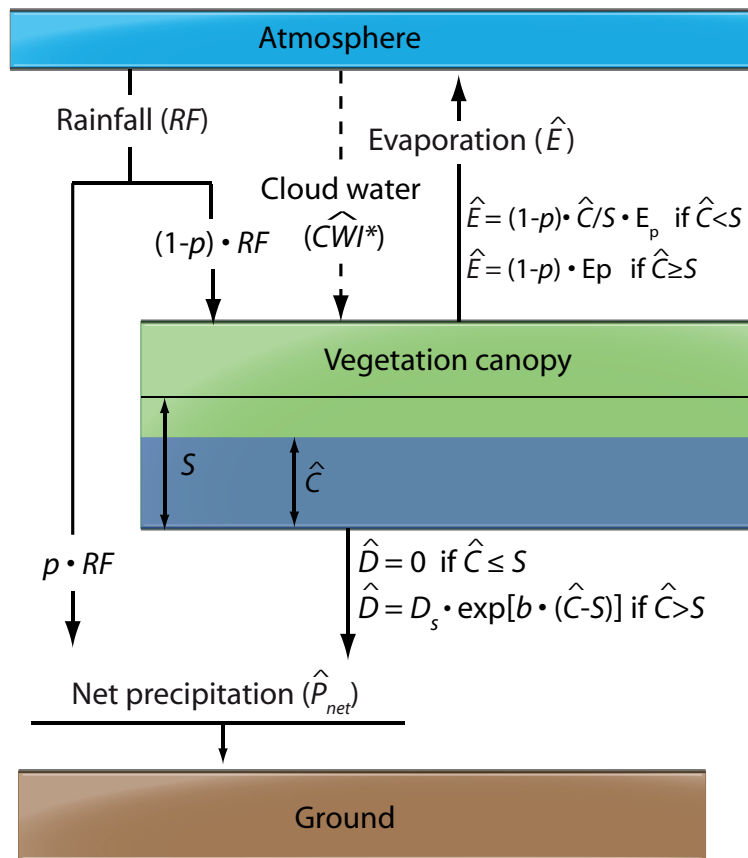


**Figure 6.4:** Schematic summary of the modified Rutter interception model [*Rutter et al.*, 1972, 1975; *Valente et al.*, 1997] with drainage function from *Gash and Morton* [1978].

## 6. QUANTIFICATION OF CLOUD WATER INTERCEPTION

---

to the *Gash*-type models [*Gash*, 1979], *Rutter*-type models are based on a running water balance and do not require the separation of the period of interest into individual rainfall events [*Muzylo et al.*, 2009]. The interception model was implemented with the software R [*R Development Core Team*, 2009].

All variables referring to a water storage, or flux, were expressed as depth of water over the whole plot area. For each time step, the canopy water storage  $\hat{C}$  is recharged by the amount of rainfall ( $RF$ ) intercepted by the canopy,  $(1-p) \times RF$ , where  $p$  is the free throughfall coefficient. The input from fog interception, which remains unknown at this point is not considered yet. Given the small amount of water diverted by stemflow in our study plots and the difficulties to implement a constant monitoring, the separated compartments for trunk water storage and evaporation introduced by *Rutter et al.* [1975] and *Valente et al.* [1997] were not included in this model. Estimates of canopy drainage ( $\hat{D}$ ) included both throughfall and stemflow. An exponential function was used to calculate drainage from the canopy [*Gash and Morton*, 1978; *Schellekens et al.*, 1999]:

$$\hat{D} = \begin{cases} D_s \times \exp[b(\hat{C} - S)] & \text{if } \hat{C} > S \\ 0 & \text{if } \hat{C} \leq S \end{cases} \quad (6.2)$$

where parameters  $S$  [mm],  $D_s$  [mm h<sup>-1</sup>] and  $b$  [mm<sup>-1</sup>] are characteristic for the canopy.  $S$  is the amount of water stored by the canopy that will not drip to the ground, defined as *adherent storage capacity* by *Liu* [2001]. Adherent storage is opposed to transient storage, the amount of water temporarily stored by the canopy which finally drips to the ground. In accordance with these definitions, drainage is set to zero when  $\hat{C} \leq S$  [*Gash and Morton*, 1978; *Schellekens et al.*, 1999].

The estimate of evaporation from the canopy was obtained following the scheme of the *sparse* version of the *Rutter* model [*Valente et al.*, 1997]. In this version, only evaporation from the canopy cover is considered and any understorey evaporation is neglected. When the canopy is saturated ( $\hat{C} \geq S$ ), estimated actual evaporation ( $\hat{E}$ ) reaches potential evaporation,  $\hat{E} = (1-p) \times E_p$ . For unsaturated canopy ( $\hat{C} < S$ ),  $\hat{E}$  is considered to be proportional to the canopy saturation ratio  $\hat{C}/S$ , which reads [*Klaassen*, 2001; *Rutter et al.*, 1975; *Valente et al.*, 1997]:

$$\hat{E} = \begin{cases} (1-p) \times E_p & \text{if } \hat{C} \geq S \\ (1-p) \times \hat{C}/S \times E_p & \text{if } \hat{C} < S \end{cases} \quad (6.3)$$

where  $E_p$  was estimated with the Penman-Monteith (P-M) equation with the surface resistance set to zero [*Monteith*, 1965]. Net long-wave radiation was not con-

sidered in the calculation, which is a common assumption in the context of dense fog [Holwerda *et al.*, 2010a; Muñoz-Villers *et al.*, 2011; Wallace and McJannet, 2006]. For moderate wind speeds, aerodynamic resistance  $r_a$  of wet vegetation may be estimated from Rutter *et al.* [1972, 1975]:

$$r_a = \frac{1}{k^2 u_z} \cdot \left( \ln \left( \frac{z-d}{z_0} \right) \right)^2 \quad (6.4)$$

where  $k = 0.4$  is the von Karman constant,  $u_z$  is wind speed and  $z$  its measurement height.  $z_0$  is the roughness length and  $d$  the zero plane displacement. For both stands, it was assumed that  $d = 0.75 \cdot h$  and  $z_0 = 0.1 \cdot h$ , which are the values stated by Rutter *et al.* [1975] for leafy vegetation. Temperature, relative humidity and wind speed measured at the weather station in the clearings were assumed to be representative of the conditions at 2 m above the instrumented canopy. Pearce *et al.* [1980] showed that this assumption could induce an overestimation of potential evaporation, but this effect will be supposed to be of limited effect in the present study, since canopy heights were relatively small and meteorological variables were taken close to the forested plots. Values of relative humidity were not available at the HEES plot (cloud center), values from the MESF plot (cloud base) were used for the calculations. This is not expected to induce a significant overestimation of evaporation at the HEES plot, since relative humidity at the MESF plot was often at, or close to 100%. Given these assumptions, the estimation of  $r_a$  may be inaccurate but the estimation of potential evaporation should remain relatively fair, since the radiative term is expected to dominate evaporation from a wet canopy in contexts of small vapor pressure deficit and limited wind speeds [Holwerda *et al.*, 2010a; Klaassen, 2001].

A schematic summary of the canopy water budget model is presented in Fig. 6.4. In the absence of cloud water interception, the wet canopy water budget equation can be written as follows:

$$RF = \hat{P}_{net} + \hat{E} + \Delta \hat{C} \quad (6.5)$$

where net precipitation  $\hat{P}_{net}$  reads:

$$\hat{P}_{net} = (p \times RF) + \hat{D} \quad (6.6)$$

Canopy parameters  $p$ ,  $S$ , have been estimated from a carefully chosen set of rainfall events. These events had to be compatible with the definition given by Gash [1979]: a fully dry canopy at the beginning of the event, rainfall at a constant rate, and termination of the event at the end of dripping from the canopy. Furthermore, it was essential to select events where cloud interception was negligible. We therefore selected events with the lowest ( $TF/RF$ ) ratios, where  $TF$  is measured throughfall. The *within-event analysis* detailed by Link

## 6. QUANTIFICATION OF CLOUD WATER INTERCEPTION

---

*et al.* [2004] was implemented. The principles are relatively straightforward: at the beginning of an event, the canopy is dry and net precipitation is limited to the fraction of rain passing through canopy gaps. If we neglect evaporation during rainfall, we can write  $P_{net,cum} = p \times RF_{cum}$  where  $P_{net,cum}$  is cumulative net precipitation and  $RF_{cum}$  is cumulative rainfall. Once the canopy is saturated ( $\hat{C} = S$ ), net precipitation rate becomes close to the rainfall rate. The cumulative curve of net precipitation becomes steeper and we can write  $P_{net,cum} = -S + RF_{cum}$ . Considering the plot of cumulative net precipitation against cumulative gross precipitations, the parameters  $p$  and  $S$  can be estimated from two linear regressions. Parameter  $p$  is the slope of the first regression line before the slope break (before saturation of the canopy). Like *Takahashi et al.* [2011],  $S$  was inferred from the x-intercept of the second regression line, after the slope break (i.e. once the canopy is saturated).

The parameters  $D_s$  and  $b$  were estimated by non-linear least square optimization of the RMSE between modeled net precipitation ( $\hat{P}_{net} = \hat{D} + (p \times RF)$ ) and observed net precipitation ( $P_{net}$ ) at a 15-min time step.

Given the limited variability of canopy structure in this study, the interception model parameters characterizing the canopy ( $p$ ,  $S$ ,  $D_s$ ,  $b$ ) have been considered constant throughout the investigation period.

### 6.3.4 Cloud water interception

The interception model is first run considering only rainfall as input (Eq. 6.5). The initial estimate of cloud water interception ( $\widehat{CWI}_0$ ) is deduced as follows:

$$\widehat{CWI}_0 = P_{net} - \hat{P}_{net,1} \quad (6.7)$$

where  $P_{net}$  is observed net precipitation and  $\hat{P}_{net,1}$  is the predicted value after the first run of the interception model. The term  $\widehat{CWI}_0$  explains the difference between measured net precipitation ( $P_{net}$ ) affected by  $CWI$  and the predicted value ( $\hat{P}_{net,1}$ ), where  $CWI$  has been disregarded [*Holwerda et al.*, 2010a; *McJannet et al.*, 2007b; *Takahashi et al.*, 2011]. Considered over the whole period of interest, the water budget considering measured net precipitation reads:

$$RF_{cum} + \widehat{CWI}_{0,cum} = P_{net,cum} + \hat{E}_{1,cum} \quad (6.8)$$

where  $RF_{cum}$  and  $P_{net,cum}$  are measured cumulative rainfall and net precipitation, respectively, while  $\widehat{CWI}_{0,cum}$  and  $\hat{E}_{1,cum}$  are the first estimates of cumulative  $CWI$  and evaporation, respectively.

If  $CWI$  is negligible,  $\widehat{CWI}_{0,cum}$  should be around zero over the period of interest. With  $CWI$  occurrence,  $\widehat{CWI}_{0,cum}$  should be clearly positive. Yet, any time

lag between rainfall and throughfall may cause  $\widehat{CWI}_0$  values to be underestimated or even to become negative, which is not realistic. In order to reduce the occurrence of negative values, the time series is smoothed with a 1.75 h ( $7 \times 15$  min) moving average filter [Takahashi *et al.*, 2011]. Unless the evaporation estimate is inaccurate, the remaining negative values should then be in limited numbers and are set to zero. The smoothed, corrected estimate of  $CWI$  is written  $\widehat{CWI}_0^*$ . Setting negative values to zero introduces an error in the water balance (Eq. 6.8). The estimate of  $CWI$  is therefore adjusted:

$$\widehat{CWI}_1^* = k_1 \times \widehat{CWI}_0^* \quad (6.9)$$

where  $k_1$  reads:

$$k_1 = \frac{\left(P_{net,cum} + \hat{E}_{1,cum} - RF_{cum}\right)}{\widehat{CWI}_{0,cum}^*} \quad (6.10)$$

When the input from  $CWI$  is significant, the estimate of evaporation from the first run ( $\hat{E}_1$ ) may underestimate actual evaporation [Takahashi *et al.*, 2011]. An iterative approach is then implemented to improve the estimates of evaporation and  $CWI$ . For  $i \geq 2$ , both measured rainfall ( $RF$ ) and estimated fog interception ( $\widehat{CWI}_{i-1}^*$ ) are considered for the calculation of canopy water storage ( $\hat{C}_i$ ). The interception model water budget (Eq. 6.5) is therefore modified:

$$RF + \widehat{CWI}_{i-1}^* = \hat{P}_{net,i} + \hat{E}_i + \Delta\hat{C}_i \quad (6.11)$$

where  $i \geq 2$  is the model run number, and  $\hat{P}_{net,i}$ ,  $\hat{E}_i$  and  $\hat{C}_i$ , are the corresponding estimates of net precipitation, evaporation, and canopy water storage, respectively. After each run of the interception model, the estimate of  $CWI$  is updated from a generalization of Eqs. 6.9 and 6.10 with:

$$k_i = \frac{\left(P_{net,cum} + \hat{E}_{i,cum} - RF_{cum}\right)}{\widehat{CWI}_{i-1,cum}^*} \quad (6.12)$$

The adjustment factor  $k_i$  should become close to one after a certain number of runs (say  $i = n$ ). Further runs of the interception model don't change significantly the estimate of  $CWI$ , which can be considered as satisfactory. The finalized estimate of cloud water interception,  $\widehat{CWI}_n^*$  is written  $\widehat{CWI}^*$ .

The error of  $CWI$  depends on measurement and sampling errors for rainfall, stemflow, throughfall, temperature, solar radiation, wind speed, and relative humidity. Furthermore, it depends on the validity of the assumptions and the choice of the parameters used for the interception model. In a first attempt to characterize the error on  $CWI$ , only the sampling error on net precipitation and

---

## 6. QUANTIFICATION OF CLOUD WATER INTERCEPTION

---

the calibration error of the interception model are considered. Assuming both errors to be independent, the total uncertainty of  $\widehat{CWI}^*$  reads:

$$\epsilon(\widehat{CWI}^*) = \sqrt{\epsilon(P_{net})^2 + \epsilon(\hat{P}_{net})^2} \quad (6.13)$$

where the error of measured net precipitation is restricted to the throughfall sampling error (Eq. 6.1),  $\epsilon(P_{net})^2 = r_{se} \cdot TF$ , where  $TF$  is measured throughfall. The error in modeled net precipitation is estimated from the RMSE of the calibration dataset,  $\epsilon(\hat{P}_{net})^2 = n \cdot (RMSE)^2$  where  $n$  is the number of 15-min estimates.

## 6.4 Results

### 6.4.1 Climatic conditions

The 2010 *garúa* fog season extended from end of June to December and was characterized by low temperatures and weak continuous rainfalls (Fig. 6.5 A). With respect to long term conditions recorded at station CDF2 (1987-2010), precipitation remained close to the median in 2010 but temperatures were lower due to the *La Niña* anomaly [*National Weather Service Climate Prediction Center, 2011*] (Fig. 6.5 B).

The MESF station was operational from July 2010 onwards, but due to difficulties with setting up the HEES station, simultaneous records were only available from September 2010 onwards. Very humid conditions together with difficulty of access made the acquisition of continuous records challenging. Yet, seventy-five days with complete, quality-checked data for the two stations were obtained. Given the relatively stable climatic conditions during the *garúa* season, the current dataset can be considered as being representative for the whole 2010 *garúa* season.

Air temperature at the MESF station was 17.5°C on average, which is 2°C higher than at the HEES station. Solar radiation was comparable at the two stations, and remained low throughout the season (daily average close to 100 W m<sup>-2</sup>). Due to the observed dense cloud cover, median relative short wave radiation was close to 30% of theoretical clear-sky radiation. As may be expected in these conditions, relative humidity was for much of the time at or close to 100% at the MESF plot. Though not measured at the HEES plot, relative humidity could only be higher there due to more frequent fog occurrence. Wind speed was relatively weak at the MESF station, with a mean of 0.9 m s<sup>-1</sup>. Wind speed was significantly higher at the HEES plot, with a mean of 2 m s<sup>-1</sup>. Rainfall records at stations CDF2, MESF and HEES highlight the marked orographic effect (Fig. 6.6). During simultaneous monitoring at both stations (75 days), total rainfall

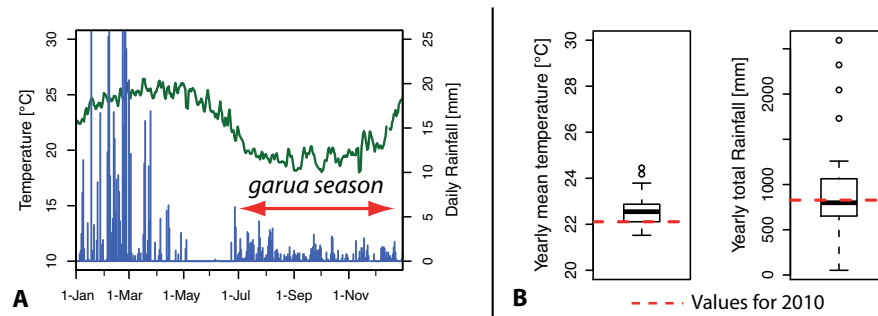


**Figure 6.5:** (A) Temperature and rainfall recorded at station CDF2 (Alt. 180 m a.s.l.) in 2010. Low temperatures and continuous low-intensity rainfalls characterize the *garúa* season (red arrow). (B) 2010 context compared to 1985-2010 long-term records. It was a relatively cooler year due to the *La Niña* anomaly (left), while total rainfall remained close to the annual median (right).

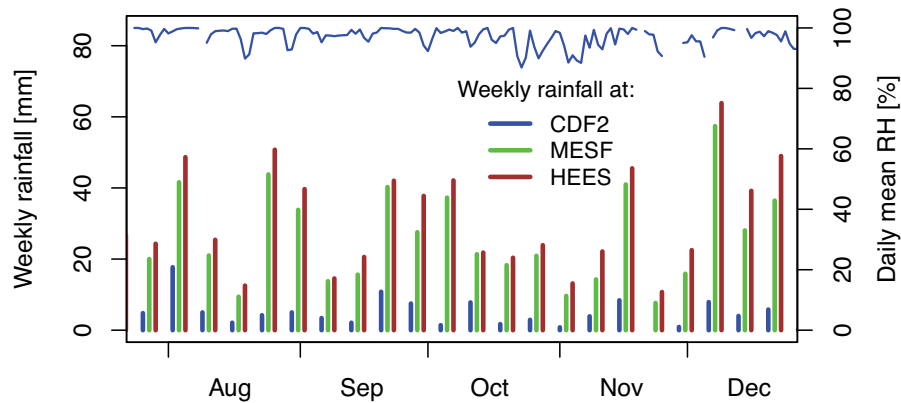


**Figure 6.6:** Weekly rainfall records for CDF2, MESF and HEES stations during the 2010 *garúa* fog season highlight the marked orographic effect. Mean daily relative humidity at the MESF station remained close to saturation.

## 6. QUANTIFICATION OF CLOUD WATER INTERCEPTION

---

was 238 mm at the MESF station, and 313 mm at HEES station (28% higher). Median precipitation rates were small at both of the stations, 0.8 mm h<sup>-1</sup> and 1.1 mm h<sup>-1</sup> respectively. Daily rainfall totals at the two stations were highly correlated ( $RF_{HEES} = 1.11 \cdot RF_{MESF} + 0.34$ , with  $r^2 = 0.89$  and  $n = 104$ ). This allowed the filling of short data gaps (of a few days).

Water collected by fog gauges could not be recorded continuously and may therefore not be fully representative of the whole period of interest. Yet, during a simultaneous recording period of 15 days, water collected by the fog gauges at the HEES plot was 5 times higher than at the MESF plot. During this recording period, rainfall total at the uppermost HEES station was only 25% higher than at the MESF station. The marked difference in catch by the fog gauges is interpreted by denser and more frequent fog blown by faster winds at the HEES station, which is compatible with field observations.

### 6.4.2 Throughfall and stemflow

Coefficients of spatial variation of throughfall ( $CV$ ) inferred from the manually read collectors were similar for both plots, ranging between 40% and 60% with a mean of 50%. This latter value was used to estimate the sampling error for the troughs (assumed to be constant). The corresponding sampling error at the 68% confidence level (Eq. 6.1) was 8.8% for the MESF plot and 13.9% for the HEES plot. Due to the clogging of the throughfall tipping buckets and issues with the instrumentation, throughfall data was unavailable during 10% and 22% of the period of interest (September-December), for MESF and HEES plot respectively. Throughfall collected during the seventy-five days of simultaneous monitoring was  $188 \pm 15$  mm at the MESF plot, and  $360 \pm 50$  mm, at the HEES plot. This corresponds respectively to  $79 \pm 8\%$  and  $115 \pm 16\%$  of incident rainfall.

During the period of stemflow collection (40 and 31 consecutive days, respectively, at MESF and HEES plots), the amount of stemflow collected was 0.7% of incident rainfall (0.8% of throughfall) at the MESF plot, and 0.6% of incident rainfall (0.5% of throughfall) at the HEES plot. High proportions of stemflow are often associated with high rainfall rates [Bruijnzeel *et al.*, 2011]. The small amount of stemflow collected in the present study may therefore be explained by the low rainfall rates observed during the *garúa* season. Epiphytes were present at the two sites, when they are partly unsaturated between rainfall events, they may store subsequent water inputs and reduce stemflow [Hölscher *et al.*, 2004; Köhler *et al.*, 2007]. Furthermore, some specific characteristics of the vegetation participate to the diversion of stemflow to throughfall [Crockford and Richardson, 2000]: leaning trunks, sub-horizontal branches, flow path obstructions such as detaching bark peaces, apex of the leaves orientated to the ground. These

features were especially represented at the MESF plot.

Given the small amount of water diverted to stemflow, it was not continuously recorded. For the estimation of  $CWI$  (Eq. 6.7), net precipitation ( $P_{net} = TF + SF$ ) was calculated at the 15-min time step from throughfall data multiplied by a constant correction factor (1.008 at MESF plot, 1.005 at HEES plot).

### 6.4.3 Interception model

Canopy characteristics for the interception model are detailed in Table 6.2. Free throughfall coefficient  $p$  and canopy storage capacity  $S$  were estimated from rainfall events with the low relative throughfall ( $TF/RF$ ), i.e. with negligible fog interception. Due to the rapid saturation of the canopy (Fig. 6.7), the relatively coarse resolution of the tipping bucket rain gauge (0.2 mm) was a limitation for an accurate estimation of  $p$ .

	MESF	HEES
$p$ [-]	0.20	0.30
$S$ [mm]	0.56	0.23
$D_s$ [mm h <sup>-1</sup> ]	0.20	0.25
$b$ [mm <sup>-1</sup> ]	1.99	1.72

**Table 6.2:** Canopy characteristics as used in the modified *Rutter* model. Free throughfall coefficient ( $p$ ) and water storage at saturation ( $S$ ) were estimated by linear regression. Drainage function parameters  $D_s$  and  $b$  were estimated by non-linear least square optimization.

Free throughfall coefficients estimated by the graphical method ( $p = 0.20$  and  $p = 0.30$ , respectively, for MESF and HEES plots) were comparable to the values of canopy gap fraction estimated from vertical photographs (0.30 and 0.26, respectively, for MESF and HEES plots) (Table 6.1). Nevertheless, gap fraction values estimated from photographs are not as appropriate in the sense that the view angle is not strictly vertical, particularly on the edges of the photographs. The graphical method will be preferred, since it is devoid of such edge effect, and takes into account the actual angle of incidence of rainfall as it reaches the canopy.

## 6. QUANTIFICATION OF CLOUD WATER INTERCEPTION

---

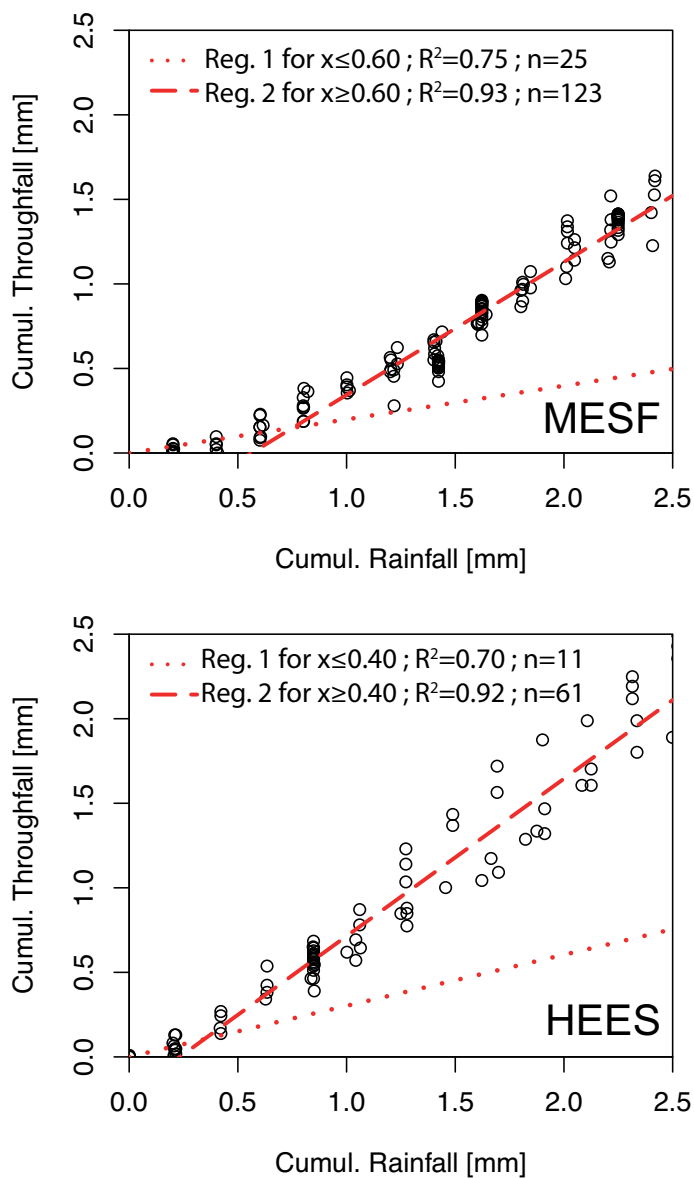


**Figure 6.7:** Estimation of canopy characteristics  $p$  and  $S$  with the *within-event* analysis for the MESF (top) and HEES (bottom) plots.

$D_s$  and  $b$  were obtained by least square optimization of predicted net precipitation ( $\hat{P}_{net}$ ) against observed values ( $P_{net}$ ) during the same events with low relative throughfall at 15 min time step. The RMSE of 15 min estimates in the calibration dataset was 0.04 mm for the MESF plot and 0.06 mm for the HEES plot. Predicted net precipitation was overestimated by 11.2% and 2.1%, respectively, for MESF and HEES plots. This reflects an under-estimation of  $E$  by the P-M equation during calibration events.

#### 6.4.4 Fog interception

During the period of simultaneous records at both of the stations (75 days, extending from September to December 2010), cumulative  $\widehat{CWI}_0$  at the MESF plot was slightly below zero (-10 mm). This negative value is the consequence of the slight bias highlighted during the optimization of  $D_s$  and  $b$ , and may conceal short periods with effective  $CWI$ . Yet, this finding indicates that  $CWI$  at the MESF plot was only a very minor input, and it was therefore neglected. In contrast, cumulative  $\widehat{CWI}_0$  was 73 mm at the HEES plot, which reflects a significant input from  $CWI$ . The smoothed, corrected, and adjusted estimate  $\widehat{CWI}_1^* = k_1 \times \widehat{CWI}_0$  was therefore computed ( $k_1 = 0.88$ ) and used for a second run of the model. With  $k_2 = 1.10$ , it was necessary to run the model a third time, which yielded  $k_3 = 1.006$ . Cumulative evaporation increased by 30% between the first and the third run of the model ( $E_{1,cum} = 27$  mm,  $E_{2,cum} = 34.5$  mm,  $E_{3,cum} = 35$  mm). The finalized estimate  $\widehat{CWI}^*$  was  $81 \pm 50$  mm at the HEES plot, representing  $26 \pm 16\%$  of incident rainfall ( $RF$ ), or  $20 \pm 13\%$  of all water inputs ( $RF + \widehat{CWI}^*$ ). The daily interception rate was in average  $1.18$  mm day<sup>-1</sup> and reached  $5.24$  mm day<sup>-1</sup> at the maximum.

The effect of wind speed on fog catch was investigated from the 15-min estimates of  $CWI$  at the HEES plot (Fig. 6.8). As depicted in Fig. 6.9, the variability of  $\widehat{CWI}^*$  increases markedly with wind speed. Median  $\widehat{CWI}^*$  is ca.  $0.03$  mm h<sup>-1</sup> for wind speed between 0 and  $2$  m s<sup>-1</sup>, while it reaches  $0.06$  mm h<sup>-1</sup> for wind speed higher than  $2$  m s<sup>-1</sup>.  $\widehat{CWI}^*$  rates for wind speed intervals [2;3] and [3;4] m s<sup>-1</sup> were significantly greater than for wind speed intervals [1;2], and [2;3] m s<sup>-1</sup>, respectively (Wilcoxon rank sum test,  $p < 0.01$  for both of the pairs). Such a pattern was not identified for other recorded parameters (temperature, solar radiation, relative humidity).

These results highlight the positive influence of wind speed over  $CWI$ , but the scatter of  $CWI$  rates for higher wind speeds demonstrates the existence of other controlling parameters, such as fog liquid water content ( $LWC$ ).

## 6. QUANTIFICATION OF CLOUD WATER INTERCEPTION

---

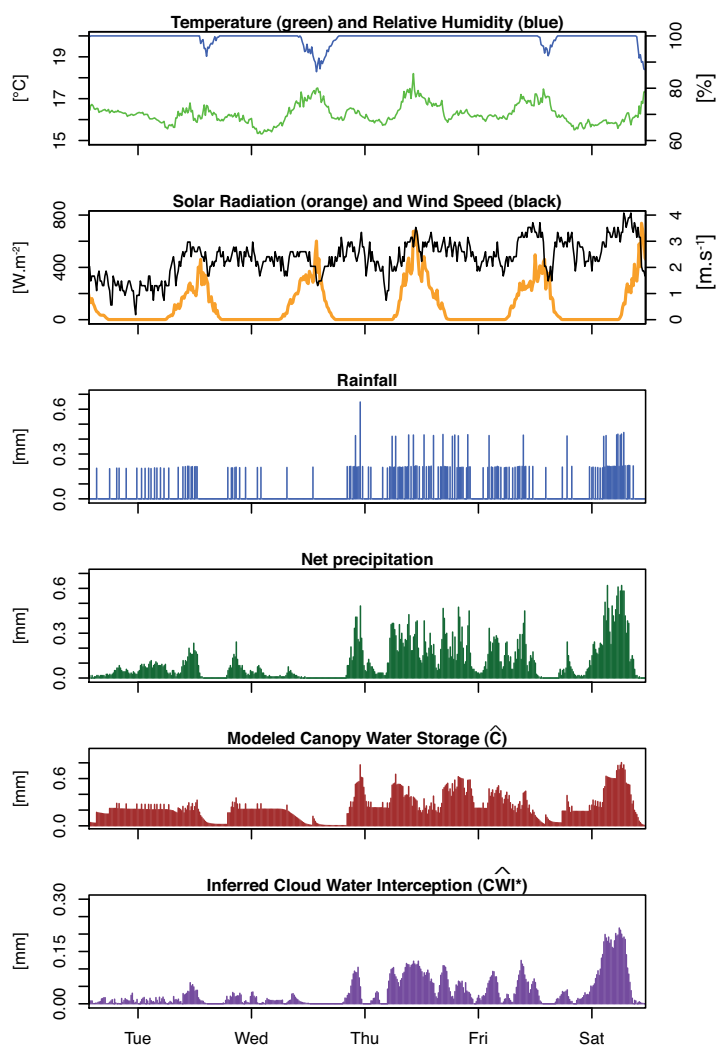


**Figure 6.8:** Climatic variables and modeled canopy water storage  $\hat{C}$  and  $\hat{CWI}^*$  estimates for the HEES station between 15 and 20 November 2010, with 15-min time steps.

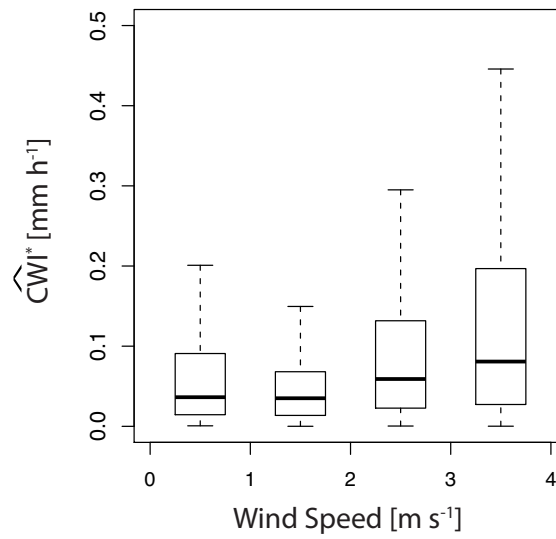


**Figure 6.9:** Statistics of cloud water interception rates ( $\widehat{CWI}^*$ ) classified for four wind speed intervals at the HEES plot. For higher wind speeds,  $CWI$  rates are higher and more scattered. Wind speed enhances  $CWI$  but is not the only controlling factor.

### 6.5 Discussion

#### 6.5.1 Interception model

*Gash*-type models require the separation of the period of interest into individual precipitation events as defined by *Gash* [1979], namely continuous rainfall and evaporation rates, as well as a dry canopy at the beginning and termination of the event. Given these restrictive conditions, event separation can be challenging and subjective [*Llorens*, 1997; *Llorens et al.*, 1997]. This is particularly true in the context of fog occurrence, with continuous rainfall, weak evaporation rates, and the vegetation canopy remaining wet. The modified *Rutter* model used in this study is based on a running canopy water budget and avoids such event separation over the whole period of interest. The selection of a set of events is yet required for the estimate of model parameters. The introduction of the drainage function proposed by *Gash and Morton* [1978] provided a more accurate estimation of net precipitation for shorter time steps.

The sensitivity of *Rutter* models to parameters  $p$  and  $S$  has been investigated by *Valente et al.* [1997] and *Gash and Morton* [1978]. Uncertainty for these parameters was relatively high in this study, which can be attributed to parameter variability from event to event [*Jackson*, 1975; *Link et al.*, 2004; *Massman*, 1983], a slight incompatibility with the *Gash* [1979] conditions for sample storms, evaporation from the canopy during rainfall [*Link et al.*, 2004], and the resolution of the rain gauge (0.2 mm), being too coarse with respect to event size and canopy storage capacity.

Free throughfall coefficients obtained for MESF and HEES plots ( $p = 0.20$  and  $p = 0.30$ , respectively) are within the common range reported in the literature (e.g. *Holwerda et al.* [2006a], *Takahashi et al.* [2011], *García-Santos* [2007], and *Návar and Bryan* [1994]). The value of canopy storage capacity found for the secondary forest of the MESF plot ( $S = 0.56$  mm) is similar to the value estimated by *Holwerda et al.* [2006a] for a plot of 3 m high, evergreen forest in Puerto Rico ( $S = 0.5$  mm). Nevertheless, higher values were generally attributed to medium-sized tropical forests: 0.85 mm for a plot of 12.5 m high guava trees in Hawaii [*Takahashi et al.*, 2011], between 1.08 and 1.23 mm for 9-13 m high laurel and mixed-tree heath/beach forests in the Canary Islands [*García-Santos*, 2007], and 1.3 mm for a 5-8 m high tropical forest in Jamaica [*Hafkenscheid et al.*, 2002]. The value of  $S$  found for the endemic shrubs of the HEES plot (0.23 mm) is particularly small, but comparable to the values of 0.29 mm found for 4 m high shrubs in Spain [*Domingo et al.*, 1998]. *Návar and Bryan* [1994] found higher values, ranging between 0.39 and 1.59 mm for 1.8-2.2 m semi-arid, dense scrub vegetation in Mexico. Apart from measurement errors, relatively common values for  $p$  associated with small values for  $S$  can be attributed to the single storey

tree architecture, and the very sparse understorey vegetation observed at the two plots.

While the accuracy of net precipitation measurements can be assessed and even reduced by the use of an adapted sampling strategy [Holwerda *et al.*, 2006b; Ziegler *et al.*, 2009; Zimmermann *et al.*, 2010], the uncertainties of evaporation estimates are difficult to overcome. On the calibration dataset, predicted net precipitation was overestimated by 11% and 2%, respectively, for MESF and HEES plots, which can be explained by an underestimation of evaporation. Other observations can be interpreted in terms of a slightly underestimated evaporation. In particular, some nightly rainfall events at the MESF plot presented relative throughfall ( $TF/RF$ ) smaller than 100%, while the P-M equation predicted zero evaporation. The accuracy of potential evaporation estimates may be affected by measurement errors and the occurrence of processes that are not taken into account in the P-M equation. Relative humidity was measured by a probe within a protection shield, which can remain soaked after a prolonged humid period, while the outside becomes drier. This issue has been highlighted by Frumau *et al.* [2006] and Holwerda *et al.* [2006a, 2010a] and may be addressed with dry- and wet-bulb temperature monitoring. The underestimation of potential evaporation could as well be explained by an overestimation of the aerodynamic resistance ( $r_a$ ). Holwerda *et al.* [2012] showed that in areas with complex topography,  $r_a$  could be overestimated, which induces an underestimation of  $E_p$ .

Various studies have highlighted an underestimation of evaporation with the P-M equation without apparent errors from the instrumentation. They invoke processes such as the condensation of water vapor above the vegetation canopy [Scatena, 1990; Schellekens *et al.*, 1999, 2000] or the effect of advection from the nearby ocean [Dykes, 1997; Holwerda *et al.*, 2006b; McJannet *et al.*, 2007a; Schellekens *et al.*, 1999, 2000]. With the occurrence of orographic rainfall and the proximity to the Pacific Ocean, both of these processes can be expected along the windward slope of Santa Cruz, but their actual significance is challenging to quantify.

The choice of the time step is critical for the interception model. Shorter time steps allow the investigation of processes related to meteorological parameters changing at small time scales such as wind speed, and improve the estimate of potential evaporation. Yet, various limitations regarding the instrumentation and the interception model prevent the use of short time steps. Tipping bucket gauges do not allow high-frequency precipitation monitoring for small precipitation rates. The device resolution (precipitation height per bucket rotation) is a limiting factor. A reduction of the bucket size is possible, but introduces measurement errors for higher precipitation rates [Calder and Kidd, 1978]. Also, it becomes challenging to predict canopy drainage at higher frequency. Canopy dripping may not be continuous but rather depend on wind gusts and other pa-

## 6. QUANTIFICATION OF CLOUD WATER INTERCEPTION

---

rameters which are not taken into account in the interception model. Given the instrumentation and context of this study, it appeared challenging and of limited interest to predict fog interception for time steps shorter than 15 min.

### 6.5.2 Cloud water interception

Cloud water interception ( $CWI$ ) was negligible at the MESF plot, significant at the HEES plot. The average daily  $CWI$  rate found for the HEES plot during the 2010 *garúa* season ( $1.18 \text{ mm day}^{-1}$ ) is comparable to other low-elevation elfin cloud forests under low precipitation:  $0.43 \text{ mm day}^{-1}$  for low shrubs and trees on the leeward side of Maui (Hawaii) [Giambelluca *et al.*, 2011],  $0.85 \text{ mm day}^{-1}$  and  $2.35 \text{ mm day}^{-1}$  in Colombia at low and high elevation respectively [Cavelier and Goldstein, 1989]. Studies reviewed by Bruijnzeel *et al.* [2011] report  $CWI$  contributions ranging between 4% and 45% with a mean of 16% of incident rainfall. This places the current estimate of  $CWI$  for the HEES plot ( $26\% \pm 16\%$  of incident rainfall) in the upper central range of other studies, similar to Holwerda *et al.* [2006a]; Hutley *et al.* [1997]; McJannet *et al.* [2007c]. Such a comparative analysis of  $CWI$  rates would be more relevant if the same methodology was employed for each of the study sites, which is not the case here.

Short time steps allowed the investigation of the correlation between wind speed and  $CWI$  rates. Mean  $CWI$  rate increases with higher wind speed (Fig. 6.9). This can be explained by a higher impaction rate of wind-driven fog droplets against leaves and branches. The scatter of  $CWI$  for higher values of wind speed highlights the effect of other controlling parameters, such as fog liquid water content ( $LWC$ ) which could not be measured in the field. Eugster *et al.* [2006] showed that net cloud water flux increases with higher  $LWC$ . The combined effects of wind speed and  $LWC$  over  $CWI$  rates have been discussed by Villegas *et al.* [2008]. They state that optimum conditions for  $CWI$  are found for medium values of liquid water content and wind speed. For higher wind speeds, it is expected that an increase in potential evaporation reduces effective  $CWI$ . This effect is not visible in the current dataset. Either wind speed, or air vapor pressure deficit remained too low for such an effect to become effective. Furthermore, it should be noted that an increase in fog droplet interception by the canopy is not the only process that can be invoked to explain the rise in net precipitation for higher wind speeds. Indeed, this may also be attributed to the sudden dripping caused by wind gusts. In fact, both processes probably act simultaneously. Defining their respective contributions appears challenging, if not impossible.

In a first attempt to characterise the uncertainty of  $CWI$ , the errors of measured and predicted net precipitation were added quadratically (Eq. 6.13). Similarly to other studies, the uncertainty of  $CWI$  was high due to the propagation of

errors from both sampling and modeling. The term related to throughfall sampling error dominates, but is expected to be an overestimation. Indeed, throughfall sampling error was estimated from the set of manual collectors, with a smaller total collection area. Instead of implementing uncertain corrections, it was preferred to keep the latter error estimate, which is safer considering that throughfall was assumed to have a random spatial distribution and a constant coefficient of variation, and that other potential sources of error were disregarded.

### 6.5.3 Comparative analysis of the two study sites

Wet canopy water budgets for the two study sites are shown to be very contrasting (Fig. 6.10). At the MESF plot, net precipitation under the secondary forest represented  $79 \pm 8\%$  of incident rainfall and  $CWI$  was found to be negligible. At the HEES plot (2 km further north and situated 150 m higher), net precipitation was two times higher. This difference is explained by the contribution of  $CWI$ , higher rainfall (+31%), and lower evaporation (-21%).

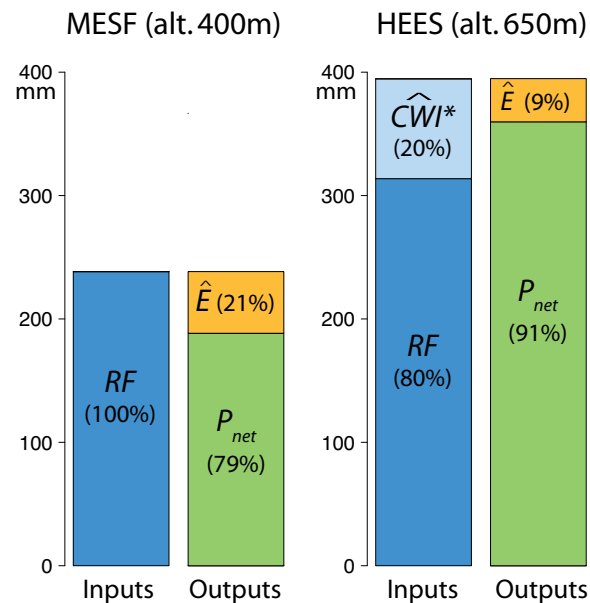


**Figure 6.10:** Canopy water budget at the MESF plot (left) and the HEES plot (right) for the seventy-five days of common monitoring. Inputs considered are corrected rainfall ( $RF$ ) and cloud water interception ( $\widehat{CWI}^*$ ).  $\widehat{CWI}^*$  was not significant at the MESF plot, while it represented 20% of water inputs at the HEES plot.

## 6. QUANTIFICATION OF CLOUD WATER INTERCEPTION

---

As illustrated by Fig. 6.9, higher wind speed is related to higher *CWI* rates. Yet, the difference in mean wind speed at the MESF and HEES stations (respectively  $0.9 \text{ m s}^{-1}$  vs.  $1.9 \text{ m s}^{-1}$ ) alone can not explain the observed difference in fog catch. The contrast between the two study sites most probably originates from the combined effects of higher wind speeds, better exposure to dominant winds, and more frequent, denser fog at the HEES station. The latter is confirmed by the higher water catch by the fog gauge at the HEES station, which was five times higher than at the MESF station. With steeper slopes and discontinuous shrub patches varying in height, the endemic *Miconia* shrubs of the very humid zone are better exposed to the dominant winds than the large patches of secondary forest on flatter terrain.

The higher storage capacity and lower free throughfall coefficient of the secondary forest (MESF plot) may partly explain that evaporation was higher at the MESF site. However, it is difficult to conclude on the role played by canopy structure with such contrasting climatic conditions between the two sites. Within the framework of future studies, it would be interesting to compare *CWI* under other species present in the very humid zone (e.g. *Cinchona pubescens*).

Secondary forests cover about one third of the agricultural humid zone of Santa Cruz Island. The MESF plot was chosen as it was thought to be sufficiently representative, but some heterogeneities in the species distribution may induce different interception rates (e.g. *Takahashi et al.* [2011]). Extending the results of the MESF plot to all forest patches of the agricultural humid zone may be hazardous. Additional plots would be needed to ascertain the associated variability in net precipitation.

The HEES plot is considered representative of a significant part of the high-elevation very humid zone (Fig. 6.2). Though the invasive *Cinchona pubescens* tree is still present in the very humid zone, it is the object of a control program by the *Galapagos National Park* so that the endemic *Miconia robinsoniana* shrub (included in this study) is expected to become more representative.

In the very humid zone, soils are thin and have a limited retention capacity, whereas atmospheric transpiration demand is very low. Runoff rapidly flows into open fractures and does not reach the agricultural zone below. Like in the Canary islands [*García-Santos, 2007*], groundwater recharge is enhanced in such a context. The very humid zone of Santa Cruz is likely to be of major importance for the groundwater resources of the island.

### 6.6 Summary and conclusions

The estimation of *CWI* was performed with the wet canopy water budget method, based on a *Rutter*-type interception model. This methodology presents the fol-

lowing characteristics:

- The *Rutter*-type interception model avoids the time-consuming, subjective separation of the whole period of interest into individual rainfall events.
- Canopy parameters  $p$  and  $S$  are estimated with the methodology detailed by *Link et al.* [2004] from a set of selected events fitting the conditions for sample storms defined by *Gash* [1979], and with negligible effect from *CWI*. From this same set of events, parameters of the drainage function ( $D_s$  and  $b$ ) are estimated by non-linear least square optimization.
- *CWI* is estimated for short time steps (15 min) as the difference between predicted and measured net precipitation. This allows the investigation of controlling factors varying in the short term, mostly wind speed. When *CWI* is significant, an iterative approach is implemented to take into account the input from fog on the estimate of evaporation.

It would be of the highest interest to compare this methodology with others at the same site, and to compare different sites with this methodology.

The results of this study highlighted the contrasting hydrological conditions along the windward slope of Santa Cruz Island during the fog *garúa* season:

- At the lower fringe of the cloud, in the secondary forest (MESF station, alt. 400 m a.s.l.), relative throughfall was 79% of incident rainfall. Fog interception was negligible.
- Only 2 km further north, in the center of the cloud belt, underneath the endemic *Miconia* shrubs (HEES station, alt. 650 m a.s.l.), relative throughfall was  $115 \pm 16\%$  of incident rainfall. This was explained by the added input from *CWI*, which was estimated at  $26 \pm 16\%$  of incident rainfall.
- Observed evaporation rates were locally higher than predicted with the P-M equation. This was interpreted as being due to difficulties with the measurement of relative humidity, the possible overestimation of aerodynamic conductance, and the effect of other sources of energy (latent heat released by condensation, advected air from the nearby ocean). As a consequence, *CWI* was to some extent underestimated.
- At the HEES plot, median *CWI* rate for wind speeds  $\leq 2 \text{ m s}^{-1}$  was ca. 50% lower ( $0.03 \text{ mm h}^{-1}$ ) than for wind speeds  $\geq 2 \text{ m s}^{-1}$  ( $0.06 \text{ mm h}^{-1}$ ).

Due to a significant input from *CWI*, higher rainfall and smaller evaporation, net precipitation underneath the endemic shrubs of the very humid zone was

## 6. QUANTIFICATION OF CLOUD WATER INTERCEPTION

---

two times higher. Given the high infiltration capacity and the limited transpiration expected in this zone, this additional input of water directly contributes to groundwater recharge. The very humid zone has therefore a significant role in the hydrology of the island and is sensitive to fog occurrence. Should climate change induce a raise of the cloud base or a reduction of fog occurrence, it would most probably induce a significant reduction of net precipitation, and therefore groundwater recharge in the very humid zone.

### 6.7 Acknowledgments

This study has been performed in the frame of the project *Galapagos Islands Integrated Water Studies* (GIIWS), funded by the Agence Nationale de la Recherche (ANR-blanc 2010 GIIWS Ref. 601-01). The GIIWS team would like to thank its local partners in the Galapagos: the Charles Darwin Research Station, the Galapagos National Park, and private land owners who allowed the installation of weather stations. Marta González del Tánago (Polytechnic University of Madrid) provided valuable advices for the set up of stemflow collectors. The authors are very grateful to Mandy Trueman (Charles Darwin Foundation & University of Western Australia), Heinke Jäger (Department of Ecology, Technische Universität Berlin), Anne Guézou (Charles Darwin Foundation), Julien Tournebize (Cemagref Antony) and Jean-Paul Lhomme (LISAH Montpellier) for their support on the field and corrections on the draft. Finally, the helpful comments by Prof. L.A. Bruijnzeel and another anonymous reviewer are gratefully acknowledged.

**Part IV**

**Groundwater flow**



This part, **Groundwater dynamics**, is dedicated to groundwater occurrence in volcanic islands.

In a first chapter, *Analytical and numerical modeling of basal aquifers*, a set of analytical solutions considering seawater intrusion are detailed, with special reference to volcanic islands basal aquifers. Using a variable-density flow and transport numerical model, errors associated with the analytical solutions are discussed. When seawater intrusion is strong, it induces a rise of the basal aquifer water table. But the most simple analytical solution disregarding seawater intrusion, used in Chapter 3, is proven to provide a reasonable estimate for a comparative study.

In the following chapter, *The basal aquifer of Santa Cruz Island*, a multi-scale approach is implemented to characterize hydraulic properties of basaltic formations. Hydraulic properties are estimated by means of tidal signal propagation, hydraulic tests, and fracture mapping. It is shown that young basaltic flows of Santa Cruz island are densely fractured with cooling joints, which confer them a high permeability. In contrast, the network of normal faults dissecting the region is not sufficiently connected to percolate and has limited hydrogeological impact.

In a last chapter, the occurrence of *High-level groundwater in Santa Cruz Island* is discussed. Geophysical results, climatic data, and hydrogeological evidences gathered in the frame of this thesis are used to characterize the conceptual model of Santa Cruz Island.



## Chapter 7

# Analytical and numerical modeling of basal aquifers

# Analytical and numerical modeling of basal aquifers\*

---

## Abstract

The presence of a basal aquifer in connection with the ocean is reported in every volcanic island. In the coastal area, basal aquifers are subjected to sea-water intrusion. Further inland, these aquifers have very contrasting geometries. In some of the islands, the water table has a gentle slope and remains at low elevation. In other islands, the water table is reported at several hundreds of meters above sea level. In order to explain these contrasts, we propose a set of 1D analytical solutions describing the water table of these aquifers. The relevance of these equations is discussed with the help of a 2D variable-density flow and transport numerical model (SUTRA). We show that the simplest analytical solution, disregarding vertical head gradients and density effects, provides a satisfactory description of the water table height for a broad range of contexts. Permeability varies markedly from one island to the other, it is identified as the determining parameter explaining the contrasting geometries of basal aquifers.

---

\* In collaboration with Jerome Fortin<sup>1</sup>. This section served as a basis for section 3.6

<sup>1</sup>*UMR 8538, Laboratoire de Géologie , Ecole normale supérieure, Paris, France*

## 7.1 Introduction

### 7.1.1 Scope of the study

In most of the basaltic volcanic islands, the *basal aquifer* is the major groundwater resource. Most often, this aquifer presents a free water table and is recharged by meteoric precipitations. In the coastal area, basal aquifers are affected by seawater intrusion at different extents. Toward the center of the island, the geometry of the basal aquifer varies markedly from island to island. In some cases, hydraulic gradient are weak and the water table remains at low elevation (e.g. in various islands of the Hawaiian, Galapagos and Cape Verde archipelagos (Fig. 7.1, A) [d'Ozouville, 2007a; Gingerich and Voss, 2005; Gingerich and Oki, 2000; Heilweil et al., 2009]. In other islands of the Hawaiian Archipelago and Canary Islands, hydraulic gradients are reported to be higher, which allows the water table to reach high elevations (Fig. 7.1, B) [Custodio et al., 1988; Gingerich, 1998; Izuka and Gingerich, 2003]. In other islands, such as La Réunion and Easter islands, the configuration is unclear or subjected to discussions [Herrera and Custodio, 2008; Join et al., 2005; Violette et al., 1997].

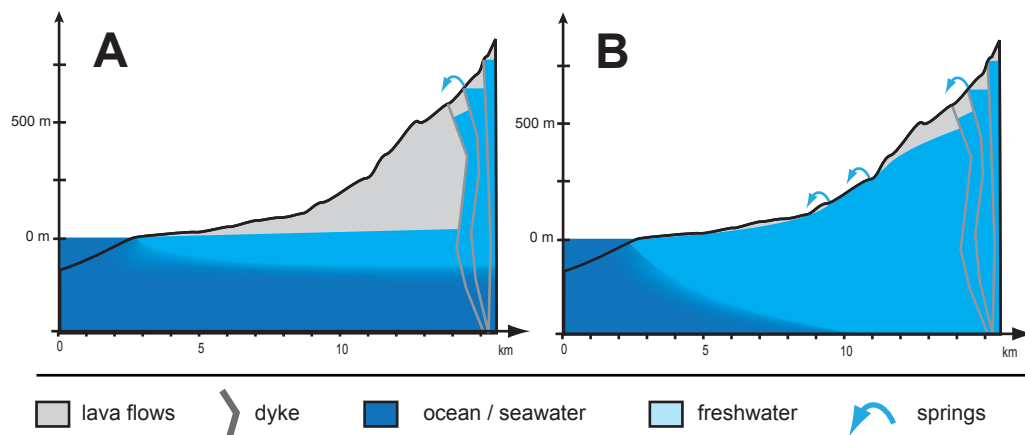


**Figure 7.1:** Two configurations reported for the basal aquifer. (A) low-elevation basal aquifer, e.g. Hawaii (Hawaii, USA), Santa Cruz (Galapagos, Ecuador), and (B) high-elevation basal aquifer, e.g. Tenerife (Canary, Spain) and Kawaii (Hawaii, USA).

The modeling approach developed hereafter aims to explain the very contrasting configuration of basal aquifers and to identify the controlling factors. We focus our concerns on the elevation of the water table, but this problem must be considered together with the effects of seawater intrusion. First, intruding

## 7. MODELING BASAL AQUIFERS

seawater may rise the elevation of the water table and secondly, the amount of stored freshwater, which is a determining factor in hydrogeological studies, also depends on seawater intrusion.

To allow comparison between islands, only simplified sketches can be used, and controlling parameters must be restricted to a limited number. Though they may have a critical importance, spatial heterogeneities are difficult to handle in a comparative studies and will not be considered. Permeability and recharge are assumed to be homogeneous, and mean values of parameters will be used.

Models presented hereafter are simplified sketches, they do not pretend to be accurate at the local scale and predict site-specific configurations. They aim to provide a simple and satisfactory solution valid in a broad range of contexts.

### 7.1.2 Specific features of volcanic island basal aquifers

The mechanism leading to the construction of a volcanic island often induce a symmetry in the edifice [Thouret, 1999]. In the case of a major elongated eruptive rift zone, the configuration may be close to the strip-island model (Fig. 7.2, A), with  $(x = L, y, z)$  as a symmetry plane. In the case of a *volcano-island* with a major eruptive center, the configuration may be closer to the circular-island model (Fig. 7.2, B). With some simplifications, the 3D problem can be simplified to a 2D model in the  $(O, x, z)$  or  $(O, r, z)$  plane. In this study, we consider a classical case of a strip-island with a vertical coast at  $x = 0$  and an impermeable barrier at a distance  $L$  of the coast.

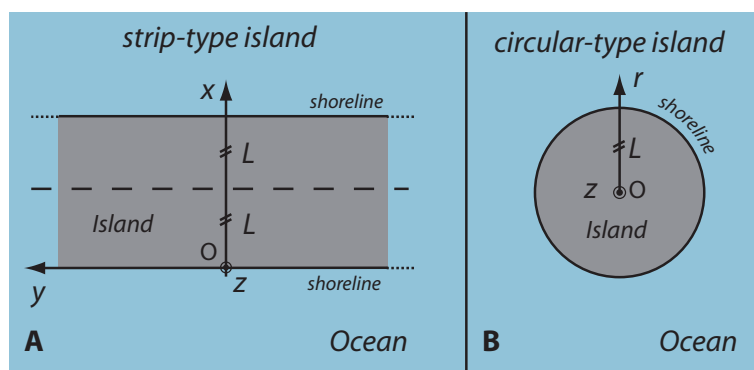


**Figure 7.2:** Symmetry of volcanic islands edifices

It is relatively straightforward to determine  $L$ , the semi-length of the island but more challenging to estimate  $H$ , the depth of the substratum. Basaltic lava flows that constitute a large proportion of the edifice owe their permeability to fractures [Custodio, 2004], mainly cooling joints, which are progressively closed

with increasing lithostatic pressure at depth. Under some assumptions (isotropic crack distribution, ...), the evolution of permeability with depth can be approximated by an exponential law [Ougier-Simonin et al., 2011; Saar and Manga, 2004]:

$$k = k_0 e^{-\gamma \rho_r g d} \quad (7.1)$$

where  $d$  [m] the depth from the ground surface,  $k_0$  [m<sup>2</sup>] is the initial permeability at zero pressure ( $d = 0$ ),  $\rho_r$  [kg/m<sup>3</sup>] the rock density, and  $g$  [m<sup>2</sup>/s] the gravity constant. According to the literature review by [Ougier-Simonin et al., 2011], values of parameter  $\gamma$  range between 0.1 and 0.4 MPa<sup>-1</sup>. Assuming a rock density of 2800 kg/m<sup>3</sup>, the permeability is divided by a factor of 100 for depth ranging between 400-1700 m below ground level. The portion of the aquifer below that depth has little influence on the basal aquifer hydrodynamics. As long as an impervious layer has not been identified at a more shallow depth, a value of 1000 m appears to be reasonable for the effective thickness of the aquifer.

### 7.1.3 Selection and values of the controlling parameters

To achieve the sensitivity analysis, a limited number of parameters must be identified. We identified four parameters: the regional hydraulic conductivity  $K$ , the mean annual recharge rate  $r$ , the depth of the substratum  $H$ , and the semi-length of the island  $L$ . They have been gathered into two dimensionless parameters  $\chi = r/K$  and  $\xi = L/H$ . Though they may as well have their importance, other parameters such as the anisotropy ratio of the permeability, the occurrence of a sedimentary layer offshore (cap rock) (see e.g. Rotzoll et al. [2010]), and the topography have not been taken into account.

From a quick review of the literature, we found that values of controlling parameters have the following ranges:  $1 \times 10^{-8}$  -  $1 \times 10^{-7}$  m/s for recharge (ca. 0.3-3 m/y), hydraulic conductivity between  $1 \times 10^{-6}$  -  $1 \times 10^{-2}$  m/s. The corresponding range of  $\chi$  is  $1 \times 10^{-6}$  -  $1 \times 10^{-1}$ . The semi-length of the island range between 3 and 30 km. For the reasons described in section 7.1, the depth of the substratum  $H$  is expected to vary between ca. 400 m and 1200 m, but the value was fixed to a median value of 1000 m. The corresponding range of  $\xi$  is 3-30.

## 7.2 Analytical solutions

### 7.2.1 Model 1: fresh water aquifer

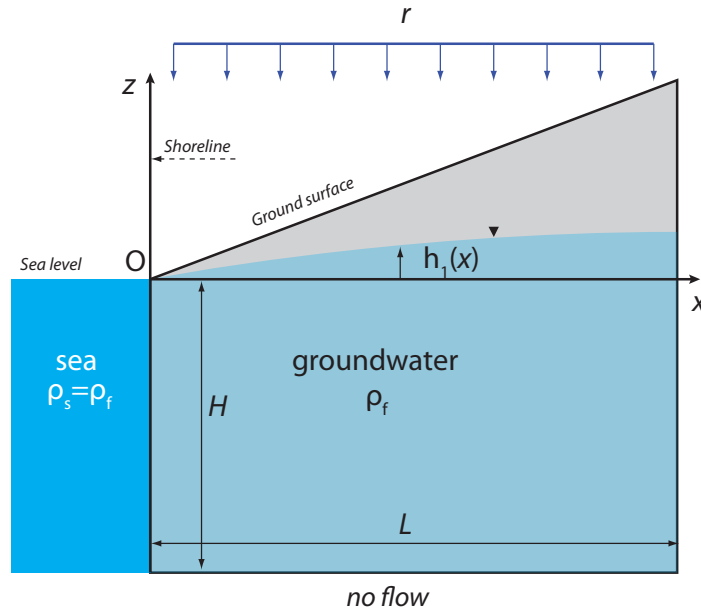


**Figure 7.3:** Description of the first model, a freshwater aquifer with a constant head at the coast. Seawater intrusion is not taken into account

We consider following hypothesis:

- steady state,
- fluid of constant density,
- isotropic, homogeneous permeability.
- Dupuits hypothesis of horizontal flow,
- vertical beach at  $x = 0$ .

Assuming the aquifer to be infinite and uniform in the  $y$  horizontal direction, the diffusivity equation *de Marsily* [1986] can be written as follows in the 2D space  $(O, x, z)$ :

$$\frac{\partial}{\partial x} \left[ \int_{-H}^{h_1(x)} K dz \frac{\partial h_1}{\partial x} \right] = -r \quad (7.2)$$

where  $h_1(x)$  [m] is the hydraulic head,  $K$  [m/s] the hydraulic conductivity,  $H$  [m] the thickness of the aquifer below sea level,  $L$  is the half-width of the island,  $r$  [m/s] the recharge rate at the upper boundary.

Given the boundary conditions  $h_1(0) = 0$  and  $-K \cdot \frac{\partial h_1}{\partial x}(L) \cdot (h_1(x) + H) = 0$ , Eq. 7.2 can be integrated into:

$$h_1(x) = -H + \sqrt{-\frac{r}{K} \cdot x^2 + 2\frac{rL}{K} \cdot x + H^2} \quad (7.3)$$

defined for  $x \in [0; L]$ .

To simplify the equation and facilitate the inter-comparison between islands and models, we can translate the expression of  $h_1$  in a dimensionless form,  $h_1' = h_1/H$ , with  $x' = x/H$ , the aspect ratio  $\xi = L/H$  and the recharge parameter  $\chi = r/K$ . For  $x' \in [0; \xi]$ , the dimensionless solution reads

$$h_1'(x') = -1 + \sqrt{-\chi x'^2 + 2\chi x' + 1} \quad (7.4)$$

### 7.2.2 Model 2: seawater intrusion with the Ghyben-Herzberg formula

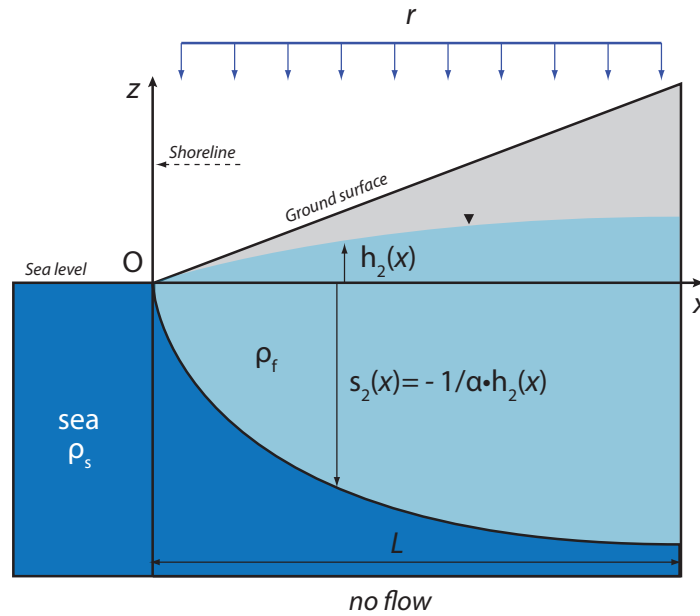


**Figure 7.4:** Description of the second model: seawater intrusion is modeled with the Ghyben-Herzberg assumptions.

## 7. MODELING BASAL AQUIFERS

---

We consider following hypothesis:

- steady state,
- Dupuit hypothesis (horizontal flow),
- static seawater, no salt diffusion, impermeable interface with salt water
- homogeneous permeability.
- vertical beach

From the hydrostatic equilibrium between fresh- and saltwater, the Ghyben-Herzberg formula states that  $s_2(x)$ , the vertical coordinate of the SWI is related to the water table of the freshwater lens  $h(x)$  by the following equation (e.g. *Bear* [1999]):

$$h_2(x) = -\alpha \cdot s_2(x) \quad (7.5)$$

where  $\rho_f$  is the density of freshwater,  $\rho_s$  the density of seawater and the buoyancy ratio  $\alpha = (\rho_s - \rho_f)/\rho_f$ . In standard conditions,  $\alpha \approx 1/40$ . The Ghyben-Herzberg equation is based on the assumption of an impermeable interface between the sea and the freshwater lens. Under this hypothesis, the SWI forms an impermeable interface delimiting the bottom of the freshwater aquifer. The diffusivity equation can be written as follows:

$$\frac{\partial}{\partial x} \left[ \int_{-\frac{1}{\alpha} \cdot h_2(x)}^{h_2(x)} K \frac{\partial h_2}{\partial x} dz \right] = -r \quad (7.6)$$

where  $h(x)$  [m] is the hydraulic head,  $K$  [m/s] the hydraulic conductivity,  $r$  [m/s] the recharge rate, and  $L$  is the semi-length of the island.

Assuming homogeneous permeability and given the boundary conditions  $h_2(0) = 0$  and  $\frac{\partial h_2}{\partial x}(L) = 0$ , Eq. 7.6 can be integrated into:

$$h_2(x) = \sqrt{\frac{\alpha}{(\alpha + 1)} \cdot \left( -\frac{r}{K} \cdot x^2 + 2\frac{rL}{K} \cdot x \right)} \quad (7.7)$$

This equation can be translated to a dimensionless form  $h'_2 = h_2/H$ :

$$h'_2(x') = \sqrt{\frac{\alpha}{\alpha + 1} \cdot \left( -\chi x'^2 + 2\chi\xi x' \right)} \quad (7.8)$$

Defined for  $x' \in [0; \xi]$ , where  $x' = x/H$ ,  $\xi = L/H$ , and  $\chi = r/K$ . The equation of the SWI in its dimensionless form,  $s'_2(x)$  simply reads  $s'_2(x') = -1/\alpha \cdot h'(x')$ .

In the Ghyben-Herzberg model, the transmissivity tends to zero at the coast, which is not fully realistic, so that this solution becomes inaccurate in the direct vicinity of the coast. Furthermore the aquifer thickness is considered as infinite at depth, the reduction of permeability due to fracture closure or the existence of an impermeable substratum is not taken into account. As a consequence, the transmissivity tends to be over-estimated and the hydraulic gradient is under-estimated. For the dimensionless equation, the condition of a SWI over the substratum can be explicited by:

$$\begin{aligned}
 s_2(x) > -H \quad \forall x \in [0; L] &\iff -\frac{1}{\alpha} \cdot h_2'(x') > -1 \quad \forall x' \in [0; \xi] \\
 &\iff -\chi x'^2 + 2\chi\xi x' - \alpha(\alpha + 1) < 0 \quad \forall x' \in [0; \xi] \\
 &\iff 4\chi^2\xi^2 - 4\chi\alpha(\alpha + 1) < 0 \\
 &\iff \chi\xi^2 < \alpha(\alpha + 1)
 \end{aligned} \tag{7.9}$$

When this condition is not verified, the thickness of the aquifer is over-estimated and the hydraulic gradient under-estimated.

### 7.2.3 Model 3: alternative analytical solutions for seawater intrusion

The Ghyben-Herzberg scheme is based on the *Dupuit* assumption and assumes fresh water discharge to be restricted to the shoreline, i.e. at a point in the 2D description. Using the potential theory *Henry* [1959], *Glover* [1959], and *Verruijt* [1968] proposed alternative descriptions of the flow regime, considering non strictly vertical flow and discharge through a strip of horizontal sea bottom. *Verruijt* [1968] and *Glover* [1959] assumed recharge to occur only from the inland vertical boundary of the aquifer (Fig. 7.5). *Henry* [1959] proposed a solution with recharge occurring at the top of the aquifer, but this problem has no purely analytical solution.

The solution proposed by *Verruijt* [1968] is detailed hereafter, since it provides a better description of the salt water interface in the vicinity of the coast. The recharge flux is lateral from the right boundary, which is a realistic condition in the coastal area.

## 7. MODELING BASAL AQUIFERS

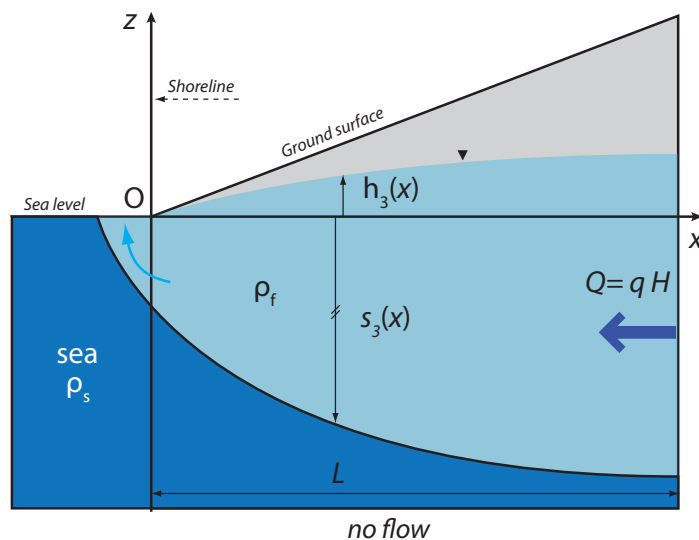


**Figure 7.5:** Description of *Verruijt* [1968] model. Recharge originates from the right vertical boundary and freshwater discharges through a strip offshore.

The hypothesis of the scheme by *Verruijt* [1968] (Fig. 7.5) can be summarized as follows:

- steady state,
- static seawater, no salt diffusion, impermeable interface with salt water
- homogeneous isotropic permeability,
- horizontal beach, infinite aquifer

The water table equation reads *Verruijt* [1968]:

$$h_3(x) = \sqrt{\frac{\alpha}{(1+\alpha)} \cdot \frac{2qH}{K} \cdot x} \quad (7.10)$$

The expressions of the interface  $s_3(x)$  reads

$$s_3(x) = -\frac{qH}{k} \sqrt{\frac{2}{\alpha(1+\alpha)} \cdot \left( \frac{(1-\alpha)}{2\alpha} + \frac{k}{qH} \cdot x \right)} \quad (7.11)$$

In turn, Eq. 7.10 and Eq. 7.11 can be translated to their dimensionless form, with  $\chi = q/K$ , and  $x' \in [0; \xi]$ :

$$h'_3(x') = \sqrt{\frac{2\alpha}{1+\alpha}} \chi \cdot x' \quad (7.12)$$

$$s'_3(x) = -\chi \sqrt{\frac{2}{\alpha(1+\alpha)} \cdot \left( \frac{(1-\alpha)}{2\alpha} + \frac{1}{\chi} \cdot x' \right)} \quad (7.13)$$

Similarly to the Ghyben-Herzberg scheme, these equations are relevant only if  $s_3(x) > -H$ , or  $s'_3(x') > -1$  for the dimensionless expression. This solution considers recharge to occur from the right boundary, and should only be considered in the coastal area. If recharge from the upper boundary becomes negligible with respect to groundwater flow in the aquifer, we can show  $h'_2$  (Eq. 7.12) and  $h'_3$  (Eq. 7.8) are equivalent. Only  $h'_2$  is discussed hereafter.

#### 7.2.4 Comparative analysis of the analytical models

Analytical models are compared in Fig. 7.6. The water table inferred from the freshwater aquifer model ( $h'_1$ ), is lower than that of the Ghyben-Herzberg model ( $h'_2$ ). In the latter, only a portion of the aquifer is made available for freshwater flow, the apparent transmissivity is smaller. With this set of parameters, and at this scale of observation, SWI inferred from the Ghyben-Herzberg and the Verruijt solutions look similar. In the second case ( $\chi = 1 \times 10^{-3}$ ),  $s'_2$  and  $s'_3$  are smaller than -1 when  $x$  is greater than ca. 0.18, which means that these estimations are not valid further inland, they would over-estimate aquifer transmissivity.  $s'_3$  intersects the vertical axis at ca.  $z = -0.4$ , which traduces a freshwater lens extending seaward

#### 7.2.5 Limitations of the analytical solutions

Analytical solutions of the water table based on SWI depth should only be considered in their domain of validity, that is for sufficiently small values of  $\chi$  and  $\xi$  for the SWI to be over the substratum. Hypothesis concerning freshwater discharge invalidate the solution based on the Ghyben-Herzberg estimate in the vicinity of the coast, the solution  $s'_3$  [Verruijt, 1968] should be preferred in this area.

Contrary to the models derived with the potential theory (e.g. Glover [1959]; Verruijt [1968]),  $h'_1$  and  $h'_2$  are based on the Dupuit assumption, which may not be relevant in the coastal area and at the far end of the aquifer inland.

Other assumptions may alter the accuracy of the water table equations detailed previously, and particularly the hypothesis of an impermeable SWI (no

## 7. MODELING BASAL AQUIFERS

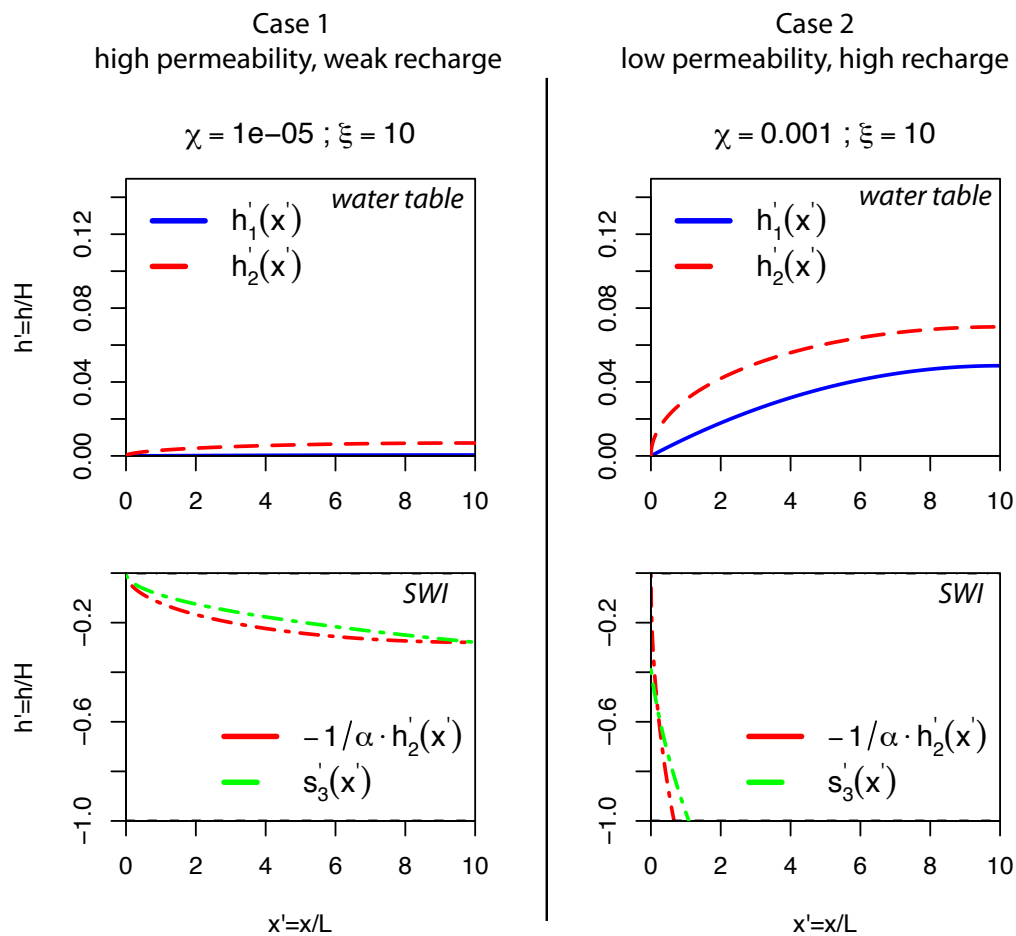


**Figure 7.6:** Water table (top row) and SWI (bottom row) estimated from the analytical solutions for two different configurations:  $\chi = 1 \times 10^{-5}$  (high permeability, left column) and  $\chi = 1 \times 10^{-3}$  (low permeability, right column).

mixing) and static seawater. Tidal oscillations imply the diffusion of salt through the SWI. This induces an outflow of salt from the aquifer to the sea [*Cooper*, 1959; *Glover*, 1959] which should necessarily be compensated by an input of salt from the sea into the aquifer. *Cooper* [1959] states that advection rather than diffusion compensates this loss, which implies a constant inflow of seawater into the aquifer. This landward flow induces an head loss likely to lessen seawater intrusion.

*Henry* [1959] proposed a semi-analytical solutions based on a modified diffusivity coefficient to take into account dispersive effects. Yet, the value of this coefficient has been discussed *Slooten et al.* [2010] and the transition zone is often larger than observed *Abarca et al.* [2007]. Alternatively, a numerical model can be used to solve the coupled transport and flow equations without the above-mentioned hypothesis and allows the estimation of the error inherent to the analytical models.

## 7.3 Numerical modeling

### 7.3.1 Theoretical background

#### 7.3.1.1 Governing equations

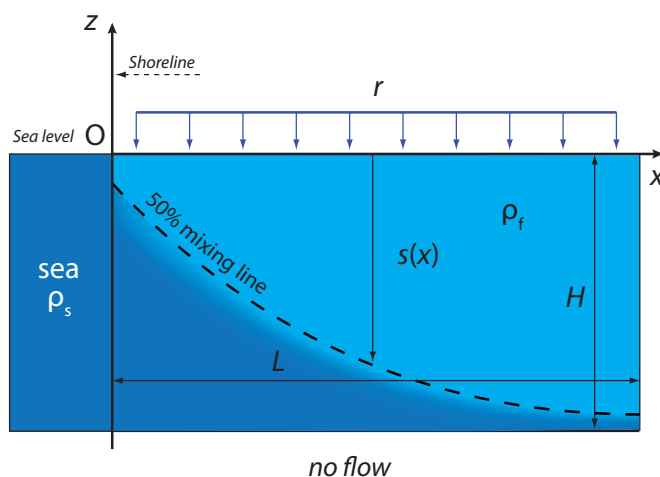


**Figure 7.7:** Geometry of the numerical model. The recharge rate  $r$  is imposed at the upper boundary, which is fixed at sea level. A fixed hydrostatic head is imposed along the left boundary. Bottom and right boundaries are impermeable.

If fluid density is variable, groundwater flow equations can be defined in terms of equivalent freshwater head  $h_f$  [Luszczynski, 1961]:

$$h_f = \frac{p(x, y, z)}{\rho_f g} + z \quad (7.14)$$

where  $\rho_f$  is the density of freshwater ( $1000 \text{ kg/m}^3$ ) and  $g$  is the gravitational constant ( $9.81 \text{ m}^2/\text{s}$ ). It is important to note that in these conditions, freshwater head  $h_f$  is not a potential but only provides the height of the equivalent freshwater column at a given point at the elevation  $z$  and pressure  $p(x, y, z, )$ .

Darcy law can be expressed in terms of  $h_f$  (e.g. Bear [1988]):

$$\mathbf{v} = -\mathbf{K}\nabla\left(h_f + \frac{\rho - \rho_f}{\rho_f} z\right) \quad (7.15)$$

where  $\mathbf{v}$  [m/s] is the Darcy velocity vector,  $\mathbf{K}$  the hydraulic conductivity tensor, and  $\rho$  the fluid density. The mass balance conservation can be written as follows:

$$\nabla(\rho \cdot \mathbf{v}) = 0 \quad (7.16)$$

where the fluid density  $\rho$  is assumed to vary linearly with salt concentration  $c$  [kg/m<sup>3</sup>]. The constitutive equation reads:

$$\rho = \rho_f + \alpha \frac{c}{c_s} \quad (7.17)$$

where  $c_s$  [kg/m<sup>3</sup>] is the salt concentration of seawater ( $c_s = 0.0357$  [kg/m<sup>3</sup>]) and  $\alpha$  is the buoyancy ratio defined previously. Combining equations 7.15 and 7.16 yields:

$$K_x \left( \frac{\partial^2 h_f}{\partial x^2} + K_r \left( \frac{\partial^2 h_f}{\partial z^2} + \frac{\alpha}{c_s} \frac{\partial^2 c}{\partial z^2} \right) \right) = \frac{\alpha \nabla c \cdot \mathbf{v}}{(c_s + \alpha c)} \quad (7.18)$$

where  $K_x$  is the horizontal permeability and  $K_r$  the anisotropy ratio  $K_z/K_x$ . The flow equation is coupled with the salt transport equation. The steady state form reads (e.g. *Bear* [1988]):

$$\mathbf{v} \cdot \nabla c - \nabla(\mathbf{D} + \phi D_m \mathbf{I}) \nabla c = 0 \quad (7.19)$$

where  $\phi$  is the porosity,  $D_m$  the molecular diffusion coefficient,  $\mathbf{I}$  the identity tensor and  $\mathbf{D}$  the dispersion tensor defined by:

$$D_{xx} = \alpha_L \frac{v_x^2}{|\mathbf{v}|} + \alpha_T \frac{v_z^2}{|\mathbf{v}|} \quad (7.20)$$

$$D_{zz} = \alpha_T \frac{v_x^2}{|\mathbf{v}|} + \alpha_L \frac{v_z^2}{|\mathbf{v}|} \quad (7.21)$$

$$D_{xz} = D_{zx} = (\alpha_L - \alpha_T) \frac{v_x v_z}{|\mathbf{v}|} \quad (7.22)$$

where  $\alpha_L$  and  $\alpha_T$  are the longitudinal and transverse dispersivity coefficients respectively.

Boundary conditions are applied to the boundaries of the rectangular domain (Fig. 7.7). So as to avoid unsaturated flow modeling, the top of the model is maintained at sea level. A null flux is imposed at the right ( $x = L$ ) and bottom ( $y = -H$ ) boundaries, considered as impermeable. Recharge is imposed at the top boundary,  $v_z|_{x \in [0:L], z=0} = -r$ , with  $r$  [m/s], the constant and uniform recharge flux of concentration  $c = 0$ . At the boundary with the sea, a constant equivalent freshwater head is specified. With sea level at  $z = 0$ , the boundary condition at

## 7. MODELING BASAL AQUIFERS

---

the left boundary is expressed by  $h_f|_{x=0} = -\alpha z$ . Water entering the model from this boundary is at concentration  $c = c_s$ .

The hypothesis of a fixed upper boundary induces an error when the elevation of the water table becomes significant with respect to the total thickness of the aquifer. But in this case, seawater intrusion becomes negligible and the use of a coupled numerical model is not justified.

### 7.3.1.2 Dimensionless form of the governing equations

So as to allow a comparative analysis with the analytical solutions, coordinates and variables are transformed to their dimensionless expressions:

$$\mathbf{v}' = \frac{\mathbf{v}}{r} ; x' = \frac{x}{H} ; z' = \frac{z}{H} ; h'_f = \frac{h_f}{H} ; c' = \frac{c}{c_0} \quad (7.23)$$

where  $r$  [m/s] is recharge rate,  $H$  [m] is the thickness of the aquifer, and  $c_0$  [kg/m<sup>3</sup>] is salt concentration of seawater. With these variables, the flow equation (Eq. 7.18) reads:

$$\left( \frac{\partial^2 h'}{\partial x'^2} + K_r \left( \frac{\partial^2 h'}{\partial z'^2} + \alpha \frac{\partial^2 c'}{z'^2} \right) \right) = \chi \frac{\alpha \nabla' c' \cdot \mathbf{v}'}{1 + \alpha c'} \quad (7.24)$$

where  $\chi$  is the recharge parameter and  $\nabla'$  is the operator  $\nabla$  written in the dimensionless coordinates. Similarly, dimensionless parameters can be defined for transport:

$$b_L = \frac{\alpha_L}{H}, \quad b_m = \frac{\phi D_m}{Hr}, \quad r_\alpha = \frac{\alpha_T}{\alpha_L} \quad (7.25)$$

where  $\phi$  is the porosity. The dimensionless dispersion tensor  $D'$  is defined by:

$$D'_{xx} = \frac{v'_x{}^2}{|v'|} + r_\alpha \cdot \frac{v'_z{}^2}{|v'|} \quad (7.26)$$

$$D'_{zz} = r_\alpha \cdot \frac{v'_x{}^2}{|v'|} + \frac{v'_z{}^2}{|v'|} \quad (7.27)$$

$$D'_{xz} = D'_{zx} = (1 - r_\alpha) \cdot \frac{v'_x v'_z}{|v'|} \quad (7.28)$$

The dimensionless transport equation is derived from 7.19 :

$$\mathbf{v}' \nabla' c' + \nabla (b_L \mathbf{D}' + b_m \mathbf{I}) \nabla' c' = 0 \quad (7.29)$$

Right ( $x = \xi$ ) and bottom ( $x = -1$ ) boundaries are impermeable, which is expressed with a null flux condition. At the top boundary, a constant and

uniform flux is imposed:  $v'_{x \in [0; \xi], z=0} = -1$ . The fluid entering this boundary is at concentration  $c' = 0$ . Head is imposed at the boundary with the sea,  $h'_f|_{x=0} = -\alpha z'$ . Water entering this boundary is at concentration  $c' = 1$ .

### 7.3.2 Results

The fine-element SUTRA code [Voss and Provost, 2010] was used to solve the coupled flow and transport equations in the 2D vertical space. The geometry of the model is described by Fig. 7.7. Boundary conditions are those described in the previous section.

As described in the preceding theoretical developed, the main hypotheses related to numerical modeling can be recalled as follows:

- steady state,
- velocity dependent dispersion of salt, fluid of variable density,
- homogeneous isotropic permeability,
- vertical beach

The domain was discretized with a 2D regular mesh of 50x500 elements for the reference aspect ratio  $\xi = 10$ . It was tested for 40x400 elements without visible change. The problem is non-linear, the steady-state coupled solution is reached with a transient simulation [Voss and Provost, 2010]. Time was discretized with 60 s time steps for the first 1000 steps. When stabilization was not reached at that stage, 120 s time steps were used. The simulation was considered successful when increasing the simulation duration had no significant effects on the result.

The numerical model does not simulate the water table. The height of the water table was estimated with the point water head  $h_m$  [Luszczynski, 1961]) of the upper boundary nodes:

$$h_p = \frac{p}{\rho g} + z \quad (7.30)$$

where  $p$  is the fluid pressure and  $\rho$  the fluid density estimated from the concentration value and Eq. 7.17.

Two contrasting values of recharge parameter  $\chi$  were chosen for the simulations (Table 7.1). Other flow and transport parameters were kept constant for the two simulations (Table 7.2). For both cases, velocity-dependent dispersion effects were considered to be dominant and molecular diffusivity was not taken into account. For the case 1 ( $\chi = 1 \times 10^{-5}$ ), stabilization was reached after 8000 min, while 2000 min were sufficient for the case 2 ( $\chi = \times 10^{-3}$ ).

## 7. MODELING BASAL AQUIFERS

---

Parameter	Case 1	Case 2
$\chi = r/K$ [-]	$1 \times 10^{-5}$	$1 \times 10^{-3}$
$r$ [m/s]	$1 \times 10^{-7}$	$1 \times 10^{-5}$
$K$ [m/s]	$1 \times 10^{-2}$	$1 \times 10^{-2}$

**Table 7.1:** Parameter values chosen for the two simulations.

Parameter	Value	Description
$L$	10 m	Semi-length of the island
$H$	-1 m	Depth of the substratum
$\xi$	10	Aspect ratio $L/H$
$\phi$	0.35	Porosity
$D_m$	0 m <sup>2</sup> /s	Molecular diffusivity
$\alpha_L$	0.1 m	Longitudinal dispersivity coefficient
$r_\alpha$	0.1	Dispersivity coefficients ratio $\alpha_T/\alpha_L$
$K_r$	1	Permeability ratio $K_x/K_z$
$\mu$	0.001 kg/ms	Fluid viscosity

**Table 7.2:** Values and descriptions of parameters kept constant for the simulations.

In the first configuration (case 1 Fig. 7.8), seawater invades a large part of the model. A thin freshwater lens is formed above a relatively thick transition zone. In the first case (Fig. 7.9), the SWI calculated with the analytical models are close to one-another but apparently under-estimate the depth to seawater. The water table of the numerical model is higher than the analytical estimates. The freshwater model markedly over-estimates the thickness of the aquifer available for freshwater flow, which induces a flat water table. The Ghyben-Herzberg estimate is closer to the modeled water table, but the model is slightly higher. This can be interpreted by mixing effects and vertical head gradients, disregarded in the Ghyben-Herzberg model.

Expectedly, multiplying  $\chi$  by a factor of 100 (case 2) has a major effect on seawater intrusion. In this second configuration, seawater forms a small edge at the bottom left portion of the domain. Velocities are higher, and the transition zone is thin. The three estimates of water table are closer in the second case. The water table estimated from the Ghyben-Herzberg model ( $s'_2$ ) is higher than the numerical model estimate, because groundwater is supposed to discharge through a point at the coast, which results in an under-estimation of the transmissivity. On the opposite, the water table estimated with the freshwater aquifer model is slightly below the model, because it over-estimates transmissivity in the vicinity of the coast. SWI  $s'_2$  and  $s'_3$  are close to the numerical model 50% mixing line, but the Verruijt solution ( $s'_3$ ) fits slightly better.

The shift between the analytical solutions and the numerical model can be described by a relative error  $\epsilon'$ :

$$\epsilon'(x) = \frac{\epsilon(x)}{H} = \frac{h_i(x) - h_p(x)}{H} = h'_i(x) - h'_p(x) \quad (7.31)$$

where  $h_i$  is the analytical estimate of the water table height (either freshwater model or Ghyben-Herzberg model), and  $h_p$  the point water head of the top boundary of the numerical model (Eq. 7.30). Errors are smaller than 1% in the case 1, and smaller than 0.02% in the case 2 (Fig. 7.12). As detailed previously, errors are negative as long as the analytical model over-estimates aquifer transmissivity and positive in the opposite case. Interestingly, the error of the freshwater model does not converge to zero toward the center of the island.

In the case 1 (large seawater intrusion, Fig. 7.9), the numerical model predicts a water table level of 0.008 at the center of the island ( $x' = \xi$ ). In the case 2 (limited seawater intrusion, 7.9), this level reaches 0.07. Assuming an aquifer thickness  $H$  of 1000 m, which is realistic, this would respectively corresponds to 8 m and 70 m above sea level.

At the center of the island, relative errors of  $h'_1$  are respectively -1% and -0.01% for cases 1 and 2 (Fig.7.12). With  $H = 1000$  m, this leads to absolute error smaller than 10 m and 0.1 m respectively. The solution  $h'_2$  inferred from

## 7. MODELING BASAL AQUIFERS

---

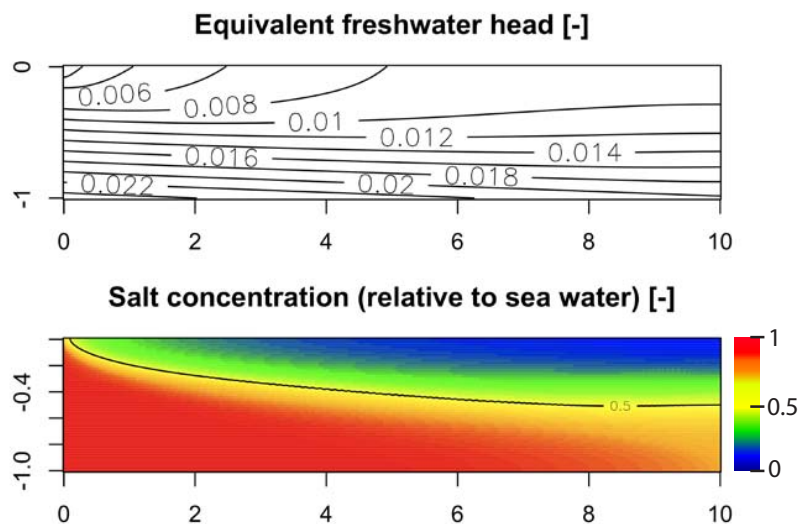


**Figure 7.8:** Result of the coupled simulation for case 1 ( $\chi = 1 \times 10^{-5}$ ). Fields of equivalent freshwater head (top) and relative salt concentration (bottom). The 50% mixing line ( $c' = 0.5$ ) is reported with a black line.

the Ghyben-Herzberg model is more accurate for low  $\chi$  and  $\xi$  values, but overestimate transmissivity for larger values.

In this section, the numerical model was considered as the reference. Yet, it could as well be inaccurate. Despite the precautions, the actual steady state may have not been reached at the end the simulation *Abarca et al.* [2007]; *Bues and Oltean* [2000]. Secondly, though flow and transport parameters were chosen to represent at best a “classic” configuration, conclusions obtained with this parameter set may not be applicable in any context. Third the water table was not modeled (the roof of the aquifer was maintained to sea level), which induces an underestimation of the aquifer transmissivity.

### 7.4 Discussion

For low values of  $\chi$  and  $\xi$ , seawater intrusion induces an apparent reduction of the transmissivity for freshwater flow. As a consequence, the freshwater aquifer model (Eq. 7.4) tends to under-estimate the height of the water-table. Yet, given the flat geometry of the water table for weak  $\chi$  values, the relative error  $\epsilon'$  remains small (less than 1%). The solution derived from the Ghyben-Herzberg model is more accurate when seawater intrusion is large (small  $\chi$  and  $\xi$  values), but

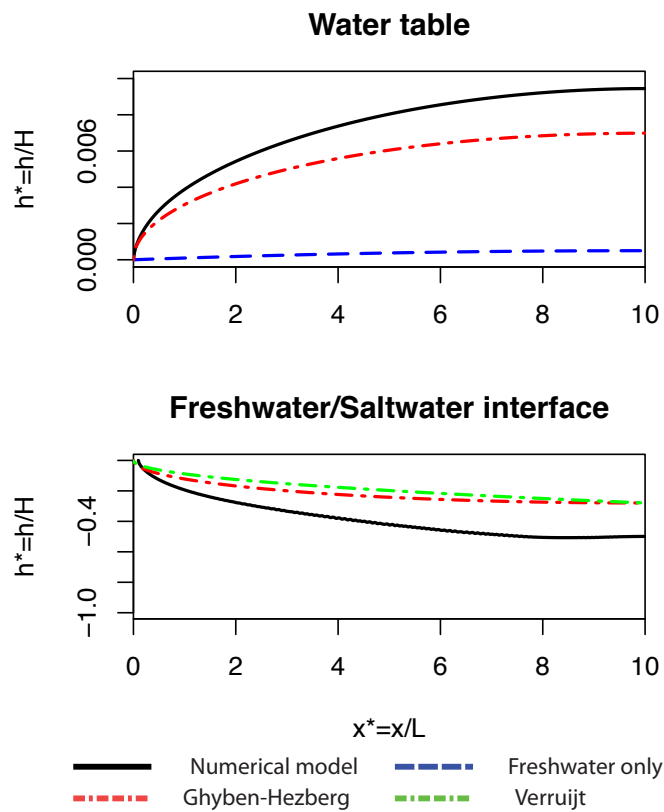


**Figure 7.9:** Case 1. Top: water table heights from the numerical model (continuous line), and the two analytical solutions (dashed lines). Bottom: SWI from the numerical model, the Ghyben-Hezberg model, and the Verruijt models.

## 7. MODELING BASAL AQUIFERS

---

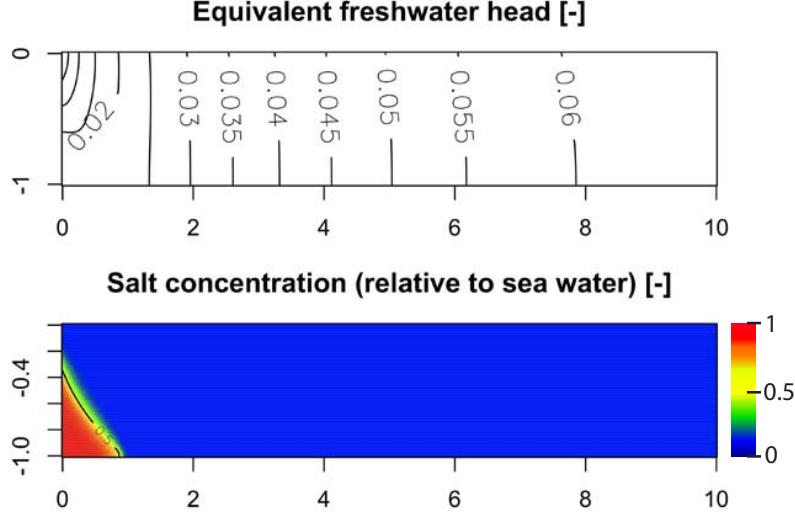


**Figure 7.10:** Result of the coupled simulation for case 2 ( $\chi = 1 \times 10^{-3}$ ). Fields of equivalent freshwater head (top) and relative salt concentration (bottom). The 50% mixing line ( $c' = 0.5$ ) is reported with a black line.

tends to over-estimate transmissivity when seawater intrusion becomes negligible. Therefore, Eq. 7.4 provides an acceptable estimate for all values of  $\chi$  and  $\xi$ .

The sensitivity of  $h'_1$  (Eq. 7.4) to parameters  $\chi$  and  $\xi$  can be quantified with scaled sensitivity parameters:

$$s_\chi = \chi \frac{\partial h'_1}{\partial \chi} = \frac{\chi(2\xi x' - x'^2)}{2\sqrt{-\chi x'^2 + \chi \xi x' + 1}} \quad (7.32)$$

$$s_\xi = \xi \frac{\partial h'_1}{\partial \xi} = \frac{\chi \xi x'}{\sqrt{-\chi x'^2 + \chi \xi x' + 1}} \quad (7.33)$$

where  $s_\xi$  and  $s_\chi$  denote the scaled sensitivity of  $h'_1$  to parameters  $\xi$  and  $\chi$  respectively. The ratio of sensitivities  $r_s$  reads:

$$r_s = \frac{s_\chi}{s_\xi} = 1 - \frac{x'}{2\xi} \quad (7.34)$$

At mid-slope,  $x' = \xi/2$  and  $r_s = 3/4$ , which means that the sensitivity of  $h'_1$  to parameters  $\chi$  and  $\xi$  is of the same order of magnitude.

Considering a reference recharge rate of 1 m/y ( $3 \times 10^{-8}$  m/s) and hydraulic conductivity ranging between  $3 \times 10^{-2}$  and  $3 \times 10^{-6}$  m/s, parameter  $\chi$  ranges between  $1 \times 10^{-6}$  and  $1 \times 10^{-2}$ . Assuming that they can be classified under the strip

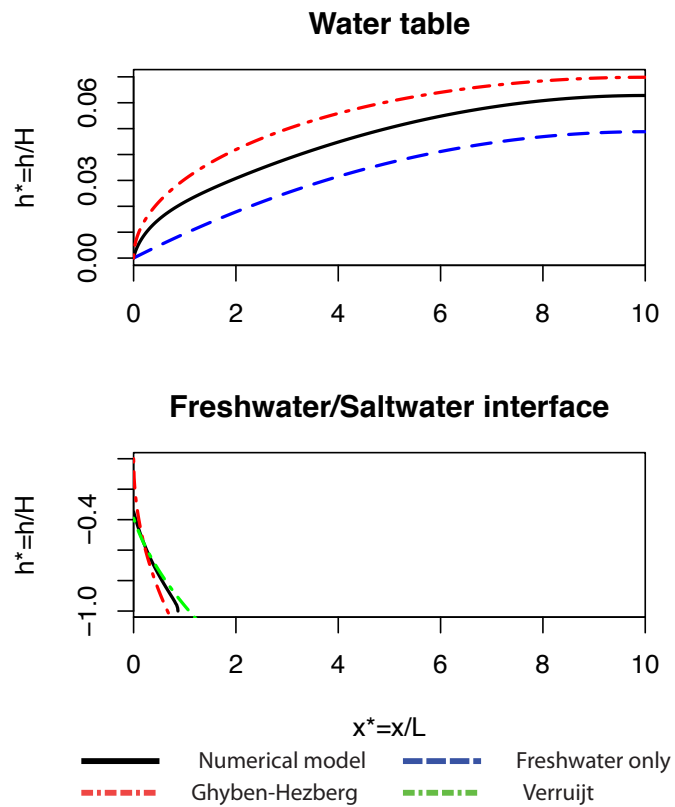


**Figure 7.11:** Case 2. Top: water table heights from the numerical model (continuous line), and the two analytical solutions (dashed lines). Bottom: SWI from the numerical model, the Ghyben-Hezberg model, and the Verruijt model

## 7. MODELING BASAL AQUIFERS

---

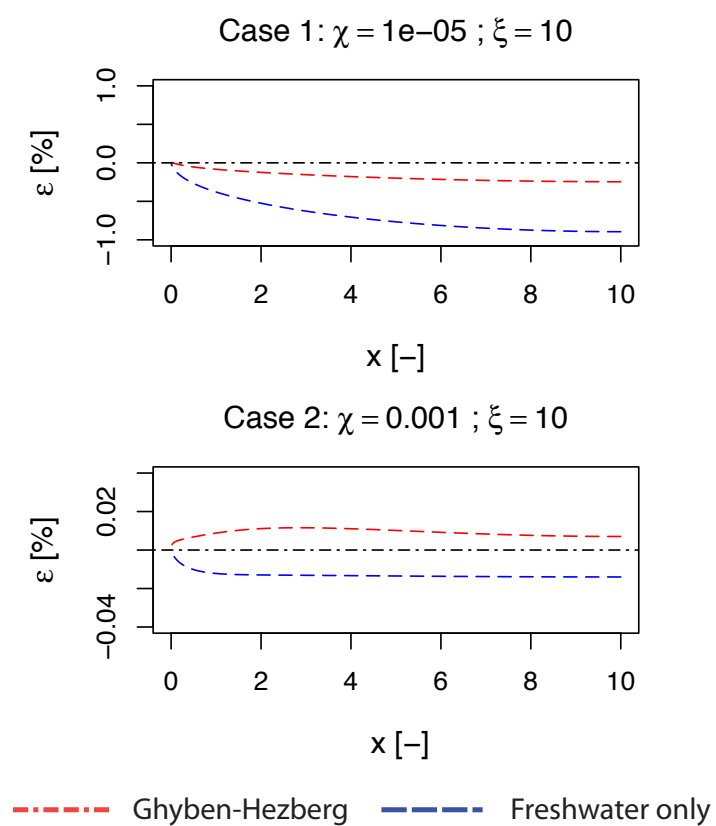


**Figure 7.12:** Relative error  $\epsilon'$  on water table estimates with respect to the numerical model estimate

island model (Fig. 7.2), most of the basaltic volcanic islands present a semi-length ranging between 3 and 30 km. Due to weathering effects and fracture closure (Eq. 7.1), permeability decreases with depth. The portion of the aquifer below 1000 m is not expected to have a significant effect on groundwater flow. An equivalent aquifer thickness of 1000 m may reasonably be assumed. Under these assumptions, the aspect ratio  $\xi$  ranges between 3 and 30.

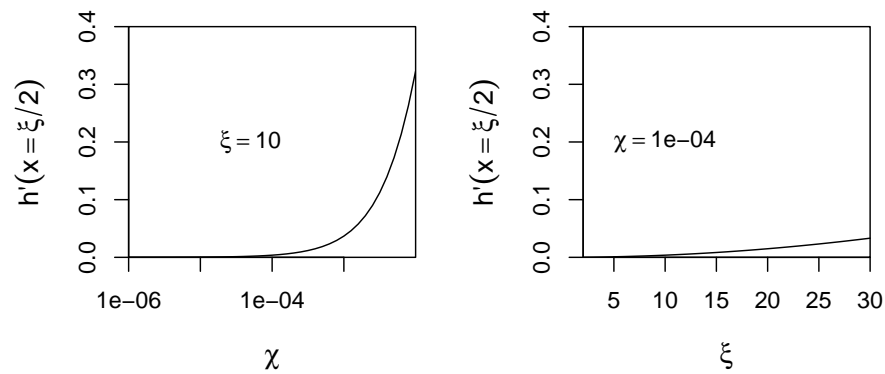


**Figure 7.13:** Freshwater aquifer water table height  $h'_1$  at a mid-distance from the coast ( $x' = \xi/2$ ) for varying  $\chi$  (left) and  $\xi$  values (right).

At mid-slope, the water table height is shown to be equally sensitive to relative variations of  $\chi$  and  $\xi$ . Given the much wider range of variation of  $\chi$ , this parameter explains the contrasting configurations reported in the literature (Fig. 7.13).

The shape of the water table for various values of  $\chi$  is presented in Fig. 7.14, and highlights very contrasting geometries. The wide range of variation of parameter  $\chi = r/K$  is to a great extent attributed to variations of the hydraulic conductivity. This parameter is therefore identified as the variable explaining the rise of the water table at high elevation. Contrasts in groundwater recharge alone cannot explain the occurrence of very high water tables, though humid environment can favor rock weathering and reduce permeability.

## 7. MODELING BASAL AQUIFERS

---

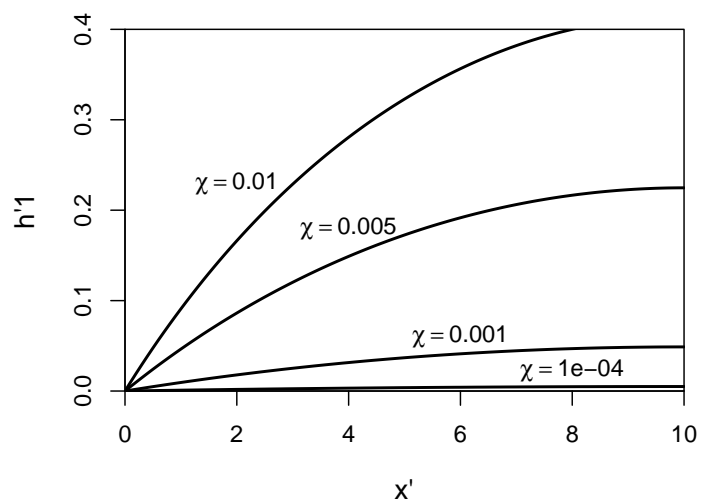


**Figure 7.14:** Shape of the water table height  $h'_1$  for various values of  $\chi$ .

## 7.5 Conclusion

In an attempt to explain the contrasting hydrogeological settings of basaltic volcanic islands, the parameters controlling the height of basal aquifers have been investigated. This aquifer is unconfined, affected by seawater intrusion and characterized by an impermeable boundary at the centre of the island. Analytical solutions for the water table height have been derived for the case of a freshwater aquifer, and the case of an aquifer subjected to seawater intrusion under the Ghyben-Herzberg assumptions. These solutions have been confronted to a variable-density flow and transport model. The results show that the relative error of analytical estimates are small. The Ghyben-Herzberg model performs better when seawater intrusion is large but over-estimates transmissivity in other situations. The freshwater aquifer solution proposes a relatively reliable estimate of water table height in contrasting configurations and allows the comparison of the water table height for a wide range of  $\chi$  and  $\xi$  values, the recharge parameter and aspect ratio respectively. Variations of  $\chi$ , and in particular the hydraulic conductivity  $K$  explains the contrasting hydrogeological settings of volcanic islands basal aquifers.



## Chapter 8

# The basal aquifer of Santa Cruz Island

# The basal aquifer of Santa Cruz Island\*

---

## Abstract

The main shield of Santa Cruz Island is composed of young piles of thick basaltic lava flows fractured by a dense network of cooling joints. At the southern coast, these formations are dissected by numerous fault scarps deep enough to reach the basal aquifer. Hydraulic properties were estimated by independent methods at several scales (1-5 km, 10-100 m, 1-10m). Observed tidal fluctuations in the aquifer fitted well to a 1D-analytical wave propagation model with *homogeneous* hydraulic properties (i.e. disregarding faults). The regional hydraulic diffusivity was estimated to  $D \approx 140 \text{ m}^2/\text{s}$ , and corresponding hydraulic conductivity to  $K \approx 10^{-3} \text{ m/s}$ . This is compatible with local estimates obtained from hydraulic tests. Fracture mapping at the outcrop revealed that the permeability of cooling joints could explain alone the high regional permeability. Fault scarps are locally highly conductive, but do not appear to behave as regional permeable anomalies. Faults are in their initial stage of tectonic development with discontinuous *en echelon* tension joints and ramifications. The network of highly conductive scarps does not percolate, and has little effect on the regional diffusivity. Cooling joints and interflow voids confer a high permeability to basaltic formations and explain the observed weak hydraulic gradient and seawater intrusion.

---

\* In collaboration with Benoit Deffontaines<sup>1</sup>, Tan Minh Vu<sup>2</sup>, Pierre Adler<sup>2</sup>, Sophie Violette<sup>2</sup>, and Justine Lichter<sup>2</sup>. Will be submitted shortly.

<sup>1</sup> UPE, GTMC Laboratory, Marne-La-Vallée, France

<sup>2</sup> UPMC Univ. Paris 6 & CNRS, UMR Sisyphe, 4 place Jussieu, 75252 Paris cedex 05, France

## 8.1 Introduction

If they are sufficiently connected, fracture networks are said to “percolate”, and they increase the permeability of a geological medium [Adler and Thovert, 1999; Berkowitz and Balberg, 1993; Mourzenko *et al.*, 2005]. Faults are known to play a major effect over regional groundwater flow [Caine *et al.*, 1996], they are often transmissive and regarded as preferential locations for bore wells (e.g. [Lachasagne *et al.*, 2001]). Yet, such conductive anomalies may have undesirable effects in coastal areas, inducing preferential drainage and seawater intrusion [Post, 2005].

Santa Cruz is the most populated and second largest island of the Galapagos Archipelago. Relatively monotonous dike-free basaltic lava flows compose the bulk of the edifice. At the south, numerous fault scarps dissect the coastal apron [Bow, 1979]. These scarps are sufficiently deep and wide to provide a direct access to the *basal* aquifer in connection with the ocean. Though it is brackish, this aquifer represents the main perennial water resource on the island. The location of the main city of the island, *Puerto Ayora* was probably chosen for the accessibility of this resource.

One may wonder if these fault scarps, considered as a providence because they supply a direct access to the aquifer, may not regretfully behave as conductive anomalies, causing strong seawater intrusion and freshwater discharge to the ocean.

We address this issue from an multi-scale hydrogeological study. Faults were mapped with satellite imagery, and fracture networks characterized at the local and regional scales from field work and satellite imagery. The propagation of the tidal signal was tracked by means of water level monitoring and analyzed with a 1D-analytical model. This information is then assembled to form a comprehensive analysis and conclude on the influence on fault scarps on the hydrogeology of the island.

## 8.2 Geographical settings

### 8.2.1 Geology

Santa Cruz island has an elliptical shape, with 40 km and 30 km main axes and a total surface of 985 km<sup>2</sup>. The island culminates at 855 m.a.s.l. [d’Ozouville *et al.*, 2008b], and has a subdued profile with a large, gently dipping coastal apron [Cullen *et al.*, 1987].

Younger formations rests over old tholeiitic and ferro-basaltic volcanic units, of the *platform series* dated to 1.1-1.3 Ma [Bow, 1979; Geist and Reynolds, 1998].

## 8. THE BASAL AQUIFER OF SANTA CRUZ ISLAND

These formations are part of the oldest sub-province of the Galapagos Archipelago which comprises Española and the fault block islands of Santa Fe, Baltra and north Seymour [McBirney and Williams, 1969]. Baltra and Santa Cruz islands are separated by a narrow N-NE trending grabben, the Itabaca channel (Fig. 8.1). The *Platform series* locally outcrop at the northern coast of Santa Cruz Island and reveal basal submarine flows and limestone overlain by a tier of thin subaerial *pahoehoe* and *aa'* flows [Bow, 1979]. Emerged bioclastic sand levels with bioclasts, as well as sub-aerial lavas overlain by submarine units are evidences of both uplift and subsidence.

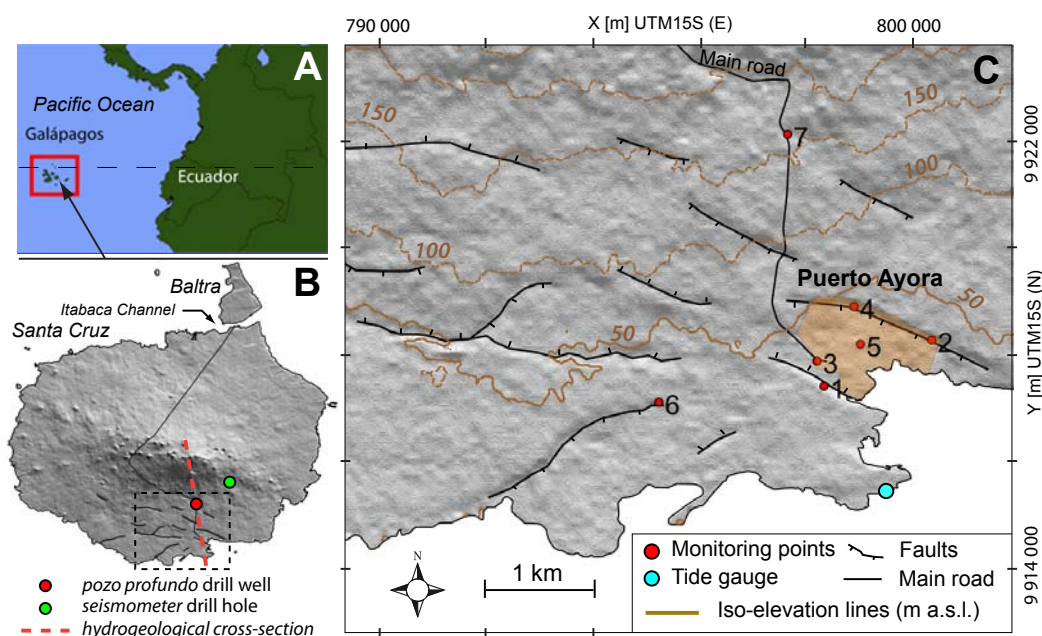


**Figure 8.1:** (A) Geographical context of the Galapagos Archipelago (B) Santa Cruz and Baltra Islands, shaded relief map from SRTM DEM. Dots are the location of drill holes : (1) pozo profundo (loc. 7) and (2) seismometer hole (dry well). Dashed red line is the cross-section presented in Fig. 8.3 (C) The coastal apron in the vicinity of Puerto Ayora, shaded relief map from radargrammetric DEM [d'Ozouville *et al.*, 2008b]. Numbered red dots refer to basal aquifer monitoring locations listed in Table 8.1.

The bulk of Santa Cruz is composed of alkali-basaltic *pahoehoe* flows, the *Shield Series*, with ages ranging between  $590 \pm 270$  ka and  $24 \pm 11$  ka [Geist and Reynolds, 1998]. Available geological logs describe piles of compact 2-10 m thick *aa'* and *pahoehoe* grey lava flows with numerous voids and cooling joints,

but few pyroclastic interbeddings [Dixon Hydrogeology Limited, 1996; Woodward *et al.*, 1996]. Lava erupted from series of WSW-ENE aligned vents, which gave the island its elliptical shape. The culminating eruptive episode left large cinder cones on the summit zone, and an irregular pyroclastic blanket of finely comminuted ash. A part of these cones was subsequently flooded by alkali-olivine and hawaiite-type short flows from isolated fissures and small shields aligned along the summit axis [Bow, 1979].

In the summit part of Santa Cruz pit craters formed by the collapse of high level magmatic reservoirs reveal relatively monotonous 1-2 m thick massive lava flows. Numerous lava tunnels have been identified on Santa Cruz, sometimes kilometer long and up to 10 m in diameter. A small 2 m high tunnel was found 92 m below ground level in the drill hole executed at mid-slope, 7 km from the coast and 260 m a.s.l. [Woodward *et al.*, 1996].

At the exception of the windward southern slopes at high elevation (> 200 m a.s.l.), climatic conditions are dry over the island, the relatively young *Shield Series* and weakly weathered.

*Shield Series* of the southern low elevation apron are dissected by E-SE trending antithetic sub-vertical normal faults forming a grabben and a protected bay, Bahia Academia [Bow, 1979] (Figs. 8.2 and 8.6). The faults form large scarps and reveal large outcrops in and around the city (Fig. 8.2).

### 8.2.2 Climate

The climate of Santa Cruz island is oceanic, with temperatures anomalously low due to the upwelling of the cold *Humboldt* ocean current [Eden and Timmermann, 2004]. Median annual rainfall is weak: 277 mm in Puerto Ayora (4 m a.s.l.) and 800 mm at Bellavista (180 m a.s.l.) (Data from the Charles Darwin Foundation). Spatial and temporal variability is strong. Due to the orographic effect, contrasts are more acute during the cool *garúa* season, when a fog layer is observed along the windward slope from 400 m a.s.l. up to the summit [Pryet *et al.*, 2012; Trueman and d'Ozouville, 2010]. Inter-annual variations are dominated by the Niño/Niña alternates, which are characterized by heavy rainfalls and droughts respectively [Snell and Rea, 1999].

### 8.2.3 Hydrogeology

Water resources are scarce on Santa Cruz Island. At the exception of intermittent short streams and few springs in the highlands, there is no surface water on the island. As it was the case for the first settlers, groundwater is abstracted from the brackish basal aquifer in fault scarps of the coastal apron around Puerto Ayora

## 8. THE BASAL AQUIFER OF SANTA CRUZ ISLAND

---

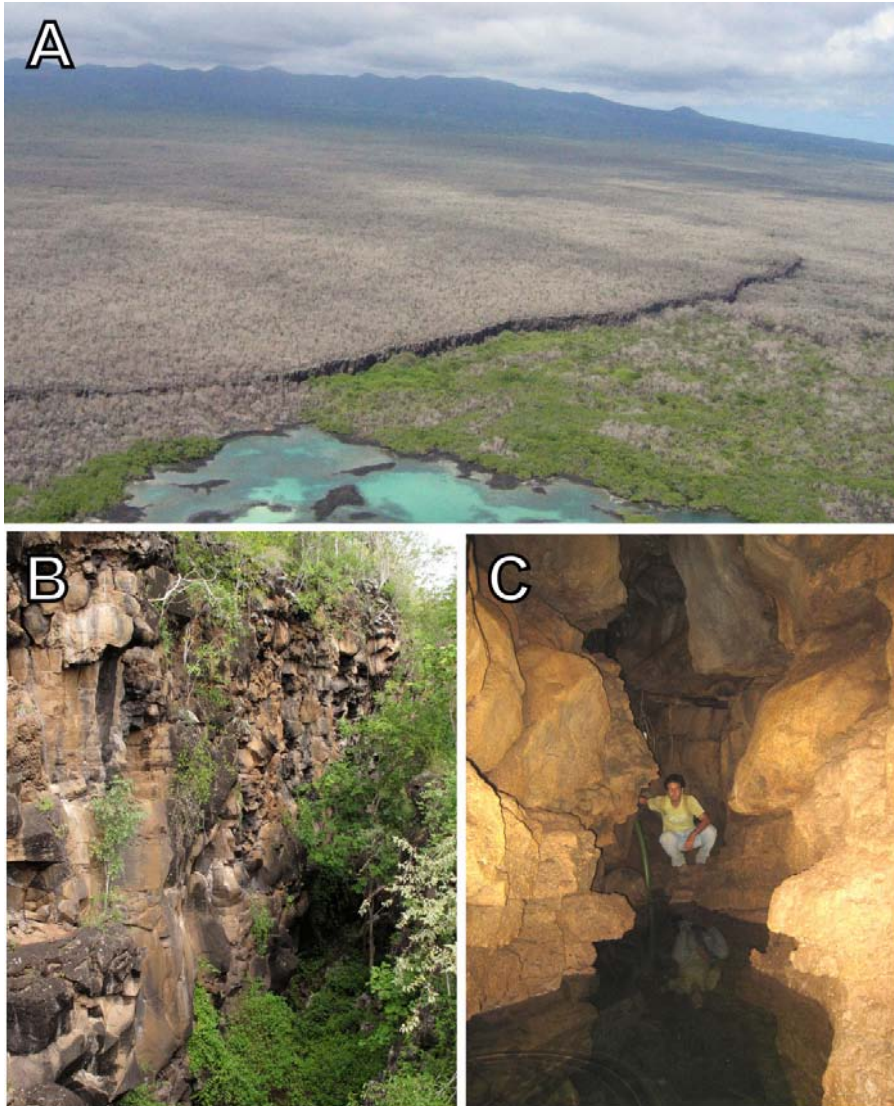


**Figure 8.2:** Fault scarps on the southern apron of Santa Cruz Island. (A) Aerial view of the western end of *Grieta La Camiseta*, (B) *Grieta Finch*, (C) the water table is visible inside *Grieta Baranco*.

[d'Ozouville, 2007a].

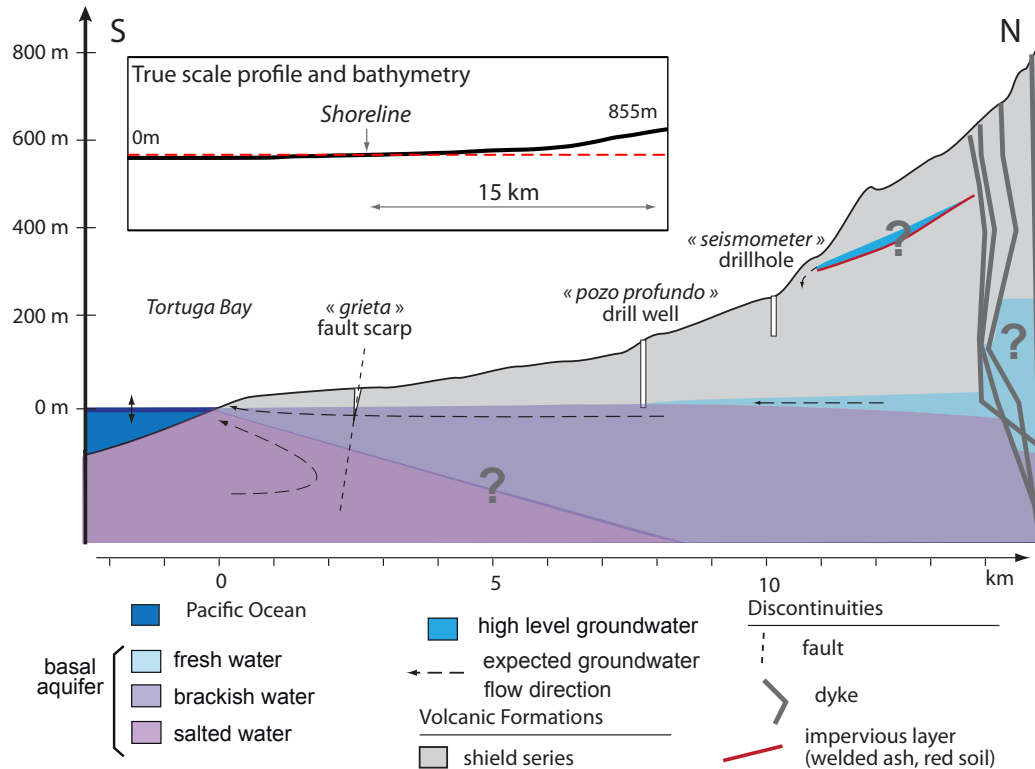


**Figure 8.3:** Hydrogeological diagram of the basal aquifer of Santa Cruz Island. Refer to inset on Fig. 8.1 for the location of this cross-section. Seawater intrusion is extensive and hydraulic gradients are weak. At the *pozo profundo* drill well 4.7 km inland, the water table is close to mean sea level and groundwater is brackish.

The *basal aquifer* is the only groundwater body identified so far on Santa Cruz Island (Fig. 8.3). Hydraulic gradients are weak ( $< 1 \times 10^{-4}$ ) and the water table remains at low elevation. Tidal oscillations are detected at all monitoring locations (Table 8.1). Due to seawater intrusion, groundwater is brackish up to 4.7 km, and possibly further inland (see groundwater electrical conductivities listed in Table 8.1).

Only two pairs of drill holes have been bored on the island. A pair of ca. 160 m deep wells drilled 4.7 km from the coast intercept the basal aquifer: the *pozo profundo*, is a pumping well exploited by the municipality, and the *pozo testigo* is an observation well located at a distance of 20 m (see inset Fig. 8.1 and Fig. 8.3). These wells were sited along a fracture identified from aerial photography [Dixon Hydrogeology Limited, 1996], but this fracture could hardly be identified

## 8. THE BASAL AQUIFER OF SANTA CRUZ ISLAND

---

	Name	Long.	Lat.	Dist. sea	$\alpha$	$\Delta t$	$\chi$
1	Finch	-90.320	-0.746	0.48	0.27	1.42	5.4
2	FCD	-90.302	-0.738	1.21	0.28	1.08	8.1
3	Ingala	-90.321	-0.742	1.14	0.22	1.92	3.1
4	Baranco	-90.315	-0.733	1.17	0.12	2.25	2.5
5	Mission	-90.314	-0.739	0.68	0.23	1.5	4.0
6	Camiseta	-90.347	-0.749	1.57	0.19	2.75	2.8
7	Pozo testigo	-90.326	-0.704	4.77	0.009	7.17	1.9

**Table 8.1:** Location of monitoring points in the basal aquifer, geographical coordinates (WGS84) and distance to the sea (km). With  $\alpha$  [-], the attenuation and  $\Delta t$  [hours] the phase shift with respect to the tidal signal at the coast. Indicative values of groundwater conductivity  $\chi$  [mS/cm] are provided, measurements were performed with a field conductivimeter ca. 10 cm below the surface of the water table in July 2009

on recent satellite imagery and digital elevation model. Well characteristics are reported in Table 8.2. Another pair of deep drill holes were bored in the highlands 7.6 km from the coast, 250 m a.s.l (see inset Fig. 8.1 and Fig. 8.3). The holes are ca. 100 m deep and their bottom is located at 150 m a.s.l. These holes were dry which confirms that the basal aquifer remains at low elevation on this island [Woodward *et al.*, 1996].

In the observation well, a 8 m thick massive unit is reported 4 m above static water level, and is underlain by a very conductive unit in the saturated zone. If it is continuous, the massive unit could constitute a confining unit to the basal aquifer. The geological log is unavailable for the pumping well, but a major fracture is reported 2.5 m below static water level. A pumping rate of 9 L/s was considered as sustainable by the consultant [Dixon *Hydrogeology Limited*, 1996], since it induces a long-term drawdown of about 2 m in the pumping well and the water level in the well remains above the transmissive fracture.

The *pozo profundo* is the deepest drill hole available on Santa Cruz island but ends close to sea level, before reaching any impervious substratum [Dixon *Hydrogeology Limited*, 1996]. The old *platform series* outcropping on the north-eastern coast, could be found beneath the *Shield series* and constitute the substratum, but its actual depth and extension, as well as hydraulic properties are much a

## 8.2 Geographical settings

---

characteristic	observation well	pumping well
	<i>pozo testigo</i>	<i>pozo profundo</i>
ground level [m a.s.l.]	151.74	150.41
total depth [m]	162.5	168.8
total diameter [mm]	127	305
casing diameter [mm]	-	205
screen level [m b.g.l.]	-	157.8 to 163.8
static water level [m b.g.l.]	151.73	150.95
static water level [m a.s.l.]	+0.01	(-0.54)
pump level [m b.g.l.]	-	154.2

**Table 8.2:** Characteristics of the two wells (loc. 7, Fig. 8.1). “m a.s.l.” stands for meters “above sea level”, “m b.g.l.” stands for meters “below ground level”. Ground level may not be accurate, and static levels were not measured simultaneously. Static water level above sea level are provided as indicative value, a negative value is not realistic.

## 8. THE BASAL AQUIFER OF SANTA CRUZ ISLAND

---

matter of speculations.

In similar environments, three effects contribute to the reduction of permeability with depth: pore filling by secondary mineralization, compaction, and fracture closure. From observations made by *Keller et al.* [1979] and *Kauahikaua* [1993], the maximum effective depth of basaltic insular aquifers is often considered to range between 1000 and 2000 m under ground level [*Gingerich*, 1998]. Basalts fracture closure can be modeled with an exponential law, stating that permeability is divided by a factor of 100 every 400-1700 m [*Ougier-Simonin et al.*, 2011; *Saar and Manga*, 2004]. In these conditions, even though the actual depth of the substratum is not known in Santa Cruz Island, there is little doubt that the effective depth of the aquifer exceeds 1000 m below sea level and this value will be assumed in further developments.

Interestingly enough to mention it, the observation well and the dry seismometer drill holes are reported to “breathe”, sucking and blowing air probably in accordance with tidal oscillations (*Dixon Hydrogeology Limited* [1996]; *Woodward et al.* [1996] and *pers. comm* John Derr, USGS). This is explained by the relatively high amplitude of tidal fluctuations in the aquifer, and suggests that a continuous impervious layer confines the unsaturated zone (probably the soil).

Due to the lack of drill holes in the highlands, conditions of occurrence of high-level groundwater is poorly understood on Santa Cruz. Yet, a small spring is identified at the base of a partly collapsed pyroclastic cone in the summit area above Santa Rosa village, and another spring located in a short and shallow ravine at 580 m a.s.l. This latter spring is intermittent but exploited by locals farmers. From an air-borne electromagnetic survey, *d’Ozouville et al.* [2008a] interpreted an extensive low-resistivity layer as a possible perched aquifer.

### 8.3 Structural analysis and fracture mapping

#### 8.3.1 Regional structural context

Faults with vertical offset were digitalized from a 20 m radargrammetric DEM [*d’Ozouville et al.*, 2008b] (Fig. 8.1). Faults and tension joints cracks have been digitalized from the high resolution image available on Google Earth® exported for further processing to a GIS software. Thin soils and sparse vegetation allowed a relatively comprehensive mapping. It was more complex in the urbanized zone of Puerto Ayora, where short cracks without significant vertical offset were identified on the field but were not visible on the satellite image.

Normal fault segments are 2 to 6 km long (Fig. 8.1) with a downthrow up to 10 m. Fault scarps may be locally as wide as 4 m. The distance between sub-parallel individual fault segments ranges between 1-3 km.

### 8.3 Structural analysis and fracture mapping

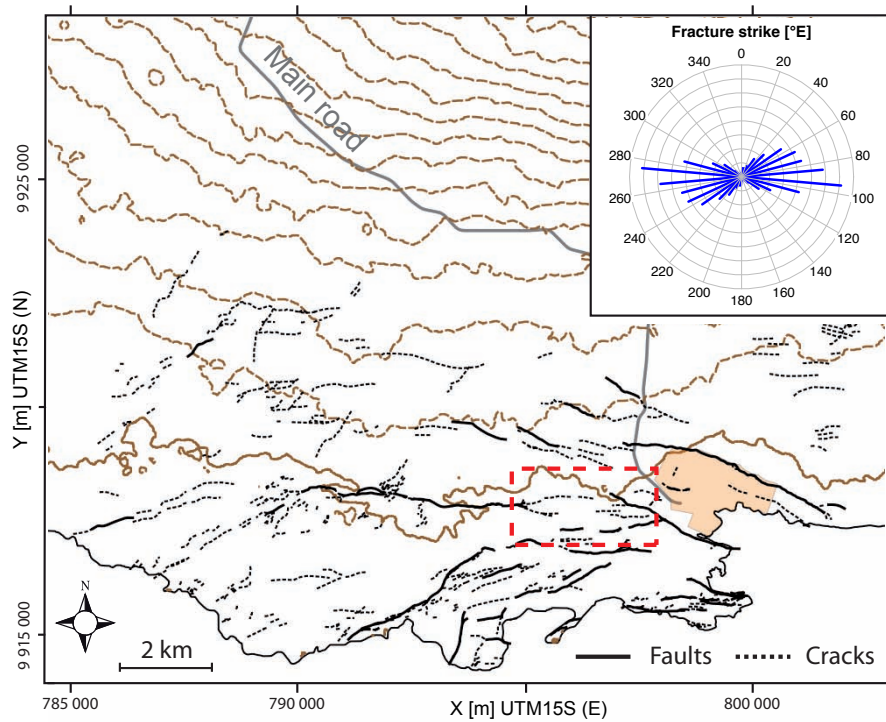


**Figure 8.4:** Fractures mapped with Google Earth® provided by Digital Globe ©2011 and LeadDog Consulting ©2011. The radial plot (top-right) describes the distribution of fault segments orientation. Red dashed outlined area is interpreted in Fig. 8.5. Faults were mapped by Justine Lichter with Qgis ([www.qgis.org](http://www.qgis.org)).

## 8. THE BASAL AQUIFER OF SANTA CRUZ ISLAND

---

In addition to the major fault segments with vertical offset, numerous cracks were mapped on the satellite image (Fig. 8.4). Cracks are neither perfectly aligned to fault segments nor continuous. Instead, the tips of fault segments progressively ramify into discontinuous en echelon tension joints cracks (Fig. 8.5).

The orientation of fault segments range between  $N50^\circ E$  and  $N120^\circ E$ , with a dominant direction at  $N95^\circ E$  (Fig. 8.4).

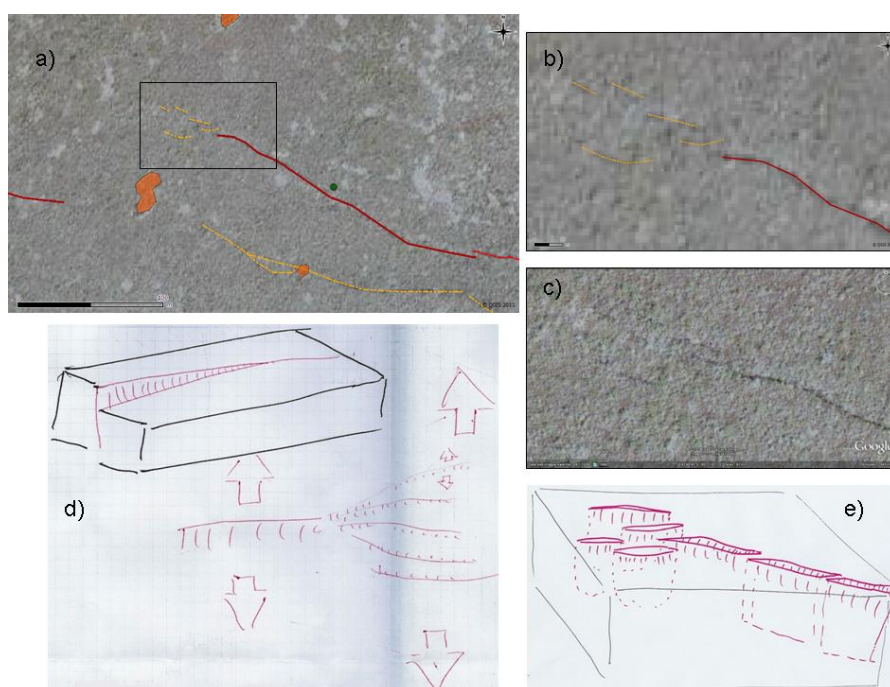


**Figure 8.5:** Block diagram and Google-Earth images displaying the termination of a fault with a ramp and ramified tension joints. Refer to outline on Fig. 8.4 for the location. Fracture mapping was performed by Justine Lichter, and the diagram by Benoit Deffontaines.

Two antithetic normal faults form a grabben in Puerto Ayora (Fig. 8.6) [Bow, 1979]. The central compartment (hanging wall) is affected by a flexure at the border and is cut by sub-parallel fault segments without vertical downthrow. At many locations in the city, fault scarps are sufficiently wide and free of rubble for the basal aquifer be reached, at a depth varying between 3 and ca. 10 m below ground.

Flank collapse and gravitationnal deformation are common in volcanic islands. A spectacular example in Galapagos is Volcan Ecuador at the north of Isabela

### 8.3 Structural analysis and fracture mapping

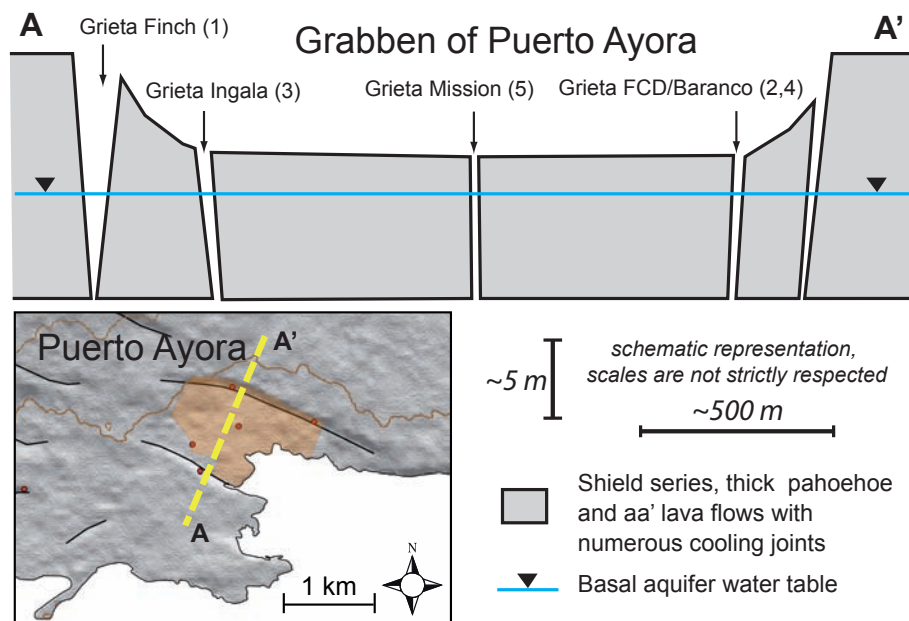


**Figure 8.6:** Structural diagram of Puerto Ayora grabben. Border faults present marked vertical offset, up to 5 m. Faults in the grabben are less continuous and do not present vertical offset. The basal aquifer water table is reached at 3-10 m below ground, in faults scarps sufficiently wide and free of rubble.

## 8. THE BASAL AQUIFER OF SANTA CRUZ ISLAND

---

Island *Geist et al.* [2002]. The configuration in Puerto Ayora appears similar to that of Hawaii Island (US), the southern flank of the Kilauea volcano is dissected by numerous faults, apparently similar to that of Santa Cruz [*Martel and Langley*, 2006; *Parfitt and Peacock*, 2001; *Podolsky and Roberts*, 2008]. Processes at the origin of these faults are still discussed, but most authors relate faulting to the deformation of the edifice induced by magmatic stresses and large scale thrust over the sea floor *Parfitt and Peacock* [2001].

Faults at the south of Santa Cruz trend from ENE to ESE, which confer them a somehow horse-shoe organization, typical of slump. Gravitational spreading and flank collapse could be invoked for the faults. Yet, the Galapagos Archipelago lies on a shallow extensive platform, and available bathymetric data at <http://www.geomapapp.org> present gently sloping bathymetry offshore Santa Cruz, in continuation with the gently sloping coastal apron. In these conditions, the submerged flank should buttress the island and avoid slumping.

Faults may therefore rather be the consequence of regional tectonic stresses. Given the ESE orientation of the main eruptive ridge of Santa Cruz, a regional NNE-SSW extensive tectonic stress regime present during the period of volcanic activity may have persisted, inducing the observed faulting. This extensional regime, may as well account for the faults observed in Baltra *Simkin* [1984] and Santa Fe Island [*Geist et al.*, 1985], which could confirm the regional extent of the extensional stresses.

The continuity at depth of observed fault segments is a matter of debate and can hardly be addressed from surface observations alone. At depth, isolated fault segments may join to form an individual fault as proposed in Hawaii by *Parfitt and Peacock* [2001].

### 8.3.2 Field fracture mapping

Numerous outcrops are available in the fault scarps around Puerto Ayora. They reveal thick lava flows of the *Shield series*, a majority of which of *pahoehoe* type with massive fractured cores (e.g. Fig. 8.7). Locally, massive units are interlayered by scoriaceous interbeddings and interflow voids attributed to summit and bottom of *aa'* flows. Though they are reported in the drill logs executed further inland, no pyroclastic level was found.

A dense network of fractures is observed on all the outcrops. As described by *Khaleel* [1989], fractures in lava flows can be separated into two categories: sub-vertical cooling joints, and sub-horizontal interflows.

A graduated tape was stretched horizontally across each unit of the outcrop faces. The aperture, trace length and dip angle of each intersected sub-vertical fractures were measured. As it was often the case, the tips of the sub-vertical

### 8.3 Structural analysis and fracture mapping

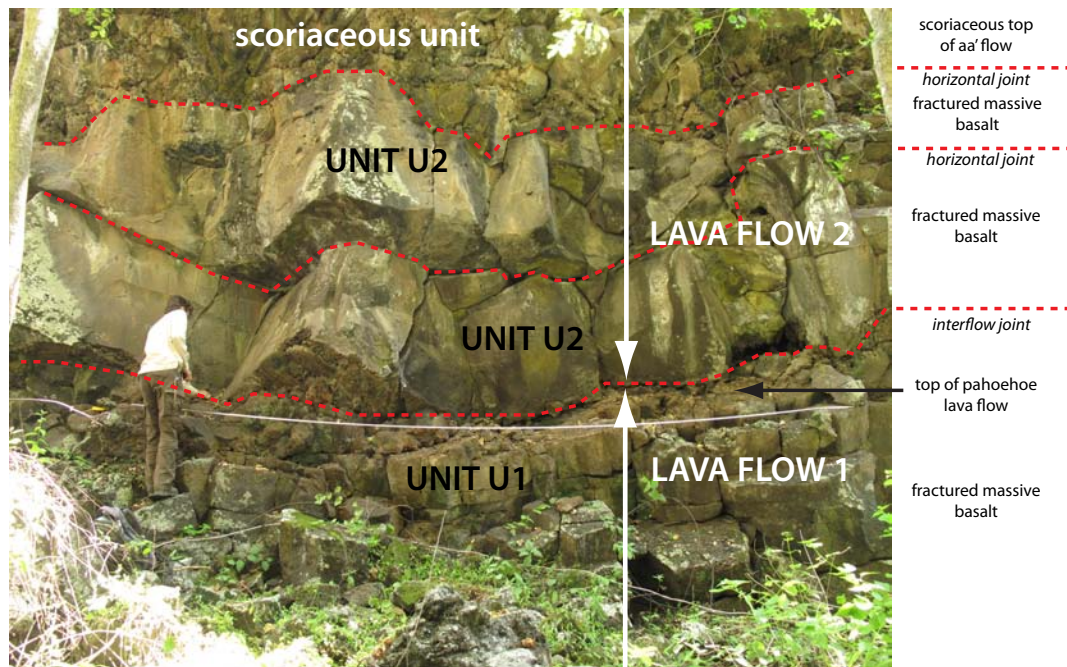


**Figure 8.7:** Fracture mapping at *Grieta Finch*, where massive fractured *pahoehoe* and *aa'* basaltic flows outcrop.

## 8. THE BASAL AQUIFER OF SANTA CRUZ ISLAND

---

cooling joints intersected a sub-horizontal discontinuity (fracture, interflow). The aperture of the sub-horizontal discontinuity was measured at each intersection. Results are presented in Fig. 8.8.

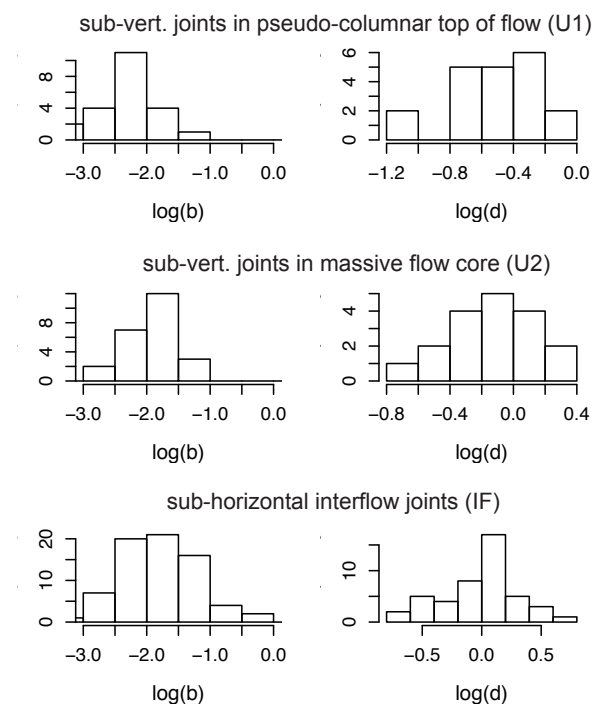


**Figure 8.8:** Statistics on fracture network from mapping along fault scarps *Finch* (loc. 1) and *Baranco* (loc. 4). Log-transformed aperture  $b$  [m], distance between fractures  $d$  [m]. Refer to Fig. 8.7 for the location of units U1 (lava flow 1), U2 (lava flow 2), and IF (interflow joints).

Outcrops are formed by fault scarps, all striking between  $N40^\circ E$  and  $N120^\circ E$ . It was impossible to find orthogonal surfaces to estimate possible fracture anisotropy. Yet, cooling joints have no reasons to follow a preferential orientation. Though they were oriented in the same direction, outcrops surfaces were assumed to be representative of the medium. Secondly, outcrops along fault scarps may not be representative of the medium. In particular, fracture apertures may be bigger.

### 8.4 Hydraulic properties

In this section, three methods are used to characterize the hydraulic properties of the basaltic formations of Santa Cruz. The analysis of tidal signal propagation

(Section 8.4.1) provides estimate at the regional scale (1 - 5 km), hydraulic tests (Section 8.4.2) at the local scale (10-100 m), and fracture mapping (Section 8.4.3) at the outcrop scale (1-10 m).

## 8.4.1 Tidal signal propagation

### 8.4.1.1 Theoretical background

We consider a water table (unconfined) semi-infinite aquifer with a substratum at elevation  $z = 0$ . Hydraulic conductivity  $K$  and porosity  $\epsilon$  are homogeneous. Let  $h(x, t)$ , be the water table height. Under the Dupuit hypothesis and assuming constant fluid density, the mass balance conservation and Darcy's law yield:

$$Kh \frac{\partial^2 h}{\partial x^2} = \epsilon \frac{\partial h}{\partial t} \quad (8.1)$$

where  $x$  is the horizontal distance to the coast,  $t$  is time. This equation is not linear. Assuming time-dependent variations of  $h$  to be small with respect to the total thickness of the aquifer, we write :  $h = h_0 + h'(t)$ , where  $h_0$  is the static (mean) level of the aquifer. From Eq. 8.1, we obtain a linear second order differential equation:

$$D \frac{\partial^2 h'}{\partial x^2} = \frac{\partial h'}{\partial t} \quad (8.2)$$

where  $D = h_0 K / \epsilon$  is the diffusivity. We impose a periodic sinusoidal forcing at the coast ( $x = 0$ ):

$$h'(x = 0) = h'_0 e^{i\omega t} \quad (8.3)$$

where  $h'_0$  is the tidal wave amplitude and  $\omega = 2\pi/\tau$  the phase.

We seek a solution of Eq. 8.2 such as  $h'(x) = f(x) \cdot h'_0 e^{i\omega t}$ .  $f$  is a solution of the differential equation  $f'' - i\omega/(2D) \cdot f = 0$ . The corresponding characteristic equation has two roots, we keep the solution of  $f$  with remains finite for  $x = +\infty$ . After the extraction of the real part, the solution reads:

$$h'(x, t) = \exp\left(-\sqrt{\frac{\omega}{2D}} \cdot x\right) \cdot \cos\left(\omega t - \sqrt{\frac{\omega}{2D}} \cdot x\right) \quad (8.4)$$

This expression was attributed to *Ferris* [1952].

At a distance  $x$  from the coast, the attenuation parameter  $\alpha$  and the phase shift  $\Delta t$  read:

## 8. THE BASAL AQUIFER OF SANTA CRUZ ISLAND

---

$$\alpha = \exp\left(-\sqrt{\frac{w}{2D}} \cdot x\right) \quad (8.5)$$

$$\Delta t = \sqrt{\frac{1}{2Dw}} \cdot x \quad (8.6)$$

### 8.4.1.2 Groundwater monitoring and sea level data

Groundwater level fluctuations have been monitored with a Schlumberger CTD-Diver® probes in six fault scarps and a deep drill hole (Fig. 8.1 and Table 8.1). The probes were immersed at a depth of ca. 1 m below mean water level, and therefore measured an absolute pressure. The height of water above the probe is obtained by compensation, that is by subtracting the barometric pressure. To this effect, barometric pressure was simultaneously recorded at an hourly frequency in Puerto Ayora (ca. 4 m.a.s.l.) and at the top of the deep drill hole (150 m.a.s.l.) with Schlumberger Baro-Diver®. Sea level is monitored by a tide gauge located on the sea shore west of Puerto Ayora (Fig. 8.1). This station is operated by the *University of Hawaii Sea Level Center*, corresponding data is available at <http://ilikai.soest.hawaii.edu/> at the hourly frequency.

The variations of sea level attributed to the tidal wave have an amplitude of 63 cm in Puerto Ayora. The lunar semi-diurnal component M2 has an amplitude of 47 cm (i.e. it explains 75% of the variations).

### 8.4.1.3 Data processing

Sea level fluctuations are dominated by a tidal signal at a period  $\tau = 12.42$  hours. In order to characterize the propagation of this signal into the aquifer, pressure records have been processed following the scheme depicted in Fig. 8.10:

1. Pressure records are available at the hourly or quarter frequency, they were first sub-sampled down to a frequency of one minute by spline interpolation.
2. Disturbances from pumping, interferences, and potential measurement errors, were removed when necessary with a cubic smoothing spline.
3. The water height above the probe is then deduced by compensation.
4. A high-pass filter (Eq. 8.7) is applied to the water level records so as to keep only the tidal wave  $w_{hp}(t)$ , at a frequency  $\tau = 745$  min (12.42 hours). Finally, the signal is resampled to a 5 min frequency, which is sufficient in this case and saves memory.

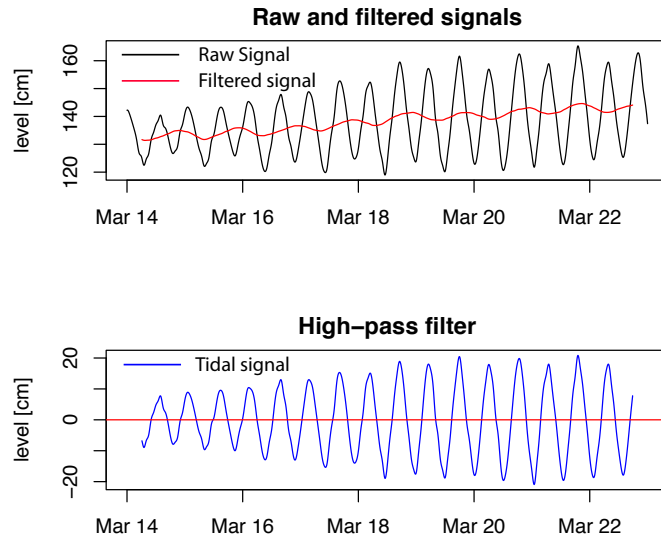


**Figure 8.9:** Filtering of water level records. Raw signal (black) and trend (red lines). Tidal signal (red) obtained from the high-pass filter (Eq. 8.7). Example for 8 days of monitoring at grieta *La Camiseta*.

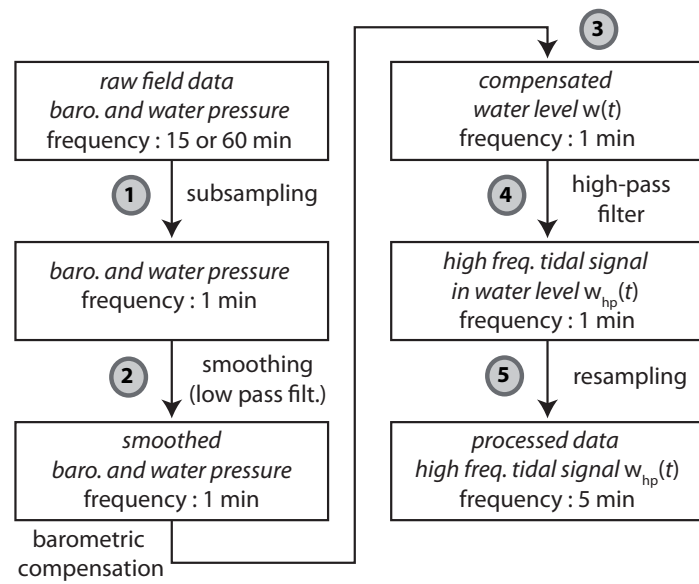


**Figure 8.10:** Data processing of water level records

## 8. THE BASAL AQUIFER OF SANTA CRUZ ISLAND

---

$$w_{\text{hq}}(t) = w(t) - \frac{1}{\tau} \int_{t-\tau/2}^{t+\tau/2} w(t') dt' \quad (8.7)$$

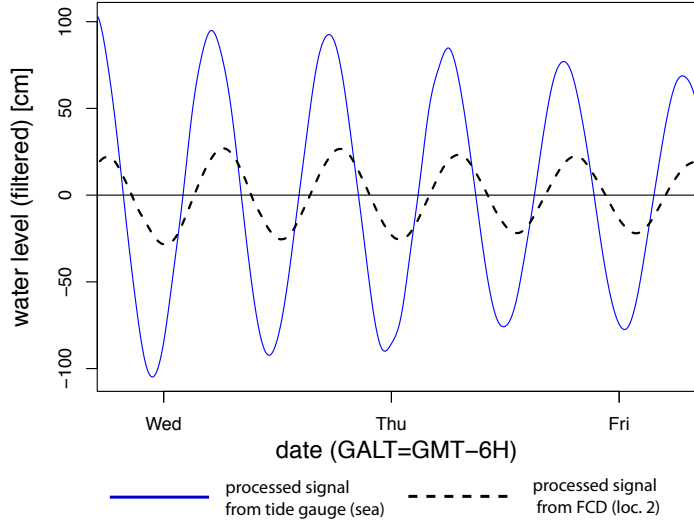


**Figure 8.11:** High frequency ( $\tau = 12.4$  hours) components of sea level and ground-water level at *Grieta FCD*. The tidal wave is attenuated ( $\alpha = 0.28$ ) and shifted ( $\Delta t = 1.21$  hours) in the aquifer.

With respect to  $s_{\text{hp}}(t)$  the tidal signal at the coast, the tidal wave in the aquifer  $w_{\text{hp}}(t)$  appears attenuated and shifted in the aquifer (Fig. 8.11). The amplitude ratio  $\alpha$  is computed from the ratio of the quadratic norms (Eq. 8.8). The amplitude of the tidal signal varies, so that its norm is a function of time. For an accurate estimate of  $\alpha$ , the quadratic norms should therefore be computed for corresponding periods in the two signals. The phase shift  $\Delta t$  is estimated by means of a cross-correlation diagram (Fig. 8.12).

$$\alpha = \frac{\|s_{\text{hp}}(t)\|}{\|w_{\text{hp}}(t)\|} \quad (8.8)$$

### 8.4.1.4 Results

The results of the tidal signal analysis (attenuation and phase shift) have been assembled in Table 8.1. Parameters  $\alpha$  and  $\Delta t$  are plotted against the shortest distance to the coast in Fig. 8.13. Correlations coefficients are respectively  $R^2 =$

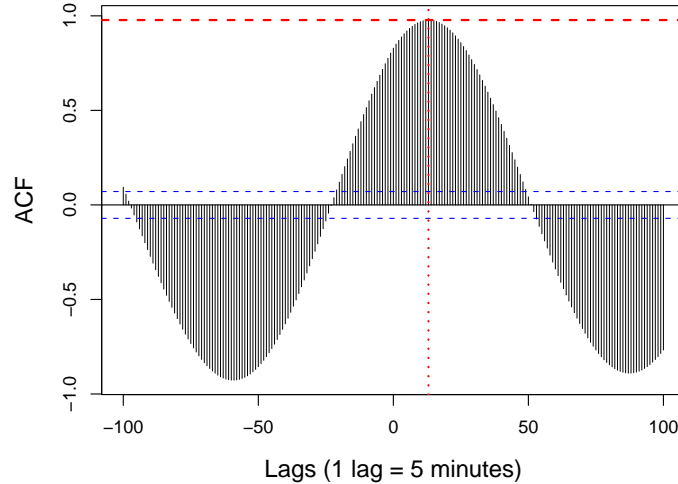


**Figure 8.12:** Cross-correlation diagram between sea level and groundwater level at *Grieta FCD*

0.96 and  $R^2 = 0.99$ . The hydraulic diffusivity is estimated to  $D = 144$  [m<sup>2</sup>/s] from the attenuation regression (Eq. 8.5). and  $D = 143$  [m<sup>2</sup>/s] from the phase shift (Eq. 8.6). As detailed in the aquifer test section, the noise to signal ratio is quite high for the *pozo testigo*, this may affect the estimation of  $\alpha$ , but to a limited extent only the estimation of  $\Delta t$ .

At the coast ( $x = 0$ ), we could expect  $\alpha=1$  and  $\Delta t=0$ , but a negative intersect is observed, reaching  $x = -729$  m and  $x = -175$  m for the models of  $\ln(\alpha)$  and  $\Delta t$  respectively. This may be interpreted as the effect of fractures, which could offer longer but more permeable path to groundwater flow. In these conditions, the more appropriate distance  $x$  for the 1D analysis is no longer the shortest distance to the coast, but the distance in a direction parallel to the fractures. These two solutions are compared in Fig. 8.14 without the furthest point inland (loc. 7). Linear regression based on distances along the fractures have higher r-squared, and the intersects are even further offshore,  $x = -2841$  m and  $x = -1499$  m for the regressions based on  $\alpha$  and  $\Delta t$  respectively.

Another interpretation must be found for the offset of distances. Such a phenomenon has been observed by *Ferris* [1952], who interpreted the negative intersect as the distance to the submarine outcrop. This explanation does not appear to be valid on the southern coast of Santa Cruz Island, where no geological evidence indicates the existence of an interface (such as a coastal sedimentary cap-rock) offshore Puerto Ayora. Instead, interface between the ocean and the

## 8. THE BASAL AQUIFER OF SANTA CRUZ ISLAND

---

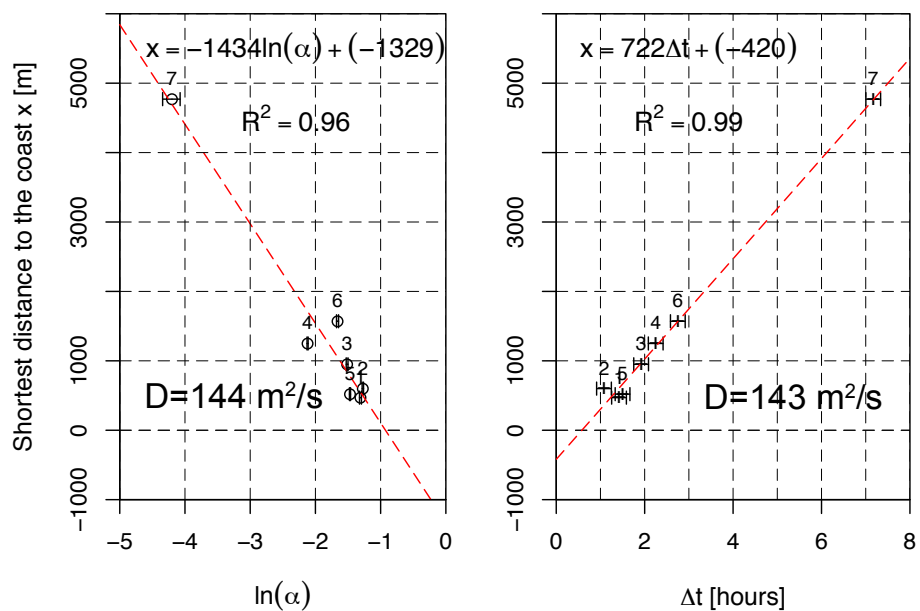


**Figure 8.13:** Linear regression of the amplitude ratio  $\ln(\alpha)$  (left) and phase shift  $\Delta t$  (right). On the vertical axis, the shortest distance to the sea. Identification numbers refer to Table 8.1 and Fig. 8.1.

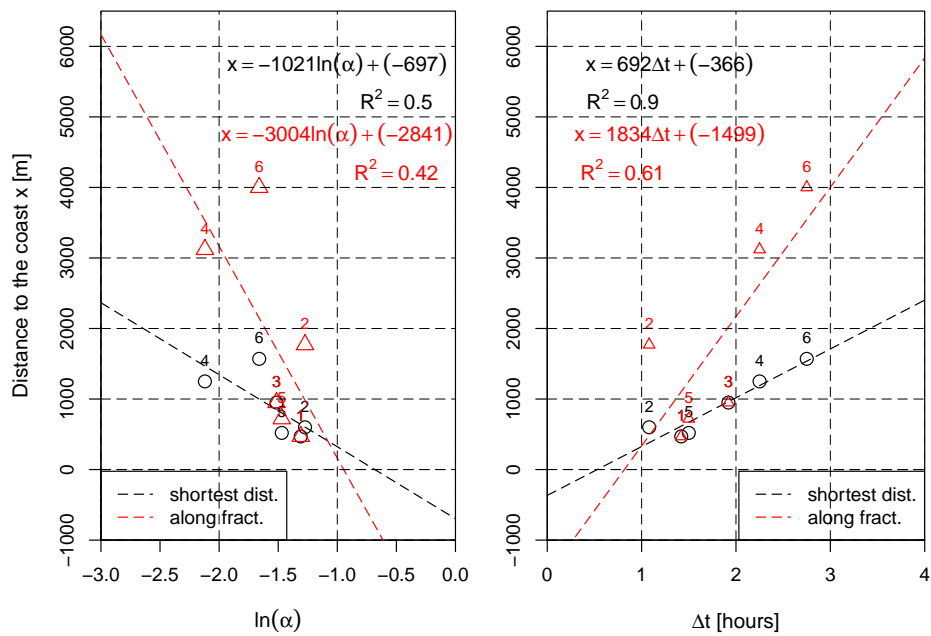


**Figure 8.14:** Linear regression of the amplitude ratio  $\ln(\alpha)$  (left) and phase shift  $\Delta t$  (right). On the vertical axis, the distance to the sea along the fracture path. Identification numbers refer to Table 8.1 and Fig. 8.1

## 8. THE BASAL AQUIFER OF SANTA CRUZ ISLAND

---

fractured basalts constituting the aquifer is expected to be a thin layer of sand and the aquifer directly outcrops at the coast. Instead, the negative intersects can more likely be attributed to the relatively gently sloping lava fields forming the coastal apron of Santa Cruz, and most probably continuing offshore (see inset Fig. 8.3). In this configuration, the assumption of a vertical beach is invalid. This effect does not affect the estimate of  $D$  from Fig. 8.13 because several locations have been monitored.

Aquifer transmissivity ( $T$ ) can be inferred from the diffusivity ( $D$ ),  $T = D \cdot \epsilon$ , where  $\epsilon$  is the drainage porosity. In turn the hydraulic conductivity ( $K$ ) can be inferred from transmissivity ( $T$ ),  $K = T/H$ , where  $H$  is the thickness of the aquifer. As detailed in section 8.2.1, an impervious substratum has not been identified in available drill holes. Yet, several processes (fracture closure, weathering, pore and fracture filling) tend to reduce permeability at depth. The effective depth of the aquifer was estimated to  $H = 1000$  m. Porosity is not known, but was estimated from the literature in similar context,  $\epsilon = 0.01$  [Custodio, 2004]. From  $D = 143$  m<sup>2</sup>/s (value from the phase shift, which presents a better correlation coefficient), we get  $T = 1$  m<sup>2</sup>/s, and  $K = 10^{-3}$  m/s.

### 8.4.2 Hydraulic test

#### 8.4.2.1 Multiple-step well test

A multiple-step well test was performed on the pumping well (Table 8.3, Fig. 8.15). The well characteristic curve model was fitted to the Jacob model [de Marsily, 1986]:

$$s = BQ + CQ^n \quad (8.9)$$

where  $B$  [s/m<sup>2</sup>] is the aquifer loss coefficient and  $C$  [s<sup>2</sup>/m<sup>5</sup>] the well loss coefficient. Assuming  $n = 2$ , a linear regression of  $s/Q$  against  $Q$  yielded  $B = 66$  s/m<sup>2</sup> and  $C = 17257$  s<sup>2</sup>/m<sup>5</sup>, with  $r^2 = 0.99$ .

The multiple test was interpreted with the *Harr/Polubarinova-Kochina* method (see e.g. *Gingerich* [1999]; *Rotzoll et al.* [2007]), which allows the determination of hydraulic conductivity of a thick unconfined aquifer that is only partially penetrated by a pumped well:

$$K^* = \frac{Q}{2\pi L s_s} \ln \left( 1.6 \frac{L}{r_w} \right) \quad (8.10)$$

where  $K$  [m/s] is the hydraulic conductivity (assumed to be isotropic and homogeneous),  $Q$  [m<sup>3</sup>/s] the withdrawal rate,  $L$  [m] the screened interval of the pumped well,  $r_w$  [m] the radius of pumped well, and  $s_s$  [m] the steady-state drawdown in

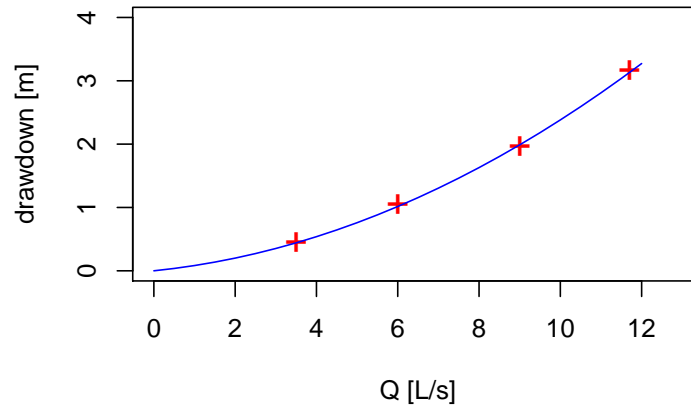


**Figure 8.15:** Characteristic curve of the pumping well from multiple step well test.

the pumped well. The steady-state drawdown was assumed to be reached after 120 min pumping, when drawdown stabilized. Hydraulic conductivity  $K^*$  obtained with this method ranged between  $4 \times 10^{-4}$  and  $9 \times 10^{-4}$  m/s depending on pumping rate, which is interpreted as the effect of turbulent losses in and around the well.

$Q$ [L/s]	$s$ [m]	$K^*$ [m/s]
3.5	0.41	$9 \times 10^{-4}$
6	1.15	$6 \times 10^{-4}$
9	2.04	$5 \times 10^{-4}$
11.7	3.24	$4 \times 10^{-4}$

**Table 8.3:** Results of the multiple step pumping test on the *pozo testigo* pumping well [Dixon Hydrogeology Limited, 1996]. Hydraulic conductivity  $K^*$  estimated with the Harr/Polubarinova-Kochina method.

Gravel was not inserted during the well test, but the casing was present. The effect of head losses in the well are probably important, since the screened interval was not installed right in front of the pumping level (Table 8.1). To limit such effects on hydraulic conductivity estimates with the *Harr/Polubarinova-Kochina* method, the aquifer loss term  $B$  obtained from the multiple-step well test may

## 8. THE BASAL AQUIFER OF SANTA CRUZ ISLAND

---

be introduced in Eq. 8.10, which yields [Rotzoll *et al.*, 2007]:

$$K = \frac{1}{2\pi LB} \ln \left( 1.6 \frac{L}{r} \right) \quad (8.11)$$

Hydraulic conductivity estimate from the step-test (Eq. 8.11) yielded  $K = 1.7 \times 10^{-3}$ , which is supposed to be more representative of the aquifer hydraulic properties than estimates from individual steps (Table. 8.3).

### 8.4.2.2 Transient aquifer test

Transient aquifer tests are usually interpreted with the “Theis method” or the related logarithmic approximation, the “Cooper-Jacob” method [de Marsily, 1986]. The fundamental hypotheses associated with these methods can be summarized as follows:

- fully penetrating well,
- confined aquifer,
- homogeneous, isotropic medium.

Transmissivity was estimated to  $1 \times 10^{-2}$  m<sup>2</sup>/s with the Cooper-Jacob method by [Dixon Hydrogeology Limited, 1996]. As drawdown in the observation well was too small to be detected, this estimate was based from drawdown measured in the pumped well itself, so that storage coefficient could not be estimated [Dixon Hydrogeology Limited, 1996].

By means of a Schlumberger CTD-Diver® probe, water level fluctuations in the observation well were monitored each 15 min at a high resolution (0.2 cm for water level). The combined effects of tidal wave propagation and drawdown caused by pumping in the neighboring pumping well could be observed. At the time scale considered (a few days), effects of recharge were assumed to be negligible.

Water level fluctuations in the observation well can be modeled as the sum of tidal signal and drawdown [Alcolea *et al.*, 2007]. Tidal signal was modeled from shifted and attenuated sea level records. The *Theis* function was used to model pumping effects under the hypothesis of an homogeneous isotropic medium. The expression of drawdown  $s$  at a distance  $r$  from the well at time  $t$  since pumping started reads [de Marsily, 1986]:

$$s(r, t) = \frac{Q}{4\pi T} \int_0^t \frac{e^{-\frac{r^2 S}{4T\tau}}}{\tau} d\tau = \frac{Q}{4\pi T} \left( -E_i \left( \frac{-1}{u} \right) \right) \quad (8.12)$$

where  $u = (4Tt)/(r^2S)$  and  $E_i$  is the exponential integral function.

Since pumping is performed on a daily basis by the Municipality, the aquifer may not have fully recovered from preceding days, the cumulated drawdown was estimated from the superposition principle. Aquifer transmissivity and storage coefficient have been adjusted for modeled and observed signals to best fit after a minimum of two days of drawdown modeling (Fig. 8.16).

The transmissivity was estimated to  $T = 6 \times 10^{-2} \text{ m}^2/\text{s}$ , that is close to the estimation proposed by [Dixon Hydrogeology Limited, 1996]. This value is different by two order of magnitudes of the transmissivity value inferred from the tidal signal propagation (Section 8.4.1). This can be explained by the gap between the actual configuration and the idealized conditions required for the Theis method: the well is far from being fully penetrating and drawdown is important with respect to the total screened level.

The storage coefficient was estimated to  $S = 0.8$ . This latter value is out of the “reasonable” range for basaltic formations,  $1 \times 10^{-2} \leq S \leq 1 \times 10^{-3}$  [Custodio, 2004]. This particularly high value of  $S$  can be explained by:

- **heterogeneities**, which are proven to have a significant impact on estimates of  $S$  from hydraulic tests [Meier *et al.*, 1998]. The numerous voids reported below the water table during drilling of the observation well [Dixon Hydrogeology Limited, 1996] could explain such a *capacitive* effect.
- **anisotropy** effects. The wells are said to be located on a major fracture whose direction is unclear [Dixon Hydrogeology Limited, 1996]. This may induce a strong anisotropic effect on hydraulic conductivity.

Due to the gap between idealized and actual conditions, transmissivity, and storage coefficient obtained from the transient aquifer test may not be not reliable. This highlights that the hypothesis of an isotropic, homogeneous medium is probably not valid at the scale of the pumping test (10-100 m). The estimate of  $K$  from the *Harr/Polubarinova-Kochina* should be preferred, but at this scale, this estimate is probably biased by the anisotropic effect.

### 8.4.3 Fracture network

#### 8.4.3.1 Theoretical background

Hydraulic properties of a fractured medium can be estimated from the characterisation of the fracture network. If this network follows a simple geometry, the permeability can be determined from analytical expressions (e.g. Adler and Thovert [1999]; Khaleel [1989]). In other cases, numerical models are used (e.g. Chesnaux *et al.* [2009]).

## 8. THE BASAL AQUIFER OF SANTA CRUZ ISLAND

---

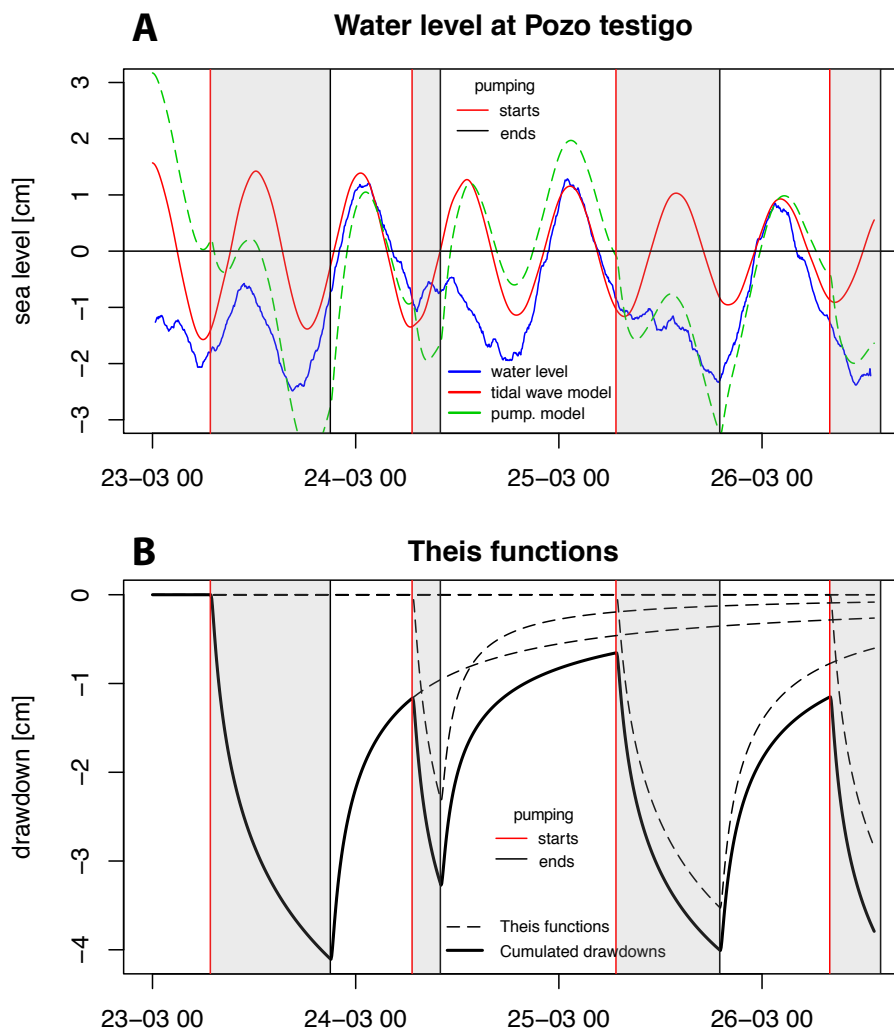


**Figure 8.16:** Pumping test under the influence of tidal fluctuations. The tidal wave is modeled from the attenuated and shifted sea level records. Former withdrawals affect water level up to 3 days after pumping, the drawdown is estimated as the sum of 3 shifted *Theis* functions. Transmissivity and storage coefficient are adjusted for both signals to fit.

The hydraulic conductivity of a smooth infinite fracture bounded by two parallel planes distant of  $b$  reads [Adler and Thovert, 1999]:

$$k_0 = \frac{b^2}{12} \tag{8.13}$$

From this equation, we can show that a medium fractured by infinite parallel fractures with constant spacing  $d = 1/n$  is equivalent to a porous medium of permeability:

$$k_n = \frac{b^3}{12} \cdot n \tag{8.14}$$

where  $n$  is the fracture density  $m^{-1}$ . With the same assumptions, the porosity reads  $\epsilon = bn$ .

In basaltic contexts, most of the fractures are due to cooling joints, which are not sub-parallel but tend to follow a spatial organization that can be idealized to a network of vertical hexagonal columns. *Khaleel* [1989] proposed analytical expressions of vertical and horizontal permeability for such contexts. It is based on the division of the fracture network into flow cells (Fig. 8.17).

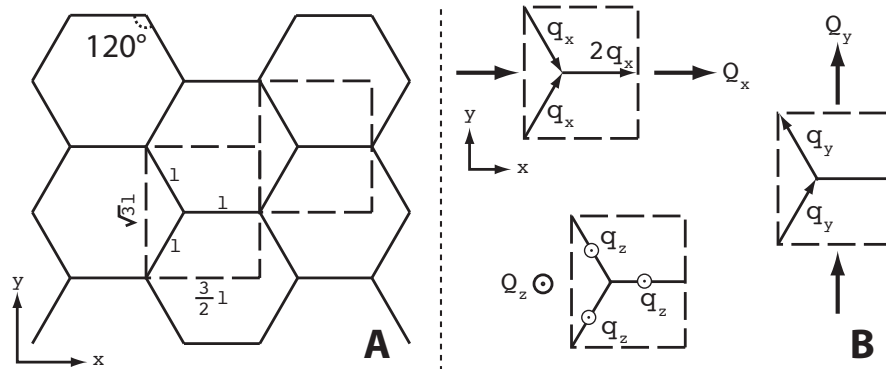


**Figure 8.17:** (A) Idealized network of hexagonal columnar vertical cooling joints. (B) Flow regions used to determine equivalent hydraulic conductivity [Khaleel, 1989].

Fluxes  $Q_x$ ,  $Q_y$ ,  $Q_z$  through the cell in directions x, y, and z respectively can be determined with Darcy's law applied on the discrete fracture network. From Eq. 8.13 and classical compositions laws (harmonic and arithmetic means) we

## 8. THE BASAL AQUIFER OF SANTA CRUZ ISLAND

---

have:

$$\begin{aligned}
 Q_x &= \frac{\rho g}{\mu} k_{f,x} \cdot \frac{\Delta H_x}{L_{f,x}} \cdot S_{f,x} = \frac{\rho g}{\mu} \left(\frac{4}{3}k_0\right) \left(\frac{(J_x \cdot (3/2)l)}{2l}\right) (eb) = \frac{\rho g}{\mu} k_0 J_x eb \\
 Q_y &= \frac{\rho g}{\mu} k_{f,y} \cdot \frac{\Delta H_y}{L_{f,y}} \cdot S_{f,y} = \frac{\rho g}{\mu} k_0 \left(\frac{(J_y \cdot \sqrt{3}l)}{2l}\right) (eb) = \frac{\rho g}{\mu} \frac{\sqrt{3}}{2} k_0 J_y eb \quad (8.15) \\
 Q_z &= \frac{\rho g}{\mu} k_{f,z} \cdot \frac{\Delta H_z}{L_{f,z}} \cdot S_{f,z} = \frac{\rho g}{\mu} k_0 \left(\frac{(J_z \cdot e)}{e}\right) (3lb) = \frac{\rho g}{\mu} \frac{2}{\sqrt{3}l} k_0 J_z lb
 \end{aligned}$$

where  $k_{f,x}$ ,  $k_{f,y}$ ,  $k_{f,z}$  are the fracture permeabilities,  $\Delta H_x$ ,  $\Delta H_y$ ,  $\Delta H_z$  the hydraulic head variations,  $L_{f,x}$ ,  $L_{f,y}$ ,  $L_{f,z}$ , fracture lengths, and  $J_x$ ,  $J_y$ ,  $J_z$  the directional hydraulic gradients.

In turn, Darcy law based on the equivalent porous medium permeabilities  $k_{l,x}$ ,  $k_{l,y}$ ,  $k_{l,z}$  reads:

$$\begin{aligned}
 Q_x &= k_{l,x} \frac{\rho g}{\mu} J_x S_x \\
 Q_y &= k_{l,y} \frac{\rho g}{\mu} J_y S_y \quad (8.16) \\
 Q_z &= k_{l,z} \frac{\rho g}{\mu} J_z S_z
 \end{aligned}$$

where  $S_x, S_y, S_z$  are the cell surfaces. From Eq. 8.15 and 8.16, the medium is shown to be isotropic in the horizontal plane and we get:

$$k_{l,h} = k_{l,x} = k_{l,y} = \frac{1}{\sqrt{3}l} \cdot \frac{b^3}{12} \quad (8.17)$$

$$k_{l,z} = \frac{2}{\sqrt{3}l} \cdot \frac{b^3}{12} \quad (8.18)$$

where  $k_{l,h}$  and  $k_{l,z}$  are the horizontal and vertical permeabilities of a porous medium equivalent to the hexagonal columnar fracture network of side  $l$ .

### 8.4.3.2 Application

As described in section 8.3.2, fractures were mapped on two outcrops of *pahoehoe* flows. Three units were defined: the top of the flow dissected by dense sub-vertical cooling joints (unit U1), the flow core (unit U2), and interflow joints (IF).

Though observed vertical cooling joints were quite far from the idealized description proposed by *Khaleel* [1989], this scheme was preferred to the parallel fracture network.

The length of the vertical columns  $l$  is challenging to measure on sub-vertical outcrops. We can assume that  $l$  was close to the distance between sub-vertical

fractures observed at the outcrop. From Eq. 8.17 and 8.18, this approximation leads to:

$$k_{l,h} = \frac{1}{\sqrt{3}} \cdot k_n \quad (8.19)$$

$$k_{l,v} = \frac{2}{\sqrt{3}} \cdot k_n \quad (8.20)$$

Unit	$\log(b) \pm \sigma$	$n$	$e = bn$	$\log(k_n)$	$\log(k_{l,h})$	$\log(k_{l,v})$
U1	$-2.2 \pm 0.4$	3.3	0.02	$-7.2 \pm 2$	$-7.4 \pm 2$	$-7.14 \pm 2$
U2	$-1.8 \pm 0.35$	1.3	0.02	$-6.4 \pm 1$	$-6.6 \pm 1$	$-6.46 \pm 1$
IF	$-1.7 \pm 0.58$	1	0.02	$-6.2 \pm 2$	-	-

**Table 8.4:** Results of fracture mapping at the outcrop scale for units U1 (top flow) and U2 (flow core), and interflow joints (IF) (Fig. 8.7).  $b$  [m] is fracture aperture, and  $n$   $\text{m}^{-1}$  fracture density. Permeabilities are determined from idealized fracture networks:  $k_n$  with parallel infinite fractures,  $k_{l,h}$  and  $k_{l,v}$  with an hexagonal columnar fracture network, in the horizontal and vertical directions respectively.

The top layer with numerous small columnar joints (U1) does not exceed 1.5 m, we considered  $L(U1) = 1$  m. The thickness of the massive lava *pahoehoe* lava flow core (U2) range between 2 and 5 m, we considered  $L(U2) = 3$  m. The total porosity whole lava flow (U1, U2 and IF) was estimated from the arithmetic mean to  $\epsilon = 0.04$  (Table 8.4). This value is compatible with estimates proposed by *Custodio* [2004] for volcanic contexts.

The equivalent horizontal permeability of a whole lava flow (U1, U2 and IF) can be inferred as follows:

$$k_{h,eq} = \frac{L(U1)k_{h,l}(U1) + L(U2)k_{h,l}(U2)}{L1 + L2} + k(IF) \quad (8.21)$$

where  $L(U1)$  and  $L(U2)$  are the thicknesses of U1 and U2 respectively.

$$k_{v,eq} = \frac{L(U1) + L(U2)}{\frac{L(U1)}{k_{v,l}(U1)} + \frac{L(U2)}{k_{v,l}(U12)}} \quad (8.22)$$

From Eq. 8.21 and 8.22, we get  $k_{h,eq} = 8 \times 10^{-7} \text{ m}^2$  and  $k_{v,eq} = 1.2 \times 10^{-7} \text{ m}^2$  which corresponds to  $k_{h,eq} = 8 \text{ m/s}$  and  $1.2 \text{ m/s}$  respectively.

Permeability values obtained from fracture mapping are very high, which is due to the large fracture apertures. With the same methodology in a similar

## 8. THE BASAL AQUIFER OF SANTA CRUZ ISLAND

---

context (La Fournaise, Réunion), *Folio* [2001] obtained horizontal permeabilities ranging between  $10^{-12}$  and  $10^{-11}$  m<sup>2</sup>, and vertical permeabilities ranging between  $10^{-14}$  and  $10^{-11}$  m<sup>2</sup>. The permeability of Santa Cruz basaltic formations may be higher than in la Réunion, but values obtained from fracture mapping in this study are significantly higher compared to estimates obtained from tidal signal propagation and hydraulic tests ( $K = 10^{-3}$  m/s).

Several reasons can be at the origin of an over-estimation of permeability from fracture mapping:

- The available outcrops are restricted to *grietas*, i.e. fault zones that may present additional fractures with respect to undisturbed basaltic flows.
- Among these outcrops, and along the same outcrop, we observe a large variability of the density of cooling joints. Selecting only two outcrops may not be sufficient
- Though it is not the case in the unsaturated zone, fractures may be partly filled in the saturated zone.
- The idealized network are quite far from the reality. In particular, fractures are neither infinite, nor do they form a perfect columnar network.

Estimates of hydraulic conductivity inferred from fracture network mapping are too high to be realistic. Yet, they testify that cooling joints and interflow voids may confer a high permeability to the basaltic formations of Santa Cruz. Better estimates could be obtained from further mapping and more advanced methods with complex fracture networks.

### 8.5 Discussion

Two arguments from the analysis of the tidal wave propagation highlight the compatibility of the observations with the assumption of an homogeneous aquifer [Townley, 1995; Trefry, 1999]. First, the log-transformed attenuations  $\ln(\alpha)$  and the time lags  $\Delta t$  evolve linearly with the distance to the coast (Fig. 8.13). Second, the estimates of hydraulic diffusivity from the attenuation and the phase shift are in good accordance ( $D = 144$  m<sup>2</sup>/s and  $D = 143$  m<sup>2</sup>/s respectively).

In spite of the presence of numerous fault scarps, it appears that the diffusivity is isotropic and homogeneous. Several explanations can be proposed:

- Conductive anomalies are parallel to the coast and have little effect on tidal signal propagation [Slooten *et al.*, 2010].

- In fault scarps, the increase in hydraulic conductivity is accompanied by a higher storage capacity, so that the diffusivity remains constant.
- The network of conductive fault segments is below the percolation threshold [Mourzenko *et al.*, 2005]. The observed discontinuities do not modify the regional hydraulic permeability.

The first hypothesis can be discarded, Fig. 8.4 clearly shows that fault segments are not parallel to the coastline. The second hypothesis deserves to be considered. Fault scarps are sometimes more than to 1 m wide, they constitute “capacitive” anomalies that can locally attenuate the tidal wave. Yet, attenuations and phase shifts measured and the grietas are consistent with the attenuation and phase shift of the observation well (pozo profundo), where such a capacitive effect could be smaller. As consequence, the last explanation appears as the most relevant: fault segments do not percolate, they are not sufficiently connected to have an effect on the regional hydrodynamics. This was compatible with Fig. 8.4 and 8.5. Faults are not continuous, but form individual segments terminated by series are ramified discontinuous tension joints.

Though hydrodynamic properties appear as isotropic at the regional scale, hydraulic tests highlighted anisotropic effects at the smaller scale (10-100 m).

The hydraulic conductivity inferred from tidal signal propagation is consistent with the estimate from the multiple-step pumping test interpreted with the *Harr/Polubarinova-Kochina* method. The high value ( $K = 1 \times 10^{-3}$  m/s) is attributed to the dense network of cooling joints and interflow voids.

## 8.6 Conclusions

Faults of the southern slope of Santa Cruz Islands are too discontinuous to percolate, they have very limited impact over the regional hydrodynamism. Observed groundwater level tidal fluctuations fitted well to a 1D analytical model with homogeneous diffusivity ( $D = 143$  m<sup>2</sup>/s). Nevertheless, the transient aquifer test highlighted that anisotropic effects are present at the local scale (10-100 m).

As confirmed by fracture mapping at the outcrop, the high transmissivity ( $T \approx 1$  m<sup>2</sup>/s) and hydraulic conductivity ( $K \approx 1 \times 10^{-3}$  m/s) is attributed to the numerous cooling joints and interflow voids.

Faults do not to behave as preferential corridor for seawater intrusion. Yet, aquifer transmissivity is high and climatic conditions relative dry. This confer a poor hydrogeological potential to the coastal area of Santa Cruz Island.

### 8.7 Acknowledgments

This study has been performed in the frame of the project *Galapagos Islands Integrated Water Studies* (GIIWS), funded by the Agence Nationale de la Recherche (ANR-blanc 2010 GIIWS Ref. 601-01). The GIIWS team would like to thanks its local partners in Galapagos: the Charles Darwin Research Station, the Galapagos National Park. The digitilization of faults with a GIS software (QGis) was performed by Justine Lichter.

## Chapter 9

# High-level groundwater in Santa Cruz Island

## High-level groundwater in Santa Cruz Island\*

---

### Abstract

In order to investigate groundwater occurrence on Santa Cruz island, a SkyTEM survey was conducted in 2006. Results highlight an extensive, continuous low-resistivity body (50-200 ohm.m) [Auken *et al.*, 2009; d'Ozouville *et al.*, 2008a], which is interpreted as a perched aquifer. This dataset has been re-inversed with the spatially constrained inversion scheme [Viezzoli *et al.*, 2008] to “smooth” 19-layer resistivity models, and later interpolated with the methodology proposed by Pryet *et al.* [2011]. The geometry of the low-resistivity (50-200 ohm.m) body is now described more accurately. It has a median thickness of ca. 30 m and a median slope of ca. 10%. Additionally, a very low resistivity body (30-70 ohm.m) was identified. Newly available climatic records in the highlands allow further hydrogeological discussion. Recharge rates were estimated to  $R = 1153$  mm/year in the very humid and summit zones. For a perched aquifer to be stable under these conditions, the hydraulic conductivity should be around  $4 \times 10^{-5}$  m/s. This is two order of magnitudes lower than values inferred from tidal signal propagation and hydraulic tests performed in the basal aquifer of this island. Perched horizons may exist, but they are probably intermittent and restricted to preferential areas, where low resistivity layers are gently sloping and recharge conditions optimum.

---

\* In collaboration with James Ramm<sup>1</sup> and Benoit Deffontaines<sup>2</sup>

<sup>1</sup> *University of Aarhus, HydroGeophysics Group, Department of Earth Sciences, Høgh-Gulbergs Gade 2, 8000 Århus C, Denmark.*

<sup>2</sup> *UPE, GTMC Laboratory, Marne-La-Vallée, France*

## 9.1 Introduction

A low-lying basal aquifer is present in Santa Cruz island, but it is subjected to seawater intrusion (Chap. 8). The occurrence of fresh groundwater at higher elevation, above the basal aquifer, is still under debate. To date, the only drill hole available at high elevation is dry, and only two springs were identified. The first is found at the base of a pyroclastic cone (*Santa Rosa*) and is probably associated to a small aquifer developing in the cone. The second, *Finca Herrera*, is located at mid-slope but may be related to intermittent superficial flow [d'Ozouville, 2007a].

In order to investigate high-level groundwater occurrence, an airborne electromagnetics SkyTEM survey was conducted over Santa Cruz Island in 2006 [d'Ozouville, 2007a]. Results revealed an extensive low resistivity layer (50-200 ohm.m) (Fig. 9.1) [Auken *et al.*, 2009; d'Ozouville *et al.*, 2008a].

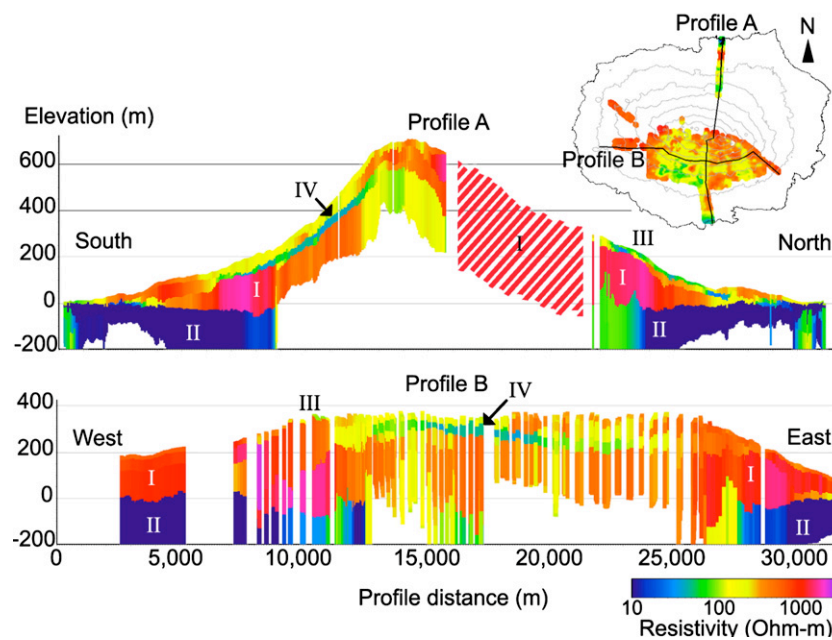


**Figure 9.1:** Geophysical cross-sections from [d'Ozouville *et al.*, 2008a], divided into four units depending on resistivity ranges: (I) High resistivity ( $> 800$  ohm.m) (II) Low-resistivity  $< 10$  ohm.m (III) Near-surface, low-resistivity (50-200 ohm.m) ; (IV) Subsurface, low-resistivity (50-200 ohm.m).

In volcanic contexts, very low resistivities ( $< 15$  ohm.m) are related to weathered or hydrothermalized formations and/or formations saturated with salt water [Aizawa *et al.*, 2009; Lénat *et al.*, 2000; Muller *et al.*, 2002; Revil *et al.*, 2004].

## 9. HIGH-LEVEL GROUNDWATER IN SANTA CRUZ ISLAND

Intermediate resistivities (15-800 ohm.m) are interpreted as weathered or saturated formations with different grades of weathering and saturation [Descloitres *et al.*, 1997; Lénat *et al.*, 2000; Muller *et al.*, 2002]. In particular, formations between 100-250 ohm.m can be associated to freshwater saturated formations [Robineau *et al.*, 1997]. High electrical resistivities (> 800 ohm.m) are associated with unweathered dry basaltic formations [Descloitres *et al.*, 1997, 2000].

As proposed by d'Ozouville *et al.* [2008a], it is relatively straightforward to associate high resistivities of the Santa Cruz dataset to dry unweathered basalts. Furthermore, the existence of a basal aquifer intruded by seawater is proven, unit II can easily be associated to basalts saturated by seawater [d'Ozouville *et al.*, 2008a]. The interpretation of the buried low resistivity unit (50-200 ohm.m) is less straightforward.

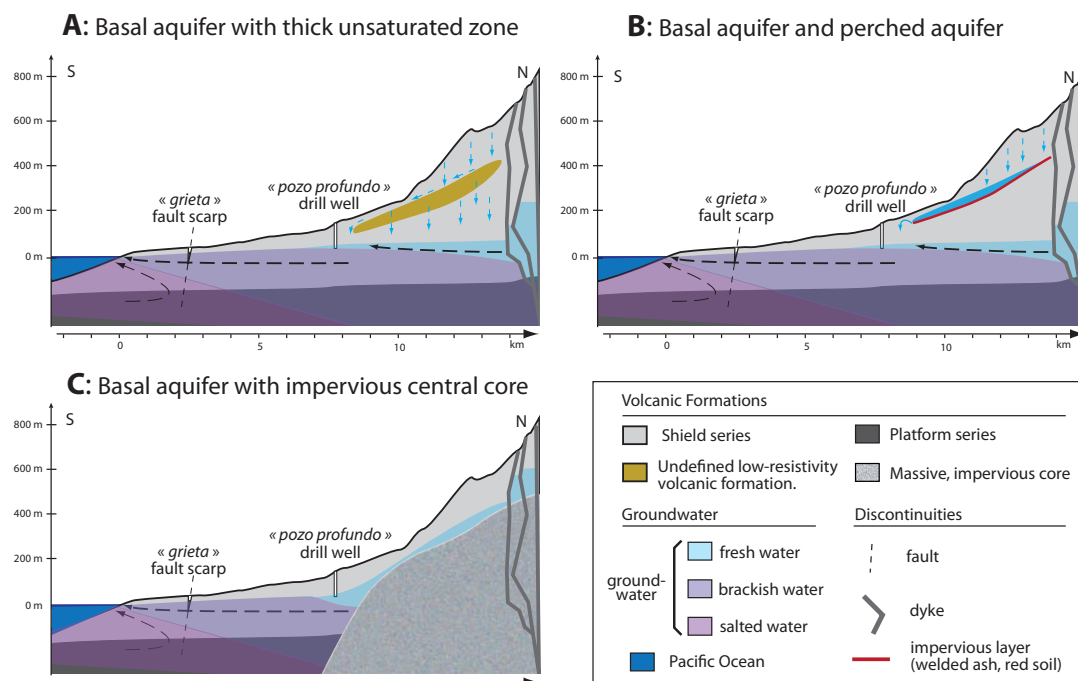


**Figure 9.2:** The three simplified hydrogeological conceptual models that could be *a priori* proposed for Santa Cruz Island.

Though they are more or less probable, three conceptual models can be *a priori* proposed to account for the presence of a low resistivity layer under the windward side of Santa Cruz island (Fig. 9.2):

- Fig. 9.2, A: Low resistivities are associated to weathered volcanic formations

- Fig. 9.2, B: Low resistivities are associated to a perched aquifer, formed over a relatively thin impervious layer (ash, baked soil, massive lava flow)
- Fig. 9.2, C: “skin flow” over an impervious core.

Solution B, with a perched aquifer was proposed by [d’Ozouville *et al.*, 2008a].

Since then, recently acquired climatic records are available in the highlands [Domínguez González, 2011; Pryet *et al.*, 2012], and the geophysical dataset has been reprocessed. These results are presented, and the hydrodynamic stability of the perched aquifer is then discussed.

## 9.2 Climatic conditions

### 9.2.1 General conditions

The climate of Santa Cruz island is characterized by relatively dry conditions with respect to its equatorial location (0.4° S, 90.2° W). Due to the south-east trade winds, conditions are very contrasted between the southern windward side, and the northern, dry, leeward side.

Seasons alternate between the hot *invierno* season (January to May) and the cool *garúa* season (June to December). Mean temperatures are 26 °C and 22 °C respectively [Trueman and d’Ozouville, 2010]. During the cool *garúa* season, an atmospheric temperature inversion impedes further rise of moist air, and leads to the formation of a fog layer covering the summit zones [Pryet *et al.*, 2012; Trueman and d’Ozouville, 2010]. Cloud water interception by the vegetation presents an additional input of water.

As a consequence of the orographic effect, the windward slope of Santa Cruz can be subdivided into five eco-climatic stages [Hamann, 1979; Pryet *et al.*, 2012]. Conditions are arid at low elevation (< 200 m a.s.l.), cactuses grow over bare volcanic rocks. After a transition zone, The humid zone (200-500 m a.s.l.) is characterized by relatively thick soils and dense vegetation cover (pasture and secondary forest). The very humid and summit zones (500-850 m a.s.l.) are covered by endemic shrubs and ferns growing on thin soils. Conditions are optimum for deep infiltration.

Except during flash floods associated with scarce intense precipitations associated with *El Niño* anomalies, surface run off is negligible on Santa Cruz [d’Ozouville, 2007a]. During the cool season, small streams form in the very humid and summit zones, but disappear into fractures and do not reach the underlying stages (Fig. 9.4).

## 9. HIGH-LEVEL GROUNDWATER IN SANTA CRUZ ISLAND

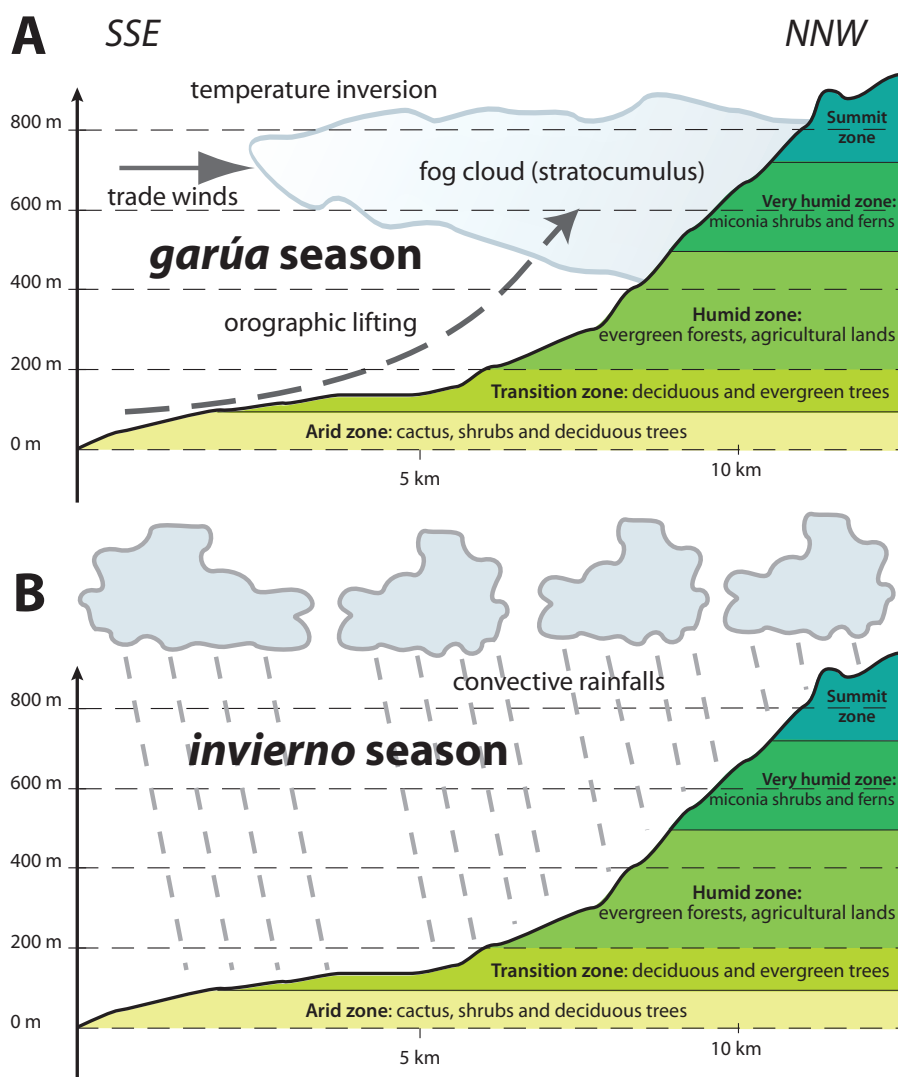


**Figure 9.3:** Eco-climatic staging of the windward slope of Santa Cruz Island (after Hamann [1979]). Two stations are operated by the *Charles Darwin Foundation* (CDF), and two others by the GIIWS project. Three recharge zones have been delimited in this study (see section 9.2.3).

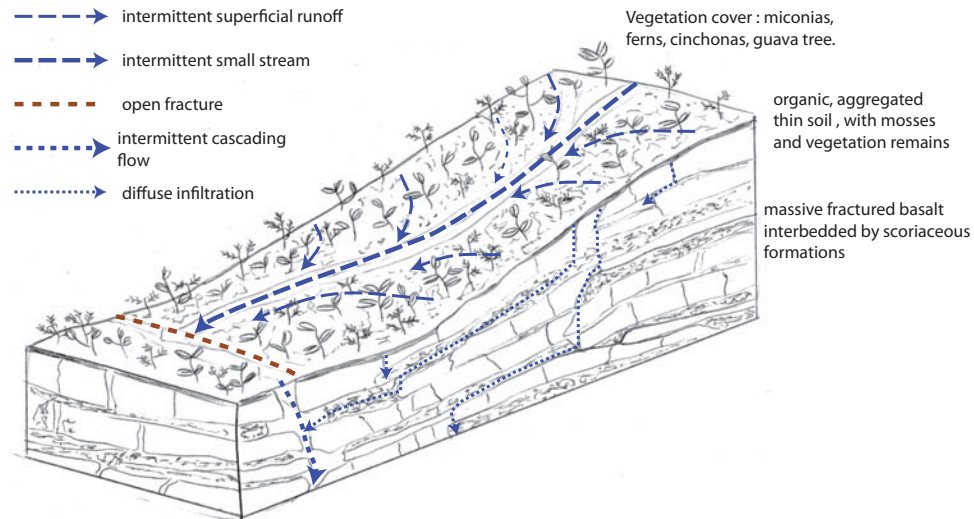


**Figure 9.4:** Hydrological conceptual model of the very humid zone (> 500 m a.s.l.). Soils are thin and rocks fractured, precipitated water forms short intermittent streams, but they rapidly disappear into open fractures.

### 9.2.2 Rainfall

In complement of the two weather stations operated by the Charles Darwin Station (at 4 m a.s.l. and 180 m a.s.l.), two stations were installed by the GIIWS project in mid-2010, at 400 and 650 m a.s.l. respectively (Fig. 9.3). From ongoing monitoring, preliminary results are presented in Fig. 9.5.

Correlations between daily rainfall at the four stations were analyzed by linear regression. It was taken into account that FCD stations are manually recorded at 6AM, 12AM and 18PM. Daily rainfall at day  $d$  is the rainfall collected between 6AM at day  $d$  to 6AM at day  $d + 1$ . To allow comparison of daily rainfalls between FCD and GIIWS stations, an identical procedure was applied to GIIWS automatic stations. Correlation of daily rainfall was relatively poor between CDF2 and GIIWS1 stations ( $R^2 = 0.2$  and  $N=136$  for cool season 2010,  $R^2 = 0.5$  and  $N = 168$  for hot season 2011), and high between GIIWS1 and GIIWS2 stations ( $R^2 = 0.9$ ,  $N = 136$  for cool season 2010,  $R^2 = 0.7$ ,  $N = 168$  for hot season 2011). To obtain continuous chronicles at GIIWS1 and GIIWS2, data gaps were filled by means of linear regression with the nearest station from CDF2 and GIIWS1 respectively (Fig. 9.5).

At each station, seasonal cumulated precipitations (Fig. 9.6, A) has been estimated from gap-filled chronicles (Fig. 9.5). During the cool fog season, cloud water interception contributed to 22% of total incident precipitation at high el-

## 9. HIGH-LEVEL GROUNDWATER IN SANTA CRUZ ISLAND

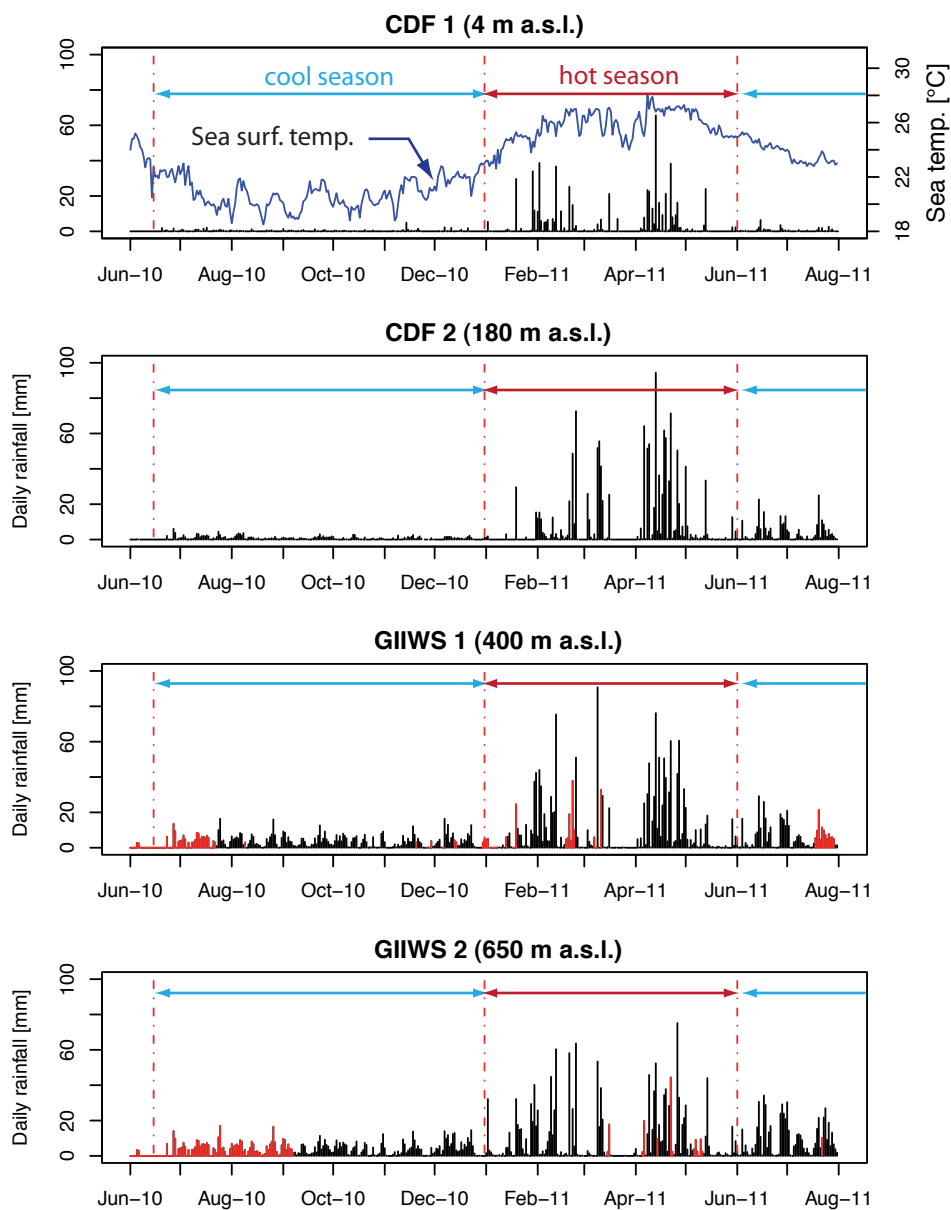


**Figure 9.5:** Rainfall records at the four weather stations for 2010/2011. Red portions of rainfall data correspond to data gaps where records were reconstructed by linear regression.

		Rainfall [mm] (seasonal contribution [%])	
		CDF1 (Puerto Ayora)	CDF2 (Bellavista)
CDF dataset, from <i>Trueman and d'Ozouville</i> [2010]:			
Annual	median	277	813
	minimum	64	448
	maximum	2769	2666
Hot season	median	196 (71 %)	351 (43 %)
Cool season	median	81 (29 %)	462 (57 %)
Unpublished dataset from CDF:			
Total	2010	503	826
Hot season	2010	446 (91%)	667 (89%)
Cool season	2010	57 (9%)	159 (11%)
Hot season	2011	609	1310

**Table 9.1:** Statistics on rainfall heights measured at stations CDF1 and CDF2 with inter-annual statistics from 1964 and 1987 respectively [*Trueman and d'Ozouville, 2010*]. 2010 and 2011 hot seasons were particularly wet, while 2010 cool season was particularly dry.

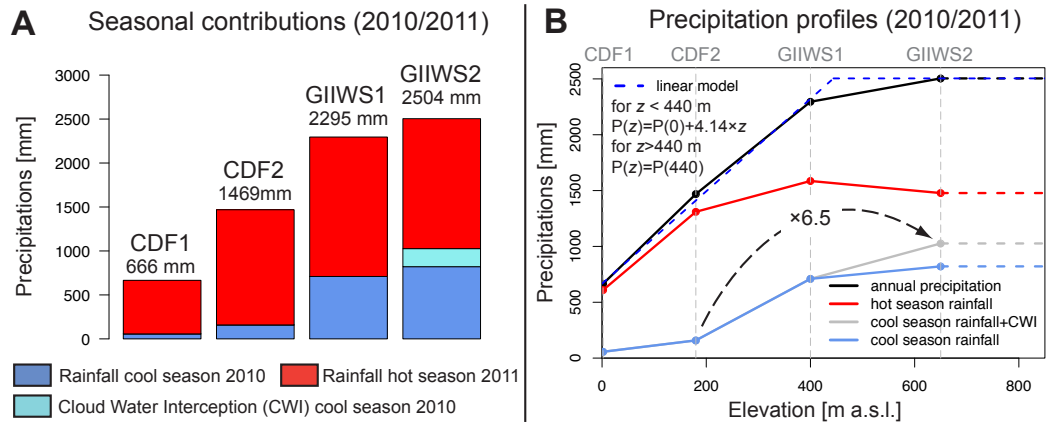


**Figure 9.6:** (A) Contribution of hot and cool season rainfalls and cloud water interception (CWI) to 2010/2011 totals at the four stations. (B) Orographic precipitation and rainfall gradients inferred from 2010/2011 monitoring. A linear model is proposed for total precipitations including cloud water interception (CWI), with a plateau for high elevations,  $z > 440$  m.

## 9. HIGH-LEVEL GROUNDWATER IN SANTA CRUZ ISLAND

---

evation (GIIWS2, 650 m a.s.l.), but was negligible at the cloud base (GIIWS2, 400 m a.s.l.) [Pryet *et al.*, 2012].

The orographic gradient of precipitation is strong during the cool season (Fig. 9.6, B), when orographic rainfall is accompanied by fog. In contrast, precipitation are convective and more evenly distributed during the invierno season.

From seal level up to 440 m a.s.l., precipitations increase linearly with elevation with a gradient of 414 mm / 100 m, but appear to reach a plateau at 440 m a.s.l. (Fig. 9.6, B). *d'Ozouville* [2007a] obtained a similar gradients from a previous dataset (2003-2007), but highlighted that the precipitation gradient varies from year to year. *d'Ozouville* [2007a] proposed the existence of a plateau at 700 m a.s.l., but this estimate was relatively speculative. At that time, no weather station was available at elevations higher than 480 m a.s.l.

Admittedly, more weather stations would still be required to conclude. Yet, instrumenting the summit area ( $> 750m$ ) is challenging because of difficulties of access to the field and relatively strong winds. Furthermore, it is of limited interest, since the area above 750 m a.s.l. is representative of a very small portion of the island.

Compared to long-term records at CDF1 and CDF2, the 2010 cool season (June to December) was dryer, particularly at station CDF2. This is probably related to the prevailing *La Niña* anomaly observed in 2010 [*National Weather Service Climate Prediction Center*, 2011]. In contrast, 2010 and 2011 hot seasons (January to May) were clearly wetter than long term records (Table 9.1).

### 9.2.3 Recharge

Given contrasting ecological, geological and climatic conditions, the windward slope of Santa Cruz Island can be sub-divided into three recharge zones (Fig. 9.3):

- Recharge zone 1 (0-200 m a.s.l., stations CDF1 and CDF2): sparse vegetation and thin soils ( $< 30$  cm) over fractured basaltic rocks. Infiltration potential is high, but rainfall is weak. Recharge is probably negligible, except during extreme rainfall events [*d'Ozouville*, 2007a; *d'Ozouville et al.*, 2008b].
- Recharge zone 2 (200-500 m a.s.l., station GIIWS1): relatively dense vegetation cover and well developed soils (30-120 cm) [*Adelinet et al.*, 2008]. Rainfall is higher than in the lower zone, but soil storage capacity and potential evapotranspiration is high. Recharge is probably small. For 2006, *d'Ozouville* [2007a] estimated effective rainfall to 100 mm/ year in this zone.

- Recharge zone 3 (500-855 m a.s.l., station GIIWS2): Soils are thin and rocks fractured (Fig. 9.4). Rainfall is high and completed by fog interception [Pryet *et al.*, 2012]. Conditions are favorable to infiltration. From measurements performed in 2006 in a gaged watershed in this Recharge zone, *d'Ozouville et al.* [2008b] estimated runoff to account only for 10% of effective rainfall. Conditions are favorable to infiltration and groundwater recharge.

From these observations, it was assumed that groundwater recharge was small in recharge zones 1 and 2 and significant in zone 3.

In the frame of this project, recharge estimates with the soil water budget and the “Darcy” method [Healy, 2010; Scanlon *et al.*, 2002] are undergoing studies. In a preliminary approach, a simpler method was used with for unique purpose to provide an order of magnitude for the renewal capacity of high-level groundwater in Santa Cruz.

Recharge rates in Recharge zone 3 were estimated from the equation developed by *Izuka et al.* [2010] in a similar geographical and geological context (Hawaii, USA). This equation is based on the correlation between rainfall and recharge estimated with the soil water budget in several watersheds of the Hawaiian Archipelago. For rainfall  $> 880$  mm/year, annual recharge  $R$  is related to annual incident precipitation  $P$  by following equation:

$$R = 0.71 \cdot P - 626 \tag{9.1}$$

Cumulated over the last two seasons (cool season 2010, hot season 2011), incident precipitation at GIIWS2 was 2301 mm, and cloud water interception to 205 mm. This yields incident precipitation  $P = 2506$  mm. From Eq. 9.1, we obtain  $R = 1153$  mm/year ( $3.6 \times 10^{-8}$  m/s).

*Izuka et al.* [2010] recall that actual recharge rate depends on the characteristics of the study area, and Eq. 9.1 yields results that differ by -25% to +47% with respect to recharge estimates from the soil water budget. Recharge zone 3 are particularly favorable to recharge, estimates of  $R$  from *Izuka et al.* [2010] are likely to be an under-estimation.

Considering the profile of the island (Fig. 9.3), let  $L$  be the horizontal length of recharge zone 3 in the N-S direction. At the lower limit of recharge zone 3, recharge flux per unit width can be estimated as follow:

$$\phi = R \times L \tag{9.2}$$

$$= 3.6 \times 10^{-8} \times 3000 \tag{9.3}$$

$$= 1.1 \times 10^{-4} \text{ m}^3/\text{s} \tag{9.4}$$

## 9. HIGH-LEVEL GROUNDWATER IN SANTA CRUZ ISLAND

---

This value is not a fine estimate, but actual recharge is probably of the same order of magnitude. It will be used in further discussion.

### 9.3 Re-processing of geophysical data

The SkyTEM survey conducted in Santa Cruz [Auken *et al.*, 2009; d'Ozouville *et al.*, 2008a] was re-inversed with a “smooth” 19 layers spatially constrained inversion model [Viezzoli *et al.*, 2008, 2010]. Though they “smooth” contrasts, models with numerous thin layers can be more reliable in uncalibrated environments and improve vertical resolution. Inverted vertical soundings have then been interpolated and processed with the methodology developed by Pryet *et al.* [2011].

The construction of a 3D grid of resistivity allows 3D visualization, volumic computations, and resistivity extraction based on resistivity thresholds. This is particularly useful for the extraction of 3D formations with a given range of resistivity.

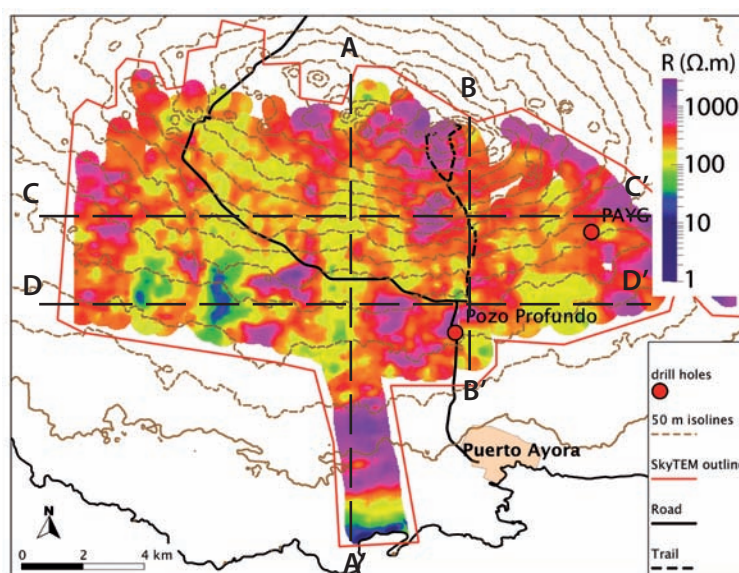


**Figure 9.7:** Surface resistivity of the 19 layers resistivity model.

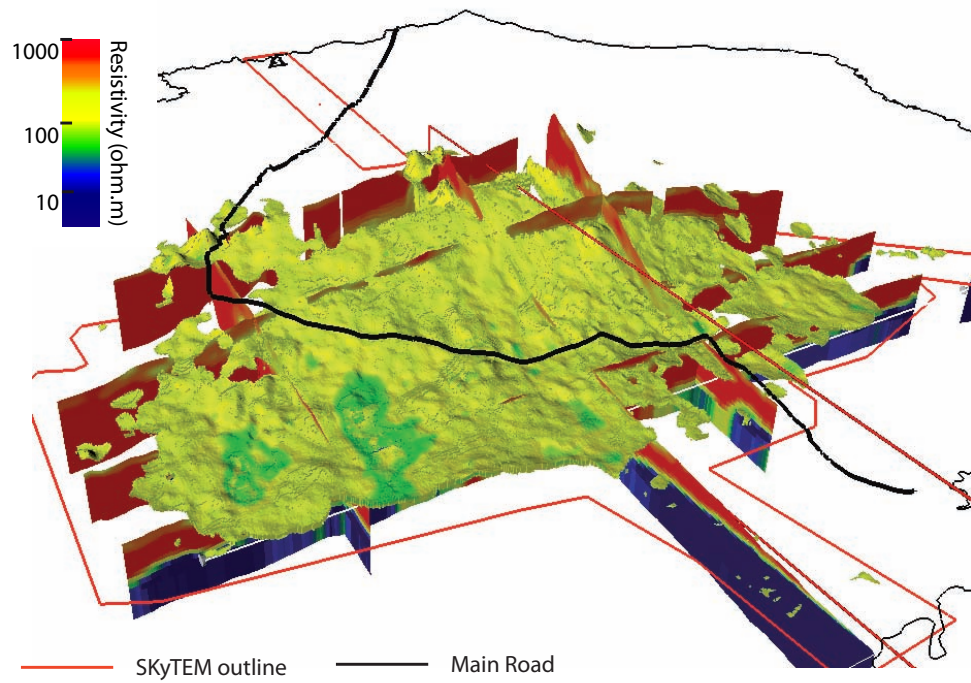


**Figure 9.8:** 3D View of the 50-200 ohm.m resistivity threshold.

## 9. HIGH-LEVEL GROUNDWATER IN SANTA CRUZ ISLAND

---

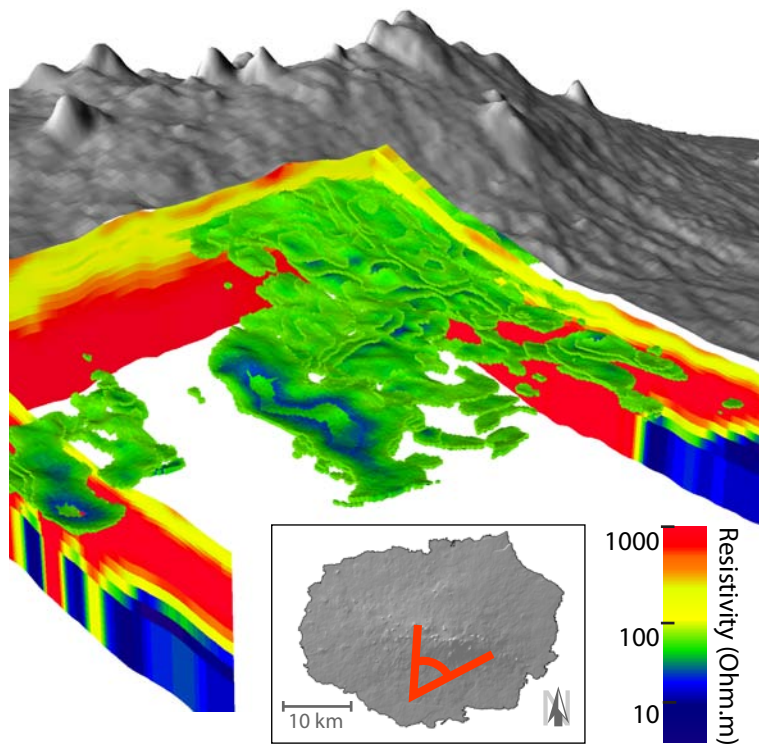


**Figure 9.9:** 3D View of the 30-70 ohm.m resistivity threshold, draped by the DEM from *d'Ozouville et al.* [2008b].

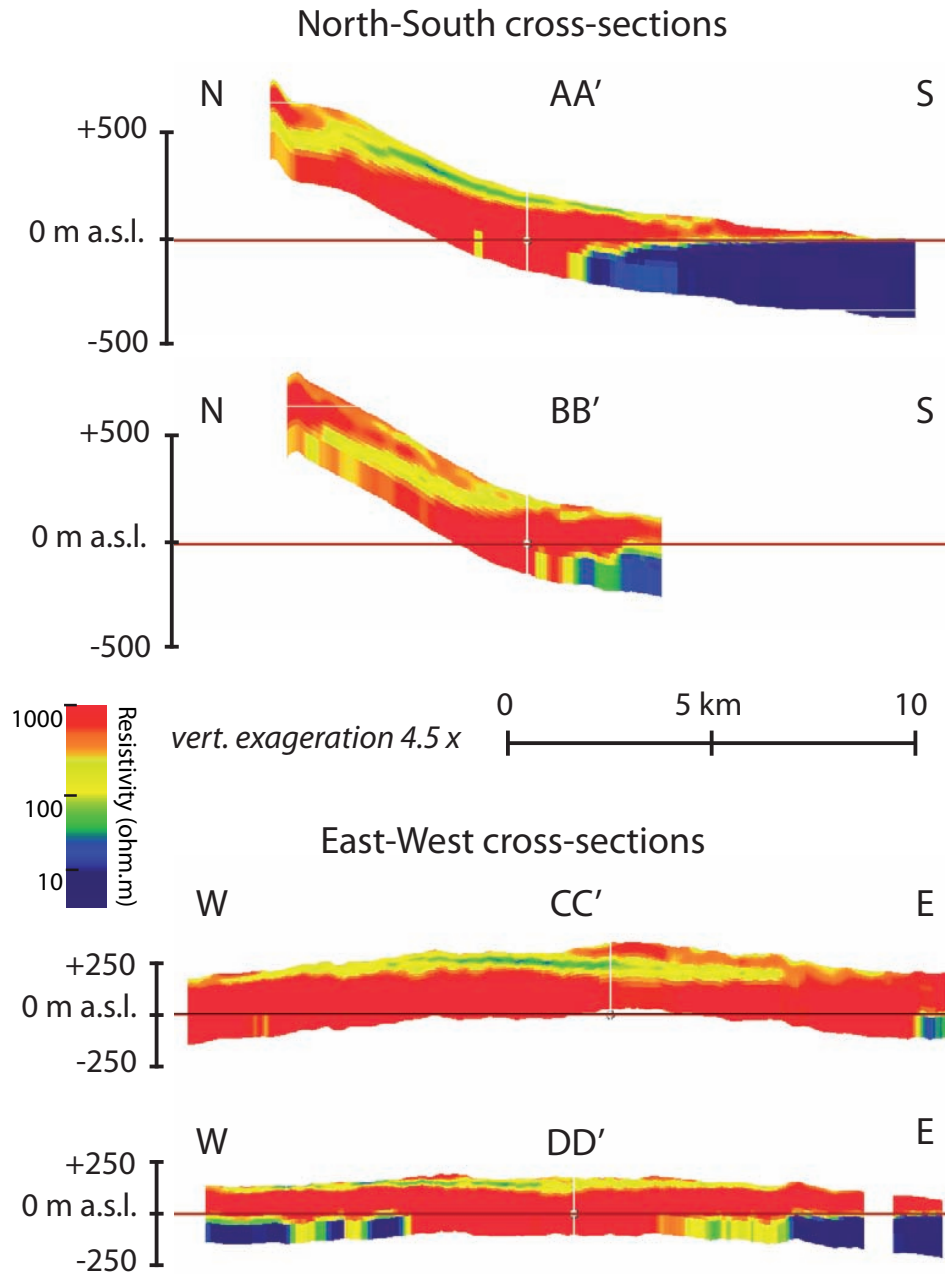


**Figure 9.10:** Cross sections in the 3D resistivity grid. See Fig. 9.7 for the position of the cross-sections.

Interpolated surface resistivity from the 19-layer model presents low-resistivity areas that can be associated to runoff gullies (Fig. 9.7) [d'Ozouville *et al.*, 2008a].

## 9. HIGH-LEVEL GROUNDWATER IN SANTA CRUZ ISLAND

---

The partly buried low-resistivity (50-200 ohm.m) body identified by [d'Ozouville *et al.*, 2008a] remains clearly visible on the re-interpreted dataset. This feature covers ca. 50 km<sup>2</sup> for a median thickness of 31 m and a total volume of 6 km<sup>3</sup> (Table 9.2). At the heart of the 50-200 ohm.m formation, a lower resistivity body (30-70 ohm.m) can be identified (Fig. 9.9 and cross-section AA' on fig 9.10). Locally, several low resistivity units are superimposed (cross-section BB' on Fig. 9.10). The low-resistivity body is roughly sub-parallel to ground slope (cross-sections AA' and BB' on Fig. 9.10).

The cells of the 3D grids have been extracted with two thresholds: 50-200 ohm.m and 30-70 ohm.m. The first range could *a priori* be associated to fresh-water saturated or weathered basalts. The second range was chosen because it highlights an interesting feature, which may be associated to clayey, potentially water saturated formations. Unfortunately, none of the drill holes available on the island (Pozo profundo and PAYG) intersect these resistivities of interest (Fig. 9.8 and 9.9)

From the 50-200 and 30-70 ohm.m extractions, several thematics maps have been computed: depth to the top of the low-resistivity body (Fig. 9.11 and 9.12), thickness (Fig. 9.13 and 9.14), and slope (Fig. 9.15 and 9.16). In the case of the superimposition of low-resistivity bodies (e.g. cross-sections BB' on Fig. 9.10), only the upper low-resistivity unit was considered in the calculations. As a consequence, deeper (possibly thicker) low-resistivity bodies can be concealed.

The deep very low resistivity layers (< 15 ohm.m) of the geophysical model provide an indicative values of the depth of the salt water interface (SWI) [Auken *et al.*, 2009]. A 2D map of SWI depth was computed from the 3D grid of resistivity (Fig. 9.17). This depth inferred from geophysical results may approximate the position the 50% mixing line between salt and the overlying freshwater lens. But vertical profiles of groundwater salinity are not available and the geophysical model cannot be calibrated. SWI depth provided on Fig. 9.17 are only indicative, but coherent. At the exception of some artefacts (SWI values above sea level), SWI appears shallower close to the coast and thicker inland.

### 9.3 Re-processing of geophysical data

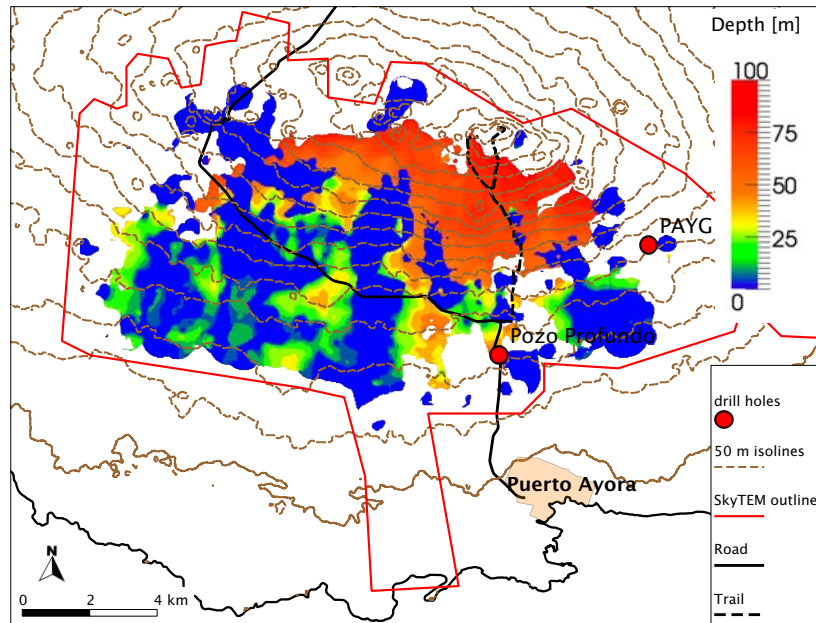


Figure 9.11: Depth from ground surface (threshold 50-200 ohm.m)

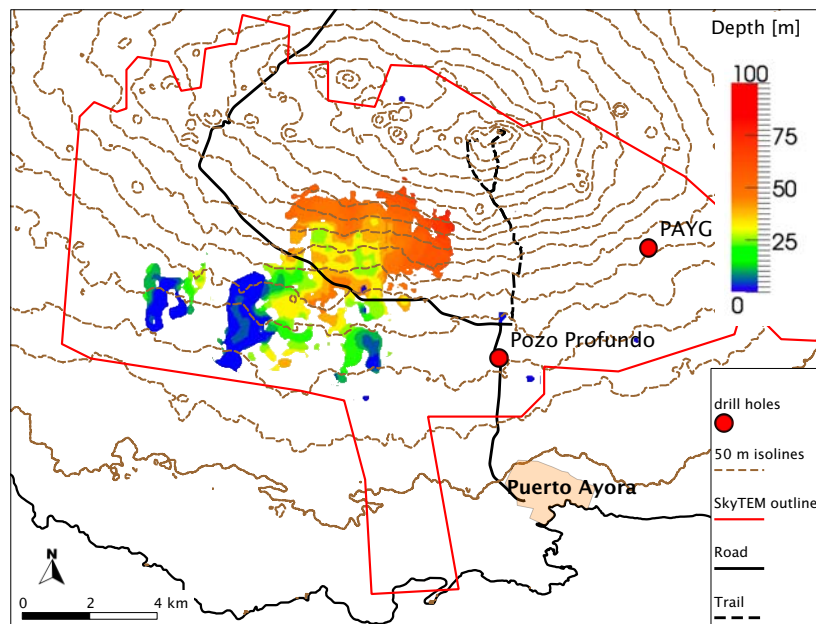


Figure 9.12: Depth from ground surface (threshold 30-70 ohm.m)

## 9. HIGH-LEVEL GROUNDWATER IN SANTA CRUZ ISLAND

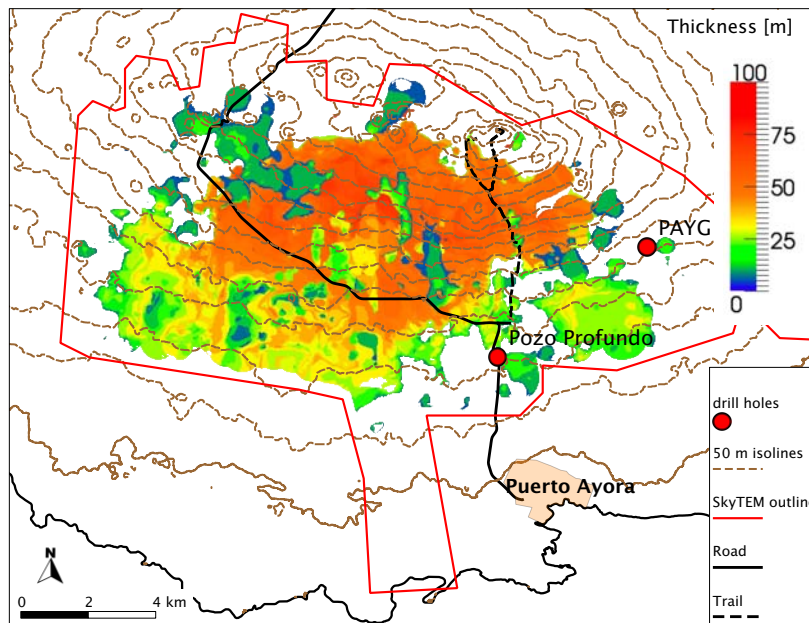


Figure 9.13: Thickness (threshold 50-200 ohm.m)

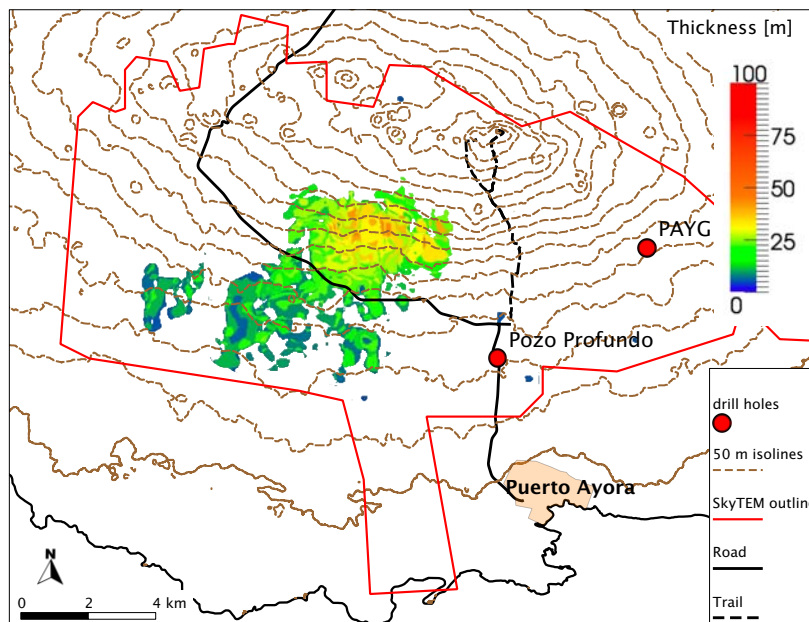


Figure 9.14: Thickness (threshold 30-70 ohm.m)

### 9.3 Re-processing of geophysical data

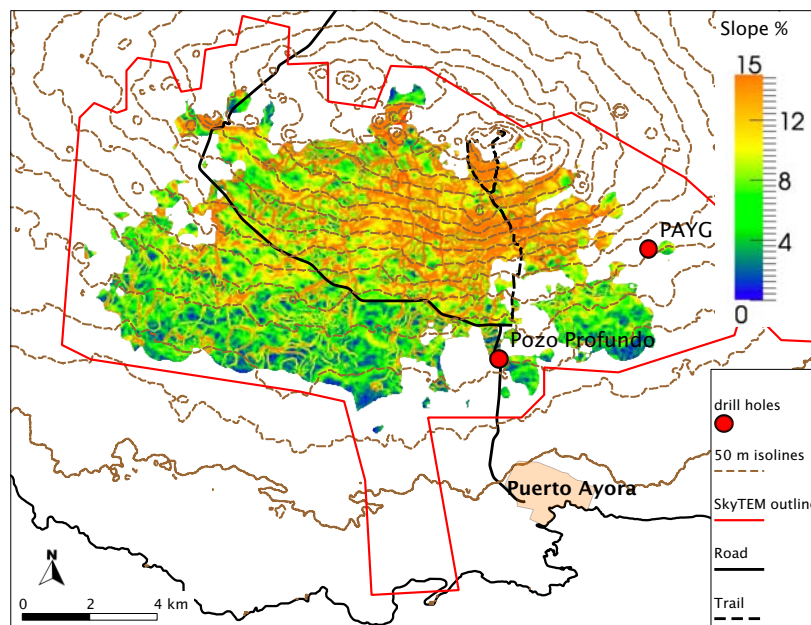


Figure 9.15: Slope (threshold 50-200 ohm.m)

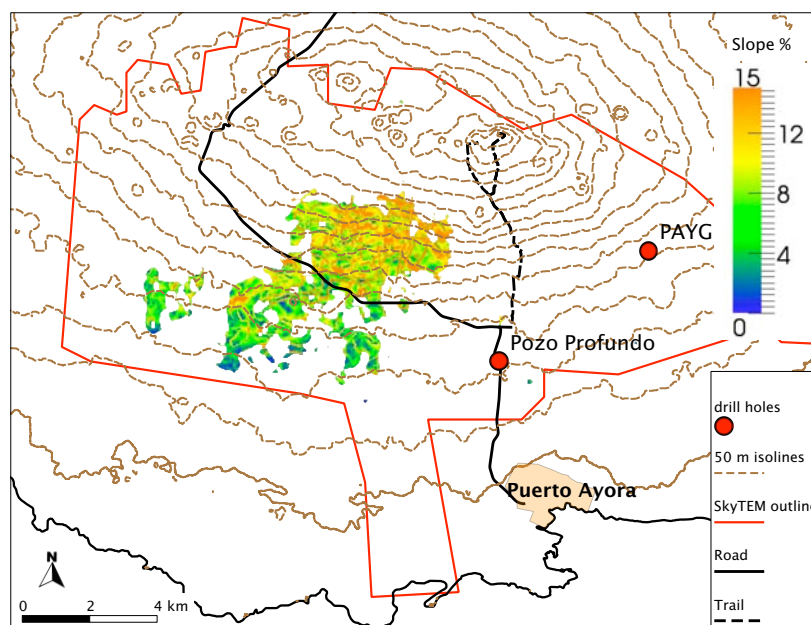
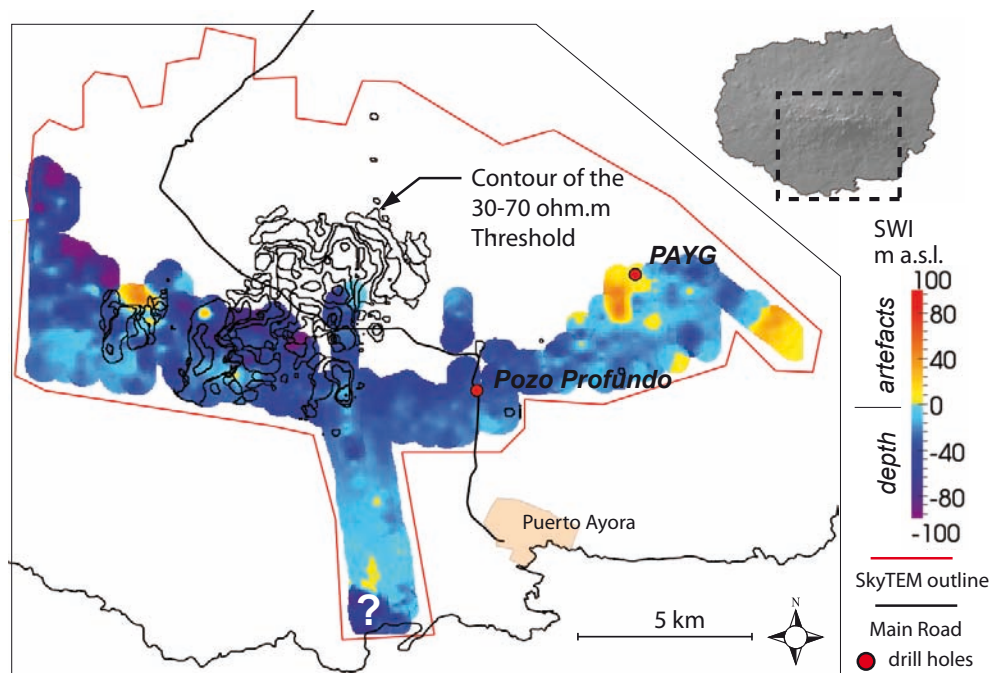


Figure 9.16: Slope (threshold 30-70 ohm.m)

## 9. HIGH-LEVEL GROUNDWATER IN SANTA CRUZ ISLAND



**Figure 9.17:** Depth to the Salt Water Interface (SWI), estimated from the depth to very low resistivity layer ( $R < 15$  ohm.m). The outline of the 30-70 ohm.m threshold (Fig. 9.12) is presented to facilitate interpretation.

### 9.3 Re-processing of geophysical data

---

		50-200 ohm.m	30-70 ohm.m
		threshold	threshold
depth [m]	median	32	31
	min	0	0
	max	250	170
thickness [m]	median	31	14
	min	5	5
	max	150	47
slope [%]	median	9	8
	min	0	0
	max	100(*)	100(*)

**Table 9.2:** Statistics on the geometry of 50-200 and 30-70 ohm.m thresholds. (\*) Slopes of 100% are artifacts related vertical lateral boundaries of extracted units.

The depth of the top of the 50-200 ohm.m resistivity extraction ranges between 0 m downslope (the formation outcrops) and ca. 100 m below ground level upslope (Fig. 9.11). Low-resistivity bodies are found deeper at the east than at the west, where it largely outcrops (Fig. 9.7). The lower resistivity extraction (30-70 ohm.m) (Fig. 9.12) forms a patch at the center and south-western parts of the surveyed area. It is deep to the north (50-80 m below ground), and shallower to the south, on the lower slopes. It outcrops at a location identified as a pond on the field on the lower slopes.

The thickness of the 50-200 ohm.m extraction ranges between 5 m and 100 m. It is thicker below the steeper, higher slopes above ca. 250 m a.s.l. These values of thickness should be considered with care when several low-resistivity units are superimposed. A shallow, thin low-resistivity unit may conceal another underlying, thicker low-resistivity body (e.g. cross-section BB' on Fig. 9.10). The thickness of the 30-70 ohm.m resistivity extraction range between 5 and 30 m. A thicker part is found at the center of the surveyed area.

For both low-resistivity extractions, the slope of top surfaces generally follows the topography. Ground slope is steeper at the east and more gentle at the center of Santa Cruz. As a consequence, the top of the 50-200 ohm.m extraction is steeper at the east (10-15%), than at the center of the surveyed area (8-12%). The slope of the top of the 30-70 ohm.m is slightly less steep.

From these observations, low-resistivity bodies appear relatively thick, but have a complex organization with super-imposed low-resistivity units. The top of the low-resistivity unit dips relatively steeply (4-12 %). Observations are sum-

## **9. HIGH-LEVEL GROUNDWATER IN SANTA CRUZ ISLAND**

---

marized in Table 9.2 for further discussion.

## 9.4 Discussion

Three models were *a priori* likely to describe the hydrogeological configuration of Santa Cruz (Fig. 9.2). All three models are compatible with the presence of a 50-200 ohm.m, partly buried low resistivity body below the windward slope of the island.

In model C, the low-resistivity body is associated with groundwater flowing over an impervious core. Such a core could be constituted by older, weathered, and possibly hydrothermalized volcanics. However, such formation would likely have a weak resistivity [Desclotres *et al.*, 1997; Robineau *et al.*, 1997]. This is not compatible with current resistivity maps (Fig. 9.10), revealing high resistivities at depth. As a consequence, model C can be discarded.

Two models remain (A and B). The 50-200 ohm.m low resistivity body can be associated to weathered volcanics (model A) or water saturated basalt (model B) (Fig. 9.2). We discuss the condition of stability of a perched aquifer as described on model B. Nevertheless, reliable conclusions are suspended to validation through the execution of drill holes, sufficiently deep to reach the layers of interest.

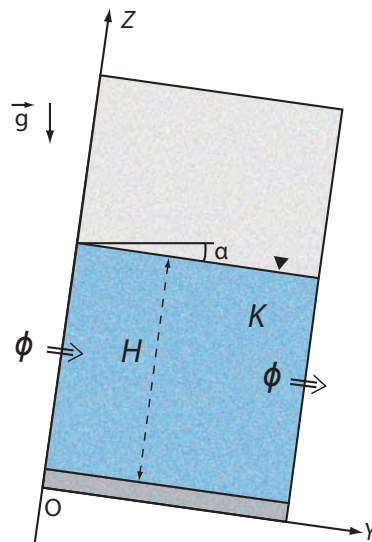


**Figure 9.18:** Small portion of a perched aquifer over an impervious layer, with recharge flux  $\phi$  restricted to the left boundary

We consider a N-S cross-section of a portion of a perched aquifer at a distance of 3 km from the summit (lower limit of recharge zone 3). The water table dips with an angle  $\alpha$ , sub-parallel to the sustaining layer (Fig. 9.18). It is assumed

## 9. HIGH-LEVEL GROUNDWATER IN SANTA CRUZ ISLAND

---

that:

- Climatic conditions of 2010/2011 were close to the conditions prevailing prior to the geophysical survey. Recharge is supposed to be constant.
- The totality of recharge from zone 3 (Eq. 9.4) transits through the idealized perched aquifer (i.e. no direct flow to the basal aquifer).
- The thickness of the perched aquifer is the median thickness of the 50-200 ohm.m low-resistivity extraction (31 m, from Table 9.2).
- the slope of the water table is parallel to the low-resistivity layer. The hydraulic gradient is estimated from the median slope of the 50-200 ohm.m resistivity extraction (9%, from Table 9.2).

Groundwater flux  $\phi$  flows through the aquifer without recharge from the upper boundary, nor losses through the sustaining layer. Under steady conditions, Darcy's law yields:

$$\phi = H \times K \times i \quad (9.5)$$

where  $\phi$  is groundwater flow per unit width of the aquifer,  $H$  the thickness of the aquifer,  $K$  hydraulic permeability, and  $i = \tan(\alpha)$  the hydraulic gradient.

With  $\phi = 1.1 \times 10^{-4}$  m<sup>3</sup>/s,  $H = 31$ , and  $i = 0.09$ , we obtain  $K = 4 \times 10^{-5}$  m/s. This value does not present an estimate of hydraulic conductivity. Instead, it provides a condition for an aquifer (Fig. 9.18, B) to be stable under the conditions detailed above.

The geology of Santa Cruz is dominated by thick *pahoehoe* and *aa'* lava flows dissected by cooling joints [Bow, 1979]. Locally, these formations are interbedded by 0-2.5 m ash and red soils [Bow, 1979; Woodward *et al.*, 1996]. Currently available estimates of hydraulic conductivity on this island were inferred from tidal signal propagation and aquifer test in the low-elevation apron, between the coast to the *pozo profundo* (Fig. 9.2). Estimates of hydraulic conductivity range around  $1 \times 10^{-3}$  m/s (Chap. 8). This is two order of magnitudes higher than the permeability required for the perched aquifer to be stable.

Yet, some factors could induce a reduction of permeability at higher elevation. Though it is not observed on the available drill hole (PAYG, Fig. 9.7), a higher ratio of pyroclastic units is expected closer to the eruptive center. Weathering of these formations is faster, and could be enhanced by the humid conditions. Cooling joints may be partly filled. Yet, a *general* reduction of the permeability by 2 orders of magnitude is relatively unlikely. From these observations, the idealized perched aquifer has little chance to be stable.

Assumptions made above for the estimation of the groundwater flux  $\phi$  were favorable to the existence of a perched aquifer. In fact, only a portion of recharge may actually transit through the perched aquifer and the sustaining layer may be discontinuous and induce leakage. These effects, combined with natural fluctuations of recharge rates would make the existence of the idealized perched aquifer more unlikely.

These elements may explain why the outcropping of the 50-200 ohm.m extraction does not appear to be associated with lines of springs. The thick, continuous low-resistivity body could rather be interpreted by an undefined weathered geological unit, with a higher ratio of pyroclastic material.

The very low resistivity threshold (30-70 ohm.m) is *a priori* related to hydrothermalized or weathered, clayey formations. This unit is above sea level and the low resistivity cannot be attributed to seawater intrusion. Its flat geometry and location remote from any eruptive area tend to discard any relation with hydrothermal activity at the surface. This very low resistivity unit is probably a clayey horizon, possibly saturated. The hydraulic conductivity of this formation is probably too low for the formation to be considered as aquifer. Nevertheless, it may, if recharge is sufficient, sustain an overlying saturated horizon.

Perched horizons may exist, but they are probably intermittent and circumscribed to more “favorable” areas, i.e. the presence of a sufficiently thick and relatively shallow layer of resistivity 50-200 ohm.m, overlying a continuous and relatively flat, very low resistivity (30-70) layer. The slope of the “sustaining” impervious layer is an important condition: perched groundwater units are more likely to be stable over gently sloping surfaces, rather than over steep sloping surfaces, where the hydraulic gradient is necessarily high.

A “favorable” configuration for a perched aquifer can be found at the intersection between the 30-70 threshold and the main road (Fig. 9.14 and 9.16). In this zone, the very low (30-70 ohm.m) layer is 20 to 50 m below ground, it has a thickness of 7-25 m and is sloping at 7-20%

Precisely in the “favorable” area, the salt water interface (SWI) depth appears deeper south of the intersection between the 30-70 ohm.m threshold and the main road. This is precisely in this area that the 30-70 ohm.m resistivity extraction becomes thinner and discontinuous and where perched groundwater could discharge to the underlying basal aquifer.

Better recharge estimates, a good description of the perched aquifer water table (see appendix), and the consideration of variable recharge rates with numerical modeling could reveal further insights. Yet, it would be of the highest hydrogeological interest to drill exploratory holes in this area.

### 9.5 Conclusion

Re-processing of the 2006 SkyTEM survey to “smooth” 19-layer models revealed new insights on the dataset and provides a better description of the geometry of the low-resistivity units below the windward slope of Santa Cruz island.

Considering that all groundwater recharge transits through the idealized perched aquifer with a geometry fitting the 50-200 ohm.m resistivity extraction, the hydraulic conductivity should be  $4 \times 10^{-5}$  m/s for the aquifer to be stable. This is two orders of magnitude smaller than current permeability estimates on the coastal apron of this island, inferred from tidal signal propagation and aquifer tests. Perched aquifer may exist but they are probably intermittent and restricted to “favorable” areas, over gently sloping, very low resistivity, probably clayey 30-70 ohm.m unit.

Drilling is an expensive and complicated task in volcanic insular contexts. Nevertheless, validation with drill holes perforating the 30-70 and 50-200 ohm.m extractions where they are superimposed would be of the highest hydrogeological interest.

## Appendix: 1D analytical modeling of a perched aquifer.

We consider an aquifer in a formation of hydraulic conductivity  $K_1$ , perched over an impervious layer of hydraulic conductivity  $K_2$ , *gently* dipping with an angle  $\alpha$  with respect to the horizontal (Fig. 9.19).

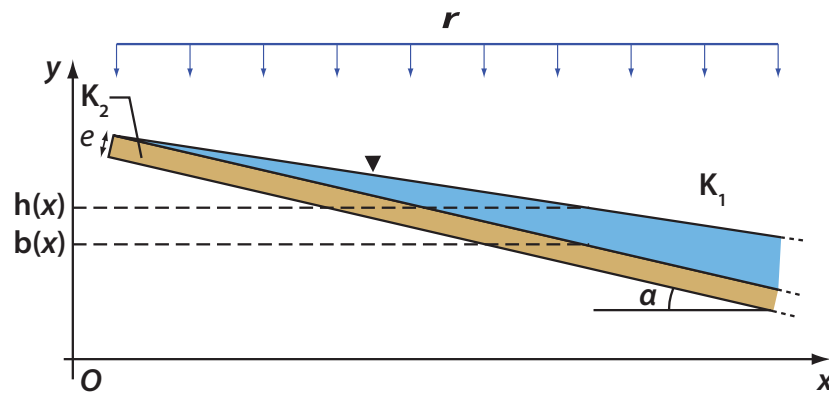


**Figure 9.19:** Idealized model of a perched aquifer.

Under the Dupuit assumption, Darcy law and mass conservation [*de Marsily*, 1986], yield:

$$K_1(h(x) - b(x)) \frac{\partial^2 h}{\partial x^2} = r + \frac{h(x)}{e} \cdot K_2 \quad (9.6)$$

where  $h(x)$  is the hydraulic head,  $b(x)$  is the height of the sustaining layer, and  $e$  its thickness, assumed to be constant.

Considering  $K_2 \gg K_1$ , losses through the sustaining layer can be neglected. Assuming that the sustaining layer is straight, with  $b(x) = -\tan(\alpha) \cdot x + b_0$ , Eq. 9.7 can be simplified to:

$$K_1(h(x) + \tan(\alpha) \cdot x - b_0) \frac{\partial^2 h}{\partial x^2} = r \quad (9.7)$$

This is a non-linear differential equation. To the author's current knowledge, it does not accept a simple solution.



**Part V**

**Conclusions**



## Chapter 10

# Hydrogeology of basaltic volcanic islands in perspectives

## 10. HYDROGEOLOGY OF BASALTIC VOLCANIC ISLANDS IN PERSPECTIVES

---

### 10.1 AEM surveys in volcanic contexts

Airborne electromagnetics (AEM) surveys allow electrical resistivity mapping over extensive surfaces in a short space of time. In the frame of this thesis, the results of two extensive surveys conducted in a volcanic context have been interpreted. The following conclusions emerge:

- Through the development of a new gridding method, results can now be visualized as coherent 3D models.
- AEM surveys are proven to be applicable in volcanic contexts. They provided valuable insights in the hydrogeological interpretation of the Galapagos dataset.
- Volcanic formations are complex and heterogeneous. The absence of drill holes in the surveyed zone makes the interpretation of AEM surveys challenging and speculative. It may turn frustrating not be able to provide striking conclusions from amazing 3D images with numerous “Unidentified Geological Objects” (UGO).

## 10.2 Fog interception

In the frame of this thesis, two weather stations were installed in the highlands of Santa Cruz. A first at lower fringe of the fog layer and the second at the cloud center. Cloud water interception was estimated with a *Rutter*-type canopy interception model. Results can be summarized as follow:

- During fog season, cloud water interception contributed to 22% of total incident precipitation at the center of the cloud, while it was negligible at the lower fringe of the cloud.
- Fog-interception appears to be enhanced by higher wind speeds (up to 4 m/s), but the density of the cloud is expected to have a bigger importance.
- Fog interception may bring a non-negligible amount of water. If it is circumscribed to a season of the year, and effective over a small region, the actual input from fog becomes small.

## 10.3 Evolution of basaltic islands

The literature regarding the hydrogeology of basaltic volcanic islands has been reviewed and completed by new elements from the Galapagos islands.

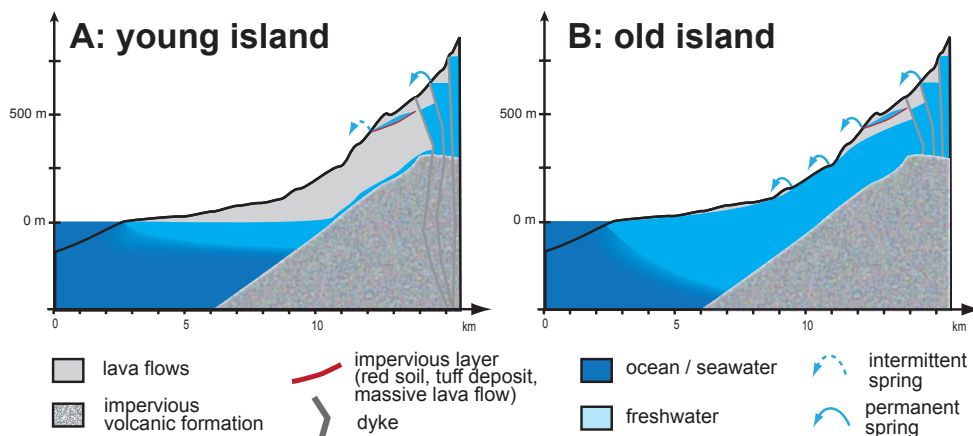


**Figure 10.1:** Simplified evolution sketch of the hydrogeological settings of basaltic islands. (A) Young island (< 1 Ma) with a low-lying basal aquifer subjected to seawater intrusion. (B) Old island (> 1 Ma)

## 10. HYDROGEOLOGY OF BASALTIC VOLCANIC ISLANDS IN PERSPECTIVES

---

Though it is modulated by climatic conditions, the geological age of the islands appears to condition groundwater occurrence:

- A basal aquifer in connection with the ocean is found in all basaltic islands. In younger islands ( $< 1$  Ma), regional permeability is high ( $K \approx 1 \times 10^{-3}$  m/s), the basal aquifer remains at low elevation and may be continued toward the center of the island by *skin flow* over an impervious substratum. In old islands ( $> 1$  Ma), regional permeability is lower ( $K \approx 1 \times 10^{-6}$  m/s) and a thick freshwater lens may develop. The basal aquifer reaches high elevation, feeding springs and streams.
- At higher elevations, groundwater is found in perched and dike impounded aquifers. In young islands, these resources may be intermittent and difficult of access. With time, permeability decreases, aquifers are thicker and likely to be perennial. Valleys are incised and flanks may collapse. This allows aquifers to outcrop and lead to the existence of springs.





# Chapter 11

## Solutions for Galapagos

## 11.1 Conceptual models for Santa Cruz and San Cristóbal Islands

Two contrasting hydrogeological conceptual models are proposed for Santa Cruz and San Cristóbal islands.

On Santa Cruz (Fig. 11.1), basaltic formations are relatively young and permeable ( $K \approx 1 \times 10^{-3}$ ). The basal aquifer is low-lying and subject to seawater intrusion. In the highlands, perched aquifers may exist but they are likely to be intermittent or limited to the more favorable areas with high recharge potential and the presence of gently sloping impervious geological layer.

On San Cristóbal, springs are fed by high-level aquifers, which do not appear to be connected to the basal aquifer. They are most-probably perched over an impervious unit (soil, ash) or over a geological discontinuity.

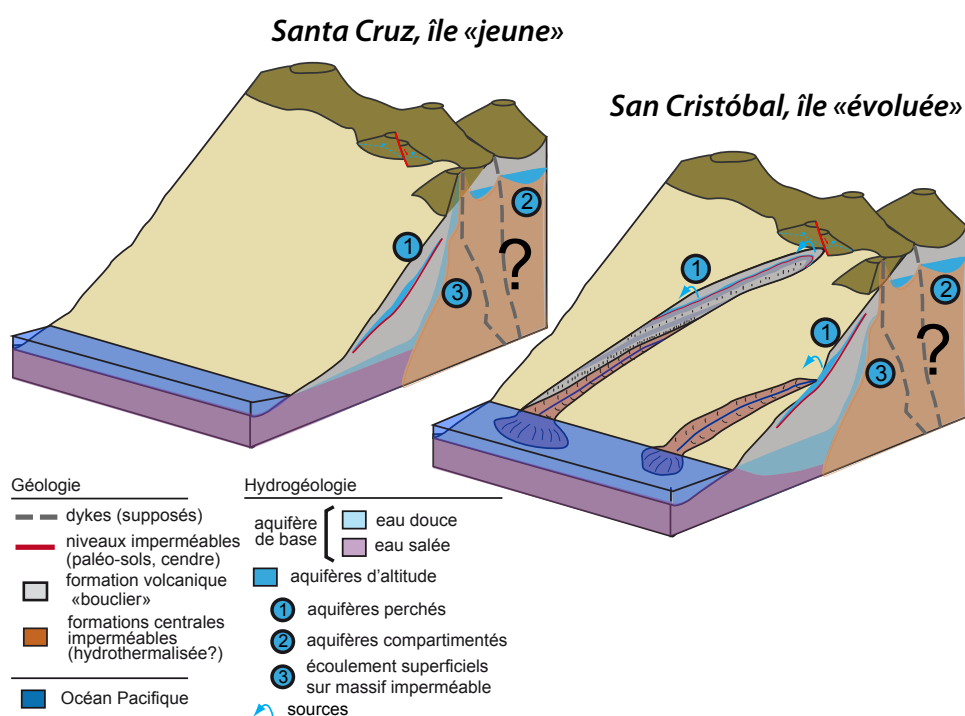


**Figure 11.1:** Simplified hydrogeological conceptual models proposed for Santa Cruz and San Cristóbal islands

## 11.2 Solving the Galapagos “water issue”

The Galapagos “water issue” is the most conspicuous on Santa Cruz Island. Other studies showed that bacterial contamination, rather than salt, is at the origin of the reported diseases. It is out of the scope of this study to propose solutions to decontaminate the water distributed by the municipality but it appears to be the first priority on this island.

The geological conditions of Santa Cruz Island are not favorable to groundwater storage. Nevertheless, as detailed in this dissertation, groundwater may be found:

- In relatively shallow (30 -100 m below ground level) perched aquifers at preferential areas designated in Chap. 9.
- The basal aquifer appears thicker at 6-8 km from the coast. At 150-300 m below ground level, it may provide fresh or slightly brackish groundwater.

Given the acute stress over freshwater resources, it appears worth executing a set of exploratory drill holes in these areas. The absence of drill hole on Santa Cruz is a scientific frustration, but it goes beyond the scope of the GIIWS project to finance and conduct the executions of drill holes in Galapagos.



# Chapter 12

## Perspectives

Many aspects of Galapagos hydrology were handled. Results provided in this dissertation are not ultimate answers, and numerous interesting questions remain open. Two master thesis of the Polytechnic School of Quito are undergoing and one will be shortly defended [*Domínguez González, 2011*]. Based on the dataset collected in the frame of this thesis, they will improve our understanding of hydrological processes in Santa Cruz.

This is a non-comprehensive list of what could be dealt in further studies regarding the hydrology of Galapagos:

- In the frame of this thesis, the first hydrogeological investigations were conducted in Floreana and Isabela Islands. Results are too light to be presented here, but are encouraging enough to promote further investigations.
- The extensive geophysical campaign deserves to be completed by an extensive drilling campaign. The author is aware of the financial and technical challenges associated with such a project, but would be extremely interested in the results.
- Long-term climatic monitoring is a valuable resource for investigators and a requirement to provide relevant conclusions. The climatic stations installed in the frame of this thesis, could still provide valuable results if they are frequently maintained.



# References

- Abarca, E., J. Carrera, X. Sanchez-Vila, and M. Dentz, Anisotropic dispersive Henry problem, *Advances in Water Resources*, 30(4), 913 – 926, doi:DOI:10.1016/j.advwatres.2006.08.005, 2007. 169, 176
- Acocella, V., and M. Neri, Dike propagation in volcanic edifices: Overview and possible developments, *Tectonophysics*, 471(1-2, Sp. Iss. SI), 67–77, doi:{10.1016/j.tecto.2008.10.002}, 2009. 42, 46, 47, 96
- Adelinet, M., Etude hydrologique des bassins versants de l’île de San Cristóbal (Galapagos, Equateur), Master’s thesis, ENS Paris and UPMC Univ. Paris 6, Sisyphé Lab., 2005. xxiii, 98, 100, 102
- Adelinet, M., J. Fortin, N. d’Ozouville, and S. Violette, The relationship between hydrodynamic properties and weathering of soils derived from volcanic rocks, Galapagos Islands (Ecuador), *Environmental Geology*, 56, 45–58, 2008. 96, 112, 228
- Adler, P., and J. Thovert, *Fractures and fracture networks*, vol. 15, Kluwer Academic Publishers, 1999. 187, 211, 213
- Aizawa, K., Y. Ogawa, and T. Ishido, Groundwater flow and hydrothermal systems within volcanic edifices: Delineation by electric self-potential and magnetotellurics, *Journal of Geophysical Research - Solid Earth*, 114, B01,208, 2009. 103, 107, 221
- Alcolea, A., E. Castro, M. Barbieri, J. Carrera, and S. Bea, Inverse modeling of coastal aquifers using tidal response and hydraulic tests, *Ground Water*, 45(6), 711–722, 2007. 210
- Amelung, F., S. Jónsson, H. Zebker, and P. Segall, Widespread uplift and ‘trap-door’ faulting on Galapagos volcanoes observed with radar interferometry, *Nature*, 407(6807), 993–996, 2000. 10, 44

## REFERENCES

---

- Auken, E., and A. Christiansen, Layered and laterally constrained 2D inversion of resistivity data, *Geophysics*, *69*(3)(3), 752–761, 2004. 73, 77
- Auken, E., A. V. Christiansen, L. H. Jacobsen, and K. I. Sorensen, A resolution study of buried valleys using laterally constrained inversion of TEM data, *Journal of Applied Geophysics*, *65*(1)(1), 10–20, doi:{10.1016/j.jappgeo.2008.03.003}, 2008. 73
- Auken, E., S. Violette, N. d'Ozouville, B. Deffontaines, K. I. Sørensen, A. Viezzoli, and G. de Marsily, An integrated study of the hydrogeology of volcanic islands using helicopter borne transient electromagnetic: Application in the Galapagos Archipelago, *Comptes rendus-Géoscience*, *341*, 899–907, 2009. 21, 81, 103, 220, 221, 230, 234
- Bardintzeff, J., and A. McBirney, *Volcanology*, Jones and Barlett, 2006. 42, 46
- Bear, J., *Dynamics of fluids in porous media*, Dover publications, 1988. 170, 171
- Bear, J., *Seawater intrusion in coastal aquifers: Concepts, methods, and practices*, chap. Conceptual and Mathematical Modeling, pp. 163–191, Springer, 1999. 58, 103, 164
- Berkowitz, B., and I. Balberg, Percolation theory and its application to groundwater hydrology, *Water resources research*, *29*(4), 775–794, 1993. 187
- Bosch, J., M. J. Bakker, J. Gunnink, and B. Paap, Airborne electromagnetic measurements as basis for a 3D geological model of an Elsterian incision, *Zeitschrift der Deutschen Gesellschaften für Geowissenschaften*, *160*, 249–258, 2009. 73
- Bow, C. S., The Geology and Petrogenesis of the Lavas of Floreana and Santa Cruz Islands: Galapagos Archipelago, Ph.D. thesis, University of Oregon, USA, 1979. 9, 10, 40, 80, 112, 113, 187, 188, 189, 196, 242
- Brauman, K. A., D. L. Freyberg, and G. C. Daily, Forest structure influences on rainfall partitioning and cloud interception: A comparison of native forest sites in Kona, Hawai'i, *Agr. Forest Meteorol.*, *150*(2), 265 – 275, doi:DOI: 10.1016/j.agrformet.2009.11.011, 2010. 54, 123
- Bruijnzeel, L. A., Hydrology of tropical montane cloud forests: a reassessment, *Land Use and Water Resources Research*, *1*(1), 1–18, 2001. 123
- Bruijnzeel, L. A., W. Eugster, and R. Burkard, Fog as a hydrologic input, in *Encyclopaedia of Hydrological Sciences*, edited by M. G. Anderson, pp. 559–582, John Wiley & Sons, Chichester, 2005. 123

## REFERENCES

---

- Bruijnzeel, L. A., R. Burkard, A. Carvajal, A. Frumau, L. Köhler, M. Mulligan, J. Schellekens, S. Schmid, and C. Tobón, Final Technical Report DFID-FRP Project no. R7991. Hydrological impacts of converting tropical montane cloud forest to pasture, with initial reference to northern Costa Rica., *Tech. rep.*, VU University, Amsterdam and Aylesford, UK: Forestry Research Program of the UK Department for International Development, <http://www.falw.vu/~fiesta/>, 2006. 128
- Bruijnzeel, L. A., M. Mulligan, and F. N. Scatena, Hydrometeorology of tropical montane cloud forests: emerging patterns, *Hydrol. Process.*, *25*, 465–498, 2011. 123, 127, 140, 148
- Bues, M., and C. Oltean, Numerical simulations for saltwater intrusion by the mixed hybrid finite element method and discontinuous finite element method, *Transport in porous media*, *40*(2), 171–200, 2000. 176
- Cabrera, M., and E. Custodio, Groundwater flow in a volcanic–sedimentary coastal aquifer: Telde area, Gran Canaria, Canary Islands, Spain, *Hydrogeology Journal*, *12*(3), 305–320, 2004. 40
- Caine, J., J. Evans, and C. Forster, Fault zone architecture and permeability structure, *Geology*, *24*(11), 1025, 1996. 187
- Calder, I. R., and C. H. R. Kidd, A note on the dynamic calibration of tipping-bucket gauges, *J. Hydrol.*, *39*(3-4), 383–386, 1978. 130, 147
- Cane, M., The evolution of El Niño, past and future, *Earth and Planetary Science Letters*, *230*(3-4), 227–240, 2005. 13
- Carracedo, J. C., et al., The NE Rift of Tenerife: towards a model on the origin and evolution of ocean island rifts, *Estudios Geológicos Madrid*, *65*(1), 5–47, doi:{10.3989/egeol.39755.056}, 2009. 42, 47
- Carreira, P. M., J. M. Marques, A. Pina, A. M. Gomes, P. A. Galego Fernandes, and F. M. Santos, Groundwater Assessment at Santiago Island (Cabo Verde): A Multidisciplinary Approach to a Recurring Source of Water Supply, *Water Resources Management*, *24*(6), 1139–1159, doi:{10.1007/s11269-009-9489-z}, 2010. 40
- Cavelier, J., and G. Goldstein, Mist and fog interception in elfin cloud forests in colombia and venezuela., *J. Trop. Ecol.*, *5*(3), 309–322, 1989. 148
- Chadwick, W., and K. Howard, The pattern of circumferential and radial eruptive fissures on the volcanoes of Fernandina and Isabela islands, Galapagos, *Bulletin of Volcanology*, *53*(4), 259–275, 1991. 47, 94, 96

## REFERENCES

---

- Chadwick, W. W., and J. Dietrich, Mechanical modeling of circumferential and radial dike intrusion on Galapagos volcanoes, *Journal of Volcanology and Geothermal Research*, 1995. 9
- Charlier, J.-B., P. Lachassagne, B. Ladouche, P. Cattan, R. Moussa, and M. Voltz, Structure and hydrogeological functioning of an insular tropical humid andesitic volcanic watershed: A multi-disciplinary experimental approach, *Journal of Hydrology*, 398(3-4), 155 – 170, doi:DOI:10.1016/j.jhydrol.2010.10.006, 2011. 41
- Chesnaux, R., D. Allen, and S. Jenni, Regional fracture network permeability using outcrop scale measurements, *Engineering Geology*, 108(3-4), 259–271, 2009. 211
- Chilès, J., and P. Delfiner, *Geostatistics: Modeling Spatial Uncertainty second ed.*, Wiley, New York, 2011. 76, 80, 83
- Clarke, H., V. Troll, and J. Carracedo, Phreatomagmatic to Strombolian eruptive activity of basaltic cinder cones: Montaña Los Erales, Tenerife, Canary Islands, *Journal of Volcanology and Geothermal Research*, 180(2-4), 225–245, 2009. 46
- Clemente, C. S., E. B. Amoros, and M. G. Crespo, Dike intrusion under shear stress: Effects on magnetic and vesicle fabrics in dikes from rift zones of Tenerife (Canary Islands), *Journal of Structural Geology*, 29(12), 1931–1942, doi:{10.1016/j.jsg.2007.08.005}, 2007. 47
- Colinvaux, P., Climate and the Galapagos islands, *Nature*, 240, 17–20, 1972. xix, 10, 11, 96
- Conroy, J., A. Restrepo, J. Overpeck, M. Steinitz-Kannan, J. Cole, M. Bush, and P. Colinvaux, Unprecedented recent warming of surface temperatures in the eastern tropical Pacific Ocean, 2008. 13
- Cooper, H., A hypothesis concerning the dynamic balance of fresh water and salt water in a coastal aquifer, *Journal of Geophysical Research*, 64(4), 461–467, 1959. 169
- Cox, L., G. Wilson, and M. Zhdanov, 3D inversion of airborne electromagnetic data using a moving footprint, *Exploration Geophysics*, 41(4), 250–259, 2010. 73
- Crockford, R. H., and D. P. Richardson, Partitioning of rainfall into throughfall, stemflow and interception: effect of forest type, ground cover and climate, *Hydrol. Process.*, 14(16-17), 2903–2920, 2000. 132, 140

## REFERENCES

---

- Cruz, J., Groundwater and volcanoes: examples from the Azores archipelago, *Environmental Geology*, 44(3), 343–355, 2003. 40, 48, 49, 53, 61, 67
- Cruz, V., and O. Silva, Hydrogeologic framework of Pico Island, Azores, Portugal, *Hydrogeology Journal*, 9(2), 177–189, 2001. 39, 40, 61, 93
- Cullen, A., A. McBirney, and R. Rogers, Structural controls on the morphology of Galapagos shields, *Journal of volcanology and geothermal research*, 34(1-2), 143–151, 1987. 187
- Custodio, E., *Groundwater studies : an international guide for hydrogeological investigations - IHP-VI, Series on Groundwater No.3*, chap. Hydrogeology of volcanic rocks, pp. 395–425, UNESCO, Paris, 2004. 39, 44, 45, 46, 47, 48, 49, 50, 51, 52, 54, 55, 58, 59, 61, 96, 98, 113, 160, 208, 211, 215
- Custodio, E., J. Guerra, J. Jiménez, J. Medina, and C. Soler, The effects of agriculture on the volcanic aquifers of the canary islands, *Environmental Geology*, 5(4), 225–231, 1983. 61
- Custodio, E., L. Lopez Garcia, and E. Amigo, Simulation in the volcanic island of Tenerife (Canary island) by mathematical model, *Hydrogéologie*, 1988. 39, 40, 49, 51, 55, 61, 65, 93, 159
- Darwin, C., *On the origin of species by means of natural selection, or the preservation of favoured races in the struggle for life*, The complete work of Charles Darwin Online, <http://darwin-online.org.uk>, 1859. 14, 124
- de Marsily, G., *Quantitative hydrogeology: groundwater hydrology for engineers*, Academic Press, Inc., Orlando Florida, 1986. 63, 162, 208, 210, 245
- Descloitres, M., M. Ritz, B. Robineau, and M. Courteaud, Electrical structure beneath the eastern collapsed flank of Piton de la Fournaise volcano, Reunion Island: Implications for the quest for groundwater, *Water Resources Research*, 33(1), 13–19, 1997. 103, 222, 241
- Descloitres, M., R. Guérin, Y. Albouy, A. Tabbagh, and M. Ritz, Improvement in TDEM sounding interpretation in presence of induced polarization. A case study in resistive rocks of the Fogo volcano, Cape Verde Islands, *Journal of Applied Geophysics*, 45(1), 1–18, 2000. 103, 222
- Dhurmea, K., R. Boojhawon, and S. Rughooputh, Geostatistical approaches for estimating rainfall over mauritius, *Tech. rep.*, University of Mauritius, 2010. 40

## REFERENCES

---

- Dixon Hydrogeology Limited, Construction and testing of TW1 and TW2 drill holes, *Tech. rep.*, 1996. xxiii, 21, 189, 191, 192, 194, 209, 210, 211
- Domingo, F., G. Sánchez, M. J. Moro, A. J. Brenner, and J. Puigdefábregas, Measurement and modelling of rainfall interception by three semi-arid canopies, *Agr. Forest Meteorol.*, *91*(3-4), 275 – 292, doi:10.1016/S0168-1923(98)00068-9, 1998. 146
- Domínguez González, C., Análisis de la variabilidad espacial y temporal de la trascolación en la isla Santa Cruz, Master's thesis, Escuela Politécnica Nacional, Facultad de ingeniería civil y ambiental, Quito, Ecuador, <http://bibdigital.epn.edu.ec/handle/15000/3982>, 2011. 131, 132, 223, 259
- d'Ozouville, N., Etude du Fonctionnement Hydrologique Dans les Iles Galápagos : caractérisation d'un milieu volcanique insulaire et préalable à la gestion de la ressource., Ph.D. thesis, Université Paris 6 Pierre et Marie Curie, 2007a. 16, 19, 21, 26, 55, 61, 93, 94, 96, 98, 102, 109, 110, 112, 124, 159, 191, 221, 223, 228
- d'Ozouville, N., Agua dulce: la realidad de un recurso crítico, *Informe Galápagos 2006-2007*, pp. 150–160, 2007b. 21, 39, 61, 124
- d'Ozouville, N., Manejo de recursos hídricos: caso de la cuenca de Pelican Bay, *Informe Galápagos 2007-2008*, pp. 158–166, 2008. 21
- d'Ozouville, N., E. Auken, K. Sorensen, S. Violette, G. de Marsily, B. Deffontaines, and G. Merlen, Extensive perched aquifer and structural implications revealed by 3D resistivity mapping in a Galapagos volcano, *Earth and Planetary Science Letters*, *269*(3-4), 517–521, 2008a. xxii, 21, 73, 79, 81, 88, 194, 220, 221, 222, 223, 230, 233, 234
- d'Ozouville, N., B. Deffontaines, J. Benveniste, U. Wegmüller, S. Violette, and G. de Marsily, DEM generation using ASAR (ENVISAT) for addressing the lack of freshwater ecosystems management, Santa Cruz Island, Galapagos, *Remote Sensing of Environment*, *112*(11), 4131–4147, 2008b. xxii, 21, 86, 88, 111, 113, 126, 187, 188, 194, 228, 229, 232
- Duncan, R., and M. Richards, Hotspots, mantle plumes, flood basalts, and true polar wander, *Rev. Geophys.*, *29*(1), 31–50, 1991. 39
- Dunkerley, D., A new method for determining the throughfall fraction and throughfall depth in vegetation canopies, *J. Hydrol.*, *385*(1-4), 65 – 75, doi:DOI:10.1016/j.jhydrol.2010.02.004, 2010. 130

## REFERENCES

---

- Dykes, A. P., Rainfall interception from a lowland tropical rainforest in Brunei, *J. Hydrol.*, 200(1-4), 260 – 279, doi:DOI:10.1016/S0022-1694(97)00023-1, 1997. 147
- Ecker, A., Groundwater behaviour in Tenerife, volcanic island (Canary Islands, Spain), *Journal of Hydrology*, 28(1), 73–86, 1976. 40
- Eden, C., and A. Timmermann, The influence of the Galapagos Islands on tropical temperatures, currents and the generation of tropical instability waves, *Geophysical Res. Lett.*, 31, L15,308, 2004. 124, 189
- Eugster, W., R. Burkard, F. Holwerda, F. N. Scatena, and L. A. Bruijnzeel, Characteristics of fog and fogwater fluxes in a Puerto Rican elfin cloud forest, *Agr. Forest Meteorol.*, 139(3-4), 288–306, doi:{10.1016/j.agrformet.2006.07.008}, 2006. 148
- Falkland, A., Tropical Island Hydrology and Water Resources Current Knowledge and Future Needs, in *Hydrology and water management in the humid tropics. Proceedings of the Second International Colloquium, Panama*, 1999. 39, 61
- Feighner, M., and M. Richards, Lithospheric structure and compensation mechanisms of the Galapagos Archipelago, *Journal of geophysical research*, 99(B 4), 6711–6729, 1994. 9
- Ferris, J., *Cyclic fluctuations of water level as a basis for determining aquifer transmissibility*, US Dept. of the Interior, Geological Survey, Water Resources Division, Ground Water Branch, 1952. 49, 201, 205
- Fetter, C., *Applied Hydrogeology*, 691 pp., Prentice Hall, 1994. 98, 102
- Folio, J.-L., Distribution de la perméabilité dans le massif du Piton de la Fournaise : Apport à la connaissance du foncitionnement hydrogéologique d'un volcan-bouclier, Ph.D. thesis, Université de la Réunion, 2001. 49, 53, 216
- Foster, P., The potential negative impacts of global climate change on tropical montane cloud forests, *Earth-Sci. Rev.*, 55(1-2), 73 – 106, doi:DOI:10.1016/S0012-8252(01)00056-3, 2001. 123
- Fowler, C., *The Solid Earth - An Introduction to Global Geophysics (Second Edition)*, Cambridge University Press, 2005. 42, 45, 46
- Frumau, K. F., L. A. Bruijnzeel, and C. Tobón, Precipitation measurement and derivation of precipitation inclination in a windy mountainous area in northern Costa Rica, *Hydrol. Process.*, 25, 499–509, 2011. 131

## REFERENCES

---

- Frumau, K. F. A., L. A. Bruijnzeel, and C. Tobón, Hydrological measurement protocol for montane cloud forest. Annex 2, Final Technical Report DFID-FRP Project R7991, *Tech. rep.*, VU University, Amsterdam and Aylesford, UK: Forestry Research Program of the UK Department for International Development, <http://www.falw.vu/~fiesta/>, 2006. 147
- Gabriel, G., and L. Jauze, Fog water interception by *Sophora denudata* trees in a Reunion upper-montane forest, Indian Ocean, *Atmos. Res.*, *87*(3-4), 338–351, doi:{10.1016/i.atmosres.2007.11.014}, 2008. 54, 123
- García-Santos, G., An ecohydrological and soils study in a montane cloud forest in the national park of garajonay, la gomera (canary islands, spain), Ph.D. thesis, PhD Thesis, VU University Amsterdam, Amsterdam, The Netherlands., 2007. 146, 150
- García-Santos, G., and L. A. Bruijnzeel, Rainfall, fog and throughfall dynamics in a subtropical ridge top cloud forest, National Park of Garajonay (La Gomera, Canary Islands, Spain), *Hydrol. Process.*, *25*, 411–417, 2011. 54, 123
- García-Rodríguez, L., Seawater desalination driven by renewable energies: a review, *Desalination*, *143*(2), 103 – 113, doi:DOI:10.1016/S0011-9164(02)00232-1, 2002. 39
- Gash, J. H. C., Analytical model of rainfall interception by forests, *Q. J. Roy. Meteorol. Soc.*, *105*(443), 43–55, 1979. 123, 134, 135, 146, 151
- Gash, J. H. C., and A. J. Morton, An application of the Rutter model to the estimation of the interception loss from Thetford forest, *J. Hydrol.*, *38*(1-2), 49–58, 1978. 133, 134, 146
- Gash, J. H. C., F. Valente, and J. S. David, Estimates and measurements of evaporation from wet, sparse pine forest in Portugal, *Agr. Forest Meteorol.*, *94*(2), 149 – 158, doi:10.1016/S0168-1923(99)00008-8, 1999. 123
- Geist, D., and B. Reynolds, A Field Trip Guide to the Geology of the Galapagos Islands, *Penrose Conference on the Evolution of Ocean Island Volcanoes sponsored by the Geological Society of America, IAVCEI, and the Charles Darwin Foundation*, 1998. 8, 94, 113, 187, 188
- Geist, D., A. McBirney, and R. Duncan, Geology of Santa Fe Island: The oldest Galápagos volcano, *Journal of Volcanology and Geothermal Research*, *26*(3-4), 203–212, 1985. 198

## REFERENCES

---

- Geist, D., A. McBirney, and R. Duncan, Geology and petrogenesis of lavas from San Cristobal Island, Galapagos Archipelago, *Bulletin of the Geological Society of America*, 97(5), 555–566, 1986. 40, 94, 95, 97, 98, 106
- Geist, D., W. White, F. Albarede, K. Harpp, R. Reynolds, J. Blichert-Toft, and M. Kurz, Volcanic evolution in the Galapagos: the dissected shield of Volcan Ecuador, *Geochemistry Geophysics Geosystems*, 3(10), 1061, 2002. 198
- Geist, D., B. A. Diefenbach, D. J. Fornari, M. D. Kurz, K. Harpp, and J. Blusztajn, Construction of the Galapagos platform by large submarine volcanic terraces, *Geochemistry Geophysics Geosystems*, 9, doi:{10.1029/2007GC001795}, 2008. 7, 8
- Geist, D. J., Geology and Petrology of San Cristobal Island, Galapagos Archipelago, Ph.D. thesis, University of Oregon, 1985. 112, 113
- Giambelluca, T., M. Nullet, and T. Schroeder, Rainfall Atlas of Hawai'i, *Tech. rep.*, Water Resources Research Center and Departement of Meteorology, University of Hawaii at Manoa, 1986. 40, 54
- Giambelluca, T. W., J. Fox, S. Yarnasarn, P. Onibutr, and M. A. Nullet, Dry-season radiation balance of land covers replacing forest in northern Thailand, *Agr. Forest Meteorol.*, 95(1), 53 – 65, doi:DOI:10.1016/S0168-1923(99)00016-7, 1999. 130
- Giambelluca, T. W., J. K. DeLay, M. A. Nullet, M. A. Scholl, and S. B. Gingerich, Canopy water balance of windward and leeward Hawaiian cloud forests on Haleakalā, Maui, Hawai'i, *Hydrol. Process.*, 25, 438–447, 2011. 54, 123, 148
- Giambelluca, W. T., and D. Nullet, Influence of the trade-wind inversion on the climate of a leeward mountain slope in Hawaii, *Clim. Res.*, 1, 207–216, 1991. 124
- Gingerich, S., Numerical modelling of vertically extensive groundwater bodies in Maui, Hawaii: an alternative to perched aquifers, *IAHS Publication*, pp. 167–174, 1998. 51, 53, 55, 58, 65, 159, 194
- Gingerich, S., Estimating transmissivity and storage properties from aquifer tests in the southern Lihue Basin, *Kauai, Hawaii: US Geological Survey Water-Resources Investigations Report*, pp. 99–4066, 1999. 49, 52, 208
- Gingerich, S., and C. Voss, Three-dimensional variable-density flow simulation of a coastal aquifer in southern Oahu, Hawaii, USA, *Hydrogeology Journal*, 13(2), 436–450, 2005. 46, 49, 51, 55, 58, 61, 159

## REFERENCES

---

- Gingerich, S. B., and D. S. Oki, Ground Water in Hawaii, *Tech. rep.*, USGS Pacific Islands Water Science Center, 2000. 54, 55, 57, 61, 107, 159
- Glover, R., The pattern of fresh-water flow in a coastal aquifer, *Journal of Geophysical Research*, 64(4), 457–459, 1959. 165, 167, 169
- Grehan, J., Biogeography and evolution of the Galapagos: integration of the biological and geological evidence, *Biological Journal of the Linnean Society*, 74(3), 267–287, 2001. 13, 14
- Gudmundsson, A., Emplacement and arrest of sheets and dykes in central volcanoes, *Journal of Volcanology and Geothermal Research*, 116(3-4), 279–298, 2002. 46, 47
- Guyot-Tephany, J., Perceptions, usages et gestion de l'eau à Santa Cruz, Galápagos, Equateur, Ph.D. thesis, Département de Géographie de l'Université de Metz Paul Verlaine, 2010. 20
- Hafkenscheid, R. L. L. J., L. A. Bruijnzeel, D. J. R. A. M., and B. N. J., Water Budgets of two upper montane rain forests of contrasting stature in the Blue Mountains, Jamaica, in *Proceedings of the Second International Colloquium on Hydrology and Water Management*, Gladwell JS (ed). Cathalac: Panamá City, Panamá, 2002. 146
- Hahn, J., Y. Lee, N. Kim, C. Hahn, and S. Lee, The groundwater resources and sustainable yield of Cheju volcanic island, Korea, *Environmental Geology*, 33(1), 43–53, 1997. 40
- Hamann, O., On climatic conditions, vegetation types, and leaf size in the Galapagos Islands, *Biotropica*, 11(2), 101–122, 1979. 12, 126, 127, 223, 224
- Healy, R., *Estimating groundwater recharge*, Cambridge University Press, 2010. 229
- Heilweil, V. M., D. K. Solomon, S. B. Gingerich, and I. M. Verstraeten, Oxygen, hydrogen, and helium isotopes for investigating groundwater systems of the Cape Verde Islands, West Africa, *Hydrogeology Journal*, 17(5), 1157–1174, doi: {10.1007/s10040-009-0434-2}, 2009. 40, 55, 93, 159
- Henry, H., Salt intrusion into fresh-water aquifers, *Journal of Geophysical Research*, 64(11), 1911–1919, 1959. 165, 169
- Herrera, C., and E. Custodio, Conceptual hydrogeological model of volcanic Easter Island (Chile) after chemical and isotopic surveys, *Hydrogeology Journal*, 16(7), 1329–1348, doi: {10.1007/s10040-008-0316-z}, 2008. 40, 58, 159

## REFERENCES

---

- Hey, R., G. Johnson, and A. Lowrie, Recent plate motions in the Galapagos area, *Bulletin of the Geological Society of America*, 88(10), 1385–1403, 1977. 7
- Hinds, J., S. Ge, and C. Fridrich, Numerical Modeling of Perched Water Under Yucca Mountain, Nevada, *Ground Water*, 37(4), 498–504, 1999. 59
- Hölscher, D., L. Köhler, A. I. J. M. van Dijk, and L. A. Bruijnzeel, The importance of epiphytes to total rainfall interception by a tropical montane rain forest in Costa Rica, *J. Hydrol.*, 292(1-4), 308 – 322, doi:10.1016/j.jhydrol.2004.01.015, 2004. 140
- Holwerda, F., Water and energy budgets of rain forests along an elevation gradient under maritime tropical conditions, Ph.D. thesis, Vrije Universiteit Amsterdam, 2005. 130
- Holwerda, F., R. Burkard, W. Eugster, F. N. Scatena, A. G. C. A. Meesters, and L. A. Bruijnzeel, Estimating fog deposition at a Puerto Rican elfin cloud forest site: comparison of the water budget and eddy covariance methods, *Hydrol. Process.*, 20(13), 2669–2692, doi:{10.1002/hyp.6065}, 2006a. 123, 146, 147, 148
- Holwerda, F., F. N. Scatena, and L. A. Bruijnzeel, Throughfall in a Puerto Rican lower montane rain forest: A comparison of sampling strategies, *J. Hydrol.*, 327(3-4), 592 – 602, doi:DOI:10.1016/j.jhydrol.2005.12.014, 2006b. 131, 132, 147
- Holwerda, F., L. A. Bruijnzeel, L. E. Munoz-Villers, M. Equihua, and H. Asbjornsen, Rainfall and cloud water interception in mature and secondary lower montane cloud forests of central Veracruz, Mexico, *J. Hydrol.*, 384(1-2), 84–96, doi:{10.1016/j.jhydrol.2010.01.012}, 2010a. 123, 135, 136, 147
- Holwerda, F., L. A. Bruijnzeel, A. L. Oord, and F. N. Scatena, Fog interception in a puerto rican elfin cloud forest: a wet-canopy water budget approach, in *Tropical Montane Cloud Forests: science for conservation and management*, edited by L. Bruijnzeel, S. F.N., and H. L.S., International hydrology series - Cambridge University Press, 2010b. 123
- Holwerda, F., L. A. Bruijnzeel, and F. N. Scatena, Comparison of passive fog gauges for determining fog duration and fog interception by a Puerto Rican elfin cloud forest, *Hydrol. Process.*, 25, 367–373, 2011. 123
- Holwerda, F., L. A. Bruijnzeel, F. N. Scatena, H. F. Vugts, and A. Meesters, Wet canopy evaporation from a puerto rican lower montane rain forest: the importance of realistically estimated aerodynamic conductance, *J. Hydrol.*, 414-415, 1–15, 2012. 123, 147

## REFERENCES

---

- Hunt, Geohydrology of the island of Oahu, *Tech. rep.*, USGS Pacific Islands Water Science Center, 1996. 45, 47, 48, 50, 51, 52, 53, 58, 59, 61, 67, 113
- Hutley, L. B., D. J. Yates, D. Doley, and A. Boonsaner, Water balance of an Australian subtropical rainforest at altitude: the ecological and physiological significance of intercepted cloud and fog, *Aust. J. Bot.*, *45*(2), 311–329, 1997. 148
- INEC-CGG, Encuesta de Condiciones de Vida 2009-2010, *Tech. rep.*, Instituto Nacional de Estadística y Censos, Quito, Ecuador, 2010. 6, 18, 19, 20, 93, 124, 126
- Ingala, Pronareg, and Orstom, Inventario cartografico de los recursos naturales, geomorfologia, vegetacion, ecologicos, y biofisicos de las islas Galápagos, Ecuador, 1989. 21, 96, 98
- Ingebritsen, S., and M. Scholl, The hydrogeology of Kilauea volcano, *Geothermics*, *22*(4), 255–270, 1993. 49, 61, 106
- ISTAC-IET, Estadística de Movimientos Turísticos en Fronteras de Canarias en 2010 (FRONTUR-Canarias), *Tech. rep.*, Instituto Canario de Estadística (ISTAC) e Instituto de Estudios Turísticos (IET), 2010. 18
- Izuka, S., Effects of Irrigation, Drought, and Ground-Water Withdrawals on Ground-Water Levels in the Southern Lihue Basin, Kauai, Hawaii, *Tech. rep.*, USGS Pacific Islands Water Science Center and Geological Survey (US), 2006. 61
- Izuka, S., and S. Gingerich, Ground water in the southern Lihue Basin, Kauai, Hawaii, *Tech. rep.*, U.S. Geological Survey Survey Water-Resources Investigations Report 98-4031,, 1998a. 58, 59
- Izuka, S., and S. Gingerich, Estimation of the depth to the fresh-water/salt-water interface from vertical head gradients in wells in coastal and island aquifers, *Hydrogeology Journal*, *6*(3), 365–373, 1998b. 58, 103, 106
- Izuka, S., and S. Gingerich, A thick lens of fresh groundwater in the southern Lihue Basin, Kauai, Hawaii, USA, *Hydrogeology Journal*, *11*(2), 240–248, 2003. 51, 55, 58, 65, 67, 93, 106, 159
- Izuka, S. K., D. S. Oki, and J. A. Engott, Simple method for estimating groundwater recharge on tropical islands, *Journal of Hydrology*, *387*(1-2), 81 – 89, doi:DOI:10.1016/j.jhydrol.2010.03.034, 2010. 54, 229

## REFERENCES

---

- Jackson, I. J., Relationships between rainfall parameters and interception by tropical forest, *J. Hydrol.*, *24*(3-4), 215 – 238, doi:10.1016/0022-1694(75)90082-7, 1975. 146
- Jäger, H., I. Kowarik, and A. Tye, Destruction without extinction: long-term impacts of an invasive tree species on Galápagos highland vegetation, *J. Ecol.*, *97*, 1252–1263, doi:10.1111/j.1365-2745.2009.01578.x, 2009. 124, 127
- Jawaheer, K., and V. Proag, Groundwater aquifers of Mauritius, *Hydrogéologie*, *2*, 125–134, 1988. 40
- Jefferson, A., G. Grant, S. Lewis, and S. Lancaster, Coevolution of hydrology and topography on a basalt landscape in the Oregon Cascade Range, USA, *Earth Surface Processes and Landforms*, *35*(7), 803–816, 2010. 67
- Join, J., Caractérisation hydrogéologique du milieu volcanique insulaire. Piton des neiges, île de la Réunion, Ph.D. thesis, Université de Montpellier 2, France, 1991. 48, 52
- Join, J., J. Folio, and B. Robineau, Aquifers and groundwater within active shield volcanoes. Evolution of conceptual models in the Piton de la Fournaise volcano, *Journal of Volcanology and Geothermal Research*, *147*(1-2), 187–201, 2005. xix, 44, 51, 57, 58, 159
- Kauahikaua, J., Geophysical characteristics of the hydrothermal systems of Kilauea volcano, Hawaii, *Geothermics*, *22*(4), 271 – 299, doi:DOI:10.1016/0375-6505(93)90004-7, 1993. 194
- Keller, G., L. Grose, J. Murray, and C. Skokan, Results of an experimental drill hole at the summit of Kilauea volcano, Hawaii, *Journal of Volcanology and Geothermal Research*, *5*(3-4), 345–385, 1979. 48, 53, 194
- Khaleel, R., Scale Dependence of continuum models for fractured basalts, *Water Resources Research*, *25*(8), 1847–1855, 1989. 48, 49, 198, 211, 213, 214
- Kimmins, J. P., Some statistical aspects of sampling throughfall precipitation in nutrient cycling studies in British Columbian coastal forests, *Ecology*, *54*(5), 1008–1019, doi:{10.2307/1935567}, 1973. 132
- Klaassen, W., Evaporation from rain-wetted forest in relation to canopy wetness, canopy cover, and net radiation, *Water Resour. Res.*, *37*(12), 3227–3236, 2001. 134, 135

## REFERENCES

---

- Köhler, L., C. Tobón, K. Frumau, and L. A. Bruijnzeel, Biomass and water storage dynamics of epiphytes in old-growth and secondary montane cloud forest stands in Costa Rica, *Plant Ecol.*, *193*, 171–184, 10.1007/s11258-006-9256-7, 2007. 140
- Kolivras, K. N., and A. C. Comrie, Regionalization and variability of precipitation in Hawaii, *Phys. Geogr.*, *28*(1), 76–96, 2007. 124
- Lachassagne, P., R. Wyns, P. Bérard, T. Bruel, L. Chéry, T. Coutand, J. Desprats, and P. Strat, Exploitation of High-Yields in Hard-Rock Aquifers: Down-scaling Methodology Combining GIS and Multicriteria Analysis to Delineate Field Prospecting Zones, *Ground Water*, *39*(4), 568–581, 2001. 187
- Lawton, R. O., U. S. Nair, R. A. Pielke, and R. M. Welch, Climatic impact of tropical lowland deforestation on nearby montane cloud forests, *Science*, *294*(5542), 584, 2001. 123
- Link, T. E., M. Unsworth, and D. Marks, The dynamics of rainfall interception by a seasonal temperate rainforest, *Agr. Forest Meteorol.*, *124*(3-4), 171–191, 2004. 135, 146, 151
- Liu, J., Investigación de la Calidad Bacteriológica del Agua y de las Enfermedades Relacionadas al Agua en la Isla Santa Cruz - Galápagos, *Tech. rep.*, Fundación Charles Darwin and Fulbright Ecuador, Becaria, 2011. 20
- Liu, S. G., Evaluation of the Liu model for predicting rainfall interception in forests world-wide, *Hydrol. Process.*, *15*(12), 2341–2360, 2001. 134
- Llorens, P., Rainfall interception by a *Pinus sylvestris* forest patch overgrown in a Mediterranean mountainous abandoned area II. Assessment of the applicability of Gash's analytical model, *J. Hydrol.*, *199*(3-4), 346 – 359, doi:DOI:10.1016/S0022-1694(96)03335-5, 1997. 146
- Llorens, P., and F. Gallart, A simplified method for forest water storage capacity measurement, *J. Hydrol.*, *240*(1-2), 131 – 144, doi:DOI:10.1016/S0022-1694(00)00339-5, 2000. 130
- Llorens, P., R. Poch, J. Latron, and F. Gallart, Rainfall interception by a *Pinus sylvestris* forest patch overgrown in a Mediterranean mountainous abandoned area I. Monitoring design and results down to the event scale, *J. Hydrol.*, *199*(3-4), 331 – 345, doi:DOI:10.1016/S0022-1694(96)03334-3, 1997. 146
- Luszczynski, N., Head and flow of ground water of variable density, *Journal of Geophysical Research*, *66*(12), 4247–4256, 1961. 170, 173

## REFERENCES

---

- Lénat, J., D. Fitterman, D. Jackson, and P. Labazuy, Geoelectrical structure of the central zone of Piton de la Fournaise volcano (Réunion), *Bulletin of Volcanology*, 62(2), 75–89, 2000. 103, 221, 222
- Macfarlane, C., M. Hoffman, D. Eamus, N. Kerp, S. Higginson, R. McMurtrie, and M. Adams, Estimation of leaf area index in eucalypt forest using digital photography, *Agr. Forest Meteorol.*, 143(3-4), 176–188, 2007. 128, 130
- Mark R. Underwood, C. I. V., Frank L. Peterson, Groundwater Lens Dynamic of Atoll Islands, *Water Resources Research*, 28, 1992. 41
- Martel, S., and J. Langley, Propagation of normal faults to the surface in basalt, Koaie fault system, Hawaii, *Journal of Structural Geology*, 28(12), 2123–2143, 2006. 48, 198
- Massman, W. J., The derivation and validation of a new model for the interception of rainfall by forests, *Agr. Meteorol.*, 28(3), 261 – 286, doi:DOI: 10.1016/0002-1571(83)90031-6, 1983. 146
- McBirney, A., and H. Williams, *Geology and petrology of the Galapagos Islands*, Geological Society of America, 1969. 9, 21, 94, 188
- McJannet, D., J. Wallace, P. Fitch, M. Disher, and P. Reddell, Water balance of tropical rainforest canopies in north Queensland, Australia, *Hydrol. Process.*, 21(25), 3473–3484, doi:10.1002/hyp.6618, 2007a. 147
- McJannet, D., J. Wallace, and P. Reddell, Precipitation interception in Australian tropical rainforests: I. Measurement of stemflow, throughfall and cloud interception, *Hydrol. Process.*, 21(13), 1692–1702, doi:10.1002/hyp.6347, 2007b. 123, 132, 136
- McJannet, D., J. Wallace, and P. Reddell, Precipitation interception in Australian tropical rainforests: II. Altitudinal gradients of cloud interception, stemflow, throughfall and interception, *Hydrol. Process.*, 21(13), 1703–1718, doi:10.1002/hyp.6346, 2007c. 148
- Meier, P., J. Carrera, and X. Sánchez-Vila, An evaluation of Jacob’s method for the interpretation of pumping tests in heterogeneous formations, *Water Resources Research*, 34(5), 1011–1025, 1998. 49, 211
- Meinzer, O., *Ground water in the Hawaiian Islands: Geology and water resources of the Kau district, Hawaii*, vol. 616, chap. Ground water in the Hawaiian Islands, pp. 1–28, United States Dept. Interior, Geological Survey, 1930. 55

## REFERENCES

---

- Miller, K., et al., The phanerozoic record of global sea-level change, *Science*, *310*(5752), 1293–1298, doi:{10.1126/science.1116412}, 2005. 10
- Mittelstaedt, E., and G. Ito, Plume-ridge interaction, lithospheric stresses, and the origin of near-ridge volcanic lineaments, *Geochemistry Geophysics Geosystems*, *6*, doi:{10.1029/2004GC000860}, 2005. 8, 94
- Mogi, T., K. Kusunoki, H. Kaieda, H. Ito, A. Jomori, N. Jomori, and Y. Yuuki, Grounded electrical-source airborne transient electromagnetic (GREATEM) survey of Mount Bandai, north-eastern Japan, *Exploration Geophysics*, *40*(1, Sp. Iss. SI), 1–7 Sp.Iss. SI., doi:{10.1071/EG08115}, 2009. 73
- Monteith, J. L., Evaporation and environment, *Symposia for the Society of Experimental Biology*, *19*, 205–234, 1965. 134
- Mourzenko, V. V., J.-F. Thovert, and P. M. Adler, Percolation of three-dimensional fracture networks with power-law size distribution, *Phys. Rev. E*, *72*, 036,103, doi:10.1103/PhysRevE.72.036103, 2005. 187, 217
- Mullen, I., and J. Kellett, Groundwater salinity mapping using airborne electromagnetics and borehole data within the lower Balonne catchment, Queensland, Australia, *International journal of applied earth observation and geoinformation*, *9*(2), 116–123, 2007. 73
- Muller, M., A. Hordt, and F. Neubauer, Internal structure of Mount Merapi, Indonesia, derived from long-offset transient electromagnetic data, *Journal of Geophysical Research - Solid Earth*, *107*(B9), B9, doi:{10.1029/2001JB000148}, 2002. 103, 107, 221, 222
- Muzylo, A., P. Llorens, F. Valente, J. J. Keizer, F. Domingo, and J. H. C. Gash, A review of rainfall interception modelling, *J. Hydrol.*, *370*(1-4), 191 – 206, doi:DOI:10.1016/j.jhydrol.2009.02.058, 2009. 134
- Muñoz-Villers, L. E., F. Holwerda, M. Gómez-Cárdenas, M. Equihua, H. Asbjornsen, L. A. Bruijnzeel, B. E. Marín-Castro, and C. Tobón, Water balances of old-growth and regenerating montane cloud forests in central Veracruz, Mexico, *J. Hydrol.*, *In Press, Corrected Proof*, doi:DOI:10.1016/j.jhydrol.2011.01.062, 2011. 123, 135
- National Weather Service Climate Prediction Center, ENSO Cold and Warm Episodes by Season, [http://www.cpc.ncep.noaa.gov/products/analysis\\_monitoring/ensostuff/ensoyears.shtml](http://www.cpc.ncep.noaa.gov/products/analysis_monitoring/ensostuff/ensoyears.shtml), 2011. 138, 228

## REFERENCES

---

- Návar, J., and R. B. Bryan, Fitting the analytical model of rainfall interception of Gash to individual shrubs of semi-arid vegetation in northeastern Mexico, *Agr. Forest Meteorol.*, *68*, 133 – 143, doi:10.1016/0168-1923(94)90032-9, 1994. 146
- Newman, G., G. Hohmann, and W. Anderson, Transient electromagnetic response of a 3-dimensional body in layered earth, *Geophysics*, *51*(8), 1608–1627, 1986. 73
- Nordlie, B., Morphology and structure of the western Galapagos volcanoes and a model for their origin, *Bulletin of the Geological Society of America*, *84*(9), 2931–2955, 1973. 9
- Nullet, D., J. O. Juvik, and A. Wall, A Hawaiian mountain climate cross-section, *Clim. Res.*, *5*(2), 131–137, 1995. 124
- Oki, D., Geohydrology and numerical simulation of the ground-water flow system of Molokai, Hawaii, *Tech. rep.*, USGS Water-Resources Investigations Report, 1997. 51, 52, 53, 67
- Oki, D., Geohydrology of the Central Oahu, Hawaii, Ground-Water Flow System and Numerical Simulation of the Effects of Additional Pumping, *Tech. Rep. 97-4276*, USGS Pacific Islands Water Science Center, 1998. 58, 93
- Oki, D., W. Souza, E. Bolke, and G. Bauer, Numerical analysis of the hydrogeologic controls in a layered coastal aquifer system, Oahu, Hawaii, USA, *Hydrogeology Journal*, *6*(2), 243–263, 1998. 61
- Ougier-Simonin, A., Y. Guéguen, J. Fortin, A. Schubnel, and F. Bouyer, Permeability and elastic properties of cracked glass under pressure, *Journal of Geophysical Research*, *116*, B07,203, 2011. 53, 161, 194
- Palamara, D., V. Boero Rodriguez, J. Kellett, and S. Macaulay, Salt mapping in the Lower Macquarie area, Australia, using airborne electromagnetic data, *Environmental Earth Sciences*, *61*, 613–623, 2010. 73
- Parfitt, E., and D. Peacock, Faulting in the South Flank of Kilauea Volcano, Hawai'i, *Journal of Volcanology and Geothermal Research*, *106*(3-4), 265–284, 2001. 48, 198
- Pearce, A. J., J. H. C. Gash, and J. B. Stewart, Rainfall interception in a forest stand estimated from grassland meteorological data, *J. Hydrol.*, *46*(1-2), 147 – 163, doi:10.1016/0022-1694(80)90040-2, 1980. 135

## REFERENCES

---

- Pebesma, E., Gstat user's manual, *Dept. of Physical Geography, Utrecht University, Utrecht, The Netherlands*, 2001. 77
- Pebesma, E., and C. Wesseling, Gstat: a program for geostatistical modelling, prediction and simulation, *Computers & Geosciences*, 24(1), 17–31, 1998. 76, 83
- Peterson, D. W., and R. B. Morre, Geologic History and Evolution of Geologic Concepts, Island of Hawaii, *U.S. Geological Survey Professional Papers 1350 - Volcanism in Hawaii, Chapter 7*, 149–189, 1987. 40, 44, 45, 47
- PNG, Informe Ingreso Turistas, *Tech. rep.*, Parque Nacional Galapagos, 2010. 6, 18, 126
- Podolsky, D. M., and G. P. Roberts, Growth of the volcano-flank Koa'e fault system, Hawaii, *Journal of Structural Geology*, 30(10), 1254 – 1263, doi:DOI:10.1016/j.jsg.2008.06.006, 2008. 48, 198
- Porter, D., *Journal of a Cruise made to the Pacific Ocean, by Captain David Porter, in the United States Frigate ESSEX, in the years 1812, 1813, and 1814*, Bradford and Inskeep, Philadelphia, 1815. 124
- Post, V., Fresh and saline groundwater interaction in coastal aquifers: Is our technology ready for the problems ahead?, *Hydrogeology Journal*, 13(1), 120–123, 2005. 187
- Pouchan, P., F. Faissole, L. Humbert, and G. Pelissier-Hermitte, Aspect de l'hydrogéologie en Polynésie Française, *Hydrogéologie*, 2, 169–182, 1988. 41, 59
- Prada, N., M. Olivera da Silva, and V. Cruz, Groundwater behaviour in Madeira, volcanic island (Portugal), *Hydrogeol. J*, 13, 800–812, 2005. 40, 61
- Prada, S., M. Menezes de Sequeira, C. Figueira, and M. O. da Silva, Fog precipitation and rainfall interception in the natural forests of Madeira Island (Portugal), *Agr. Forest Meteorol.*, 149, 1179–1187, 2009. 54, 123
- Pryet, A., J. Ramm, J.-P. Chilès, E. Auken, B. Deffontaines, and S. Violette, 3D resistivity gridding of large AEM datasets: A step toward enhanced geological interpretation, *Journal of Applied Geophysics*, 75(2), 277 – 283, doi:DOI:10.1016/j.jappgeo.2011.07.006, 2011. 102, 220, 230
- Pryet, A., C. Dominguez, P. Fuente Tomai, C. Chaumont, N. d'Ozouville, M. Villacís, and S. Violette, Quantification of cloud water interception along the

- 
- windward slope of Santa Cruz Island, Galapagos, *Agricultural and Forest Meteorology*, 161, 94–106, 2012. 54, 110, 189, 223, 228, 229
- R Development Core Team, R: A Language and Environment for Statistical Computing, *R Foundation for Statistical Computing, Vienna, Austria*, ISBN 3-900051-07-0, 2009. 134
- Rançon, J., P. Lerebour, and T. Auge, The Grand Brûlé exploration drilling: new data on the deep framework of the Piton de la Fournaise volcano. I: Lithostratigraphic units and volcanostructural implications, *Journal of volcanology and geothermal research*, 36(1-3), 113–127, 1989. 53
- Reid, J., A. Pfaffling, and J. Vrbancich, Airborne electromagnetic footprints in 1D earths, *Geophysics*, 71(2), G63–G72, 2006. 73
- Revil, A., A. Finizola, F. Sortino, and M. Ripepe, Geophysical investigations at Stromboli volcano, Italy: implications for ground water flow and paroxysmal activity, *Geophysical Journal International*, 157(1), 426–440, 2004. 103, 221
- Reynolds, R., D. Geist, and M. Kurz, Physical volcanology and structural development of Sierra Negra volcano, Isabela Island, Galapagos archipelago, *Bulletin of the Geological Society of America*, 107(12), 1398–1410, 1995. 9, 10
- Ritter, A., C. M. Regalado, and G. Aschan, Fog water collection in a subtropical elfin laurel forest of the Garajonay National Park (Canary Islands): a combined approach using artificial fog catchers and a physically based impaction model, *J. Hydrometeorol.*, 9(5), 920–935, doi:{10.1175/2008JHM992.1}, 2008. 131
- Ritter, A., C. M. Regalado, and G. Aschan, Fog reduces transpiration in tree species of the Canarian relict heath-laurel cloud forest (Garajonay National Park, Spain), *Tree Physiol.*, 29(4), 517–528, doi:{10.1093/treephys/tpn043}, 2009. 123
- Robineau, B., M. Ritz, M. Courteaud, and M. Descloitres, Electromagnetic Investigations of Aquifers in the Grand Brule Coastal Area of Piton de la Fournaise Volcano, Reunion Island, *Ground Water*, 35(4), 585–592, 1997. 103, 222, 241
- Rotzoll, K., Effects of groundwater withdrawal on borehole flow and salinity measured in deep monitor wells in Hawaii: implications for groundwater management, *Tech. rep.*, USGS Pacific Islands Water Science Center, 2010. 59
- Rotzoll, K., A. El-Kadi, and S. Gingerich, Estimating Hydraulic Properties of Volcanic Aquifers Using Constant-Rate and Variable-Rate Aquifer Tests, *JAWRA Journal of the American Water Resources Association*, 43(2), 334–345, 2007. 49, 52, 208, 210

## REFERENCES

---

- Rotzoll, K., D. Oki, and A. El-Kadi, Changes of freshwater-lens thickness in basaltic island aquifers overlain by thick coastal sediments, *Hydrogeology Journal*, 18(6), 1425–1436, 2010. 59, 61, 161
- Rutter, A. J., K. A. Kershaw, P. C. Robins, and A. J. Morton, A predictive model of rainfall interception in forests, 1. Derivation of the model from observations in a plantation of Corsican pine, *Agr. Meteorol.*, 9, 367 – 384, doi:DOI:10.1016/0002-1571(71)90034-3, 1972. 123, 132, 133, 135
- Rutter, A. J., A. J. Morton, and P. C. Robins, A predictive model of rainfall interception in forests. II. Generalization of the model and comparison with observations in some coniferous and hardwood stands, *J. Appl. Ecol.*, 12(1), 367–380, 1975. 132, 133, 134, 135
- Saar, M., and M. Manga, Depth dependence of permeability in the Oregon Cascades inferred from hydrogeologic, thermal, seismic, and magmatic modeling constraints, *Journal of Geophysical Research, Solid Earth*, 109, B04,204, 2004. 53, 161, 194
- Sachs, J. P., and S. N. Ladd, Climate and oceanography of the Galapagos in the 21st century: expected changes and research needs, *Galapagos Res.*, 67, 50–54, 2010. 13, 124
- Scanlon, B. R., R. W. Healy, and P. G. Cook, Choosing appropriate techniques for quantifying groundwater recharge, *Hydrogeol. J.*, 10(1), 18–39, doi:{10.1007/210040-00101762-2}, 2002. 229
- Scatena, F. N., Watershed scale rainfall interception on two forested watersheds in the Luquillo Mountains of Puerto Rico, *J. Hydrol.*, 113(1-4), 89 – 102, doi: DOI:10.1016/0022-1694(90)90168-W, 1990. 147
- Scatena, F. N., L. Bruijnzeel, P. Bubb, and S. Das, Setting the stage, in *Tropical Montane Cloud Forests: science for conservation and management*, edited by B. L.A., S. F.N., and H. L.S., International Hydrology Series - Cambridge University Press, 2010. 127
- Schellekens, J., F. N. Scatena, L. A. Bruijnzeel, and A. J. Wickel, Modelling rainfall interception by a lowland tropical rain forest in northeastern Puerto Rico, *J. Hydrol.*, 225(3-4), 168 – 184, doi:DOI:10.1016/S0022-1694(99)00157-2, 1999. 134, 147
- Schellekens, J., L. A. Bruijnzeel, F. N. Scatena, N. J. Bink, and F. Holwerda, Evaporation from a tropical rain forest, Luquillo Experimental Forest, eastern Puerto Rico, *Water Resour. Res.*, 36(8), 2183–2196, 2000. 147

## REFERENCES

---

- Sharon, D., The distribution of hydrologically effective rainfall incident on sloping ground, *J. Hydrol.*, 46(1-2), 165–188, 1980. 131
- Simkin, T., Geology of Galapagos, *Biological Journal of the Linnean Society*, 21(1-2), 61–75, 1984. 7, 8, 9, 10, 13, 21, 198
- Singhal, B., and R. Gupta, *Applied Hydrogeology of Fractured Rocks*, chap. Hydrogeology of Volcanic Rocks, pp. 257–268, Springer Netherlands, 2010. 52
- Slooten, L. J., J. Carrera, E. Castro, and D. Fernandez-Garcia, A sensitivity analysis of tide-induced head fluctuations in coastal aquifers, *Journal of Hydrology*, 393(3-4), 370 – 380, doi:DOI:10.1016/j.jhydrol.2010.08.032, 2010. 49, 169, 216
- Snell, H. L., and S. Rea, The 1997-98 El Niño in Galapagos: can 34 years of data estimate 120 years of pattern, *Noticias de Galápagos*, 60, 1999. 13, 124, 189
- Soler, O., R. Meteo-France. Direction interregionale. Reunion, and B. d'étude climatologique, *Atlas climatique de la Réunion*, Météo-France, Direction interrégionale de la Réunion, 1997. 40, 54
- Souza, W., and C. Voss, Analysis of an anisotropic coastal aquifer system using variable-density flow and solute transport simulation, *Journal of Hydrology(Amsterdam)*, 92(1), 17–41, 1987. 50, 58
- Stadtmüller, T., *Cloud Forests in the Humid Tropics: a bibliographic review*, CATIE, Turrialba, Costa Rica, 1987. 127
- Staelens, J., A. D. Schrijver, K. Verheyen, and N. E. Verhoest, Spatial variability and temporal stability of throughfall water under a dominant beech (*Fagus sylvatica* L.) tree in relationship to canopy cover, *J. Hydrol.*, 330(3-4), 651 – 662, doi:DOI:10.1016/j.jhydrol.2006.04.032, 2006. 131
- Steuer, A., B. Siemon, and E. Auken, A comparison of helicopter-borne electromagnetics in frequency- and time-domain at the Cuxhaven valley in Northern Germany, *Journal of Applied Geophysics*, 67(3, Sp. Iss. SI), 194–205, doi: {10.1016/j.jappgeo.2007.07.001}, 2009. 73
- Still, C. J., P. N. Foster, and S. H. Schneider, Simulating the effects of climate change on tropical montane cloud forests, *Nature*, 398(6728), 608–610, 1999. 123
- Supper, R., K. Motschka, A. Ahl, P. Bauer-Gottwein, B. Gondwe, G. Alonso, A. Romer, D. Ottowitz, and W. Kinzelbach, Spatial mapping of submerged cave systems by means of airborne electromagnetics: an emerging technology

## REFERENCES

---

- to support protection of endangered karst aquifers, *Near Surface Geophysics*, 7(5-6), 613–627, 2009. 73
- Takahashi, M., T. W. Giambelluca, R. G. Mudd, J. K. DeLay, M. A. Nullet, and G. P. Asner, Rainfall partitioning and cloud water interception in native forest and invaded forest in Hawai'i Volcanoes National Park, *Hydrol. Process.*, 25, 448–464, 2011. 54, 123, 136, 137, 146, 150
- Thimonier, A., Measurement of atmospheric deposition under forest canopies: some recommendations for equipment and sampling design, *Environ. Monit. and Assess.*, 52(3), 353–387, 1998. 132
- Thouret, J., Volcanic geomorphology - an overview, *Earth Science Reviews*, 47(1-2), 95–131, 1999. 42, 43, 44, 46, 48, 160
- Townley, L. R., The response of aquifers to periodic forcing, *Advances in Water Resources*, 18(3), 125 – 146, doi:DOI:10.1016/0309-1708(95)00008-7, 1995. 216
- Trefry, M. G., Periodic forcing in composite aquifers, *Advances in Water Resources*, 22(6), 645 – 656, doi:DOI:10.1016/S0309-1708(98)00037-2, 1999. 216
- Trueman, M., and N. d'Ozouville, Characterizing the Galapagos terrestrial climate in the face of global climate change, *Galapagos Res.*, 67, 26–37, 2010. 10, 12, 40, 96, 111, 123, 124, 126, 127, 189, 223, 227
- Upton, B., and W. Wadsworth, The basalts of Reunion Island, Indian Ocean, *Bulletin of Volcanology*, 29(1), 7–23, 1966. 40
- Vacher, H., and T. Quinn, *Geology and hydrogeology of carbonate islands*, vol. 54, Elsevier Science Ltd, 1997. 41, 44
- Valente, F., J. S. David, and J. H. C. Gash, Modelling interception loss for two sparse eucalypt and pine forests in central Portugal using reformulated Rutter and Gash analytical models, *J. Hydrol.*, 190(1-2), 141–162, 1997. 132, 133, 134, 146
- Valerio, A., A. Tallarico, and M. Dragoni, Mechanisms of formation of lava tubes, *Journal of Geophysical Research-Solid Earth*, 113(B8), doi:{10.1029/2007JB005435}, 2008. 44
- Verruijt, A., A note on the Ghyben-Herberg Formula, *Bulletin of the International Association of Scientific Hydrology*, 1968. xxi, 165, 166, 167
- Veza, J. M., Desalination in the Canary Islands: an update, *Desalination*, 133(3), 259 – 270, doi:DOI:10.1016/S0011-9164(01)00106-0, 2001. 39

## REFERENCES

---

- Viezzoli, A., A. V. Christiansen, E. Auken, and K. Sorensen, Quasi-3D modeling of airborne TEM data by spatially constrained inversion, *Geophysics*, *73*(3), F105–F113, doi:10.1190/1.2895521, 2008. 73, 81, 102, 220, 230
- Viezzoli, A., T. Munday, E. Auken, and A. Christiansen, Accurate quasi 3D versus practical full 3D inversion of AEM data, *Preview*, pp. 23–31, 2010. 73, 230
- Vilain, G., Emissions de N<sub>2</sub>O dans un versant agricole de grandes cultures (Brie, Bassin de la Seine) Observations, expérimentations et modélisation dans un continuum "plateau/zone enherbée/rivière, Ph.D. thesis, Université Pierre et Marie Curie, 2010. x
- Villegas, C., C. Tobón, and D. D. Breshears, Fog interception by non-vascular epiphytes in tropical montane cloud forests: dependencies on gauge type and meteorological conditions, *Hydrol. Process.*, *22*(14), 2484–2492, doi:{10.1002/hyp.6844}, 2008. 148
- Violette, S., E. Ledoux, P. Goblet, and J. Carbonnel, Hydrologic and thermal modeling of an active volcano: the Piton de la Fournaise, Reunion, *Journal of Hydrology*, *191*(1-4), 37–63, 1997. xix, 49, 51, 55, 60, 61, 93, 159
- Voss, C. I., and A. M. Provost, SUTRA : A Model for Saturated-Unsaturated Variable-Density Ground-Water Flow with Solute and Energy Transport, *Tech. Rep. 02-4231*, U.S. Department of the Interior - U.S. Geological Survey, 2010. 173
- Wallace, J., and D. McJannet, On interception modelling of a lowland coastal rainforest in northern Queensland, Australia, *J. Hydrol.*, *329*(3-4), 477–488, 2006. 135
- Walter, T., V. Troll, B. Cailleau, A. Belousov, H. Schmincke, F. Amelung, and P. Von der Bogaard, Rift zone reorganization through flank instability in ocean island volcanoes: an example from Tenerife, Canary Islands, *Bulletin of Volcanology*, *67*(4), 281–291, doi:{10.1007/s00445-004-0352-z}, 2005. 47, 48
- Weathers, K. C., G. M. Lovett, and G. E. Likens, Cloud deposition to a spruce forest edge, *Atmos. Environ.*, *29*(6), 665 – 672, doi:10.1016/1352-2310(94)00317-E, 1995. 128
- Whittier, R. B., K. Rotzoll, S. Dhal, A. I. El-Kadi, C. Ray, and D. Chang, Groundwater source assessment program for the state of Hawaii, USA: methodology and example application, *Hydrogeology Journal*, *18*(3), 711–723, doi:{10.1007/s10040-009-0548-6}, 2010. 39

## REFERENCES

---

- Wilson, D., and R. Hey, History of rift propagation and magnetization intensity for the Cocos-Nazca spreading center, *Journal of Geophysical Research-Solid Earth*, 100(B6), 1041–1056, 1995. 8
- Won, J., J. Kim, G. Koh, and J. Lee, Evaluation of hydrogeological characteristics in Jeju Island, Korea, *Geosciences Journal*, 9(1), 33–46, 2005. 40
- Won, J., J. Lee, J. Kim, and G. Koh, Groundwater occurrence on Jeju Island, Korea, *Hydrogeology Journal*, 14(4), 532–547, 2006. 40
- Woodward, D., D. Dobbs, and P. Gardiner, Drilling Seismometer Hole, Santa Cruz, Galapagos Islands, *Tech. rep.*, Institute of Geological and Nuclear Sciences (Ltd), 1996. 189, 192, 194, 242
- Wu, Y., A. Ritcey, and G. Bodvarsson, A modeling study of perched water phenomena in the unsaturated zone at Yucca Mountain, *Journal of Contaminant Hydrology*, 38(1-3), 157–184, 1999. 59
- Ziegler, A. D., T. W. Giambelluca, M. A. Nullet, R. A. Sutherland, C. Tantasarin, J. B. Vogler, and J. N. Negishi, Throughfall in an evergreen-dominated forest stand in northern Thailand: Comparison of mobile and stationary methods, *Agr. Forest Meteorol.*, 149(2), 373 – 384, doi:DOI:10.1016/j.agrformet.2008.09.002, 2009. 131, 147
- Zimmermann, B., A. Zimmermann, R. M. Lark, and H. Elsenbeer, Sampling procedures for throughfall monitoring: A simulation study, *Water Resour. Res.*, 46(1), W01,503, 2010. 131, 147

**Part VI**  
**Appendices**



# Appendix A

## Carbon footprint of this thesis

With a field of study located some 10 000 km from the lab in Paris, and several congresses abroad, the carbon footprint of this PhD thesis may be damaging for the planet.

The purpose of this aside is not to deprive next PhD students of field work and congresses. These activities were determining for my investigations and rich personal experiences.

Yet, human-induced carbon dioxide emissions are proven to induce global warming (REF). It appears important to be conscious that travelling by plane increases significantly the carbon footprint.

Destination	Reason	CO <sub>2</sub> (tons)	Times	Total
Galapagos (Ecuador)	Field work	2.26	3	6.78
San Francisco (USA)	Congress (AGU)	1.50	1	1.50
Vienna (Austria)	Congress (EGU)	0.22	1	0.22
Aarhus (Denmark)	Work Univ. Aarhus	0.24	1	0.24
Total (tons CO <sub>2</sub> ) :				8.74
Total (tons CO <sub>2</sub> /year) :				2.91

**Table A.1:** Carbon emissions per flights (roundtrip from Paris), estimation from Air-France, at <http://corporate.airfrance.com/en/sustainable-development/co2-calculator/co2-calculator/>

## A. CARBON FOOTPRINT OF THIS THESIS

---

My personal carbon emissions are estimated to 4.5 tons CO<sub>2</sub>/year ([www.carbonfootprint.com](http://www.carbonfootprint.com)). This is smaller than mean rate in France (6.2 T CO<sub>2</sub>/year), mainly because I don't have a car, and try to have a somehow "eco" way of life. If we add carbon emissions related to my flights (Table A.1), my emissions increase by 64% and exceed average value per capita in France (Fig. A.1).

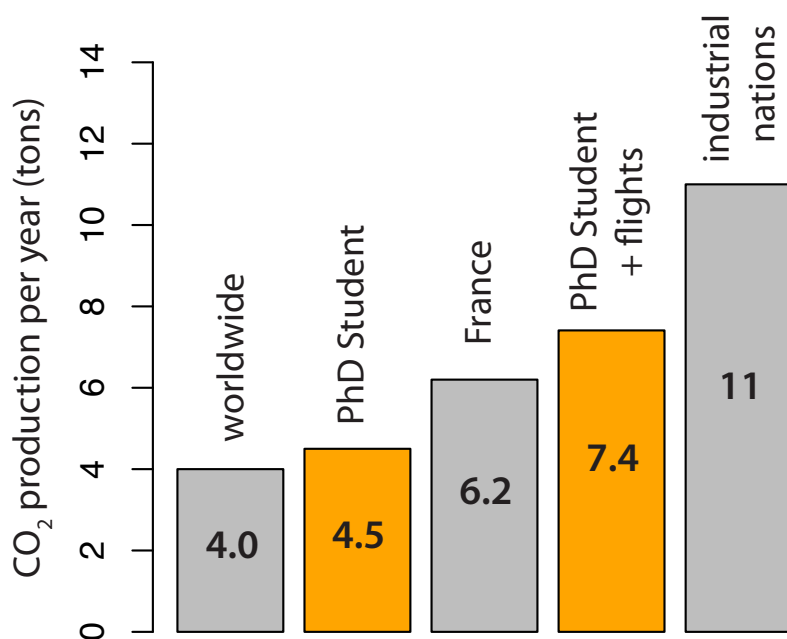


**Figure A.1:** Carbon emissions (CO<sub>2</sub>/year) . Average values in grey, PhD Student values in orange. Estimations from [www.carbonfootprint.com](http://www.carbonfootprint.com) and Table A.1.

What conclusions can we deduce from these figures? Travelling by plane, I participated to global warming, this is indisputable. Could I respond fairly, declaring that my investigations are supposed to serve sustainable development, and that my footprint may be neutral. Too early to conclude...